Waveguide sources of Photon Pairs

by

Rolf Horn

A thesis
presented to the University of Waterloo
in fulfillment of the
thesis requirement for the degree of
Doctor of Philosophy
in
Physics

Waterloo, Ontario, Canada, 2011

I hereby declare that I am the sole author of this thesis. This is a true copy of the thesis, including any required final revisions, as accepted by my examiners.

I understand that my thesis may be made electronically available to the public.

Abstract

This thesis describes various methods for producing photon pairs from waveguides. It covers relevant topics such as waveguide coupling and phase matching, along with the relevant measurement techniques used to infer photon pair production. A new proposal to solve the phase matching problem is described along with two conceptual methods for generating entangled photon pairs. Photon pairs are also experimentally demonstrated from a third novel structure called a Bragg Reflection Waveguide (BRW).

The new proposal to solve the phase matching problem is called Directional Quasi-Phase Matching (DQPM). It is a technique that exploits the directional dependence of the non-linear susceptiblity ($\chi^{(2)}$) tensor. It is aimed at those materials that do not allow birefringent phase-matching or periodic poling. In particular, it focuses on waveguides in which the interplay between the propagation direction, electric field polarizations and the nonlinearity can change the strength and sign of the nonlinear interaction periodically to achieve quasi-phasematching.

One of the new conceptual methods for generating entangled photon pairs involves a new technique that sandwiches two waveguides from two differently oriented but similar crystals together. The idea stems from the design of a Michelson interferometer which interferes the paths over which two unique photon pair processes can occur, thereby creating entanglement in any pair of photons created in the interferometer. By forcing or sandwiching the two waveguides together, the physical space that exists in the standard Micheleson type interferometer is made non-existent, and the interferometer is effectively squashed. The result is that the two unique photon pair processes actually occupy the same physical path. This benefits the stability of the interferometer in addition to miniaturizing it. The technical challenges involved in sandwiching the two waveguides are briefly discussed.

The main result of this thesis is the observation of photon pairs from the BRW. By analyzing the time correlation between two single photon detection events, spontaneous parametric down conversion (SPDC) of a picosecond pulsed ti:sapph laser is demonstrated. The process is mediated by a ridge BRW. The results show evidence for type-0, type-I and type-II phase matching of pump light at 783nm, 786nm and 789nm to down converted light that is strongly degenerate at 1566nm, 1572nm, and 1578nm respectively. The inferred efficiency of the BRW was $9.8 \cdot 10^{-9}$ photon pairs per pump photon. This contrasts with the predicted type-0 efficiency of $2.65 \cdot 10^{-11}$. This data is presented for the first time in such waveguides, and represents significant advances towards the integration of sources of quantum information into the existing telecommunications infrastructure.

Acknowledgements

This is my chance to write down something my parents can read. A reflection on the past 30 years. Basically it's been a constant effort to build little sand castles, one of the larger ones of which is an academic one.

Pointing me in this direction when i was around 9 years old – Mrs. Simpson, Mrs. Chapin and Mrs. Muir – wherever you are, those Wednesdays every other week doing CoRT freed my imagination and gave me the confidence to voice my ideas ever since. Mr. Vanstone also encouraged me without fail. Karen Gordon – in highschool – was the first person to tell me i'd do fine in an exam, which at the time, was exceedingly calming, and has stuck with me since. In university, Sara Gross, who has no idea about this and no idea who i am, asked me why i was organizing my first year schedule to avoid classes on Friday – thereby missing out on Hans Kummer's math 120 class. Hans was a wonderful professor and as a result, i dropped out of biology and approached Hugh Evans. With a very characteristic twinkle in his eye, Hugh let me into Engineering Physics after i pleaded with him at the start of 2nd year.

I then ran into a bunch of similar minds from St. Michaels College through which i met John-Pierre Paglione who convinced me that superconductivity was the end all-be all. So, i chose a 4th year project with Prof. John Harrison. John saw something in me – i have no idea what it was – and he opened the door for a post-academic career. To this day, i can't thank him enough.

After studying with John, my personal interest in badminton led me to Calgary and coincidentally to Barry Sanders. I was fortunate enough to fit with his personality. Over a short period of a year and a half, we argued and hung out, and in our fast and furious conversations, he was oddly patient enough to listen. As a result, i learned. Through him i met Richard Cleve who in an entirely different way, was also patient with my ignorance of computing protocols and algorithms. They both fostered my interest in quantum information science.

I returned to Guelph for Madeleine – my first daughter – with the intent of starting a family concurrently with an experimental Ph.D under Gregor Weihs. Besides being gifted with physical experimentation, Gregor is also a very special person. He is exceptional at seeing and understanding all kinds of viewpoints. With him, my ideas were not met with opposition, but with further questions designed for further discovery. When time afforded, conversations with him were invaluable.

All of the people mentioned above have one thing in common - despite my strong personality - they gave willingly and I will be forever indebted.

Positivity aside, there were many low points. The lowest was probably waking up to the sound of the pumps running the dilution refrigerator while living in the basement of Stirling Hall for six straight weeks. For this thesis, the lowest point was the first Christmas. Financially drained with our 100 year old house, sleep deprived and barely

keeping up with TA duties - while failing miserably at school - i fully intended to quit after Christmas 2005. So, I suppose an honorable mention should go to Richard Exon in the HR department at Research in Motion – his incompetence with setting up an interview brought me back from the brink in January 2006.

On the flip side, I have to thank my mom and dad. Though they have no idea what i do (to them i shoot lasers), they have been steadfast with love and support – even against their better judgement. I can only hope to do the same for Madeleine, Clara and Oliver. Of course, to the original lab members – Christophe Couteau and Chris Erven, thanks for the sanity and the science. The pleasure has been all mine.

Lastly, to my lifelong partner - Karen. Through all the ‘Alice’ and ‘Bob’ comments, you’ve always brought me back down to earth. Your loyalty and love has always amazed me. I couldn’t have done any of this without you.

Dedication

To Karen.

What we do, does not define who we are. What defines us is how well we rise after falling.

TABLE OF CONTENTS

LIST OF TABLES

LIST OF FIGURES

1 INTRODUCTION AND MOTIVATION

1.1 In the beginning...

This thesis discusses non-linear optical phenomena motivated by its application to quantum information technologies.

Quantum information rests on two well known but much scrutinized abilities of quantum systems. The first is the ability of a single quantum system to exist in a superposition of more than one state at a time. The second even more bizarre reality is that two properly prepared space-like separated quantum systems can be subjected to independent measurements and still demonstrate stronger than classical correlations with each other - a property called entanglement. These two abilities are perhaps the most distinguishing features of quantum mechanics. In the field of quantum information science, both entanglement and superposition represent two new ways or channels for storing information. This idea has been exploited to yield a wealth of new theoretical and experimental results. The practical fruits of this field are found in communication and computing protocols that are significantly more powerful than their classical counterparts. However, the tastier fruits, while grounded in experiment, reside in the theoretical domain where they reveal the deep connection between information and our physical world.

The segue into non-linear optics is this: Few can argue that the biggest challenge to the field is its experimental side. To date, an 'on demand' physical resource allowing good experimental control over both channels is still not yet readily available. Of the many candidate physical systems available for study, one of the more experimentally friendly is the photon, and/or photon pairs.

The current workhorse for creating single photons and photon pairs makes use of an optical wavelength conversion process called Spontaneous Parametric Down Conversion or SPDC. Borrowing some nuclear jargon, this process describes the spontaneous fission of a single photon into two daughter photons. For this process to be efficient, usually a strong laser beam containing many photons is required to interact with a non-linear crystalline material. What this creates is a reasonable possibility that one of the photons from the beam will convert into two photons of roughly half the energy and momentum of the original. Once created, the pair can be entangled [2], or one of the photons from the pair can herald the presence of the other thereby imitating a practical single photon source [3]. The single photon can then be easily placed in a superposition state using standard optical techniques. Examples of protocols that require such resources are quantum key distribution [4]), quantum teleportation [5], quantum fingerprinting [6], super-dense coding [7], and linear optics quantum computing [8].

History of SPDC – what is all that noise?

In two papers entitled Quantum Fluctuations and Noise in Parametric Processes I and II, Louisell et al [9] and Gordon et al. [10] conceived of the notion of what is now called Spontaneous Parametric Down Conversion. The first of those papers was published in 1961. In that paper, Louisell noted that the difference between the Hamiltonian for frequency conversion and the Hamiltonian for parametric amplification was that the latter could amplify zero-point fluctuations while the former was free of such 'noise'. The second paper by Gordon concluded that a classical description of parametric amplification was valid so long as one accounted for both responses. Five years later, a Russian physicist named David. N. Klyshko presented the same idea at a conference in Chernogolovka, publishing the following year in the Soviet journal JETP Letters. Some (mainly those of Russian decent) consider Klyshko as the founding father of SPDC, however, even Klyshko himself recognized the work of Louisell and those that contributed to the subject between 1961 and 1967 in later journal publications on the topic [11] including his original publication [12]. Whatever the case, it shall suffice to say that the ideas and foundations of SPDC were put in place throughout the 1960's. In particular, at the end of 1966 and the beginning of 1967, Mollow and Glauber wrote two comprehensive papers titled Quantum Theory of Parametric Amplification I and II [13, 14]. They point immediately to the necessity of a quantum mechanical treatment and began the development of formalism necessary to predict the correlations of photon counting type experiments.

Experimentally, SPDC was first observed in 1967 by two different groups. Harris et al. [15] noted the effect in Lithium Niobate ($LiNbO_3$), while Magde et al. [16] observed the effect in Ammonium Dihydrogen Phosphate (ADP). While parametric amplification was observed prior to these results, theirs were the first in a single pass regime, where the single pass parametric gain observed was much less than the single pass absorptive loss in the crystal. Thus, in such a situation, parametric amplification was forbidden to occur in classical models, and this was evidence for quantum effects in optics. Three years later, the first observation of the simultaneous nature of SPDC was observed by Burnham and Weinberg [17], marking the beginning of numerous studies involving the statistical nature of the photon pairs produced in SPDC. Most notably, during the mid 1980's, the group led by Mandel [18][19] [20] [21] published seminal papers presenting results of interference type measurements made using the photon pairs produced by SPDC. Since those experiments and with the advent of their use in quantum information type protocols, focus has been on the development of high performance or bright sources of SPDC [2] where the output state is tailored for a specific experiment.

Back up a little bit...Classical first!

SPDC is now routinely used in numerous labs but it remains inherently weak as it stems from fluctuations and noise. So, in a laboratory setting, (unless the experimenter is really good), it turns out that the reverse process, where two daughter photons fuse to form a higher energy parent photon, is much more accessible. To see why this is so we have to compare two different models that describe wavelength conversion. The classical model and the quantum model. From a classical perspective, when one measures the power in a beam of light, a wave picture applies. Light in the wave picture is modeled as

$$\text{light} \longrightarrow Re\{Ae^{i\omega t}\}. \tag{1.1}$$

When 'fusing' two fundamental (F) waves together the result is a different wave with twice the frequency called the second harmonic (SH). To get a wave with twice the frequency, equation 1.1 tells us to multiply two waves with the fundamental frequency ω. This means that in the classical picture, the fused SH wave is the square of the original fundamental wave. Furthermore, to measure the power, the amplitude of the wave is again multiplied with itself. Thus, for the second harmonic generation (SHG) process, if an experimenter doubles the input laser or *pump* power, the measured output power is quadrupled. This is true only initially, so long as the pump remains relatively undepleted. That is,

$$P_{SH} \propto P_F^2 \tag{1.2}$$

In the quantum picture, photons are quantized waves with energy proportional to their frequency. The total number (N) of photons in a beam of light determines the total energy of the beam. When one photon fissions into two photons under energy conservation, the frequencies of those output photons have to change. Thus,

$$N_{SH} \rightarrow 2N_F \tag{1.3}$$

Because power is energy per unit of time, it is clear that doubling the power of the SH beam (doubling the number of fissionable photons) doubles the power of the down converted photons (doubles the number of fissions into photons with half the frequency). SPDC is *linear* in the power of the input 'pump' laser. The reason both reactions are referred to as non-linear will be evident later on[1] In fact, both experiments are identical, just reversed or forwarded in time. From an experimentalist viewpoint, much can be learned about the physical setting required for SPDC by using the classical equations for SHG as a *guide*. Historically, the observation of SHG only predates SPDC by about

---

[1] At first glance the two models are at odds and perhaps confusing – Nonetheless, they accurately describe the physics within their respective regimes. A small consolation is to realize that both reactions are *linear in each field*. Linearly increasing two fields, the result is quadratic, as in SHG. Linearly increasing only one, as in SPDC, the result is linear.

7 years. This is because it requires intense field amplitudes and thus was not observed until after 1960 - the year when the first pulsed Ruby laser was reported by Theodore Maiman [22]. It was the following year when, in a much cited experiment, Peter Franken observed second harmonic light by pumping quartz with intense laser light at ≈694nm [23]. Another year passed before D. A. Kleinman published his theory of the second harmonic generation of light [24]. This two year period is widely regarded as the birth of the field of Non-linear optics, and it is evident that the 1960's was a breakout decade for optics because of the laser.

1.2 Engineering

Once people get a hold of a new technology, it inevitably falls into the hands of those with an engineering mind. Thus, history aside, creating better, brighter SPDC sources is now an optimization problem. This sets the stage for the bulk of the coming thesis, where two engineered approaches to optimizing SPDC are investigated. A particular emphasis is on the 'better'. Better means compact, integratable, stable, and inexpensive.

The Main Problem - Phase matching

Inherently weak, a nonlinear optical interaction in and of itself requires two main ingredients: strong field amplitudes and highly nonlinear material. However, for appreciable nonlinear effects to be observed, a third condition is that the time over which the optical waves coherently interact should be maximized.

The third condition is naturally problematic. This is because SPDC and SHG require the fundamental and harmonic waves to interact with each other. Because their frequencies are far apart from each other, material dispersion creates the problem that their phase fronts mismatch and they do not stay coherent for very long. This decreases their effective interaction time. Some materials are birefringent, and can naturally circumvent this problem. In birefringent phase matching (BPM), the interacting waves have suitably chosen polarizations so that the birefringence effectively cancels the dispersion.

All other techniques require some kind of engineering. A particularly important technique is called quasi-phase matching (QPM) [25]. Traditional QPM methods periodically reverse the direction of the non-linear response of the material. The most common implementation is by periodic poling of a ferroelectric. The period is chosen to reverse the non-linear response of the material precisely when the accumulated phase difference between the SH and fundamental waves begins to drive energy back into the exciting field. The reversal effectively resets the phase and allows the non-linear process to continue. Traditional QPM can also be used to tailor non-linear profiles [26] as well as afford the possibility of exploiting directions in materials for non-linear interactions that would otherwise be negligible. The QPM technique, in combination with directional control afforded by an optical waveguide, underpins the main design put forth in this thesis. A good review on the subject was written by Fejer et al. [27] in 1992.

A third possibility to solve the phase matching problem involves the use of optical waveguides. Optical waveguides have an even longer history[2] the best example being the optical fiber. Optical waveguides are traditionally based on the principle of refraction. Here, light, upon entering a material, bends sharply away from the surface normal if its speed in that material is faster than the material it is exiting. If the incident angle is less than a critical angle, the light will bend back into the material it originally came from becoming effectively constrained to the material. The concept is called Total Internal Reflection (TIR), and if the material is designed properly, it can effectively contain light.

There are three important consequences of utilizing a waveguide: The first is due to the fact that a waveguide confines light and can thereby enhance the intensity of light in the guided region for the mode of interest. Further, if SPDC is facilitated in the waveguide, then its directionality enhances the photon collection process in addition to lengthening the interaction time [28].

The second is that the waveguide can display different dispersive characteristics than the bulk material from which it is made. In particular, form birefringence [29, 30], or a suitable choice of waveguide modes [31] can solve the phase-matching problem.

The third is that waveguides have the added benefit that they can be integrated. Of particular interest is the material Gallium Arsenide (GaAs), and its derivative Aluminum Gallium Arsenide (AlGaAs). GaAs is a highly nonlinear material – with a bilinear susceptibility 3 or 4 times greater than Lithium Niobate (LN). This is huge considering LN is one of the stronger nonlinear materials currently employed to facilitate SPDC. Furthermore, the transparency range of GaAs is more than double that of LN. The addition of Aluminum to form AlGaAs is an external handle to control the index of refraction. Layers of different aluminum concentration can facilitate TIR confinement via the process of TIR. Even more promising is the idea of integrating the SPDC process with other photonic structures like the laser diode. These lasers are routinely fabricated from GaAs. An in-depth review of phase matching in integrated waveguide structures has recently been published [32].

Proposed Solutions

In this thesis, two novel ideas are explored to solve this phase matching problem. As alluded to, the first proposes an alternative method that marries the light confining capabilities of waveguides with traditional quasi-phase matching techniques. It is called directional quasi-phase-matching (DQPM). The second marries the light confining ca-

---

[2] An interesting discussion can be found on the internet: http://en.wikipedia.org/wiki/Optical_fiber.

pabilities of waveguides with an alternative confinement method based on the interference of light from multiple reflectors. This effects a type of modal phase matching. The former is discussed in the chapter entitled 'Directional Quasi Phase Matching', and the latter is discussed in the chapter 'Bragg Reflection Waveguides'.

One last hurdle – Measurement and detecting SPDC

Creating efficient sources of SPDC one thing, but making an efficient measurement presents an equally difficult task. This is because SPDC is so inefficient that it requires the capability of single photon detection. I will not get into the history / development of single photon detection, but it will suffice to make the comment that equal resources are needed to improve both SPDC sources and single photon detection methods.

With this in mind, the main experimental result presented in this thesis is the observation of SPDC from ridge Bragg reflection waveguides. SPDC is inferred from data obtained from a conditional two photon coincidence measurement. What is observed experimentally is the response / detection output of two single photon detectors. A response (generated by one photon) from the first detector (Alice) conditions the second detector (Bob) to open with the expectation that a second photon will arrive there. In parallel, a timer is started by the response from Alice and stopped by a response from Bob. At a particular start-stop time t^* there is a measurably enhanced detector response from both detectors. This is called a coincidence response and the time t^* is the coincidence time. Such an experiment has its roots in the famous experiments of Hanbury-Brown and Twiss [33] and Grangier, Roger and Aspect [34]. In these experiments, a parameter was measured which could distinguish between the particle / wave nature of light. They calculated an anticorrelation parameter A,

$$A = \frac{P_c}{P_1 P_2} \tag{1.4}$$

where P_c is the probability that two detectors (1 and 2) respond at the same time (within the time resolution of the experiment), and where P_1 and P_2 are the probabilities that each individual detector responds. For random events, $P_c=P_1P_2$ and A=1. That is, the coincidence probability is precisely equal to the probability that one detector responds multiplied by the probability that the other detector responds. If P_c is greater than this random coincidence probability, then $A > 1$.[3]

From this preamble, it should be clear that the quantum mechanical version of P_c needs to be developed. In order to do this, the two photon output state of SPDC, $|\Psi_{SPDC}\rangle$ needs a derivation as well as a suitable definition for a measurement operator that models the simultaneous response of two detectors, $\hat{P}_c$. The measured response will then be

---

[3] As an unrelated remark, what Grangier et al demonstrated was a condition where A=0 – implying the particle nature of the photon.

related to the expectation value of the measurement operators acting on the quantum state of the system,

$$\langle \Psi_{SPDC} | \hat{P}_c | \Psi_{SPDC} \rangle. \tag{1.5}$$

The details of this quantum mechanical modeling are provided in the theory chapter where most of the non-linear optics and quantum optics results are given.

1.3 Future outlook - Waveguide sources of Entangled photon pairs

Throughout this Ph.D project, entanglement was frustratingly out of reach. Nonetheless, it really was the undercurrent of this thesis. In fact, the title of this thesis was originally going to be something along the lines of the section heading. As a result, ideas often came about as a result of thinking of ways to generate entanglement that circumvented some of the problems encountered by colleagues and other groups at the IQC. To conclude the thesis, the final chapter presents the fruits of such contemplation and describes two novel methods for producing polarization entangled photon sources. Unfortunately, time constraints have prohibited their experimental investigation.

What does it mean to be entangled?

The standard way of writing entanglement on a whiteboard is to take any two level quantum system and designate those levels as orthogonal states of the system. They can be labeled $|1\rangle$ and $|0\rangle$. These basis designations are typically referred to as the computational / canonical or even the standard measurement basis. For light, a photon naturally has two orthogonal polarization states, so without loss of generality, we designate $|0\rangle \rightarrow |H\rangle$ and $|1\rangle \rightarrow |V\rangle$. Two ways of writing a polarization entangled state are taken from the set of the four standard Bell states $\{|\psi^+\rangle, |\psi^-\rangle, |\phi^+\rangle, |\phi^-\rangle\}$. In the photon polarization representation, they are

$$|\psi^+\rangle = \frac{1}{\sqrt{2}}(|H\rangle|V\rangle + |V\rangle|H\rangle), \tag{1.6}$$

$$|\phi^+\rangle = \frac{1}{\sqrt{2}}(|H\rangle|H\rangle + |V\rangle|V\rangle). \tag{1.7}$$

In essence, what these equations say is the following: If an experimenter performs relevant measurements on what is promised to be a large ensemble of identically prepared two photon systems, the results will forbid the experimenter from inferring that the prepared two photon system could be represented as a tensor product of two separable systems.

Intuition

What follows is not an official interpretation of quantum mechanics, but might help the unfamiliar reader. One can think of quantum states in the context of distributions of information over the degrees of freedom of a system or systems - eg. two photons. The label ‘classical’ is given to all such systems with information distributions that correspond to what we observe everyday. Quantum systems are those that don’t have such distributions. Systems with non-classical information distributions can change into classical systems via an interaction – like a measurement. Measurements learn something about the distribution. As a sort of back-action, they in turn redistribute the information existing in the measured system accordingly. The notion of altering information distributions is not a one way street. It is possible to arrange the physical world such that the information distribution of a system can become quantum.[4] This is the idea behind creating an entangled state.

Generating Entanglement with SPDC

One way to generate entanglement is to use interferometric methods. Information is redistributed by superposing two different trajectories in space-time. If the different trajectories intersect somewhere, then along this intersection, it may be impossible to tell which original trajectory was taken unless for example a measurement is made to verify the true trajectory. This is the general concept behind an interferometer and can be accomplished in the lab using beam splitters and mirrors. One such arrangement is called a Mach-Zehnder Interferometer (MZI) (figure 1.1). A MZI has two ‘arms’ that represent the different optical paths. If the MZI is balanced, then it is impossible to tell which path was traveled by light entering and exiting the interferometer. This can enable the generation of entanglement in the following manner: Imagine that a unique type of SPDC process could occur in each arm – generating two photons accordingly. Label these processes as type ‘A’ and type ‘B’. Further imagine that upon exiting the interferometer, it is possible to split those two photons into new paths *a* and *b*. Then a measurement concerning the type of process that generated photon *a* would indicate what type of process generated photon *b* (and vice versa). In this case, ignoring a relative phase factor between the two arms, the photon pair can emerge in an entangled state of the following form:

$$\psi\rangle = \frac{1}{\sqrt{2}}\left(|A\rangle_a|A\rangle_b + |B\rangle_a|B\rangle_b\right) \tag{1.8}$$

This holds true on two accounts: 1) one and only one SPDC process can occur within

---

[4] It appears that the distributions are not granular, and that there are an infinite number of distributions any one system may have – over the distinct degrees of freedom available.

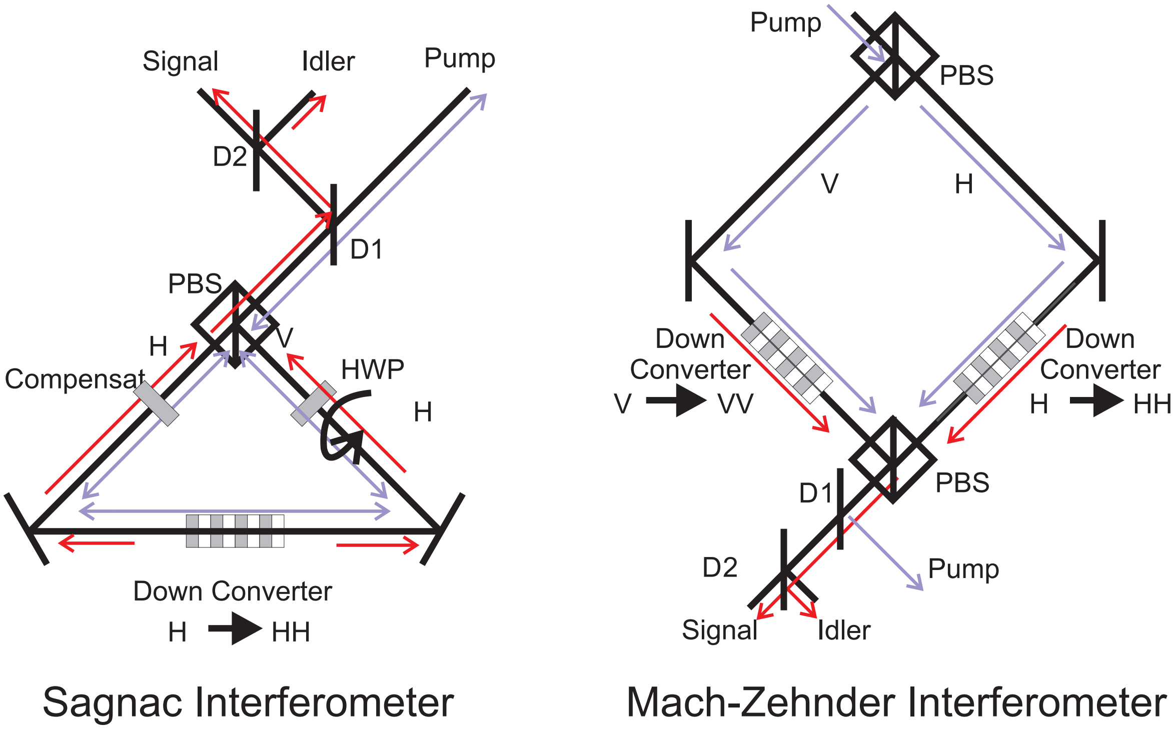

Figure 1.1: Generating Entanglement in a photonic based system: The left figure shows a triangular shaped Sagnac interferometer. At its apex is a polarizing beam splitter while at its base lies a down conversion crystal. The right figure shows a rectangular shaped Mach-Zehnder interferometer equipped with polarizing beam splitters at diagonally opposite corners. In each 'arm' lies a down conversion crystal mediating a unique SPDC process. In both figures, D1 and D2 are dichroic elements that sort the light based on frequency. For the Sagnac, 45° polarized pump light splits equally at the apex and travels in both directions around the triangular 'loop'. SPDC photons emitted from either end of the crystal recombine at the apex and exit the interferometer. Everything is identical except in one arm, a 90° rotation is applied. This creates confusion about the polarization state of the exit light. For the Mach-Zehnder, 45° polarized pump light splits equally at the first corner PBS pumping both arms before recombining at the opposing corner. If down converted light is detected and the interferometer is balanced (both arms are optically equal in length), there will be confusion about which SPDC process occurred.

the natural coherence time of the pump light entering the interferometer[5], and 2) no other distinguishing path information can be carried by the photons.

Concerning photon interference and entanglement, the MZI has been studied extensively [35], [36]. The first demonstration of entanglement using a MZI was performed in 2001. [37].

An improvement to the MZI scheme can be made by realizing that in the interferometer, there are two nearly identical down converters and two identical types of beam splitters. As such, the MZ interferometer method for generating entanglement can be improved by folding and making use of one down converter and one beam splitter. The notion of folding was first investigated by Fiorentino et al. in 2004 [38] to be refined two years later by Kim et al. [39] into what are now called 'Sagnac' sources of entanglement (figure 1.1). Because of its unique geometry, it suffers much less from path length instabilities. Nonetheless, asymmetries can still cause a degradation in the quality of the entanglement. Such Sagnac sources were the main motivation for the first novel design presented in chapter 7.

1.4 Summary

The bulk of the supporting material for the thesis is now officially out of the way. A recap of the introduction and a brief outline for the rest of the text follows for those that have skipped most of the introduction.

As the title announces, this thesis focuses on the design and test of waveguide sources of photon pairs. The thesis was motivated by appealing to the need for better resources of Quantum Information (QI); those being entanglement and superposition. The chosen method to create those sources is spontaneous parametric down conversion (SPDC). The theoretical footings upon which SPDC rests come from the fields of Non-Linear Optics and Quantum Optics. The main physical problem encountered in designing better QI resources via SPDC is that of phase matching. It is overcome via novel uses of waveguides. The introduction ends with a discussion of entanglement and how to setup an experiment to create entanglement with SPDC.

The rest of the thesis has the following layout. Chapter 2 develops the theoretical tools needed to interpret the results and understand the choices that were made over the course of the Ph.D. Those choices and results are documented in the the remaining chapters. Specifically, Chapter 3 describes the experimental configuration and setup; Chapter 4 describes the verification of the setup; Chapter 5 explores the first novel method for overcoming the phase matching problem – entitled Directional Quasi-Phase Matching; Chapter 6 investigates modal phase matching in Bragg Reflection Waveg-

---

[5] (if not, then two immediately successive SPDC processes (double pair emission) would not be distinguishable, producing four photons instead of two)

uides; Chapter 7 deals with two novel techniques for generating entanglement, and chapter 8 concludes the thesis.

2 THEORY

In this chapter the relevant words, concepts and equations from the subjects of Non Linear Optics and Quantum Optics are introduced, defined and formalized. Dispersion, Second Harmonic Generation, Spontaneous Parametric Down Conversion, Phase Matching and Quasi-Phase Matching, Waveguides, and semiconductors is included to provide background context for some of the sources discussed later on in the thesis.

2.0.1 Introduction

This thesis is about waveguide sources of photon pairs created via SPDC. The necessary ingredients for this process are three field modes $\vec{E_1}(x,y,z)$, $\vec{E_2}(x,y,z)$, $\vec{E_3}(x,y,z)$ – one that is destroyed, and the two that are created. The coupling strength can be increased in the presence of matter. Specifically by the non-linear response of the matter to the fields - symbolized by the second-order susceptibility tensor for that medium $\chi^{(2)}_{ijk}$. Thus, in essence, creating photon pairs can be reduced to four relevant parameters: $\vec{E_1}(x,y,z)$, $\vec{E_2}(x,y,z)$, $\vec{E_3}(x,y,z)$, and $\chi^{(2)}_{ijk}$.

To optimize the photon pair production rate, the overlap between the three quantities ($\vec{E_1}$,$\vec{E_2}$,$\vec{E_3}$) as well as the coupling ($\chi^{(2)}_{ijk}$) need to be optimized simultaneously. This is equivalent to maximizing the spatial overlap between the field modes as well as their orientation with respect to the host material.

If a waveguide can be built in a material system, it can be extremely beneficial. It naturally confines and directs light. Furthermore, the confinement forces boundary conditions on the wave equation, which in some cases can help overcome material dispersion. Waveguides can thus dramatically increase both the strength of the SPDC interaction as well as the interaction length over which SPDC can occur.

In order to engineer the conditions for maximal spatial overlap, the speed and spatial profile of each interacting mode in the guide needs to be determined. Typically, each field mode is characterized by a scalar frequency ω, a spatial propagation constant β (related to the wave vector $\vec{k}$), and a spatial mode profile. These parameters are determined by the linear response of the medium – symbolized by the first-order susceptibility tensor $\chi^{(1)}$, and the physical boundaries of the waveguide.

With these motivations in mind, this section begins with a treatment of the wave equation that involves $\chi^{(1)}$ to show some basic concepts like dispersion and the index of refraction. This will be followed by the wave equation modified to account for the effects of $\chi^{(2)}$ in order to show second harmonic generation. A brief introduction to quasi-phase matching (QPM) and modal analysis of waveguides is next. This is succeeded by an in depth development of the quantum mechanical model for pair production via spontaneous parametric down conversion (SPDC). To prepare for the final chapters of the thesis, the concepts are amalgamated in a discussion on the effects of temperature tuning for SPDC. This chapter summarizes all the main optical tools used to interpret the results presented in this thesis.

2.1 Classical Optics

Maxwell's Equations

This thesis begins with the famous Maxwell's equations. These were formally published in 1873 by James Clerk Maxwell in his famous book called 'A Treatise on Electricity and Magnetism' in 1873. For electrically neutral material they are:

$$\nabla \times \vec{E} = -\frac{\partial \vec{B}}{\partial t} \tag{2.1}$$

$$\nabla \times \vec{H} = \frac{\partial \vec{D}}{\partial t} \tag{2.2}$$

$$\nabla \cdot \vec{D} = 0 \tag{2.3}$$

$$\nabla \cdot \vec{B} = 0 \tag{2.4}$$

The constitutive relations are

$$\vec{D} = \varepsilon_0 \vec{E} + \vec{P} \tag{2.5}$$

$$\vec{B} = \mu \vec{H} \tag{2.6}$$

where $\vec{E}$ and $\vec{H}$ are the Electric and Magnetic fields, and $\vec{D}$, $\vec{B}$, and $\vec{P}$ represent the electric flux, the magnetic flux and the induced polarization respectively.

Different materials are electrically characterized by their permittivity ε where ε_0 is the permittivity in vacuum. Generally, most situations deal with non-magnetic material where μ is simply equal to μ_0, the permeability of vacuum.

Boundary conditions that need to be satisfied when two or more materials are involved in the problem are:

$$(\vec{E_1} - \vec{E_2}) \times \hat{n} = 0 \tag{2.7}$$

$$(\vec{H_1} - \vec{H_2}) \times \hat{n} = 0 \tag{2.8}$$

$$(\vec{D_1} - \vec{D_2}) \cdot \hat{n} = 0 \tag{2.9}$$

$$(\vec{B_1} - \vec{B_2}) \cdot \hat{n} = 0 \tag{2.10}$$

where the indices 1 and 2 represent the different materials, $\hat{n}$ represents the unit normal between the two surfaces. Briefly in words, the flux across two surfaces is continuous, and all tangential field components are continuous.

The Wave Equation

To get the wave equation for $\vec{E}$, the curl operation is performed on equation 2.1, and equations 2.2, 2.5, and 2.6 are used together with a vector identity ($\nabla \times \left(\nabla \times \vec{E}\right) = \nabla\left(\nabla \cdot \vec{E}\right) - \nabla^2 \vec{E}$) Their interrelationship results in the *wave equation*.

$$\nabla \times \left(\nabla \times \vec{E}\right) = \nabla\left(\nabla \cdot \vec{E}\right) - \nabla^2 \vec{E} \quad = \quad -\frac{1}{c^2}\frac{\partial^2 \vec{E}}{\partial t^2} - \frac{1}{\varepsilon_0 c^2}\frac{\partial^2 \vec{P}}{\partial t^2} \tag{2.11}$$

where

$$c = \sqrt{\frac{1}{\varepsilon_0 \mu_0}} \tag{2.12}$$

in the absence of matter $\vec{P}$=0, the divergence of $\vec{E}$ is zero, and a simple wave equation results adequately describing EM propagation in vacuum.

The polarization response

When matter is involved, there can be a significant electrical interaction between the input field and the more mobile electrons in the material. Locally, as the input field enters a region of the material, the electronic environment reacts and excites, temporarily absorbing the field and entering what is called a virtual excited state. The decay from the virtual excited state re-emits the field. As a result, the speed of the exciting field is modified by the presence of the material. The excitation and subsequent decay of the material to and from the virtual level results in an optical response field called the *polarization response* $\vec{P}$. The polarization response is a model wherein the medium does *not* enter a new physical state, but is only perturbed away from equilibrium.

The decay from the virtual state is mainly a strict re-emission of the driving field. However, other higher energy virtual states are accessible, and the subsequent re-emission may not be consistent with the input field (i.e re-emit a field of the same frequency, direction etc.). The polarization response is modeled as a power series in the input field. It will in general depend on the frequency and polarization of the driving field. For the purposes of this thesis, consideration is not given to a polarization response that is greater than quadratic in the input fields. Written in component form, using the Einstein summation convention, $\vec{P}$ will be limited to

$$\begin{aligned} P_j &= \varepsilon_0 \chi^{(1)}_{jk} E_k(t) + \varepsilon_0 \chi^{(2)}_{jkl} E_k(t) E_l(t) && (2.13) \\ &= P^{(1)}_j(t) + P^{(2)}_j(t) && (2.14) \\ & && (2.15) \end{aligned}$$

Where the subscripts jkl can denote any of the three orthogonal spatial directions available. The response has been split into a part that depends linearly on the applied field ($\vec{P}^{(1)}$), and one that scales quadratically ($\vec{P}^{(2)}$). The two symbols that characterize the coupling are the linear and bilinear susceptibility – denoted by $\hat{\chi}^{(1)}$ and $\hat{\chi}^{(2)}$ respectively.

2.1.1 $\vec{P}^{(1)}$– Dispersion and the Index of Refraction

In this small subsection, the concepts of dispersion and the index of refraction are introduced.

When dealing with material, the divergence of the electric flux is not necessarily zero, but nonetheless, its contribution is usually ignored. With this assumption, the wave equation can be re-written in component form as

$$-\nabla^2 E_j = -\frac{1}{c^2}\frac{\partial^2 E_j}{\partial t^2} - \frac{1}{\varepsilon_0 c^2}\frac{\partial^2 \varepsilon_0 \chi^{(1)}_{jk} E_k}{\partial t^2} \tag{2.16}$$

For lossless material, the linear susceptibility is a symmetric tensor, and is assumed to be time independent. It can therefore be diagonalized. In this co-ordinate system, the field is re-labeled with a ãccordingly.

$$-\nabla^2 \tilde{E}_j = -\frac{1}{c^2}\frac{\partial^2 \tilde{E}_j}{\partial t^2} - \frac{1}{c^2}\frac{\partial^2 \chi^{(1)}_{j'j'} \tilde{E}_j}{\partial t^2} \tag{2.17}$$

Solutions to the wave equation are time harmonic with a frequency ω (i.e. are proportional to $e^{i\omega t}$), thus, the wave equation can be simplified as

$$-\nabla^2 \vec{\tilde{E}} = \left(\mathbf{1} + \hat{\chi}^{(\mathbf{1})}\right)\frac{\omega^2}{c^2}\vec{\tilde{E}} \tag{2.18}$$

or as

$$\nabla^2 \vec{\tilde{E}} + \hat{\varepsilon}(\omega)\frac{\omega^2}{c^2}\vec{\tilde{E}} = 0 \tag{2.19}$$

$$\tag{2.20}$$

where

$$\hat{\varepsilon}(\omega) = \mathbf{1} + \hat{\chi}^{(1)}(\omega) \tag{2.21}$$

is a frequency dependent *dielectric tensor*.

Emphasis should be placed on the preferred co-ordinates that diagonalize the linear susceptibility tensor. In an experiment, these directions do not necessarily match those of the lab. Plane waves tend to be the defacto standard solution for analyzing wave equations in a general sense. For waveguides with very hard and distinct boundary conditions, a single plane wave is definitely not an eigenmode of the corresponding wave equation. Nonetheless, most wave phenomena – in particular waveguide modes – retain an oscillation frequency ω and a corresponding propagation constant β. In general, the characteristics of most problems are well demonstrated with simple plane wave solutions. Further, plane waves are a basis out of which any solution to the wave equation can be composed. Plane waves take the form

$$\vec{A}e^{i(\vec{k}\cdot\vec{r}-\omega t)} \tag{2.22}$$

where $\vec{k}$ is the propagation constant, and $\vec{A}$ is a spatially dependent amplitude representing the polarization pointing in some direction. Substituting the planewave representation for $\vec{\tilde{E}}$ into 2.19 we get *dispersion relations* given by

$$\varepsilon_{jj}(\omega)\frac{\omega^2}{c^2} = k_j^2 \tag{2.23}$$

Dispersion determines the speed $v(\omega)_j$ at which a wave polarized in a direction j and with frequency ω travels:

$$v(\omega)_j = \frac{c}{\sqrt{\varepsilon_{jj}(\omega)}} = \frac{c}{n_j(\omega)} \tag{2.24}$$

Dispersion is directly related to how light refracts when crossing an interface. Thus, it is often characterized by the index of refraction tensor $\hat{n}(\omega)$. The main point to take from this small discussion is that dispersion is a direct consequence of the linear polarization response of the medium.

2.1.2 $\vec{P}^{(2)}$ - 2nd Harmonic Generation

Since a material response that is linear in the applied field will not be able to produce different colors of light, creating photon pairs *cannot* be described with the linear response of the medium.

In this section the bilinear response is investigated from a classical vantage point – in particular as it applies to second harmonic generation (SHG). As alluded to in the introduction SHG is a very important experimental tool used to create the correct conditions for observing SPDC in the lab.

There are differing intuitive explanations of how second harmonic light arises. In the virtual state picture that was developed to model the polarization response, second harmonic light arises because of a small probability that a higher energy virtual state can be temporarily reached by the material. The de-excitation to the ground state occurs by emitting light that is consistent with that higher energy. In the case of second harmonic light, the re-radiated light has twice the frequency.

To begin modeling SHG, the wave equation is written to include the second-order polarization response.

$$\nabla^2\vec{E} - \hat{\varepsilon}(\omega)\frac{1}{c^2}\frac{\partial^2\vec{E}}{\partial t^2} = \frac{1}{\varepsilon_0 c^2}\frac{\partial^2\vec{P}^{(2)}}{\partial t^2} \tag{2.25}$$

Which in component form looks like

$$\nabla^2 E_j - \varepsilon_{jk}(\omega)\frac{1}{c^2}\frac{\partial^2 E_k}{\partial t^2} = \frac{1}{\varepsilon_0 c^2}\frac{\partial^2 \varepsilon_0 \chi^{(2)}_{jkl} E_k E_l}{\partial t^2} \tag{2.26}$$

In the following analysis, only the terms responsible for producing a second harmonic field are considered. The driving fields are characterized by a frequency ω and wavevector k_ω, and will act as source terms found in the polarization response on the right hand side of equation 2.26. On the left hand side, the wave equation will pertain only to the generated fields at frequency 2ω and wavevector $k_{2\omega}$.

The driving electric field is real and modeled as a traveling wave,

$$\begin{aligned} \vec{E}_\omega(\vec{r},t) &= Re(\vec{A}e^{-i\omega t}) && (2.27)\\ &= \frac{1}{2}\Big(\vec{A}(\vec{r})e^{i(\vec{k}_\omega\cdot\vec{r}-\omega t)} + \vec{A}^*(\vec{r})e^{-i(\vec{k}_\omega\cdot\vec{r}-\omega t)}\Big), && (2.28) \end{aligned}$$

where $\vec{A}$ is a vector in the direction of polarization whose magnitude represents the classical wave amplitude and is generally spatially dependent, here space is denoted by the vector $\vec{r}$.

The generated second harmonic electric field at frequency 2ω is similarly written, except with the wave amplitude denoted by the symbol $\vec{B}$.

$$\vec{E}_{2\omega}(\vec{r},t) = \frac{1}{2}\Big(\vec{B}(\vec{r})e^{i(\vec{k}_{2\omega}\cdot\vec{r}-2\omega t)} + \vec{B}^*(\vec{r})e^{-i(\vec{k}_{2\omega}\cdot\vec{r}-2\omega t)}\Big). \tag{2.29}$$

Both $\vec{A}(\vec{r})$ and $\vec{B}(\vec{r})$ are often referred to as envelope functions as they will vary much less than the much faster frequency oscillations of the field. The wave equation will be evaluated termwise.

From left to right, the first term of equation (2.26) involving the Laplacian expands into three subterms:

$$\frac{1}{2}\left[\Big((\nabla^2 B_j(\vec{r})) + (2i\vec{k}_{2\omega}\cdot\nabla B_j(\vec{r})) - k_{2\omega}^2 B_j(\vec{r})\Big)e^{i(\vec{k}_{2\omega}\cdot\vec{r}-2\omega t)} + c.c\right] \tag{2.30}$$

Using the dispersion relation from equation 2.23 above, the second term of equation (2.26) involving the second time derivative is:

$$k_{2\omega}^2 \frac{1}{2}\left(\vec{B}(\vec{r})e^{i(\vec{k}_{2\omega}\cdot\vec{r}-2\omega t)} + c.c\right) \tag{2.31}$$

which will cancel with the third subterm of the expanded first term.

The driving term on the right hand side of equation (2.26) is responsible for creating the SH field and is

$$\frac{1}{4c^2}\chi_{jkl}^{(2)}\left((-i2\omega)^2 A_j(\vec{r})A_k(\vec{r})e^{i(2\vec{k}_{\omega}\cdot\vec{r}-2\omega t)} + c.c\right) \tag{2.32}$$

The complex conjugate terms create a conjugate equation for SHG. For the purposes of analysis, the terms will be dropped, although they would correspond to oppositely directed SHG. Additionally for SHG, the square of the driving field produces a zero frequency or D.C. term. This term is ignored as it will not play a role in second harmonic generation.

It is assumed that the envelope $B_j(\vec{r})$ varies slowly in space, an approximation called the slowly varying envelope approximation (SVA). Then,

$$\nabla^2 B_j(\vec{r}) \ll 2i\vec{k}_{2\omega}\cdot(\nabla B_j(\vec{r})) \tag{2.33}$$

Since the polarization response oscillates with the same frequency as the produced fields, the time harmonic terms can be canceled from both sides. The resulting equation of motion for SHG is reduced to

$$\frac{1}{2}\left[2i\vec{k}_{2\omega}\cdot\nabla B_j(\vec{r})e^{i(\vec{k}_{2\omega}\cdot\vec{r})}\right] \quad = \quad \frac{1}{4c^2}\chi_{jkl}^{(2)}\left((-i2\omega)^2 A_k A_l e^{i(2\vec{k}_{\omega}\cdot\vec{r})}\right) \tag{2.34}$$

which simplifies to

$$i\vec{k}_{2\omega}\cdot\nabla B_j(\vec{r}) \quad = \quad \frac{1}{4c^2}\chi_{jkl}^{(2)}\left((-i2\omega)^2 A_k A_l e^{i(-\Delta\vec{k}\cdot\vec{r})}\right) \tag{2.35}$$

where, due to linear dispersion the momentum mismatch or phase mismatch $\Delta\vec{k}$ is defined as:

$$\vec{k}_{2\omega} - 2\vec{k}_{\omega} = \Delta\vec{k} \tag{2.36}$$

Typically, only one element of the non-linear susceptibility is accessed in an experiment (usually the strongest one). For example, imagine a non-zero element for $\chi^{(2)}_{xxx}$. Then for a plane wave propagating in the z direction and polarized in the x direction, the field components $A_j(\vec{r}) \rightarrow A_x(z)$ and $B_j(\vec{r}) \rightarrow B_x(z)$ and $\Delta\vec{k}$ has only one component Δk. The equation of motion for SHG simplifies to

$$\frac{dB_x(z)}{dz} = \frac{i(2\omega)^2}{4k_{2\omega}c^2}\chi^{(2)}_{xxx}A_x(z)^2 e^{-i\Delta kz}. \tag{2.37}$$

Some additional comments are warranted:

- For applied frequencies that produce a response that is relatively instantaneous, $\chi^{(2)}_{ijk}$ is itself independent of those frequencies and there exists a permutation symmetry that can simplify the analysis. This is called Kleinman symmetry. Kleinman symmetry is valid in general for the case of SHG because the harmonic field is generated by two fundamental fields that are by definition identical. Conventionally, a new tensor is introduced when this holds [40]

  $$\chi^{(2)}_{ijk} = 2d_{ijk} \longrightarrow 2d_{il} \tag{2.38}$$

  where the indices map according to (11→1), (22→2), (33→3), (23,32→4), (31,13→5), (12,21→6). In the case of fixed geometry – fixed polarization and fixed propagation direction – the tensor is no longer needed and an effective scalar d_{eff} can be used.

- Secondly, the conditions in the thesis for SHG were such that the pump field remained largely undepleted. Therefore, the fundamental field amplitudes can be taken as constant $E_\omega(z) \longrightarrow E_\omega$. This is known as the undepleted pump approximation.

This leaves the following simplified form of equation 2.37

$$\frac{d}{dz}E_{2\omega}(z) = -i\omega\sqrt{\frac{\mu_0}{\varepsilon_{2\omega}}}d_{\text{eff}}(E_\omega)^2 e^{i\Delta kz} \tag{2.39}$$

where $B_x(z) \rightarrow E_{2\omega}(z)$ and $A_x(z) \rightarrow E_\omega(z)$. This integrates to

$$\frac{E_{2\omega}(L)}{L} \quad \propto \quad E_\omega^2 \frac{e^{i\Delta kL} - 1}{\Delta kL} \tag{2.40}$$

Where L is now a defined position in the medium. Then the power in the second harmonic $I_{2\omega}$ as a function of propagation distance 'z' is

$$I_{2\omega}(z) \quad \propto \quad I_\omega^2 z^2 \mathrm{sinc}^2(\Delta kz/2) \tag{2.41}$$

Where I_ω is the power in the applied field. The conclusion is that for Δk=0, second harmonic generation (and conversely photon pair production), is much more efficient than for $\Delta k \neq 0$. In the former or *phase matched* case, there is a steady quadratic growth of the second harmonic power with distance. In the latter *un-phase matched* case, $I_{2\omega}$ is periodic with period defined by $\Delta kL/2 = \pi$. Half of this period defines a coherence length l_c over which power can flow into the second harmonic. The coherence length is equal to

$$l_c = \frac{\pi}{\Delta k} \tag{2.42}$$

Crystal Symmetry

Before ending this section, some interesting ramifications of the polarization model on the bilinear polarization response are pointed out. Consider a crystal that is centro-symmetric (symmetric under inversion). In such a crystal, the bilinear polarization response should physically invert under an inversion of the applied fields. However, the polarization model implies that the bilinear response would not change since such a response arises from effectively multiplying two fields together (mathematically cancelling out the inversion). Thus, if the model is an accurate description of the physical situation, it forbids a bilinear response from centro-symmetric materials[1]

Secondly, the equation for SHG just derived (and more generally those that describe sum and difference frequency generation) describes a third field as product of two existing fields. Turning to the process of Spontaneous Parametric Down Conversion (SPDC) where only one frequency exists a priori, the model does not provide a way to sum / subtract frequencies to achieve a field with a lower frequency, without a field with a lower frequency already in existence. For degenerate SPDC, where the lower frequencies are identical, the process could not be spontaneous, and the conclusion is that the classical model fails to describe SPDC.

---

[1] And that's what we find to be true in nature - quadratic nonlinearities are not observed from unstructured materials, such as glasses and liquids, except at their interfaces and surfaces.

2.1.3 Quasi-Phase Matching

Quasi-Phase Matching (QPM) addresses the issue of the oscillatory growth and decay of the bilinear response field described by equation 2.41. It is a really rough but exceedingly useful tool that maintains the direction of power flow from the pre-existing pump field to the field created by the bilinear response of the crystal. QPM achieves this by physically inverting the bilinear polarization response precisely when the pump and the response field are themselves 180° out of phase with each other. The effect is to reset the overall phase mismatch back to zero thereby allowing further growth of the bilinear response field. The inversion is repeated periodically as needed, allowing a continuous growth of the response field.[2] Depending on the desired rate of growth, the inversion period will be an integer number of twice the coherence length l_c.

It turns out that there exist materials with significant bilinear coupling, that are capable of undergoing such a molecular inversion via the application of an applied static electric field. The process will be discussed later on but the theory will be developed here.

Imagine that the inversion is periodic with a period Λ and is *constant over the inversion region* – half the period. Then the functional form is a square wave, whose fourier series is

$$\chi^{(2)}_{QPM} := \chi^{(0)} \sum_{m=-\infty}^{\infty} \frac{2e^{im\frac{2m+1\pi}{\Lambda}z}}{(2m+1)\pi} \tag{2.43}$$

Replacing $\chi^{(2)}$ in equation 2.37 with the fourier series version shows that for $\Lambda = (2m+1)l_c$ there is a new 'quasi'-phase matching, the coupling strength of which is degraded by $\frac{2}{(2m+1)\pi}$ with respect to the original coupling. Note that the material is 'built' with a Λ – a fixed minimum period with a duty cycle of 1/2 over that period. Thus it effectively chooses the term in the fourier series – m. That is, the pair parameters cannot be chosen independently. Conversely, to achieve the best approximation to the coupling available in a perfectly phase matched case then a designer would choose m=0, selecting the first, lowest-order term in the series. This determines the inversion period. The condition is called first-order quasi-phase matching where the coupling is reduced by $\frac{2}{\pi}$ and $\Lambda=2l_c$.

2.1.4 Mode solving

This subsection introduces the full vector wave equation and is meant to briefly touch on the subject of modal analysis in waveguides. Modal analysis determines the wave

---

[2] In principle, this re-phasing could be continuously done, perhaps by slowly rotating the crystal about the propagation axis, but this seems exceedingly difficult and one might be better off finding a new material rather than engineering one

vector and spatial mode profile of a particular solution to Maxwells wave equation where the boundary conditions make the problem difficult, if not impossible to solve analytically. The phase mismatch Δk can be deduced from knowledge of the propagation constants for all the modes that will be mixed in the photon pair generation process. Those propagation constants are found by solving the full vector wave equation with the appropriate boundary conditions. In addition to finding the propagation constants, the solutions determine the spatial mode profiles of each mode. This also provides important information on the spatial overlap between the different modes. For the waveguide structures in this thesis, solutions to the full vector wave equation could not be obtained in an analytical fashion and were solved numerically with a commercial mode solver created by Lumerical Inc.

Recall that a waveguide is essentially just a region of space that has an index profile $n \rightarrow n(x,y)$. Equation 2.24 can be used to give

$$\varepsilon = n^2(x,y)\varepsilon_0. \tag{2.44}$$

Conventionally, modes are solved for a single frequency, so dispersion does not enter directly into the problem. However, dispersion does determine the index of refraction profile associated with each frequency. In this case, the wave equation 2.16 becomes

$$\nabla\left(\nabla \cdot \vec{E}\right) - \nabla^2 \vec{E} = -\frac{n^2(x,y)}{c^2}\frac{\partial^2 \vec{E}}{\partial t^2} \tag{2.45}$$

using the 3rd Maxwell equation, the divergence of the flux can be re-written as

$$\begin{aligned} \nabla \cdot \varepsilon \vec{E} &= 0 && (2.46)\\ \nabla \cdot n^2(x,y)\varepsilon_0 \vec{E} &= 0 && (2.47) \end{aligned}$$

then

$$\begin{aligned} \nabla(n^2(x,y)\varepsilon_0) \cdot \vec{E} + n^2(x,y)\varepsilon_0 \nabla \cdot \vec{E} &= 0 && (2.48)\\ \nabla \cdot \vec{E} &= -\frac{1}{n^2(x,y)}\nabla(n^2(x,y)) \cdot \vec{E} && (2.49) \end{aligned}$$

and, for time harmonic fields with frequency ω, the wave equation becomes

$$\nabla\left(-\frac{1}{n^2(x,y)}\nabla(n^2(x,y)) \cdot \vec{E}\right) - \nabla^2 \vec{E} = \frac{\omega^2 n^2(x,y)}{c^2}\vec{E} \tag{2.50}$$

Replacing ω^2/c^2 with the free space wavenumber k_0^2 yields the following full vector wave equation for $\vec{E}$.

$$\nabla^2 \vec{E} + \nabla\left(\frac{1}{n^2(x,y)}\nabla(n^2(x,y)) \cdot \vec{E}\right) + k_0^2 n^2(x,y)\vec{E} = 0 \tag{2.51}$$

As alluded to, barring simple symmetrical structures, this equation is usually solved via finite difference methods in the time domain (FDTD) or finite element methods in the frequency domain (FE). Commercial mode solvers were employed in this thesis using methods similar to those outlined in [41]. The index of refraction profile was entered as an input along with the frequency of interest and appropriate boundary conditions. The solutions for $\vec{E}$ are spatial mode profiles that have an effective propagation constant in the structure. Via the inter-relationship between frequency, the propagation constant, and the index of refraction, a solution consisted of a mode profile and a single effective index for that particular mode at the desired frequency.

2.2 Quantum Optics

The derivations and equations that follow are largely taken from the lecture notes of Marek Żukowski at the University of Gdańsk in Poland. Two additional references that succinctly produce the relevant equations are the papers authored by Morton H. Rubin et al [11][42].

2.2.1 Properties of SPDC

The basic properties of SPDC that we expect to recover are

$$\begin{aligned} \omega_p &= \omega_s + \omega_i && (2.52)\\ \vec{k}_p &\equiv \vec{k}_s + \vec{k}_i + \Delta\vec{k} && (2.53)\\ & && (2.54) \end{aligned}$$

where the subscripts p, s, and i stand for the names given to the photons – pump, signal, and idler respectively, ω is the photon angular frequency, $\vec{k}$ is the photon wavenumber / wavevector. Equation (2.52) is valid to within the spectral width of the pump and represents energy conservation[3]. Equation (2.53) represents momentum conservation where $\Delta\vec{k}$ is the phase mismatch or phase detuning between the pump photon and the signal and idler photons.

Typically the lower frequency photon produced in SPDC has the distinction of being called the idler. Due to the aforementioned properties, the pair of photons exist in a non-separable state that is often referred to as a biphoton, a term coined by Klyshko.[4]

---

[3] simply multiply by $\hbar$

[4] The apparent asymmetry of the equations – placing all of the detuning onto the momentum side is related to the fact that in real experiments translational symmetry is weak, so linear momentum does not not strictly have to be conserved – as in the case of QPM etc.

Hamiltonian

SPDC is usually solved in the interaction picture. In this picture, the physical interaction is assumed weak and the energy perturbation is usually small. The interaction picture attempts to separate the unitary time evolution determined by the equilibrium potential H_0 from the time evolution due to the small interaction potential H_I. From classical electrodynamics, the energy of the electromagnetic field is associated with the full potential and can be written as

$$\hat{H} = \int d^3\vec{r}\Big[\vec{H}(\vec{r},t)\cdot\vec{B}(\vec{r},t) + \vec{E}(\vec{r},t)\cdot\vec{D}(\vec{r},t)\Big] \tag{2.55}$$

As $\vec{D}$ includes the polarization response of the material, $\vec{B}$ typically does not, so equation (2.55 can be decomposed into

$$\hat{H} = \hat{H}_0 + \hat{H}_I \tag{2.56}$$

where

$$\hat{H}_0 = \int d^3\vec{r}\left(\frac{1}{\mu_0}|\vec{B}(\vec{r},t)|^2 + \epsilon_0|\vec{E}(\vec{r},t)|^2\right) \tag{2.57}$$

and

$$\hat{H}_I = \int d^3\vec{r}\vec{E}(\vec{r},t)\cdot\vec{P}(\vec{r},t) \tag{2.58}$$

The interaction Hamiltonian is further broken down into a linear and non-linear component as

$$\hat{H}_I = \hat{H}_I^L + \hat{H}_I^{NL} \tag{2.59}$$

where

$$\hat{H}_I = \int d^3\vec{r}\vec{E}(\vec{r},t)\cdot\vec{P}^L(\vec{r},t) + \int d^3\vec{r}\vec{E}(\vec{r},t)\cdot\vec{P}^{NL}(\vec{r},t) \tag{2.60}$$

The linear component stems from the linear response of the material

$$\vec{P}_i^L(\vec{r},t) = \chi_{ij}^{(1)}(\vec{r})\vec{E}_j(\vec{r},t) \tag{2.61}$$

while the non-linear component is limited to terms involving only $\chi^{(2)}$.

$$\vec{P}_i^{NL}(\vec{r},t) = \chi_{ijk}^{(2)}(\vec{r})\vec{E}_j(\vec{r},t)\vec{E}_k(\vec{r},t) \tag{2.62}$$

so that the non-linear interaction Hamiltonian, hereafter referred to as $\hat{H}_{\text{SPDC}}$ is

$$\hat{H}_I^{NL} = \hat{H}_{\text{SPDC}} \sim \int_V \chi_{ijk}^{(2)}\vec{E}_i(\vec{r},t)(\vec{r})\vec{E}_j(\vec{r},t)\vec{E}_k(\vec{r},t)dV \tag{2.63}$$

The fields are quantized in the interaction picture as

$$\vec{E}(\vec{r},t) = \sum_{\zeta=1}^{2}\int d^3k \frac{i\hat{\epsilon}(\vec{k},\zeta)}{\sqrt{2\omega(2\pi)^3}}\left\{\hat{a}(\vec{k},\zeta)e^{i(\vec{k}\cdot\vec{r}-\omega t)} + \hat{a}^\dagger(\vec{k},\zeta)e^{-i(\vec{k}\cdot\vec{r}-\omega t)}\right\} \tag{2.64}$$

$$= \vec{E}^+(\vec{r},t) + \vec{E}^-(\vec{r},t) \tag{2.65}$$

Where $\hat{\epsilon}(\vec{k},\zeta)$ is a unit vector in the polarization direction ζ for mode $\vec{k}$ and $\vec{E}^+(\vec{r},t) = \left\{\vec{E}^-(\vec{r},t)\right\}^\dagger$. In this symbolism, the $^{(-)}$ superscript indicates the 'negative' frequency component of the quantized field containing the term with the creation operator $\hat{a}^\dagger(\vec{k},\zeta)e^{-i(\vec{k}\cdot\vec{r}-\omega t)}$. It is these terms that will create a photon from the vacuum.

The summation in equation (2.64) encompasses two polarizations ζ=1,2. $\hat{a}(\vec{k},\zeta)$, and $\hat{a}^\dagger(\vec{k},\zeta)$ are the annihilation and creation operators that annihilate / create a photon with polarization ζ and wave vector $\vec{k}$. $\hat{\epsilon}(\vec{k},\zeta)$ is a unit vector in the direction of polarization. The annihilation and creation operators are identical to those that describe a simple harmonic oscillator and therefore satisfy similar commutation relations, namely:

$$[\hat{a}(\vec{k},\zeta), \hat{a}^\dagger(\vec{k}',\zeta')] \sim \delta_{\zeta\zeta'} 2\pi \delta^3(\vec{k}-\vec{k}') \tag{2.66}$$

and where

$$[\hat{a}^\dagger(\vec{k},\zeta), \hat{a}^\dagger(\vec{k}',\zeta')] = 0 = [\hat{a}(\vec{k},\zeta), \hat{a}(\vec{k}',\zeta')] \tag{2.67}$$

Continuing the calculation, only the terms responsible for generating SPDC will be examined[5]. It is expected that the process will conserve energy, in the quantum picture this will require an annihilation of a pump photon. A priori, the pump field is typically that which exits a laser. It is a coherent state with a huge average photon number. Destroying one photon will have little effect on this state. As such, it is not necessary to quantize all three fields in equation(2.63).

For the purposes here we drop the $\vec{r}$ and the time dependence notation on the fields so that the interaction is

$$\hat{H}_{\text{SPDC}} \sim \int_V dV \chi^{(2)}_{ijk} \vec{E}^p_i \vec{E}^s_j \vec{E}^i_k \tag{2.68}$$

Where $\vec{E}^{(p)}$ is a strong pump field and is not quantized. By virtue of the fact that $\hat{a}|0\rangle$=0 and $\hat{a}^\dagger|0\rangle$=1$|1\rangle$, only the negative frequency terms survive in the interaction (they contain terms with $\hat{a}^\dagger$). The important terms that contribute to the SPDC process are retained, while those that don't survive are found in the hermitian conjugate and cross terms. The latter can be thought of in a similar way to the D.C. component that arises when two classical fields are multiplied together.

---

[5] this implicitly means that the creation and subsequent annihilation of SPDC is ignored

$$\hat{H}_{\text{SPDC}} \sim \int_V dV \chi^{(2)}_{ijk} \vec{E}^{p}_i \vec{E}^{s-}_j \vec{E}^{i-}_k \tag{2.69}$$

Up to this point in the derivation of $\hat{H}_{\text{SPDC}}$, the notation has been roughly generalized. From here on, some simplifying assumptions can be made. One such simplification arises from the choice of the form of the pump field. Commonly, the pump field is generated by a laser which typically emits coherent radiation. SPDC has been observed for both CW and pulsed laser light. Assuming linear polarized ($\hat{z}$) light in the $\hat{x}$ propagation direction, the form of $\vec{E}^p$ is either

$$\vec{E}^p = \hat{z}\frac{E_0}{2}\left(e^{i(k_p x - \omega_p t)} + c.c\right) \text{ for a single plane wave} \tag{2.70}$$

$$\vec{E}^p = \hat{z}\int d\omega_p E_0(\omega_p) e^{ik_p(\omega_p)x - \omega_p t} \text{ for a pulse of light} \tag{2.71}$$

$$\tag{2.72}$$

Further complications arise when considering waveguides where the spatial boundaries and mode confinement need consideration. More recently, the form of the pump has also been realized as a single photon [43][6]

The following assumptions will be made

- In general, an arbitrary field can be represented as a sum of plane waves. Thus, this analysis proceeds for the simple case of a monochromatic plane wave source.
- The discussion is appropriate for waveguides. Therefore both the pump, signal and idler modes will be co-linear and their wavevector will not be transverse.
- SPDC observed in this thesis was of the type-I (this definition to be made clearer later on) Thus, the signal and idler will have the same polarization - in the direction $\hat{e}$, while the pump polarization is orthogonal to $\hat{e}$.
- The polarization directions will be consistent with a single non-zero element of the bilinear susceptibility tensor. In this case, the directional dependence of the bilinear susceptibility will be replaced by a scalar coupling constant d_{eff}.
- It will be assumed that the pump amplitude will not be depleted.
- The frequency dependent pre-factor under the square root symbol in the field quantization is assumed to be roughly constant. In other words, for an SPDC center frequency ω and spectral width $\delta\omega$, it will be assumed that $\delta\omega \ll \omega$.

---

[6] In this case, it would appear that the pump field should be quantized

For clarity, we write down all three field terms:

$$\vec{E}^{p} \sim \hat{x}\frac{E_0}{2}\left(e^{i(k_p x-\omega_p t)}+c.c\right) \tag{2.73}$$

$$\vec{E}^{s-} \sim \int d^3k_s\hat{\epsilon}_s\hat{a}^\dagger(k_s,\hat{\epsilon}_s)e^{-i(k_s x-\omega_s t)} \tag{2.74}$$

$$\vec{E}^{i-} \sim \int d^3k_i\hat{\epsilon}_i\hat{a}^\dagger(k_i,\hat{\epsilon}_i)e^{-i(k_i x-\omega_i t)} \tag{2.75}$$

where E_0 is the classical amplitude of the pump and $\hat{x}$ is a unit vector in the direction of $\vec{E}_p$. Equation (2.69) becomes

$$\hat{H}_{\text{SPDC}} \sim \iiint dV d^3k_s d^3k_i E_0 d_{\text{eff}}\hat{x}\hat{\epsilon}_s\hat{\epsilon}_i\left(\hat{a}_s^\dagger\hat{a}_i^\dagger e^{i(\Delta kx-\Delta\omega)t}+h.c\right) \tag{2.76}$$

where Δk=$k_p - k_s - k_i$ and $\Delta\omega$=$\omega_p-\omega_s-\omega_i$, and the complex conjugate term in the pump field is dropped because it creates a non-energy conserving term $-\omega_p-\omega_s-\omega_i$ – somewhat similar to a rotating wave approximation.

The volume integral can be evaluated under the following assumptions.

$$\int_V dVe^{i(\Delta\vec{k}\cdot\vec{x})} \to A\int_L dxe^{i(\Delta\vec{k}\cdot\vec{x})} \tag{2.77}$$

where L is the length of the crystal along the direction of propagation, and A is the waveguide cross sectional area. In this case, the length integral evaluates to

$$\int_{-L/2}^{L/2} d^x e^{i(\Delta\vec{k}\cdot x)} \to L\,\text{sinc}(\Delta kL/2) \tag{2.78}$$

For a large volume, it is customary to take $L \to \infty$. In this case

$$\int_{-L/2}^{L/2} d^x e^{i(\Delta\vec{k}\cdot x)} \to 2\pi\delta(\Delta\vec{k}) \tag{2.79}$$

and to make this nontrivial (i.e. to generate SPDC) the result:

$$\boxed{\Delta\vec{k}\approx 0} \tag{2.80}$$

recovers the second of the two properties (2.53) that distinguishes SPDC.

Because of the inherent dispersion relationship 2.23, the integrals over $\vec{k}$ space can be replaced with integrals over angular frequency. Absorbing the area term and the signal and idler velocities into the proportionality symbol, Equation (2.76) now becomes

$$\hat{H}_{\text{SPDC}} \sim \iint d\omega_s d\omega_i d_{\text{eff}}E_0\left(\hat{a}_s^\dagger\hat{a}_i^\dagger e^{-i\Delta\omega t}\right) \tag{2.81}$$

Note that the term

$$d_{\text{eff}} E_0 \tag{2.82}$$

depends on the bilinear susceptibility ($\chi^{(2)}$), and the directions of the pump ($\hat{x}$), signal ($\hat{\epsilon_s}$) and idler ($\hat{\epsilon_i}$) fields. It is an effective amplitude of the pump field and can be replaced by the symbol $F(\omega_s, \omega_i)$. Then

$$\hat{H}_{\text{SPDC}} \sim \int\int d\omega_s d\omega_i F(\omega_s, \omega_i) \left(\hat{a}_s^\dagger \hat{a}_i^\dagger e^{-i\Delta\omega t} \right) \tag{2.83}$$

2.2.2 The quantum state of the Biphoton

In the interaction picture, the quantum state obeys the following equation (to first-order):

$$|\psi\rangle \cong |0\rangle - \frac{i}{\hbar}\int_0^t dt H_{\text{SPDC}}|0\rangle \tag{2.84}$$

In contrast to the evaluation of the spatial integral over the volume (and having to invoke an approximation to extend the length of the crystal to infinity), the limits on the time integral can be immediately extended to ± infinity. This is a subtle argument. The reason for this is that the eigenmodes of H_{SPDC} exist as soon as the crystal is positioned in the experiment, whether the laser is switched on or not. The interaction is thus not time dependent.[7].

The time integration gives

$$\int_{-\infty}^{\infty} dt e^{-i\Delta\omega t} \to 2\pi\delta(\Delta\omega) \tag{2.85}$$

implying that

$$\boxed{\Delta\omega = 0} \tag{2.86}$$

This recovers the second property of SPDC (2.52).

Ignoring the vacuum mode the final the state of the biphoton is

$$\begin{aligned} |\psi\rangle &\sim \frac{i}{\hbar}\int\int d\omega_s d\omega_i F(\omega_s,\omega_i) 2\pi\delta(\Delta\omega)\left(\hat{a}_s^\dagger(\omega_s)\hat{a}_i^\dagger(\omega_i)\right)|0\rangle & (2.87) \\ &= \frac{i}{\hbar}\int d\omega_s F(\omega_s,\omega_p-\omega_s)\left(\hat{a}_s^\dagger(\omega_s)\hat{a}_i^\dagger(\omega_p-\omega_s)\right)|0\rangle & (2.88) \end{aligned}$$

Although simplifications regarding the polarization states of the signal and idler photons were made, in general, there is a implicit relationship between polarization, frequency, coupling, and wavevector understood.

Remarks

- Although it was not considered here, historically SPDC was observed where the momenta of the photon pair were not co-linear. In this case, the volume integral in equation (2.77) cannot be as easily simplified. The designation of ‘co-linear’ is thus a classification for SPDC.

---

[7] It might help to use this analogy: The crystal does not appear and then disappear in time – it is there all the time; thus the interaction is also there all the time. The time dependence is contained in the pump field, not in the interaction.

- When the energy of each photon in the pair is identical, the SPDC process is called degenerate.
- With the restrictions imposed by equations (2.52, and **??**) combined with the dispersion relation given for a particular material, SPDC is further classified as either type-I or type-II. In type-I, the emitted pair of photons have orthogonal polarizations with respect to one another. In type-II, the emitted pairs have identical polarizations.

2.2.3 $\hat{R}_c$ – the coincidence detection operator

A physical detector of electromagnetic radiation typically responds to the electric component of the propagating wave. Moreover, it is *not* able to respond to the field itself, but rather only to the intensity or square of the field. The general rule in quantum mechanics is to promote the classically measured parameter to an operator. As such, the probability of a detection $R(\vec{x},t)$ of a photon in a state $|\Psi\rangle$ at a point $\vec{x}$ and time t can be modeled as being proportional to

$$R(\vec{x},t) = \langle\Psi|E^{(-)}(\vec{x},t)E^{(+)}(\vec{x},t)|\Psi\rangle \tag{2.89}$$

The probability of a joint detection at positions $(\vec{x_1},t_1)$ and $(\vec{x_2},t_1)$ is

$$R(\vec{x_1},t_1|\vec{x_2},t_2) = \langle\Psi|E^{(-)}(\vec{x_1},t_1)E^{(-)}(\vec{x_2},t_2)E^{(+)}(\vec{x_1},t_1)E^{(+)}(\vec{x_2},t_2)|\Psi\rangle \tag{2.90}$$

To proceed with solving equation (2.90), we fix the positions of the detectors. The detector time response is written in the fourier frequency domain

$$E^{(+)}(t_1) = \int d\omega_1 e^{-i\omega_1 t_1} f_1(\omega_1)\hat{a}_1(\omega_1) \tag{2.91}$$

$$E^{(+)}(t_2) = \int d\omega_2 e^{-i\omega_2 t_2} f_2(\omega_2)\hat{a}_2(\omega_2) \tag{2.92}$$

Where f_1 and f_2 describe the effective spectral sensitivity (spectral response plus spectral filtering) of the detectors.

The identity operator $\hat{I}$ written in the fock basis is:

$$\hat{I} = \sum_{i=0}^{\infty} |b_i\rangle\langle b_i|, \tag{2.93}$$

and can be inserted into equation (2.90) to give

$$R(t_1|t_2) = \langle\Psi|E^{(-)}(t_1)E^{(-)}(t_2)\sum_{i=0}^{\infty}|b_i\rangle\langle b_i|E^{(+)}(t_1)E^{(+)}(t_2)|\Psi\rangle \tag{2.94}$$

Note that the quantized time responses of both the detectors given in equation (2.91) contain annihilation operators that will reduce the biphoton state from SPDC to the vacuum state. Thus, the identity operator can be reduced to just the vacuum state $|0\rangle$ giving

$$P(t_1|t_2) = \langle\Psi|E^{(-)}(t_1)E^{(-)}(t_2)|0\rangle\langle 0|E^{(+)}(t_1)E^{(+)}(t_2)|\Psi\rangle \tag{2.95}$$

Defining

$$A_{12}^{(+)} = \langle 0|E^{(+)}(t_1)E^{(+)}(t_2)|\Psi\rangle \tag{2.96}$$

and recalling the state of the biphoton ψ from equation (2.87) let Ψ=ψ so that

$$A_{12}^{(+)} \sim \langle 0|E^{(+)}(t_1)E^{(+)}(t_2)\iint d\omega_s d\omega_i F(\omega_s,\omega_i)2\pi\delta(\Delta\omega)\left(\hat{a}_s^\dagger(\omega_s)\hat{a}_i^\dagger(\omega_i)\right)|0\rangle \tag{2.97}$$

Thus, we have

$$A_{12}^{(+)} \sim \langle 0|\iiint d\omega_s d\omega_2 d\omega_1 e^{-i\omega_1 t_1} f_1(\omega_1)\hat{a}_1(\omega_1)e^{-i\omega_2 t_2} f_2(\omega_2)\hat{a}_2(\omega_2)F(\omega_s,\omega_p-\omega_s)\hat{a}_s^\dagger(\omega_s)\hat{a}_i^\dagger(\omega_p-\omega_s)|0\rangle \tag{2.98}$$

$A_{12}^{(+)}$ will be non-trivial only if

a) the signal and idler modes go to different detectors, and

b) the annihilation operator for each detector annihilates the specific mode created – be it signal or idler.

Since it does not matter which goes where, the idler will be chosen to travel to detector 1. Then $\omega_s \rightarrow \omega_2$ and $\omega_i \rightarrow \omega_1$. The function $F_{(\omega_s,\omega_i)} \rightarrow F_{(\omega_2,\omega_1)}$ is assumed to be constant and not varying over the integrations, so it can be effectively pulled out. Due to the constraint the ω_p=ω_s+ω_i, then without loss of generality ω_2=ω_p−ω_1 so that there is only one remaining integral over the idler frequency.

$$\begin{aligned} A_{12}^{(+)} &\sim \int d\omega_1 e^{-i\omega_1 t_1} f_1(\omega_1)e^{-i(\omega_p-\omega_1)t_2} f_2(\omega_p-\omega_1)F(\omega_p-\omega_1,\omega_1) && (2.99)\\ &= e^{-i\omega_p t_2}F_0\int d\omega_1 e^{-i\omega_1(t_1-t_2)} f_1(\omega_1)f_2(\omega_p-\omega_1) && (2.100)\end{aligned}$$

where $F(\omega_p-\omega_1,\omega_1)$ has been replaced by F_0.

Then

$$P(t_1|t_2) \sim |A^{(+)}_{12}|^2 \tag{2.101}$$

$$\sim F_0^2 \left| \int d\omega_1 e^{-i\omega_1(t_1-t_2)} f_1(\omega_1) f_2(\omega_p - \omega_1) \right|^2 \tag{2.102}$$

which is proportional to the difference in the detection times. As a simple case, imagine degenerate SPDC with equivalent detectors centered around $\omega_p/2 = \omega_c$. Substituting $t_2 - t_1 = \tau$, equation (2.101) is just a fourier transform of the product of the spectral responses from both detectors. If each spectral response is Gaussian, then the probability is

$$P(t_1|t_2) \sim e^{-\frac{\sigma^2}{2}(\tau)^2} \tag{2.103}$$

which for an infinitely broad response ($\sigma \to \infty$) approaches a delta function in τ. To achieve this in practice, this infinity does not have to be much (i.e only a few nm). Thus for suitably placed ideal detectors, the probability of a coincidence measurement approaches unity for the biphoton. It is common to think of this result as retroactively implying that the photon pairs were created at approximately the same time and is essentially just a consequence of energy conservation in a memoryless medium. It is one of the hallmark properties of SPDC.

2.2.4 Putting it together - Dispersion, QPM, SPDC and Temperature

This section is required to understand one of the novel entanglement generation schemes presented at the end of the thesis. Further, it provides insight into an important experimental control parameter for optimizing SPDC. This section is best explained with the use of figures 2.1 and figure 2.2 which conceptually describe linear dispersion and how dispersion might be effected by different temperatures[8]. Figure 2.1 is applicable to type-II SPDC processes where the signal and idler polarizations differ by 90°.

One of the basic results from modeling SPDC is that the energy correlations are in general much tighter than the momentum correlations. In the case of a narrow line width CW pump, the input can be approximated as a plane wave with a single frequency. In this approximation, the frequencies of the signal and idler photons must sum to the pump frequency.

Figure 2.1 shows the dispersion curves for horizontally (H) and vertically (V) polarized light for a particular birefringent material at a temperature T_1 where phase matching is satisfied *naturally* and produces frequency degenerate SPDC photons. It is clear that the slopes of these dispersion curves at the frequency degenerate point are

---

[8] The effect of pressure is not considered

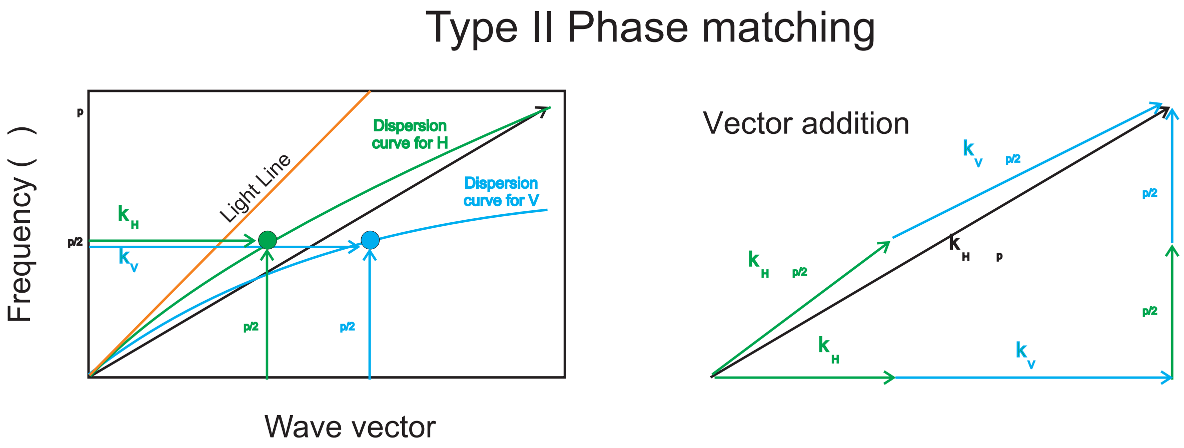

Figure 2.1: Diagram showing how type-II phase matching works in principle. The diagram on the left shows a single valued pump frequency ω_p and the down conversion photons at $\omega_p/2$, each with their own wave vector k_H and k_V. Because of birefringence the SPDC process can proceed so long as one of the photons is V polarized and the other H polarized. The diagram on the right shows how to think of this process in terms of simple vector addition.

not equal. This means that at this temperature, there can be no bandwidth to the SPDC reaction.

Realistically, the pump frequency is not singular, opening up the bandwidth for SPDC. Further, if the dispersion curves are to first-order locally equivalent, the bandwidth of the down converted signal and idler photons can widen even further.

This implies that there are a range of frequencies that can be roughly phase matched in a typical SPDC process while conserving energy.

Due to the inherent temperature dependence of the linear polarization response of the material, different temperatures will manifest different dispersion curves. If for a particular temperature, the photon frequencies created by SPDC were degenerate, then a change in temperature will lift this degeneracy.

Intuition suggests that, barring a local minima, whichever way the new dispersion curves move when increasing the temperature, the curves will move in an opposite sense if the temperature is lowered.

This develops the picture shown in figure 2.2. The figure shows how to conceptually think of dispersion as a function of temperature along with a picture that describes the frequency dependence of type-II SPDC photons on temperature.

The above description is perhaps obvious in the case of birefringent phase matching. It is less obvious if the birefringence is not sufficient to facilitate SPDC of its own accord. In this case QPM techniques like periodic poling can be employed to mitigate the phase

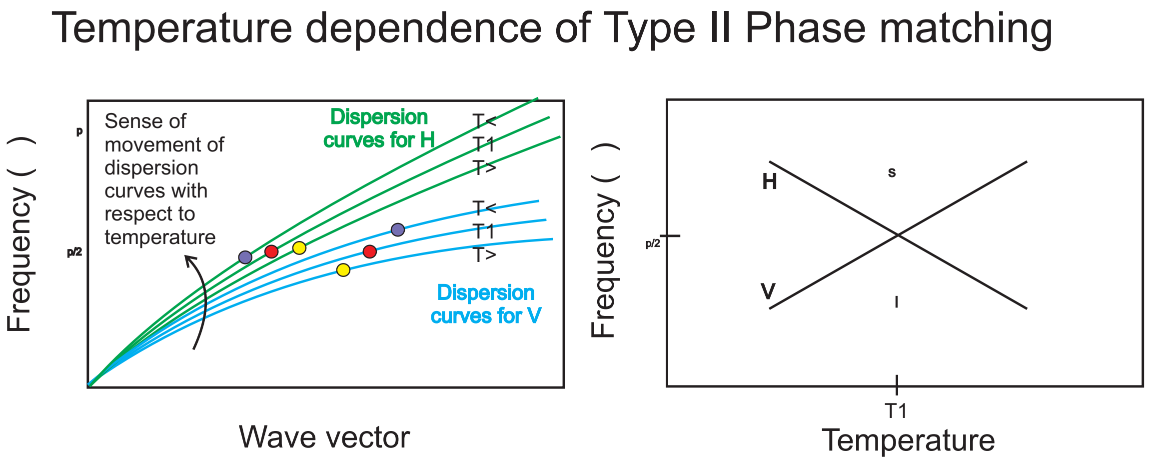

Figure 2.2: Temperature and type-II phase matching. The diagram on the left shows how the dispersion curves might change with frequency. The red circles indicate degenerate phase matching for a temperature T_1. The yellow circles depict non-degenerate phase matching upon lowering the temperature (T¡). The purple circles depict non-degenerate phase matching when raising the temperature (T¿). The diagram on the right shows the conceptual temperature dependence of the signal and idler photons emitted in a type-II phase matching scheme. The 'X' shape is another way of saying that over the bandwidth of allowed processes, the slopes of both the 'V' and 'H' dispersion curves are locally equivalent.

mismatch.

If the dependence of the poling period on temperature is sufficient, it is *possible* that tuning the temperature away from T_1 could produce a change in the poling period. This could cancel the temperature induced dispersive effects - recovering again the phase matching conditions for frequency degenerate SPDC. However, as thermal expansion is the main physical phenomenon that can have any appreciable effect on the poling period, its relatively weak dependence on temperature renders it negligible. This implies that the picture developed for birefringent phase matching is also accurate for periodically poled materials.

The last point to make re-emphasizes the tuning curve that describes the signal and idler frequencies as a function of temperature (figure 2.2). The strict energy correlations of SPDC imply that the slopes of those frequency / temperature curves need to be identically opposite at any given temperature. Thus, for any appreciable bandwidth to the SPDC process, the dispersion curves for both the extraordinary and ordinary rays should be locally equivalent to first-order.

2.3 Summary

This chapter has discussed the following concepts

- linear dispersion
- second harmonic generation
- quasi-phase matching
- mode solving
- spontaneous parametric down conversion
- temperature tuning

These ideas are used frequently and throughout the rest of the thesis.

3 Experimental Techniques

Descriptions of the various experimental configurations and their respective instrumentation are provided. In addition, the main methods to estimate efficiencies and loss in the setup are given. The chapter is divided into the following sections: introduction, purpose, equipment and experimental design, analysis of SPDC and discussion.

3.1 Introduction

Waveguiding describes the procedure of coupling light into and out of waveguides. As most measurements require instruments that are fiber coupled, the light exiting the waveguide must further be coupled into fiber. Once in fiber, the light is analyzed with various optical detectors in various configurations. Detectors are usually either silicon based (for visible and near infrared wavelengths) or InGaAs / Ge based (for light beyond those wavelengths up to about 1.8μm). For optical waveguide experiments to be successful, the experimentalist needs good control over the waveguide position and over the input and output beam position. Thus, the onus on the experimentalist is to produce a reliable coupling setup called an ’end fire rig’[1].

3.2 Purpose

To re-iterate, the experimental essence of this thesis is to facilitate efficient down conversion from a waveguide. Therefore, the experiment was designed with the following criteria in mind:

From an input standpoint, good control over intense laser fields is required i.e. good beam control, having a good handle on the emitted spectrum and the power in the fields, and being able to operate in both continuous wave (CW) and pulsed configurations.

From a mechanical standpoint, the sole purpose of the experimental setup is to facilitate the coupling of light into and out of a waveguide. The criteria for the setup are that it should be capable of:

1) Coupling in from both free space & fiber sources and coupling out to fiber.
2) Supporting wavelengths in the range .4μm to 1.65μm.
3) Accommodating both pulsed and cw light.

---

[1] End fire coupling is jargon for shooting a free space beam through some kind of focussing element and into the end of the waveguide.

4) Controlling the polarization degree of freedom.
5) Separating the pump / input light source from the up or down converted light.
6) Conducting experiments for long durations (8 - 24 hours).

From a measurement standpoint, the setup should be able to provide power, wavelength and timing information. As it is unlikely that down conversion will be detected with a power meter, power measurements will serve to infer coupling efficiencies and transmission / loss information in the various components of the setup. Spectroscopically, it is necessary to know at least one of the spectra for either up conversion or down conversion so that the correct wavelength can be pumped into the waveguide. Lastly, as the hallmark signature of down conversion is really the unique time correlation a down conversion photon shares with its counterpart, sub to single nanosecond timing information will be crucial for the success of the experiment as a whole.

3.3 Equipment and Experimental Design

The first subsection details and explains the equipment that was procured for the waveguiding experiments performed in this thesis (and can be skipped if the reader is already familiar with such equipment). The second subsection details the experimental setup (see figure 3.1). The third section describes the measurement configuration (see figure 3.2).

3.3.1 Equipment

Input sources

Injected light came from a variety of laser sources. Our main laser consisted of a 18W Verdi / Mira cavity from Coherent. The Verdi laser is hermetically sealed, water cooled and pumped by two laser diodes that emit light with a wavelength of 1064nm. The Verdi operates with a current of around 52A and emits second harmonic light with a wavelength of 532nm that pumps a Titanium Sapphire crystal in the Mira Cavity. The crystal de-excites in the infrared and has a nominal tuning range from 700-900nm. In pulsed mode, the Mira has the potential to emit 2-7 picosecond long pulses of light with a repetition rate of approximately 76MHz.

The other main input laser is a TSL210V from Santec which offers tunable output over a wavelength range between 1500nm and 1620nm with an output power greater than 20mW. When the main laser was not needed, or was unavailable, alignment was often facilitated with a 20mW fiber pigtailed laser module (from Meshtel) emitting light at a wavelength of 635nm.

When necessary, amplification up to 200mW over the C and L bands (1530-1565nm, 1570-1600nm respectively) was provided by two Erbium Doped Fiber Amplifiers from Amonics.

End Fire Rig

The end fire rig is divided into three sections. The input lens positioning system, the sample positioning system, and the output lens positioning system.

The input lens positioning system consists of a 120mm long travel crossed roller bearing aluminum stage from Optosigma, and a NanoMax 313 from Thorlabs with an additional yaw/pitch stage.

The sample positioning system is a 500mm long travel motorized stage from Zaber, and a custom 4-axis stage from Luminos.

The output positioning system is identical to the input positioning system. Both input and output lens positioners are equipped with an RMS threaded objective mount. Standard compound lens microscope objectives from Olympus in denominations of 4x, 10x, 20x, 40x were purchased as well as single aspheric lenses with similar effective magnifications. The only additional objective purchased was an Olympus (of the type 'umplfl') 100x with a numerical aperture of 0.95 and a working distance of 0.35mm.

Measurement

Power Instrumentation

Power measurements were most often made with a Newport 1831c meter outfitted with both silicon and ingaas detector heads. In some cases it was necessary to use a slim Ge detector from Thorlabs to obtain a power reading in spatially confined areas.

Spectroscopy Instrumentation

Spectroscopy was facilitated at both IR and Telecommunications wavelengths via two spectrometers. For IR light, a 750mm focal length spectrometer from Princeton Acton was employed. The spectrometer is equipped with three gratings blazed for around 900nm. The grating line spacing for the three are 600 lines per mm (lpmm), 1200 lpmm, and 1800 lpmm. A silicon based nitrogen cooled ccd camera was used to detect and convert the light to an electrical signal. For the 1.55μm region, a 500mm focal length spectrometer from DeltaNu and a MosIR 950 InGaAs ccd were purchased from Intevac. The DeltaNu is configured with three gratings (150 lpmm, 300 lpmm, and 600 lpmm) all blazed for 1550nm.

Timing and Detector Instrumentation

Timing information was inferred from the electrical signal produced by a single photon detector due to a detection event. Two brands of single photon detectors were used during the thesis – Princeton Lightwave Incorporation (PLI), and IDQuantique (IDQ). The PLI detectors are equipped with single mode fiber connectors, while the IDQ detectors are capable of multimode coupling. For this reason, and ease of use, the main detectors used in this thesis are those from IDQ, although early data was obtained with the PLI detectors. Due to technological limitations, these detectors need to be gated (cannot free run) and have an inherent dead time after detection. They can only operate safely up to 5 MHz[2]. Thus, when the experiment is pumped with pulses from the main laser (rep rate of 76MHz), it is not possible to gate the detectors directly off of the internally supplied fast photodiode. Instead the electrical repetition rate is reduced via custom electronics built by the University of Waterloo.

3.3.2 Experimental Design

In this section the physical setup is described in detail along with how it is designed to meet the criteria outlined above.

Optical Layout

The main experimental setup is shown schematically in figure 3.1. The setup is bidirectional working from left to right and right to left. As the main laser emits solely into a free space mode it could be pumped directly into the end fire rig. However, the free space mode was also coupled and decoupled to single mode fiber to create an effective fiber coupled output[3]. The TSL210V is only capable of emitting from a fiber tip and so required collimation to free space before being injected into the end fire rig. The two types of modes will be referred to as a free space mode and a fiber mode respectively, even though they are all injected from free space into the waveguide.

Detector Layout - Down Conversion

Once SHG was verified and characterized for a particular waveguide the optical configuration was reversed and attempts were made to verify the existence of down conversion from the waveguide. Because the experimental signature of SPDC is a strong emission time correlation between two single photons, the second half of the experiment involved instruments that could measure such a time correlation.

---

[2] Detectors based on InGaAs APD's generally cannot remain open for large extended periods of time. The main reason for this is that the detectors work by biasing a photo diode beyond its breakdown voltage. This is called geiger mode operation. They are therefore extremely sensitive to other physical processes responsible for creating electron hole pairs. Once an electron hole pair is generated, the over bias creates an avalanche response to produce the electrical detection signal. Further, after each detection event, there is a required dead time, where the overbias is removed from the detector to allow trapped charges born out of the avalanche process to dissipate. This avoids what is called afterpulsing, which is the condition where an avalanche induces an avalanche that induces an avalanche and on and on. The dead time is typically 10 μs and places another limitation on the operation speed.

[3] A single mode (SM) fiber acts as a very nice spatial filter.

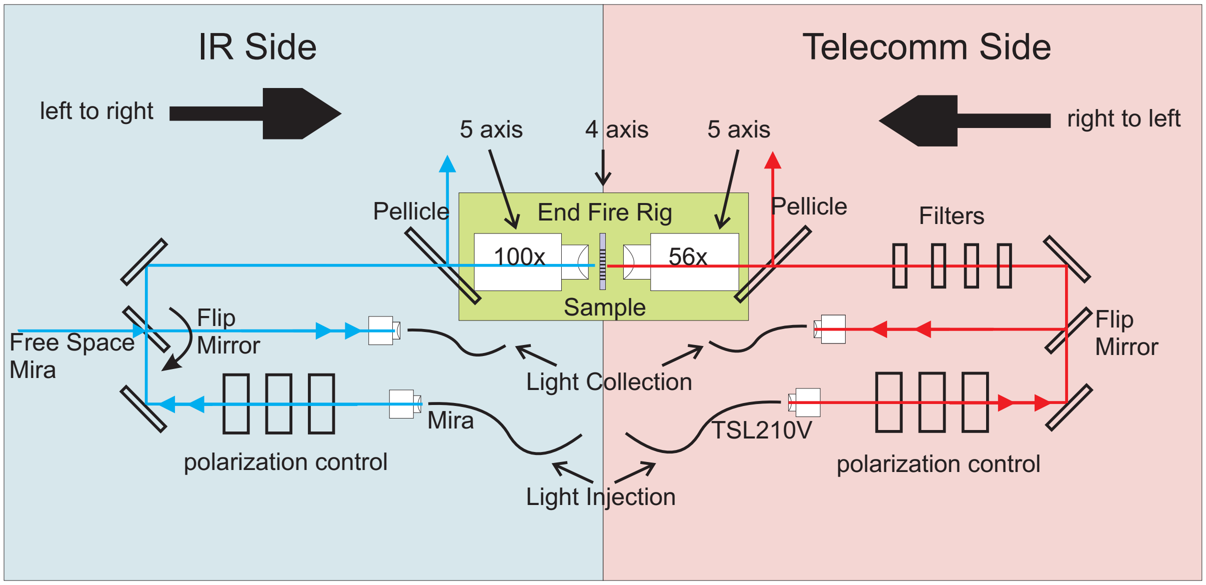

Figure 3.1: A Diagram of the experimental configuration. A pellicle provides diagnostic imaging and waveguide assistance. The flip mirror on the left is flipped up for multimode coupling of the signal, or flipped up and rotated to allow free space input from the Mira. The sample is controlled via a 4-axis stage, while the input and output coupling objectives are maniuplated using a 3-axis stage to center the objective and 2-axis tip/tilt stage to square the objective to the input beam. In the left to right or *downconversion* configuration, 775nm light (or thereabouts) is shot into the 100x and collected with the right flip mirror up. In the right to left or *up conversion* configuration, 1550nm light (or thereabouts) is shot into the 56x objective and collected with the left flip mirror up.

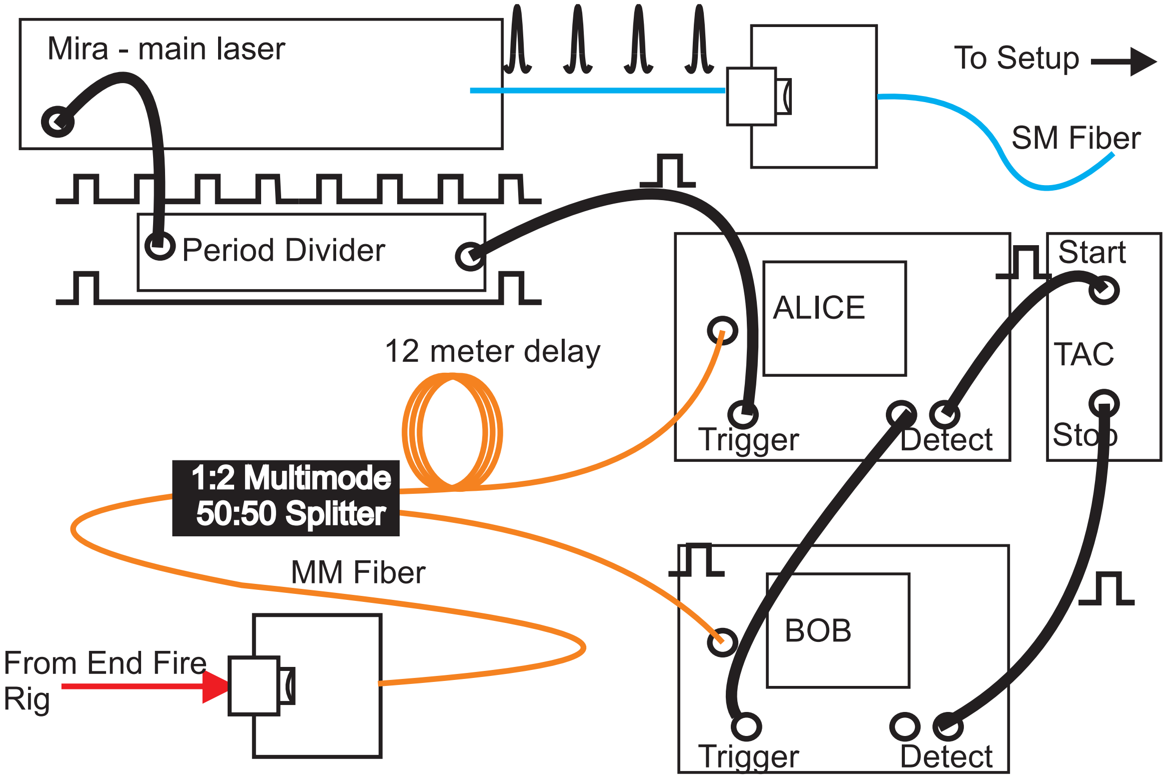

Figure 3.2: A Diagram of the detector setup. Alice is triggered by a period divided copy of the signal emitted by the fast photodiode on the main pump laser. She is synchronized to the optical source by adjusting an internal delay. After an avalanche event is detected, she in turn triggers Bob and simultaneously starts the TAC. Bob stops the TAC when he detects an avalanche event. Software converts the final amplitude from the TAC to a time and updates a running histogram of these start-stop times. The histogram is displayed via commercial software in real time.

The experimental setup that was used to gather timing information is depicted in figure 3.2. Detectors capable of sensing single photons are crucial to the experiment, however, the single photon detectors used were unable to resolve the incoming photon number[4]. This meant that simply coupling the output from the waveguide directly to a single photon detector would not be able to provide information about such a time correlation.

To get around this, it was necessary to split the output signal so that with some reasonable probability, a single photon from the pair would be spatially separated from

---

[4] For these types of detectors, an event caused by a single photon is indiscernible from an event caused by two or more photons so long as they arrive within a certain time window

its counterpart. This allowed a second single photon detector to be used[5], the challenge being to time synchronize the two detectors.

Splitting was achieved with a multimode fiber splitter with an approximate 50:50 (actually 12:16) splitting ratio and an optical delay of 14m in one arm. The optical delay of 14m provided roughly 70ns of delay. This was more than sufficient to allow the second detector to be electrically triggered by the first detector while still guaranteeing that the arrival time of the second photon would occur within the detection time window of the second detector.

The electrical detection signals were then sent to a time to amplitude converter (TAC). The TAC was started by a detection event from the first detector and stopped by an event produced by the second detector[6]. The final amplitude was then recorded and the time between the two events was inferred based on the value of the amplitude. A count was placed in a corresponding time bin, and a running histogram of the bin values was plotted via custom software that interfaced with the TAC.

What results is a picture of the relative frequencies of the occurrences of all the start/stop times between the first and second detectors. Although the TAC was capable of resolving time differences of 10 picoseconds, timing jitter (see appendix) in the various instruments decreased the actual effective time resolution of the setup. The overall time resolution of this setup was approximately 1.5ns.

From here onwards, and for largely canonical reasons, the first detector shall be referred to as Alice or as Alices detector, and the second detector shall be referred to as Bob or Bob's detector.

3.4 Analysis of SPDC

There were two types of down conversion experiments performed in this thesis – CW experiments and Pulsed experiments. They both employed the above detector configuration. The main experimental result occurred in the pulsed configuration, and so what follows is a qualitative and quantitative analysis of the pulsed optical configuration. The assumptions are that both Alice and Bob's detection probability is uniform across their gate, the pump photons are *mostly* filtered out, and the efficiency of down conversion is such that no concern for multiple pairs is needed.

Pulsed Down Conversion - Qualitative

For the pulsed case, Alice was externally triggered by the period reduced output from the fast photodiode that comes built into the Mira. The period reducer was binary, so

---

[5] for low SPDC rates, a lone single photon detector could be multiplexed

[6] In our case, the detection rate of the first detector was much greater than the second detector and this is not necessarily the optimum way to run the TAC, however, the rates were such that it didn't matter

it could reduce the 76MHz lasing repetition rate, by 64, 32, 16, etc. For most of the experiments, a setting of 32 was used, and Alice would nominally trigger at a rate of around 2.4MHz. Note that regardless of this reduction, an optical pulse is still generated at a rate of 76MHz or approximately every 13ns. In order to ensure that Alice was capable of seeing photons that might be time correlated with the pump, her detection window could either be extended to a time beyond 13ns or a suitable delay chosen to synchronize her detection window to coincide with the arrival of the optical pulse. For reasons to be discussed later on, the second option was chosen. A diagram of the timing signals is shown in figure 3.3.

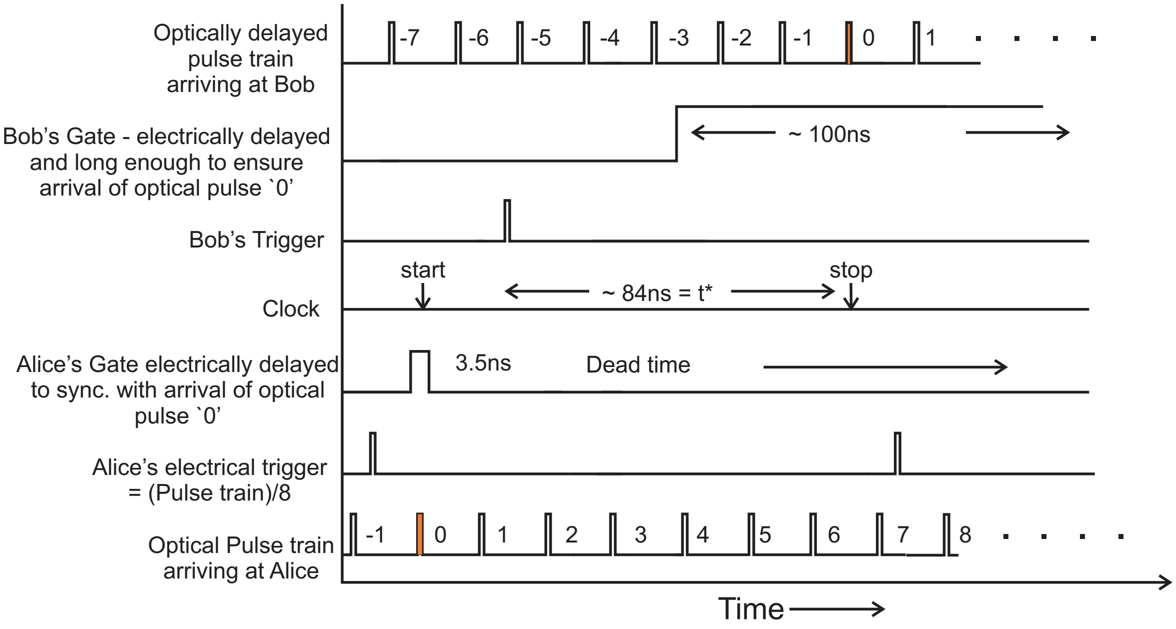

Figure 3.3: A picture of the relevant electrical signals produced by the instruments for the case when SPDC is produced, the photons are split and subsequently detected. To begin, Alice is triggered by the one out of every 8 electrical signals emitted by the fast photodiode (which produces an electrical version of the optical pulse train emitted by the main laser). By adjusting an internal delay, she is synchronized to one of the optical pulses – in this case pulse '0'. She detects the arriving photon (orange pulse) and in turn triggers Bob and simultaneously starts the clock (TAC). Bob detects the remaining photon from the pair and stops the clock (TAC). Here the start stop time is approximately 84ns.

To choose the delay, significant pump light was allowed into Alices detector to ensure a good detection probability. Her trigger out / gate output was sent to start the TAC, while her detect out stopped the TAC. The histogram generated over a sufficient duration of time (usually a minute or two) with Alices detection window set to greater than 13ns indicated where in time the pulses were arriving[7]. Then, her internal delay was adjusted and her detection window narrowed to approximately 3.5ns while still coinciding with this arrival time. Once the delay was chosen, the main detector configuration was re-established - i.e, Alice starts the TAC, Bob stops the TAC. A qualitative picture of what to expect in the final histogram is developed as follows.

Imagine that SPDC has occurred in a pulse. Let one photon from the pair arrive at Alice and be detected, starting the TAC. Alice in turn triggers Bob so that he will be armed and ready to detect the other photon from the pair. Let Bob detect this photon, stopping the TAC. Call the time taken to start and stop the TAC t^* and record this time *difference*.

Now imagine that Alice detects a random event (e.g. a dark count or stray pump photon that made it past the filters), then there is no guarantee that a down conversion counterpart is arriving at Bob at t^* (at least this is very unlikely). Consequently, if Bob does detect an event, the likelihood that this will occur at a time t^* is the same as that for any other time within his detection window t_{Bob}[8].

Since the TAC will not stop until (at the very least) Bob is triggered or it reaches its maximum amplitude, then there will be no stop times in the histogram that occur before Bob is triggered. Thus, the important points of the histogram correspond to the time when Bob immediately detects an event – say t_0 and when Bob detects an event at the very end of his detection window which is t_0+t_{Bob} where t_{Bob} is Bobs gate time. The relevant histogram (where the bin values are non-zero) is precisely equal to Bob's gate time whereas the total histogram will contain empty bins at all other times.

In summary, if SPDC occurs , then the expected histogram will have more recurrences of the time difference t^* than for any other times. Note that, admitting other pump related phenomenon – as in unblocked pump photons – there will be small recurrences every $t^* \pm n\Delta$ from unblocked pump photons. Here, Δ is the time between optical pulses, and n is an integer.

Consideration should also be given to the probability of SPDC occurring in successive pulses. If this were to happen, the final histogram would show a *signal* component at $t^* \pm n\Delta$ as well. To explain this, briefly consider the following scenario where both photons from the first event happen to go to Alice, while both photons from the second event go to Bob. Another scenario is that Alice gets both from the first pulse and Bob

---

[7] Figure A.6 in the appendix shows a typical histogram for this scenario

[8] This is really only true in the CW case. In the pulsed case where the average power is equivalent to the cw case, the change in the optical distribution has the following consequences: As long as Alices detection window is less than 13ns, then Alice will see a greater probability for both down conversion and pump photons to arrive at her detector within her detection window. Since there is no light between pulses, Alice shouldn't see any optical signal for those times. The change in the histogram is thus concomitant with the change in distribution of the photons in the pump pulse. That is, there will be an expected drop in the values stored in the time bins where no optical light exists, and an increase in the values stored in the time bins where the the pulse arrives.

only gets one from the second pulse.

To conclude the qualitative description for both CW and pulsed configurations, if the experiment can be run long enough to discern the signal from the noise then if down conversion exists, no matter how weak, the histogram generated by the TAC will have significantly more recurrences of t* than any other time.

Pulsed Down Conversion - Quantitative

For the following quantitative analysis, the main assumptions are that

- 1) The pulse length is smaller than any of the gate times.
- 2) Multiple pairs per pulse are unlikely.
- 3) Their single photon transmission probabilities (η) leading up to the probabilistic beam splitter are equal.
- 4) The probabilistic beam splitter is lossless and treats each photon independently.
- 5) The probabilistic beam splitter gives a photon to Alice with probability p_A, and a photon to Bob with probability p_B.
- 6) Detectors are time synced to the arriving optical signal so that trigger rates can be interpreted as pulse rates.
- 7) Detectors are not capable of resolving photon number.
- 8) Detector Dark counts are ignored.
- 9) Detector efficiencies (ϵ_d) are assumed to be equal.

Quantitatively, the number of SPDC photons arriving at Alice ($\frac{N_A}{pulse}$) per pulse is the number of pump photons per pulse ($\frac{N_p}{pulse}$) inside the crystal multiplied by the SPDC efficiency (ϵ) and the transmission probabilities of all the interfaces that lead up to Alices detector (η). It is further reduced by the probability that Bob receives both photons from a created pair (p_b^2)

$$\frac{N_A}{pulse} = \frac{N_p}{pulse}\epsilon\eta(1-p_B^2). \tag{3.1}$$

Similarly for Bob, the number of SPDC photons is given by

$$\frac{N_B}{pulse} = \frac{N_p}{pulse}\epsilon\eta(1-p_A^2). \tag{3.2}$$

Alices single photon detection rate (in one second) from SPDC (S_A) is then degraded by her detection efficiency (ϵ_d) but multiplied by her trigger rate (R_A).

$$S_A = \frac{N_A}{pulse}\epsilon_d R_A \tag{3.3}$$

Ideally, since SPDC comes in pairs, Bobs single photon count rate (S_B) should be equal to Alices. As Bob's trigger rate (R_B) is determined by Alices detection rate, it can be no bigger than Alices. His rate will be degraded by the effect of the probabilistic and asymmetric beam splitter[9] (Alice might have gotten both of the photons from the pair). Further, it will be lowered by both ϵ_d and η. Note that Bob's single photon count rate is identically the coincidence rate (C).

$$\begin{aligned} S_B &= S_A\epsilon_d\eta(1-p_A^2) && (3.4)\\ &= \frac{N_A}{pulse}\epsilon_d R_A\epsilon_d\eta(1-p_A^2) && (3.5)\\ &= \frac{N_p}{pulse}\epsilon\eta^2\epsilon_d^2 R_A(1-p_B^2)(1-p_A^2) && (3.6)\\ &= C && (3.7)\end{aligned}$$

A typical parameter to quote when measuring coincidence rates is the expected detection rate from random processes like dark counts or stray pump photons. If the random rate can be upper bounded, then a violation of this bound implies that the measured rate is not from a random physical process. A reasonable upper bound on Bob's random count rate is achieved by assuming his trigger rate (Alices count rate) is due to some random flux of photons. Alices count rate can then be reinterpreted as a new 'pulse' rate that arrives at Bob's detector. Bob's random coincidence rate is

$$\begin{aligned} C_{rand} &= \frac{N_B}{pulse}\epsilon_d S_A && (3.8)\\ &= \frac{N_p}{pulse}\epsilon C && (3.9)\end{aligned}$$

In the experimental configuration used (figure 3.2), the TAC data provides information on the actual time difference between two avalanche events. Assuming these events are caused by photons, then the resulting histogram displays much more information than a bulk coincidence rate. Nonetheless, a quick verification of the conditions of the experiment can be made by looking at Bob's detection rate and comparing it to the random rate.

---

[9] In this thesis, the asymmetry was measured to be approximately 16:12 so that p_A=16/28.

Comparison between CW and pulsed configurations

This subsection outlines why the pulsed configuration was chosen (over cw). Because SPDC is linear in the pump power, an intuitive way to compare the two cases is to first imagine a function whose value represents the average number of photons emitted by the laser in the CW configuration per unit time. This is approximately flat. Next, take the area under the function over 1 period, where one period is given by the inverse repetition rate of the laser in the pulsed configuration. For the experiment, this time interval was approximately 13ns. The area represents the number of photons in 13ns, or the energy in 13ns. For the experiment, the pulse length was approximately 7 picoseconds. The pulsed configuration effectively squeezes 13ns of energy into 7 picoseconds. Thus, the number of photons in 7 picoseconds of pulsed light is approximately 2000 times larger than 7 picoseconds of CW. However, note that Alices detection window is not 7 picoseconds. For most of the experiments, Alices window was approximately 3.5ns. Thus, $\frac{N_{pump}}{pulse}$ is roughly 13/3.5 = 3.7 times bigger than N$_{pump}$.[10]

3.5 Discussion

The relevant experimental tools and methods have been discussed. One final comment is warranted:

- A very big problem with the setup was the sample stability. It was and is still unclear whether the sample moved as a result of temperature changes in the lab or just mechanically drifted without cause. Tests were done that isolated the problem to the flexure stage, but it still cannot be determined whether the flexure stage itself is to blame or whether the blame can be placed on the instability of the lab *temperature*.

---

[10] The single photon detectors from IDQuantique are capable of variable length detection windows. Nominal settings are 2ns, 5ns, 20ns, 50ns and 100ns. For similar trigger rates and windows less than 13ns it is more beneficial to operate in pulsed configuration, while for windows larger than 13ns the opposite is true. Because these detectors have other issues like dark counts and dead times, it isn't completely clear that operating in CW mode with 100ns gate times is optimal.

4 QUASI-PHASE MATCHING

This chapter describes the efforts to verify the experimental procedures outlined in the previous chapter. This was accomplished by obtaining working waveguides fabricated from Periodically Poled (PP) Lithium Niobate (LN). Because Lithium Niobate is also involved in a later chapter, more detail is provided concerning its basic properties. The chapter concludes with two graphs demonstrating both SHG and SPDC.

4.1 Introduction

Lithium Niobate finds applications in surface acoustic wave physics, piezoelectricity and in non-linear optics. It is the latter application that is of interest in this thesis. Due to its ferroelectric nature, the crystallographic structure can be inverted via the application of an electric field. In turn, this allows access to a strong bilinear response that can be exploited to facilitate spontaneous parametric down conversion and the creation of single and entangled photons.

4.2 Properties of PPLN

In this section, a brief description is given detailing the more important properties of Lithium Niobate as they pertain to Quasi-Phase matching.

Crystal structure

Lithium niobate is grown via the Czochralski method; a process named after Polish scientist Jan Czochralski discovered that introducing and then pulling a small seed crystal from a melt allowed the growth of much larger cylindrically shaped versions of the seed crystal. Its structure is trigonal [44], exhibiting 3-fold symmetry about its c axis. Figure 4.1 provides conceptual drawings of the structure. Other important axes are labeled a_1, and a_2. When looking at a cross section of the unit cell of the crystal along the c axis, the structure consists of 7 planes of 3 oxygen atoms that are hexagonally close packed and intersticed with Lithium and Niobate atoms. For a temperature greater than the Curie temperature (≈ 1200 °C), Lithium Niobate occupies a paraelectric phase. In this phase, 2 Li atoms can be found with equal probability above or below a plane, the average position being in one of the planes. In contrast, the 2 Niobium atoms are found between the planes. Below this temperature, the elastic forces dominate the structure and cause the lithium and niobate ions to shift position resulting in a net space charge

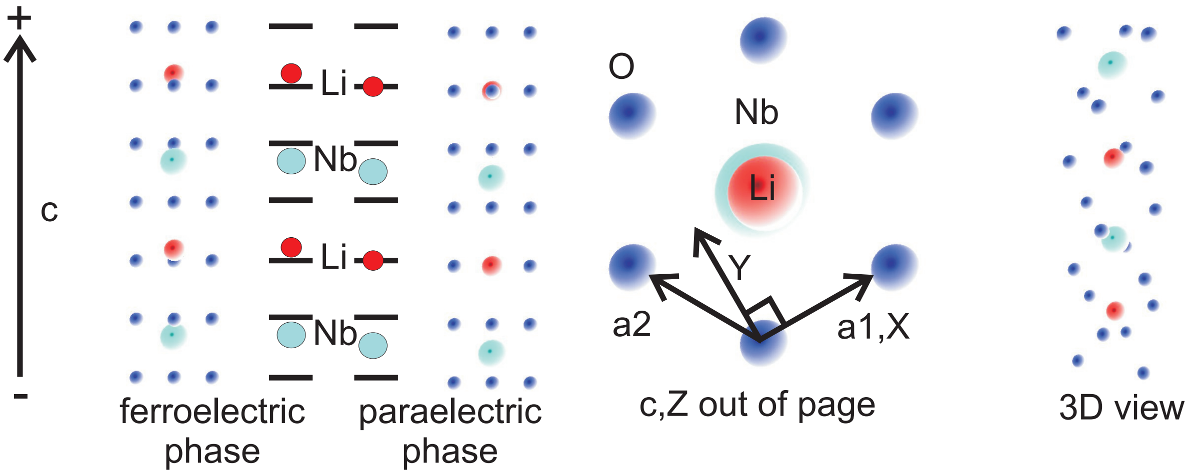

Figure 4.1: From left to right: A Diagram of the paraelectric and ferroelectric phases of Lithium Niobate. Positions are not exact, but the conceptual crystal is shown. *Average* positions for the lithium and niobate ions are shown for both phases to illustrate the difference between the two conditions. A top view showing the hexagonal structure. The c axis is identified with the cartesian Z axis, and one of the a axis is chosen to be the cartesian X axis. The Y axis is then determined for a right handed system. A 3D mockup of the crystal structure is drawn using values obtained from literature.

separation that causes a spontaneous polarization along the c axis. Thus, under normal conditions, Lithium Niobate is in a ferroelectric phase.

Permittivity

The permittivity tensor has two values. Symmetry and thermodynamical arguments (beyond the scope of this thesis) show that along $a1$ and $a2$ the permittivities are identical, while along the c axis, the permittivity attains a different value. On average, the permittivity generates an index of refraction of roughly 2.2 over the UV, visible and near infrared (see figure 4.2).

Thermal expansion

Briefly, when considering the thermal expansion of Lithium Niobate, it should be noted that as the temperature is increased, both a_1 and a_2 expand linearly, while over the range 600-1000 °C, the c axis actually compresses. As mentioned in the theory, thermal expansion has a negligible effect when considering the temperature dependence of phase matching.

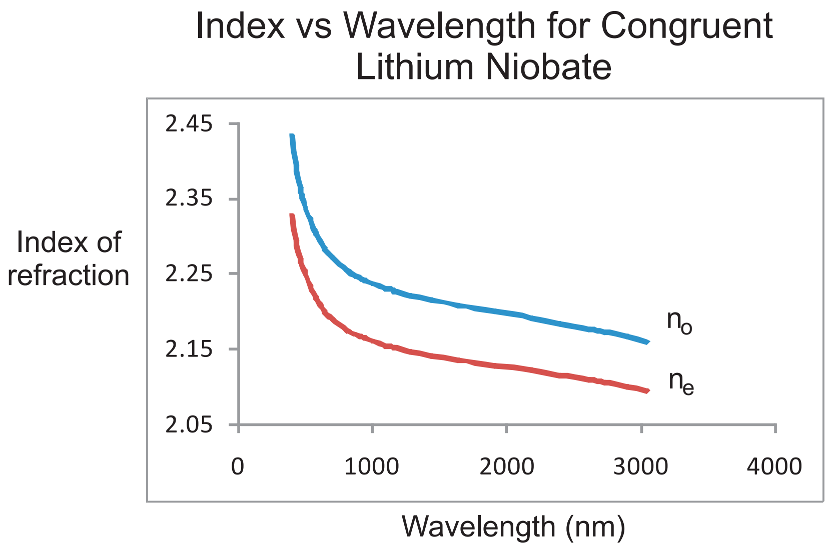

Figure 4.2: Measured index of refraction data obtained from [1] for extraordinary (n_e) and ordinary (n_o) light in Congruent Lithium Niobate.

Photorefractive Effect

Photorefractive damage is a limiting factor in optical uses for Lithium Niobate. The damage results from a combination of a photovoltaic process followed by a linear Pockels effect. First, charge migration occurs due to the photovoltaic process. This creates an internal electric field that , via the electro-optic effect, produces a change in the refractive index. This results in scattering and loss of control of the pump beam. Photorefractive damage can often be reversed by annealing, as well as protected via doping with, for example, Magnesium [45].

Bilinear Susceptibility

In contracted notation, there are three bilinear susceptibilities. They are $d_{22} \approx 3\text{pm/V}$, $d_{31} \approx 5\text{pm/V}$, and $d_{33} \approx 30\text{pm/V}$ [46]. Because it has the largest value, d_{33} is of most interest. Evidently, SPDC and SHG processes that are appropriately directed to involve d_{33} will be stronger than for other directions. In particular, for SHG, even this factor of 4 or 5 is significant as the power is quadratically dependent on d_{eff}.

4.3 History of QPM in PPLN

From both a non-linear optics and quantum optics perspective, Lithium Niobate is a very interesting material. As mentioned, it has a relatively strong non-linear coupling for z polarized fields. Further, the material is transparent from about 0.3μm-5μm and is an ideal material for many optical applications.

Proton and Reverse Proton Exchange Waveguides

Lithium Niobate has another distinct advantage as a non-linear optical material: It can support buried and surface optical waveguides. Optical waveguides are typically regions of high index with respect to their surroundings. By confining light into small areas, the local field intensity increases, and thus these structures can intensify non-linear processes like SHG.

The idea of Proton Exchange (PE) to create regions of index contrast was developed in the early 1980's [47]. Exchanging Lithium ions with protons increased the extraordinary index of refraction while decreasing the ordinary index of refraction. At the time, it was noted that in these regions, the bilinear susceptibility suffered. Ways to circumvent this potential problem were discovered as the decade progressed. In particular, it was found that to maintain the high bilinear susceptibility, low proton concentration was required. The fabrication procedure is known as the dilute melt method [48]. Further improvements in the waveguide performance involved annealing, forming Annealed Proton Exchange (APE) waveguides which exhibited a graded index profile.

Waveguides can now be buried via a process called Reverse Proton Exchange (RPE) having the effect of imposing a more symmetric mode field structure in the waveguide [49]. They can also be fabricated on various crystal cuts using various acids (for example, benzoic acid [50][51], toluic acid [52] etc.) to facilitate the exchange. Via combinations of PE and RPE as well as doping, waveguides can now support both extraordinary and ordinary polarized light [53].

Electrical Poling

At first glance, due to dispersion, any bilinear optical process involving d_{ii} where $i \epsilon \{x, y, z\}$ will not be inherently phase matched. This is because all field polarizations are identical. However, as mentioned, LiNbO3 is nominally ferroelectric, and its crystal structure can be inverted with the application of an external field. If the structure is inverted, then the bilinear polarization response will also be inverted, and this is equivalent to a π phase difference in the bilinear response between the normal and inverted regions. The application of an electric field to invert the structure initiates a process called poling. Poling can be effected in other ways, but only electrically induced poling will be considered from here on.

Poling was pioneered in the early 90's by Yamada et al. [54]. It was observed that domain inversion could occur at room temperature without breaking the sample if the sample was thin enough. For domain inversion to occur, field strengths close to those required to create an electron avalanche are required. For thin enough samples, the avalanche does not gain sufficient energy to destroy the substrate. Since then, the kinetics of the poling process has been studied [55] to a point where poling has now become a well controlled and refined process.

It is perhaps clear that if poling is effected periodically, then the bilinear response will be repeatedly and consistently inverted with the same period. If the period is chosen correctly, then the bilinear response can be re-phased to effectively match the phase of the driving field. This idea actually predates poling by some 30 years and was first proposed by Armstrong et al. [25].

That this can be achieved by electrical means implies that Periodic Poling (PP) can facilitate bilinear processes like SHG and SPDC where they might otherwise be naturally inhibited. Although only one example is referenced here [56], the literature provides numerous accounts of the use of poling to enhance the total bilinear response from a non-linear crystal. Electrical periodic poling does have limitations: it becomes more and more difficult to produce uniform periodic poling for shorter and shorter periods. This impacts the usefulness of QPM facilitated by electrical poling. The effect of a non-uniform poling period on QPM is discussed, among other tunable parameters, in an article by Martin Fejer [27].

4.3.1 Summary

For wavelength conversion involving reasonable poling periods, waveguides in electrically Periodically Poled Lithium Niobate now enjoy the status of a commercially available product. They represent the standard for wavelength conversion over most of their transparent range.

4.4 Experimental Results With PPLN

A second generation waveguide setup was created using 30mm and 60mm cage optomechanics from Thorlabs. The main positioning stage was a 3-axis CorrAlign from Luminos equipped with a rotation and pitch stage. The idea of this setup was to create a smaller footprint for free space waveguiding to remove some of the tolerances that plagued the main guiding setup outlined in the experimental chapter. From an instrumentation point of view, the equipment used to make measurements are identical to that already described. Thus, the main differences between the original setup and the 2nd generation setup are its size, the choice of optics to match the waveguide, and its fewer mechanical degrees of freedom. The setup also incorporated a custom built oven to facilitate free space coupling to the waveguide over a range of temperatures.

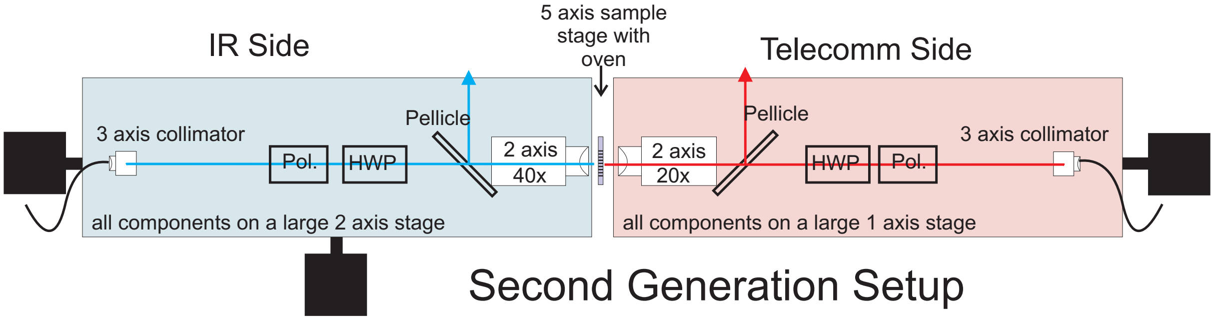

Figure 4.3: A diagram of the 2nd generation setup which consisted of fewer mechanical degrees of freedom than that of the main setup described in chapter 3. Light was collimated at either side and sent through a polarizer to select linear polarized light. The half wave plate (HWP) rotated the polarization to vertical. All optics were mounted in a 30mm cage supported by a larger 60mm cage (not shown). Positioning was accomplished with a 5-axis sample stage that included an oven to control the temperature of the crystal.

4.4.1 Results

Two samples of PPLN were graciously donated by Dr. Wanguo Liang – a research associate at McMaster University. Very little is known about these waveguides from a fabrication point of view – just that they were approximately 10μm wide and a few μm deep. The crystal was periodically poled MgO:LN and nominally phase matched for 1560nm. Further, the sample did not require temperature tuning. Most likely their method is similar to their published articles [57]. Following initial experimental results, a PPLN waveguide down conversion crystal was procured from the Taiwanese company HC Photonics with the parameters given in table 4.1.

Sample Specifications

The crystal from HC Photonics was Z cut – meaning the orientation of the plane of its largest surface was determined by the crystal c axis (the plane contained the $a1$ and $a2$ axis). Therefore the SHG and SPDC processes required vertically polarized input light.

A schematic of the waveguide is shown in figure 4.5 and the waveguide depth profile is shown in 4.4. HC Photonics does not willingly get into a discussion of their waveguide fabrication process, so the above results are all that were obtained upon purchasing the sample.

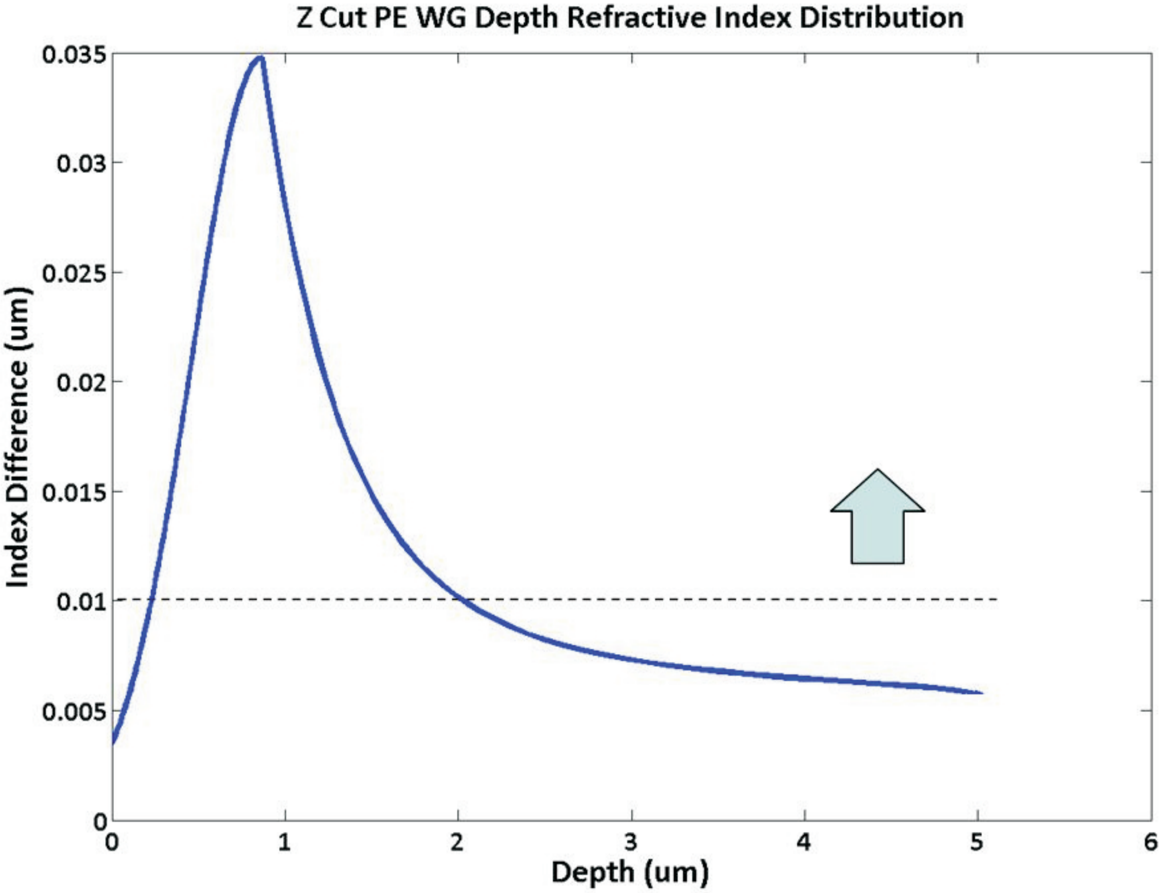

Figure 4.4: Plot of the profile of the waveguide with depth provided by HC Photonics Corp. The waveguide is buried and fairly symmetrical.

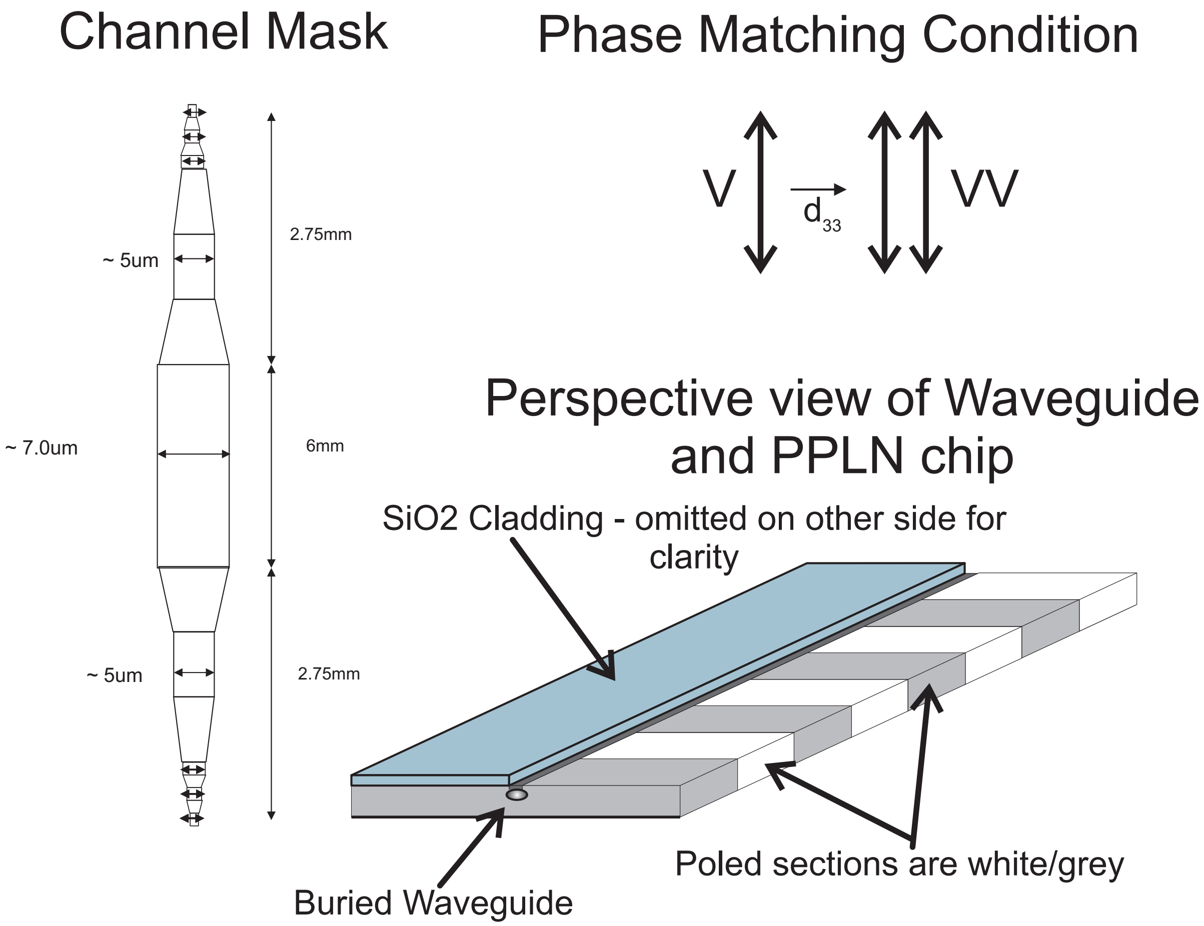

Figure 4.5: Channel mask and perspective view of a buried PE waveguide with a SiO_2 cladding. The cladding prevents PE from occurring outside the channel and is, to the authors knowledge, left on the chip. Phase matching condition is V→VV. The crystal is Z-cut. The channel mask involves straight and tapered sections presumably to facilitate matching to fiber. The effective non-linear region is 6mm.

Material	M_gO-Congruent LN
% Li	48.45
% Nb	51.55
Index of refraction (LN substrate)	2.14
Index of refraction (M_gO waveguide)	2.18
effective N. A.	0.14
Waveguide depth	.004 mm
Waveguide width	.007 mm
Waveguide length	6 mm
Chip length	11.5 mm
Y-Modal Field Diameter (1550nm)	8.53 μm
X-Modal Field Diameter (1550nm)	7.77 μm
Y-Modal Field Diameter (775nm)	4.5 μm
X-Modal Field Diameter (775nm)	3.89 μm
Walkoff Length	3.5mm
Normalized Conversion Efficiency	40 %/W/cm^2
Maximum average power	150mW
Temperature for 1550nm SHG	60±10° C

Table 4.1: HCP Sample Specifications

SHG and SPDC

Of all the many experimental measurements made with the PPLN samples, none are more pertinent than those that verified the measurements that were made while experimenting with Bragg Reflection Waveguides (BRW). In those experiments, the most important measurement involved the recording of the arrival times of single photons at two physically different locations – Alice and Bob. As a sort of dry run – to develop a sense of the expected results from that measurement – output SPDC photons from the HC Photonics sample were sent through the same detection apparatus. That result is reported in what follows.

The alignment followed a similar procedure to that described in the previous experimental chapter. To quickly review, the HC Photonics sample was optically aligned using facet imaging techniques and white light illumination to determine the positions of the waveguides. As the overall efficiency of the PPLN was much greater than that of the BRW samples, upconversion (second harmonic generation) was verified *not* with a spectrometer, but with a power meter. Figure 4.6 shows the upconversion results for three different temperatures. After optimization, the upconverted light was then sent to the spectrometer and recorded. The spectrum was re-displayed while tuning the wavelength of the main laser to match the approximate center of the spectrum.

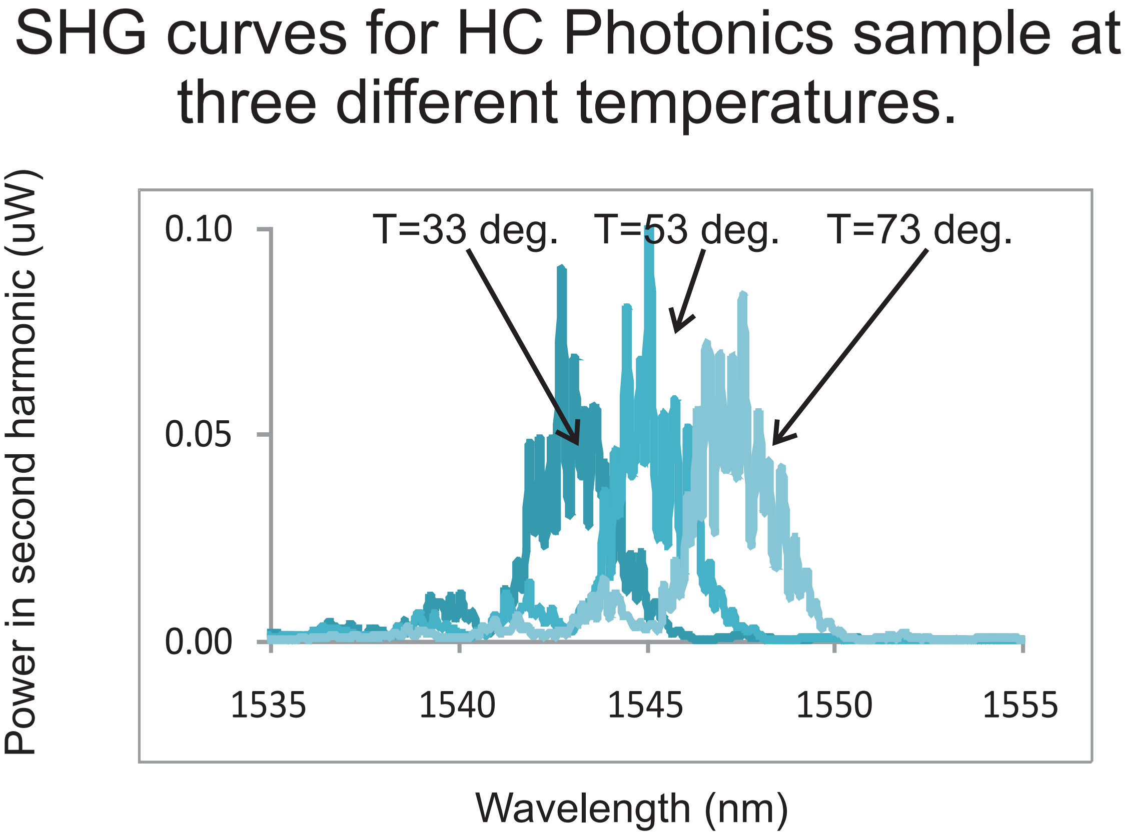

Figure 4.6: SHG vs wavelength for three temperatures. A somewhat lopsided characteristic $sinc^2$ function is seen as the phase matching condition is essentially tuned over the wavelength range indicated.

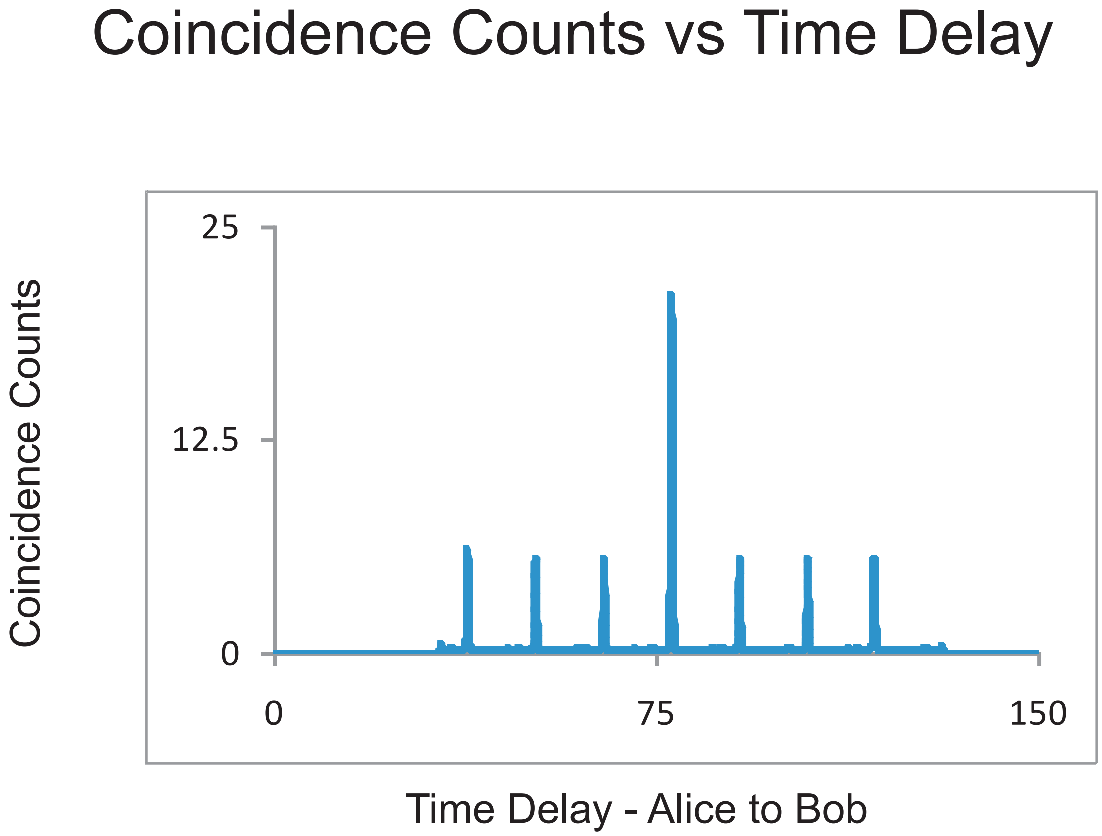

Figure 4.7: TAC histogram for a pulsed input. The picture highlights the concepts discussed in the SPDC Analysis section in the preceding chapter. The middle pulse indicates the true coincidence time between the two detectors, while the side pulses demonstrate the reduced probability of successive pair production. In between the pulses is the level of the noise floor.

Following this, the experiment was reversed, coupling the now tuned pulsed output from the main laser into the waveguide. SPDC light exited what was previously the input end of the sample, along with the pump light. Filtering the pump with 6mm of schott glass was enough to discriminate the SPDC photons. The SPDC photons and whatever pump light remained were sent to a 1:2 fiber beam splitter with an optical delay of 13m in one of the two arms. Each arm was connected to a multi-mode single photon detector - the short arm to a detector called Alice, the long arm to a detector called Bob. By setting an internal delay, Alice was time synchronized to the optical arrival time of the pump pulse and open for a nominal gate time of 5ns. A detection response from Alice triggered Bob's gate to open for approximately 100ns and also started a Time to Amplitude Converter (TAC). A detection response from Bob stopped the TAC.

Due to the properties of the biphoton emitted via SPDC, the logic is as follows: A detection response initiated by an SPDC photon at Alice implies a relatively high probability of a detection response being generated by Bob at a certain time t^* after the start time of the TAC. This time t^* is the coincidence time. All other recorded times should occur with some average rate indicating the occurrences of uncorrelated 'accidental' start-stop events. Figure 4.7 displays a few minutes worth of data collection for this experiment and shows this expected behaviour.

4.5 Conclusions

It should be mentioned that in addition to the above data, various other experiments were performed pertaining to both up and down conversion using both samples (from McMaster and HC Photonics). These experiments concerned such things as verifying the linear dependence of SPDC on pump power, verifying the quadratic dependence of SHG on pump power, inferring the pump bandwidth for SPDC, measuring the spectrum of SPDC, and observing sum frequency generation. This data is not displayed as it provides little if any novel results. That should not undermine the importance of this chapter because this thesis could not have been completed without having taken these basic steps. In essence, the experience gained by working with PPLN provided information that was crucial for building confidence in the main setup and measurement apparatus.

5 DIRECTIONAL QUASI-PHASE MATCHING

As this chapter presents a novel technique for solving the phase matching problem, the design lacks extensive historical roots. The flow of this chapter will be to describe where the idea came from, followed by the design proposal which was recently published on the arxiv [58]. This is followed by a section that provides details of how the actual fabrication parameters were chosen. This includes modeling in Matlab, mode solving using FDTD Solutions, and mask design using DW2000.

5.1 Introduction

The idea of Directional Quasi-Phase Matching (DQPM) was conceived by G. Weihs around 2005-2006 after attending a presentation by John Sipe on non-linear interactions in ring resonators [59]. Typical ring resonators are integrated waveguide structures that are fashioned in a ring or ringlike shape – having no defined input or output end. Figure 5.1 shows a simple ring and waveguide structure. A ring is usually placed in close proximity to a normal 'channel' waveguide whereby light in the channel guide can evanescently couple to the ring. If the ring 'fits' the light in the channel – as in the ring circumference is an integer number of wavelengths for a particular frequency of light, then that frequency can propagate around the ring for some time before either coupling back out to another channel or back into the original channel. If there are any available non-linear effects to exploit in the ring, the ring can enhance the interaction time, and thereby the strength of the non-linearity.

Early ideas related to DQPM began by imagining that instead of evanescently coupling to the ring, one could open the ring, thereby giving it an input and output end to directly inject and collect the light. The thinking was to mimic a single ring resonator by linking many 'almost' full rings together in series. This could enhance the non-linearity for those resonant wavelengths but with the added benefit of being able to couple light directly into and out of the resulting structure.

What is interesting about the ring geometry is that the ring confinement forces the light through a full 360°. Concomitantly, the electric field direction also sweeps over a similar directional range. Thus, when examining the bilinear response of the ring, one needs to account for the full directional dependence of $\chi^{(2)}_{ijk}$. In particular, the bilinear response will also be modulated by this circular motion.

This concept was synthesized with the notion of quasi-phase matching (QPM) which is typically a fixed modulation - a static inversion - of the bilinear susceptibility to 'rephase' the desired non-linear interaction. By wiggling or modulating the path of a waveguide, the wiggling induced modulation of the bilinear susceptibility could simu-

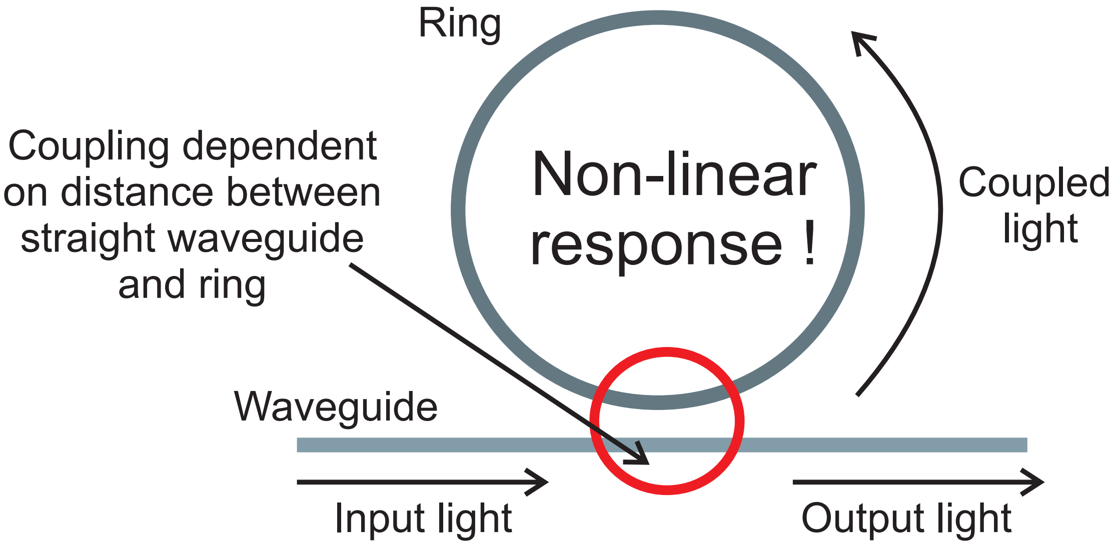

Figure 5.1: A basic ring resonator. The straight waveguide is in close proximity to the ring. Light leaks into the ring structure and can induce a nonlinear polarization response in the material. If that response is properly phase matched to the light living in the ring, then the response can be amplified by going around the ring many times. After sufficient amplification, some light will leak back into the straight waveguide.

late QPM. This led to the current name of directional quasi-phase matching - DQPM.

Originally meant for materials that do not allow birefringent phase matching or periodic poling, the idea can be applied not just to QPM, but to a generalized method for tailoring any kind of non-linear profile. Such non-linear engineering has ramifications into the development of spectrally pure photons created by spontaneous parametric down conversion [60].

5.2 Overview

DQPM makes use of the tensor structure of the bilinear susceptibility $\chi^{(2)}_{ijk}$. If the field directions of a wave in a waveguide adiabatically follow (transversely) the direction of propagation of the waveguide, then the coupling can be modulated by changing the waveguide direction. This modulation can effect both the sign and magnitude of the coupling. As mentioned, this effect was only noted very recently in connection with nonlinear optics in disk and ring resonators [59, 61, 62].

With the ultimate goal of proposing a design that will generate photon pairs, the conditions for DQPM as they apply to SHG in waveguides will be presented. Various curve shapes will be discussed in relation to the expected amplification of SHG, their bend loss and modal behavior. Our analysis applies to other material systems, but presently the focus will be on the ternary alloy Aluminum Gallium Arsenide $\mathrm{Al_xGa_{1-x}As}$; the subscript x is related to the aluminum concentration. $\mathrm{Al_xGa_{1-x}As}$ is a common optoelectronic material. It can be made transparent for telecommunications frequencies and has a high optical nonlinearity (100 pm/V). Additionally, semiconductor lasers can be manufactured in this system making it an ideal choice for integration.

5.3 Directional Quasi Phase Matching

In our analysis, the standard treatment of second harmonic generation in straight waveguides is modified to account for directional changes. The assumptions for this treatment are

- 1) charge free - the media is neutral,
- 2) $\mu = \mu_0$ - the media is non-permeable
- 3) lossless - field energy is not absorbed by the material,
- 4) the slowly varying amplitude approximation (SVA) - the amplitude of the input fields slowly vary along the direction of propagation with respect to the frequency of the field,
- 5) transversality - the fields are mainly transverse to the direction of propagation,
- 6) the undepleted pump approximation - the input field amplitude is large and remains large.

For the special case of SHG, Kleinman symmetry is valid, and the bilinear susceptibility tensor reduces to a single 3x6 contracted 'd' matrix [40]. Primed coordinates will denote the crystallographic directions, while unprimed coordinates are reserved for the field spatial directions. In the 'd' notation, the rows of 'd' are labeled x',y',z', and the columns are labeled $x'x'$,$y'y'$,$z'z'$,$y'z'$,$x'z'$,$x'y'$. Crystallographic symmetry can then further relate elements of 'd'. For $\mathrm{Al_xGa_{1-x}As}$ which belongs to the $\bar{4}3m$ point group, the only non-zero coupling constants are d_{14}=d_{25}=d_{36}, meaning that the two fundamental fields and the second harmonic are only coupled if there is some component of field along all crystallographic directions.

For $\mathrm{Al_xGa_{1-x}As}$, epitaxial growth is typically done on (100) surfaces ($y' - z'$ plane), therefore a waveguide is confined to lie in this plane. If the waveguide propagation direction (z) is parallel to z', then the transverse fields lie in the y' or x' plane where $d = 0$. On the other hand if z is directed at ±45° to the z'-axis, the transverse fields can be decomposed into all three spatial directions. In this situation the nonlinear process can, at least in principle, occur.

5.3.1 Design Equations

Recall the form of the classical equation for second harmonic generation (equation 2.39). Using this as an approximation for SHG in a straight waveguide whose guiding direction is along the spatial z direction gives,

$$\frac{d}{dz}E_2(z) = -i\omega_2\sqrt{\frac{\mu_0}{\epsilon_2}}\frac{d}{2}(E_1)^2 e^{i\Delta kz} \tag{5.1}$$

where the change in the amplitude of the second harmonic field along z is $E_2(z)$, the subscripts 1 and 2 represent the fundamental and second harmonic fields respectively. These fields are defined by their respective amplitudes (E), frequencies (ω), and wavevectors (k), and the phase mismatch $\Delta k = k_2 - 2k_1 \neq> 0$.

To demonstrate DQPM, vertically polarized (x/x') second harmonic light (E_2) will be created by injecting horizontally (plane) polarized fundamental light (E_1) into the guide. The tensor d is then,

$$\begin{aligned} d &= \sum_{ijk} d_{ijk}a_{2i}a_{1j}a_{1k} && (5.2)\\ &= d_{14}a_{2x'}a_{1y'}a_{1z'} && (5.3) \end{aligned}$$

where a_2, and a_1 are unit vectors in the polarization directions of the fields E_2 and E_1 and $d_{14} = d_{xyz}$ is non-zero. Evidently for E_2 directed always along x/x' then a_{2i} never changes and so $a_{2i} = 1$.

To develop a visual sense for DQPM, imagine the waveguide coordinate system as co-moving with the direction of propagation of light in the waveguide while the primed coordinate system remains static and aligned with the principle crystallographic directions. The situation is diagrammed in figure 5.2. In this setting, arbitrary waveguide structures can be re-parameterized by replacing the coordinate 'z' with a generalized path length 's' along the midline of the waveguide.

For these arbitrarily directed guides, the SVA and transversality approximations are retained. In addition, it is assumed that the magnitude of the phase mismatch between the fundamental and second harmonic waves remains constant $\rightarrow \Delta k \neq \Delta k(s)$.

The local direction of the waveguide is defined by its angle $\alpha(s)$ with respect to one of the primed crystal axes – for figure 5.2 it is the z'-axis. Thus, the in-plane polarization

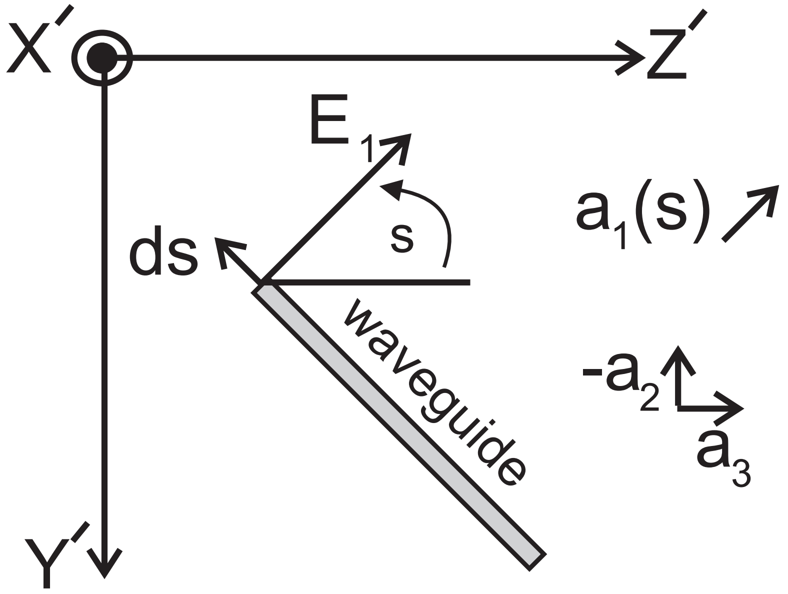

Figure 5.2: Crystal co-ordinates, the tangent vector ds, the angle $\alpha(s)$ that the waveguide makes with respect to the z' axis.

vector $\mathbf{a}_1(s)$ is all that needs to be considered. It is given by

$$\mathbf{a}_1(s) = \begin{pmatrix} 0 \\ -\sin\alpha(s) \\ \cos\alpha(s) \end{pmatrix}. \tag{5.4}$$

Replacing $\sqrt{\frac{\mu_0}{\epsilon_2}}$ with the speed of light in the material, and making the substitutions for d gives

$$\frac{\mathrm{d}E_2}{\mathrm{d}s} = i\frac{\omega_2 d_{14}}{n_2 c}\sin[2\alpha(s)]E_1^2 e^{i(\Delta k)s} \tag{5.5}$$

The growth of E_2 is now clearly dependent on both the distance traveled ($(\Delta k)s$) and the orientation of the waveguide, ($\alpha(s)$). It is zero for a waveguide whose propagation direction is along any of the crystal axes and can have positive or negative sign.

5.3.2 Proof of Concept

In the undepleted pump approximation, the exciting field E_1 has constant amplitude and $E_2(s = 0) = 0$. For straight guides with $\sin[2\alpha(s)]$=constant≥ 0 and $\Delta k(s) \neq 0$, equation 5.5 describes the familiar behaviour for unphased matched SHG. That is, E_2 oscillates with a period of $2L_c$ where $L_c = \pi/\Delta k$, between zero and its maximum value along the guide.

Now imagine the following: let $\sin[2\alpha(s)]$ be a maximum. This occurs for $\alpha = \pi/4$. Travel a distance of L_c in this direction to exploit the positive contribution from the exponential. Then, let $\sin[2\alpha(s)]$ be a minimum, which occurs for $\alpha = -\pi/4$, and travel for an additional distance of L_c. Over this next distance of L_c, both $\sin[2\alpha(s)]$ and the exponential are functionally the same as in the first L_c segment, but each contributes a negative sign. The negatives cancel and the growth of E_2 remains positive. Figure 5.3 shows the layout of the structure on the wafer.

In essence, the 90° change in orientation of the guide causes an inverted polarization response of the material that is exactly in phase with the pi-lagging optical response field E_2. For arbitrarily many repetitions of this zig-zag path, E_2 can continue to grow. This achieves precisely the same behavior as traditional first-order QPM by periodic poling. Here, in contrast it is the $\sin(2\alpha(s))$ term that is responsible for the sign change.

For the sharp 90° bends necessary to achieve first-order DQPM, it is anticipated that structure will be very difficult to fabricate. This is because simulations involving AlGaAs predict that L_c is on the order of 2μm. Further, there will most likely be significant losses and additional phases introduced in the bend region. As such perturbations of first-order DQPM as well as higher-order phase matching will be examined to allow for milder bending. Of interest is the notion of 2nd-order DQPM. This type of scaling can't be achieved with standard poling techniques. For poling to achieve even-order

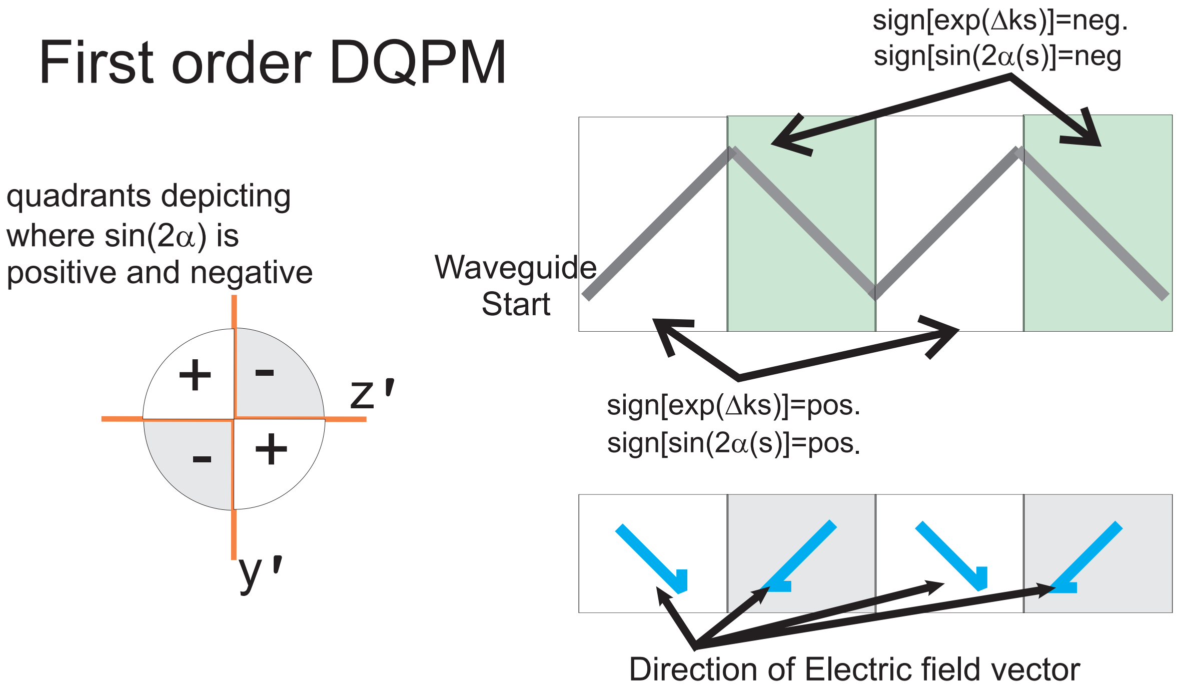

Figure 5.3: The idealized structure assuming no phase shifts, loss, or out of plane field rotation occurring at the sharp 90° bends. The field vectors switch from the positive to negative quadrants of $\sin(2\alpha(s))$ precisely when the phase fronts between the pump and SHG fields are between π and 2π of each other. This would be equivalent to first-order quasi phase matching, where after every coherence length the phase mismatch is reset to zero and the reaction revives.

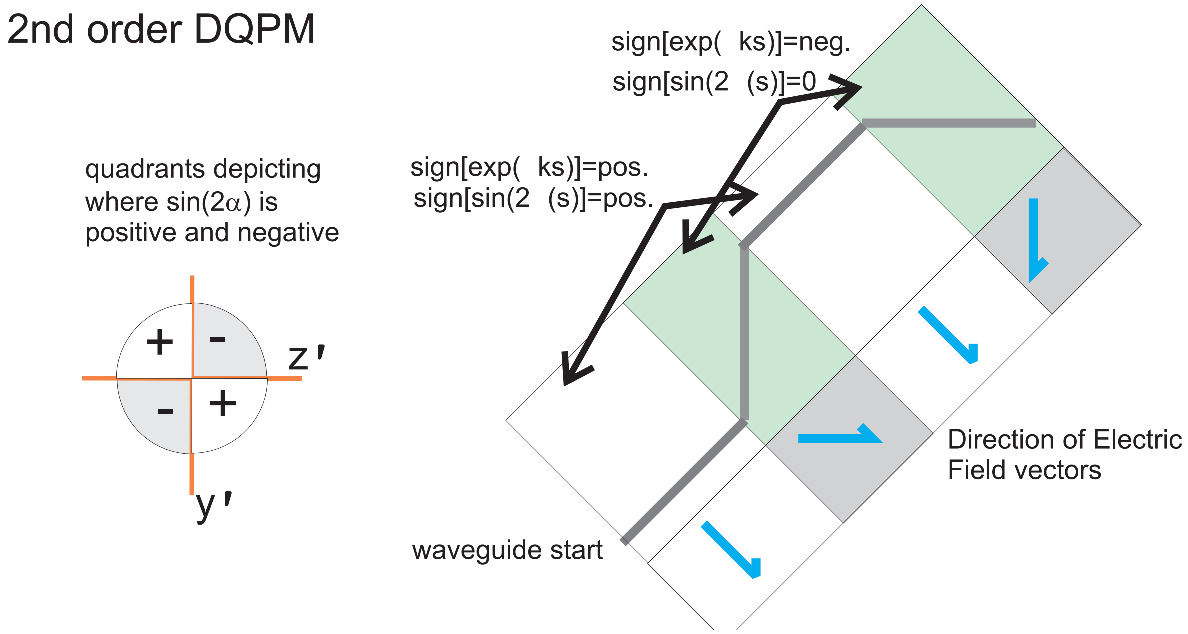

Figure 5.4: This structure is an example of an even-order quasi phase matching scheme – something that is unavailable with periodic poling methods. This is because poling can only effectively reverse the non-linearity, and therefore it is always on. In DQPM, the non-linearity can be turned off. Higher-order DQPM structures also allow for more milder bending, however for similar growth of SHG to the first-order scheme, they will be required to propagate for proportionally longer distances.

phase matching in QPM, one needs to utilize a combination of different odd-order domain inversions. For example, fourth-order QPM involves a combination of 1^{st} and 3rd-order domain inversion; sixth-order might involve 1^{st} and 5th-order domain inversion, and so on. Clearly there does not exist a combination that produces a monotone increasing 2nd-order growth of the SH field. Another advantage of 2nd-order DQPM is that it only requires 45° bends.

Figure 5.4 shows second-order DQPM. Its design is intuitive because it consists of subsections that are in units or half units of L_c. This makes it relatively easy to keep track of the phase accrual between the pump and second harmonic fields. The second-order structure turns off the non-linearity whenever its propagation axis lies along one of the crystallographic axis. True to its name, when compared to first-order DQPM, second-order DQPM requires twice the distance to generate a similar intensity in the second harmonic.

Comment on the non-linear profile

One other capability that DQPM provides is a tailoring of the so called nonlinearity profile [60]. Typically, when light enters a non-linear crystal, whether confined in a waveguide or simply as a Gaussian beam, the non-linear interaction is suddenly turned on. It is then abruptly turned off again as the light exits the crystal. The nonlinearity profile describes the strength of the interaction afforded by the non-linear crystal as a function of spatial position. The nonlinearity profile affects the factorization of the biphoton wave function or formally the spectral purity of the biphoton.

To see this, recall that the output state of the biphoton created by SPDC is of the form

$$|\Psi\rangle = \int\int d\omega_i d\omega_s f(\omega_i, \omega_s)\hat{a}_i^\dagger(\omega_i)\hat{a}_s^\dagger(\omega_s)|0\rangle \tag{5.6}$$

where $f(\omega_i, \omega_s) = \alpha(\omega_i + \omega_s)\Phi(\omega_i, \omega_s)$ is called the Joint Spectral Amplitude (JSA) of the signal and idler photons created by SPDC. It is a joint amplitude because it involves the pump envelope function $\alpha(\omega_i + \omega_s)$ and a phase matching function $\Phi(\omega_i, \omega_s)$.

Spectral purity describes the degree of spectral correlation between the signal and idler modes of the biphoton. This is an important parameter for quantum information protocols that might rely on the future interference of two photons (eg. at a beam splitter that makes use of Hong Ou Mandel type interference). To achieve spectral purity there should be no frequency correlations between the signal and idler modes, that is:

$$\int\int d\omega_i d\omega_s f(\omega_i, \omega_s)\hat{a}_i^\dagger(\omega_i)\hat{a}_s^\dagger(\omega_s)|0\rangle = g(\omega_i)\hat{a}_i^\dagger(\omega_i)|0\rangle \otimes h(\omega_s)\hat{a}_s^\dagger(\omega_s)|0\rangle. \tag{5.7}$$

Because the pump energy is naturally conserved in SPDC, spectral correlations are unavoidable in the cw case. However, for a pulsed pump, this condition is relaxed and it may be possible to achieve spectral purity if the correlations in the pump can be canceled by those created by the presence of the nonlinear crystal - the phase matching function.

Ignoring for the moment the pump envelope function, a typical phase matching function can be modeled as a spatial tophat - it turns on/off abruptly to model the presence of the crystal. It is also comprised of an oscillatory function that describes the 'in phase' - 'out of phase' behaviour between the pump and down converted light. Upon integration, the combination of the two results in a 'sinc' function of the product of the phase mismatch and the length of the crystal - $\mathrm{sinc}(\Delta kL/2)$. This shows that there can be significant contributions to the probability amplitudes in the state of the biphoton for a variety of combinations of signal and idler frequencies.

Because of the heightened interest in creating single photons without spectral correlations, there has recently been a proposal to achieve spectral purity in a waveguided scenario involving PPLN [60]. The required nonlinearity profile to achieve spectral purity was Gaussian, producing an adiabatic turn on / turn off of the non-linear interaction. It was tailored via the use of multiple-order quasi-phase matching.

By utilizing the proper combinations of such higher-order QPM schemes, the effective non-linearity was small at the edges of the crystal, reaching a maximum in the middle of the crystal. They noted that by combining the QPM orders appropriately, virtually any non-linear profile can be achieved. One of major drawbacks of their proposal was that the utilization of higher-order QPM required longer and longer sections of crystal.

DQPM can circumvent this issue as it can provide a much smoother transition between the effective non-linearity of the vacuum and the maximum non-linearity afforded by the non-linear crystal, *while still providing the conditions for first-order phase matching.*

In DQPM, the function that describes the nonlinearity profile is given by the 's' dependent argument of the integral in equation 5.5

$$f_{nl}(s) \sim \left|\sin(2\alpha(s))E_1^2 e^{i(\Delta k)s}\right| \tag{5.8}$$

Plotting this over the path of the waveguide produces the profile. Once again, the emphasis is placed on the $\sin(2\alpha(s))$ which can be used as an additional control on the effective non-linearity.

5.4 Design considerations

When considering the eigenmodes of the substructures that make up the proposed 1^{st} and 2nd-order DQPM structures, it is intuitive that such successive abrupt direction changes of the fields will almost certainly introduce unwanted side effects. Sharp bends have been shown to produce waveguide profile asymmetry that can facilitate the rotation of the polarization of the pump field E_2 [63],[64],[65][1]. Abrupt changes in direction are very much akin to reflections, which often generate an additional phase shift between the incoming and outgoing wave (eg. total internal reflection (TIR)).

Analysis of tight (small to no radius) bends [66],[67], including 90° bends[68] and more adiabatic bends [69],[70], have been carried out by various groups. Important observations are:

- 1) the effective index decreases with decreasing bend radius;

---

[1] This effect is also a form of DQPM that we don't consider here. Using bends or even transverse profile engineering, the pump field could conceivably be made to rotate from in plane to out of plane with the correct periodicity to phase match itself with the second harmonic field.

- 2) wider guides exhibit more drastic modal changes in bends than do narrower guides;
- 3) Strong radial confinement is necessary to inhibit radiative loss in a bend;
- 4) high radial symmetry is necessary to reduce intermodal mixing.

In essence both intermodal coupling and radiative (non-guided) coupling are inevitable processes in any waveguide structure that incorporates bending.

Since it is assumed that the mode profiles of the three interacting fields stay the same, the ideal structure would need to facilitate single mode behaviour everywhere along its length. Therefore a narrow waveguide with a strong index contrast (to minimize loss) between the core and cladding is desirable. Further, to avoid intermodal mixing, excellent control over the spatial profile of the waveguide is desirable. Such structures would exhibit very high aspect ratios. While this kind of structure can be fabricated, it requires state of the art manufacturing techniques that are extremely dependent on the proper chemistry during the fabrication process [71]. Unfortunately, these processes also have an unwanted side effect – sidewall roughness. These small spatial index variations along the propagation direction of the waveguide will introduce additional scattering and propagation loss along the guide. The effect is worsened for increasing index contrast.

5.4.1 Non-linear Simulations

With the above design considerations in mind, the non-linear response was simulated for the optimal 1^{st}-order and 2nd-order aforementioned designs, as well as a milder bending 1^{st}-order perturbative design. In addition, a tailored non-linear profile was investigated. Apart from the tailored design, each consisted of scalable substructures – akin to a unit cell in crystallography. The structures were repeated to further grow the intended reaction. Even though in principle the integral for such scaled or repeated structures can be done analytically, the equations pertaining to a certain design were simulated numerically using Matlab.

The guts of the program are not included, but the main equations that were used are provided below. The program categorized structures into three types: those consisting of straight sections, those consisting of circular sections, and generalized structures. Structures were defined using the following conceptual nomenclature [(slope or angle),distance]. Thus, a straight line of slope 1 and length l_c is written as $(1,l_c)$; alternatively, a circular waveguide section with an arc of length l_c subtending an angle θ is written as[2] (θ,l_c). It is useful to write the three forms of the equation used in the program. They are:

---

[2] As the first two types of structures are subsets of generalized structures, it would appear rather

$$
\begin{aligned}
dE_3(s) &\sim \sin[2\alpha(s)]e^{i(\Delta k)s}\mathrm{d}s\ldots \text{ standard form} && (5.9)\\
dE_3(\alpha) &\sim R\sin(2\alpha)e^{i\Delta kR\alpha}d\alpha\ldots \text{ polar form} && (5.10)\\
dE_3(t) &\sim \left[\frac{f'(t)}{\sqrt{(1+f'(t))}}\right]e^{i\Delta k\int_0^t dt\sqrt{(1+f'(t))}}dt\ldots \text{ generalized curve} && (5.11)
\end{aligned}
$$

For the polar transformation, a suitable choice of radius (R) and origin were employed. To arrive at the generalized form, the waveguide path was re-parameterized as a function $(t, f(t))^3$ so that.

$$
\begin{aligned}
ds &= dt\sqrt{(1+f'(t))} && (5.12)\\
\sin(2\alpha(s)) &= \frac{f'(t)}{1+f'(t)} && (5.13)\\
& && (5.14)
\end{aligned}
$$

The full details of the code are not included.

Optimal 1^{st}-order DQPM

The maximally non-linear first-order DQPM design consists of alternating angled (w.r.t. the underlying lattice) straight sections of slope 1 or -1 producing a maximum for $|\sin(2\alpha)|$. The effective unit cell is thus [(1,l_c),(-1,l_c)]. The results are plotted in figure 5.5.

2nd-order DQPM

The maximally non-linear second-order DQPM design was chosen to consist of straight sections (directed along a crystal axis) interleaved with optimally angled segments of slope 1. The effective unit cell is [(1,l_c),(∞,l_c),(1,l_c),(0,l_c)], and the simulation results are shown in figure 5.6

Perturbative 1^{st}-order DQPM

One of the first smoother structures envisioned was that of two oppositely directed ‘s’ bends, each of length L_c, placed in series with each other. Each s bend consists of two circular segments of length $L_c/2$. This produces a structure that is differentiable along its entire length. The effective unit cell is [(atan(1/10), l_c/2), (-atan(1/10),l_c/2),

---

needless to write code pertaining to all three. However, the simplicity of the first two types lent credibility to the results, and in fact the generalized code was not used in the end.

[3] Here t is not to be confused with time.

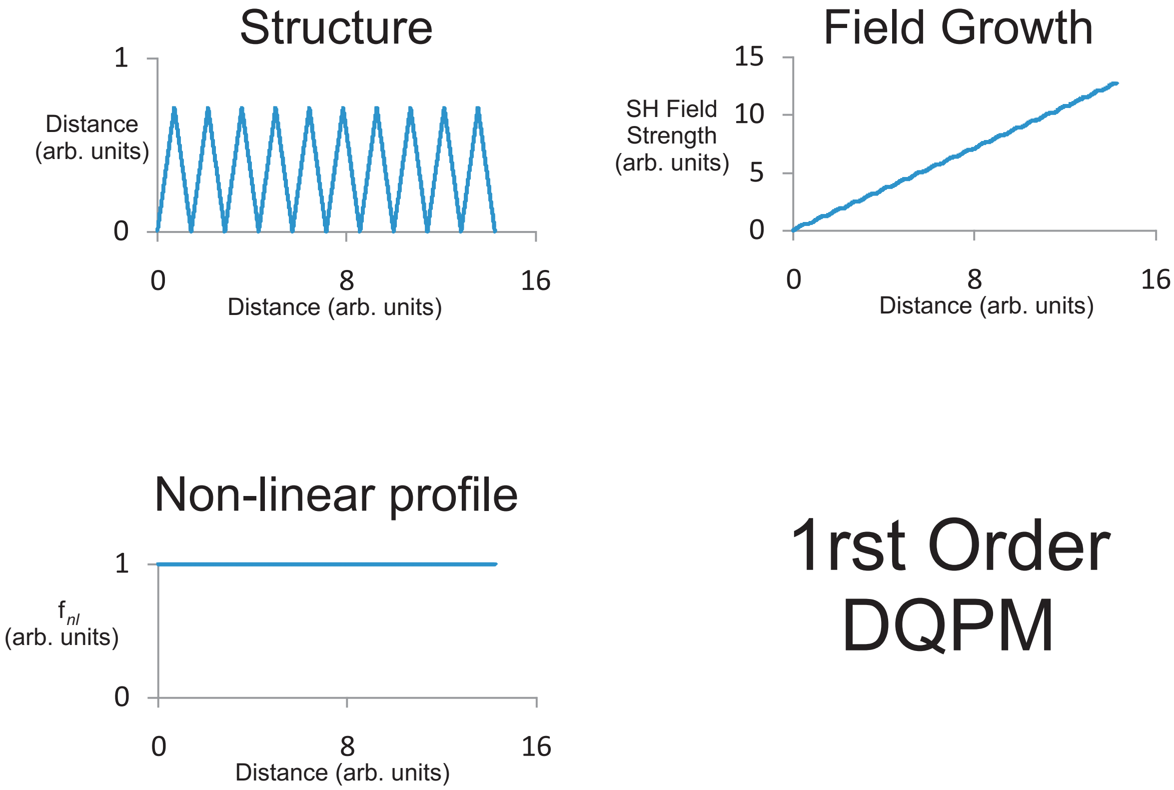

Figure 5.5: Plots of the physical structure (top left), the growth of the second harmonic field (top right) and the non-linear profile (bottom left) for an optimally non-linear 1^{st}-order DQPM design.

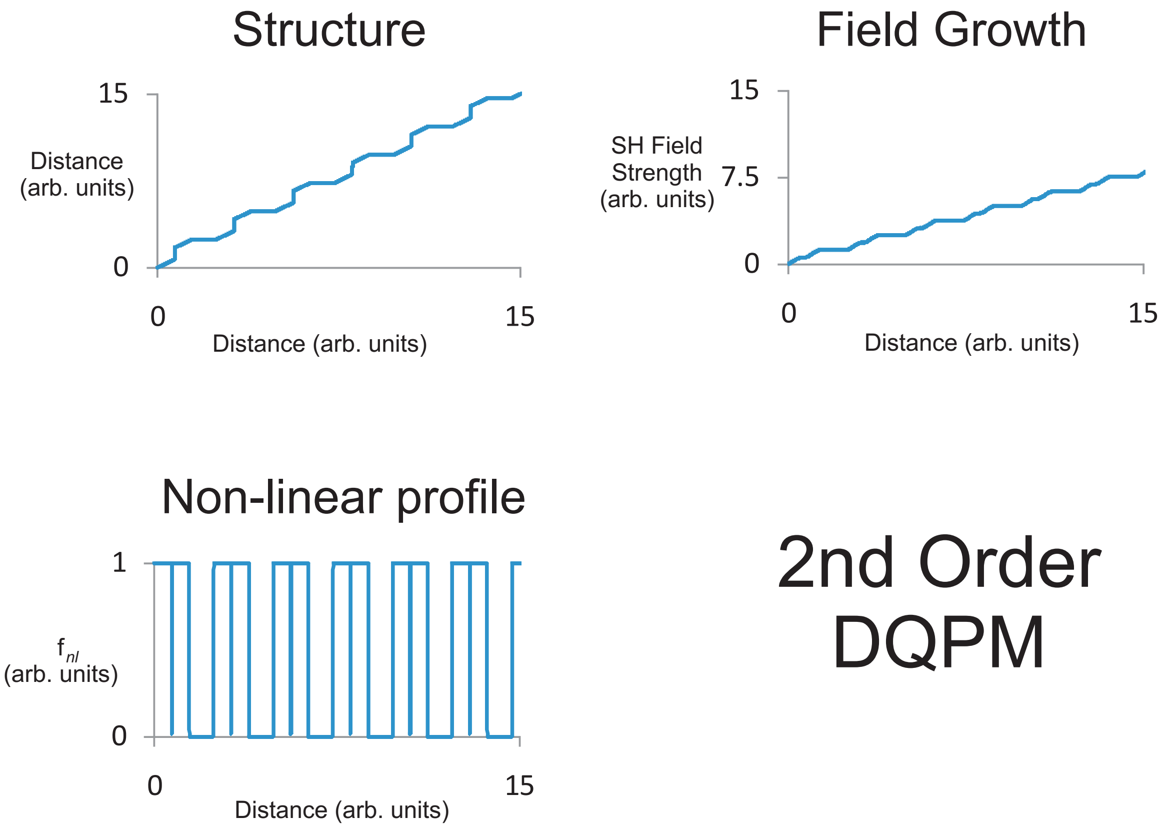

Figure 5.6: Plots of the physical structure (top left), the growth of the second harmonic field (top right) and the non-linear profile (bottom left) for an optimally non-linear 2nd-order DQPM design.

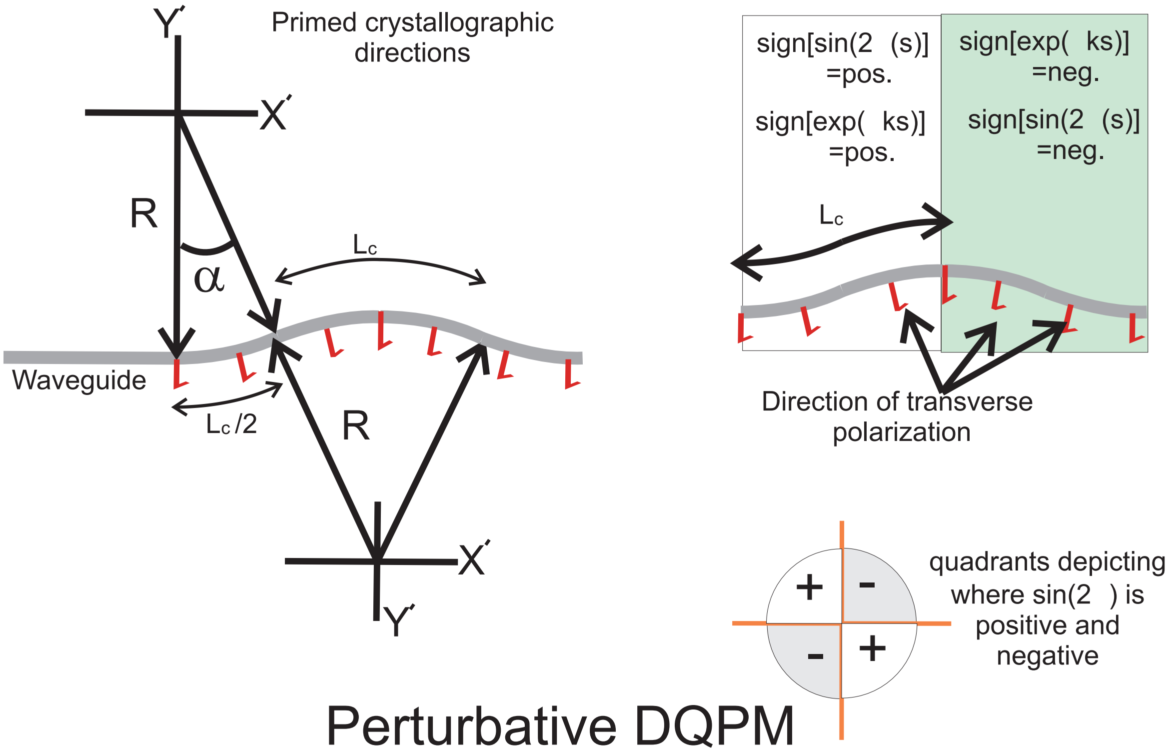

Figure 5.7: This structure represents a small perturbation to a straight guide, and is the weakest performing structure with respect to SHG. However, it will suffer the least from bend loss. Over the first *s* bend, the transverse electric field direction stays mostly in the quadrant where $\sin(2\alpha(s))$ is positive. Over the second *s* bend, the electric field direction stays mostly in the quadrant where $\sin(2\alpha(s))$ is negative. Similar to first-order DQPM, the back and forth undulation coincides with respective positive and negative contributions from the accumulated phase between the pump and second harmonic fields.

(-atan(1/10),$l_c/2$), (atan(1/10), $l_c/2$)]. It is depicted in figure 5.7 and the results from the simulation are shown in figure 5.8

The angle chosen is arbitrary, but is small to facilitate mild bending. Such bending doesn't produce nearly the amount of polarization response in the medium and thus the conversion efficiency to the second harmonic is much less than optimal first-order DQPM. This structure illustrates the concept of first-order DQPM, where the nonlinearity is made much weaker than traditional first-order QPM designs utilizing periodic poling.

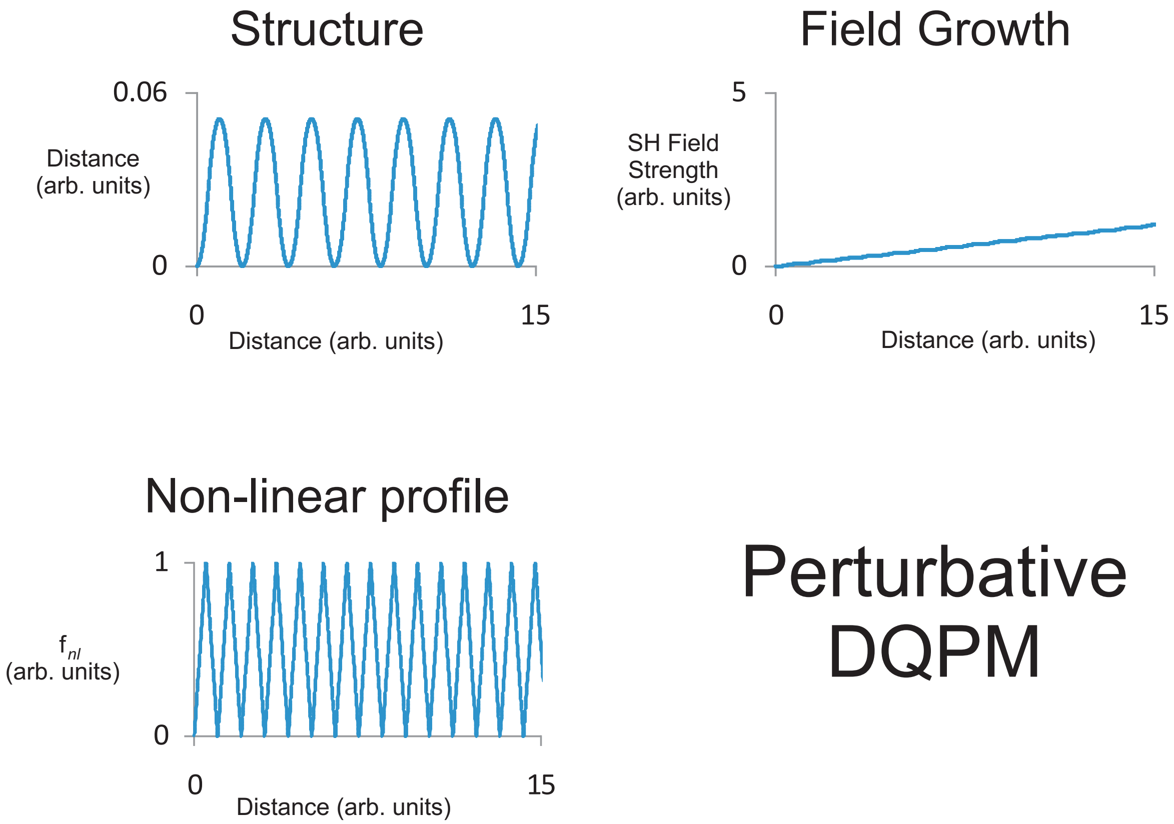

Figure 5.8: Plots of the physical structure (top left), the growth of the second harmonic field (top right) and the non-linear profile (bottom left) for a perturbative 1^{st}-order DQPM design.

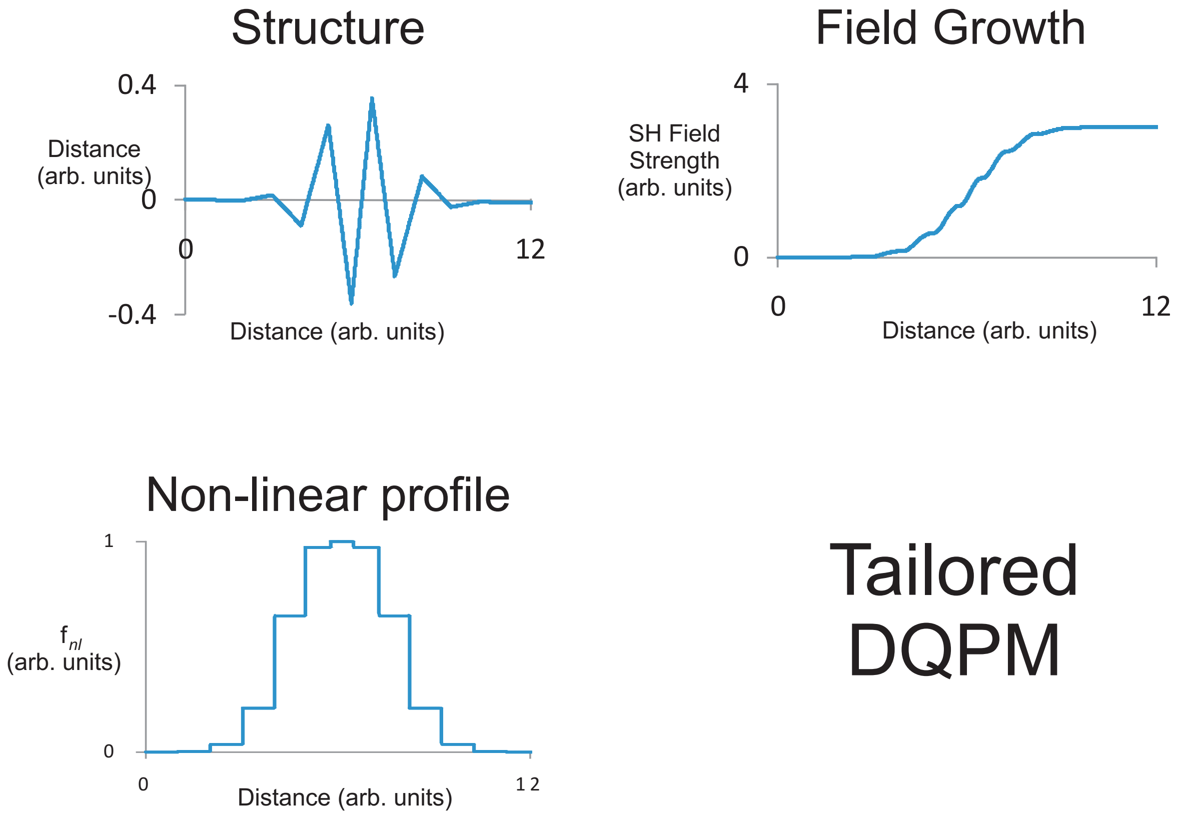

Figure 5.9: Plots of the physical structure (top left), the growth of the second harmonic field (top right) and the non-linear profile (bottom left) for a Gaussian tailored 1^{st}-order DQPM design.

Tailored Gaussian DQPM

A tailored Gaussian design was created to attempt to adiabatically turn on the non-linearity along the propagation length of the design. As the non-linearity continuously increases, there is no substructure that is repeated.

The Gaussian form was constructed in a rough manner by varying each successive slope of a 1^{st}-order DQPM design. It was implemented as [(.0001,l_c), (-0.0019,l_c), (0.0183,l_c), (-0.1054,l_c), (0.3679,l_c), (-0.7788,l_c), (1,l_c), (-0.7788,l_c), (0.3679,l_c), (-0.1054,l_c), (0.0183,l_c), (-0.0019,l_c), (.0001,l_c)]. The large granulation was chosen more due to time constraints and to the limitations and inefficiencies of the matlab program. However, it is envisioned that further work could be done to replace the structure shown here with a continuous curve to smooth out the sharp kinks.

While the principle behind such a curve is a constantly changing bend angle, to do this in first-order implies that for successively sharper bends, the undulations of the waveguide become physically closer together, while for successively milder bends, the waveguide undulations spread apart. Such a curve can be visualized as something akin to a chirped sinusoid with a Gaussian envelope.

The functional form of the correct 'chirped sinusoid' is not easily found. In principle, it can be inferred by choosing the correct profile and backtracking to find the matching DQPM waveguide. From [60], the form for the 'correct' Gaussian profile that factorizes the JSA (helps to produce spectrally pure photons) is

$$e^{(-\gamma(\Delta kL/2)^2)} \tag{5.15}$$

where L=$1/\sqrt{8\gamma\sigma_p^2(k_s-k_i)^2}$, σ_p is the pump width, and $\gamma \approx 0.193$ which is determined by matching the FWHM of the Gaussian with the FWHM of the sinc function that would normally be generated without a tailored profile.

To create this profile using DQPM, the following equation would need to be solved

$$\left[\frac{f'(t)}{\sqrt{1+f'(t)}}\right] e^{i\Delta k\int_0^t dt\sqrt{(1+f'(t))}} = e^{(-\gamma(\Delta kL/2))^2} \tag{5.16}$$

Further analysis is required, but the proof of principle has been demonstrated and thus, DQPM, as it has been modeled, presents a valid new tool for engineering an optical non-linear profile.

5.5 Physical Design

With the belief that it is possible to control the foreseeable loss mechanisms, 1^{st}-order DQPM structures were designed and fabricated. The basic waveguide structure was first simulated using a commercial mode solver (Lumerical, FDTD Solutions, Mode Solutions) to determine the effective indices of the relevant modes and thereby the coherence length. The structures were finally drawn with commercial fabrication oriented software (Design Workshop 2000). The software produced the necessary lithographic parameters needed for patterning and fabrication.

The layout of the section follows the design process closely. A waveguide structure was first proposed followed by linear modeling using FDTD solutions to determine its eigenmodes. Once the coherence length was calculated, various different DQPM designs were constructed and a final image of the photoreticle was produced using DW2000.

5.5.1 Mode solving and modeling in FDTD Solutions

Due to the constraints of the fabrication process, the structure chosen was a waveguide with a width of 1um and an aspect height:width ratio of 4:1. The core layer was chosen to be 1μm thick, the top cladding 0.5μm thick, and the bottom cladding 4μm thick. Because the presence of Aluminum monotonically lowers the refractive index of AlGaAs, the core material was chosen to contain 40% Aluminum while the cladding was chosen to contain 60% Aluminum. This ensured that the condition for total internal reflection could be obtained in the vertical direction. The appropriate index of refraction data for the wavelength range of interest and pertaining to the correct Aluminum composition were entered using values obtained from Adachi [72][4]. Choosing appropriate boundary conditions on the simulation region, the built in mode-solver was used to determine the eigenmodes of the structure. The ideal design would have the structure being solely single mode for both wavelengths, thus reducing the chance for intermodal mixing. Less ideal, but more realistic would be for the structure to at least be single mode for the longer fundamental wavelength. However, the fabrication capabilities were such that this was not able to be achieved and the structure modeled is multimode for both wavelengths. For the fundamental wavelength of 1550nm, the effective index of the lowest-order fundamental TE mode was found to be approximately 3.08, while the effective index of the lowest-order fundamental TM mode at the second harmonic wavelength was found to be 3.34. Thus, the index difference is .26 or approximately 1/4,

$$\begin{aligned} l_c &= \frac{\pi}{\Delta k} && (5.17) \\ &= \frac{\lambda_{1550}}{4}\frac{1}{n_{1550}-n_{775}} && (5.18) \\ &\approx 1.48\mu m. && (5.19) \end{aligned}$$

---

[4] see also figure 6.2 in the next chapter

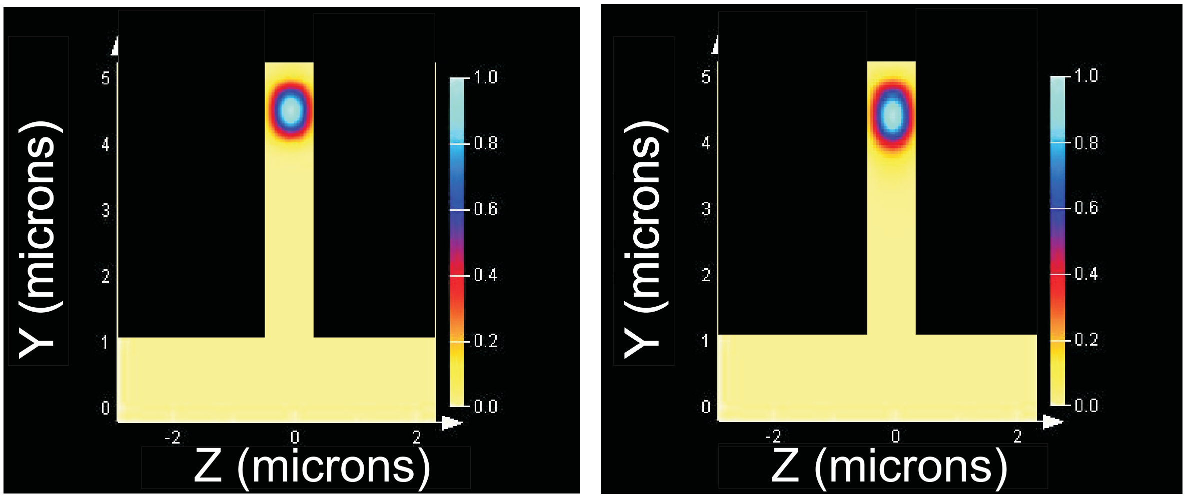

TM mode at 775nm

TE mode at 1550nm

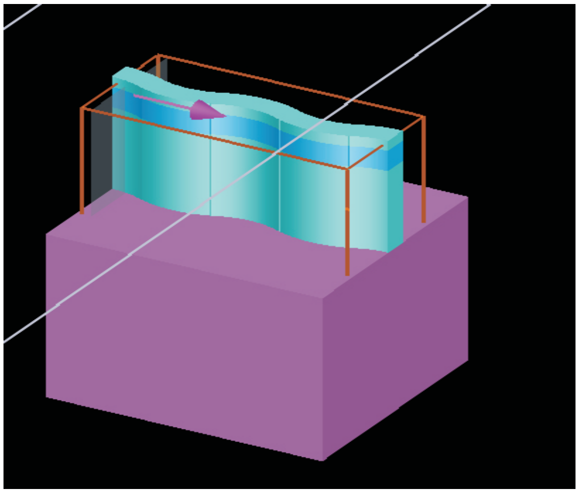

3D Structure

Pictures of FDTD Solutions Software

Figure 5.10: Pictures from the FDTD software used to model the linear properties of DQPM structures. Top left is the fundamental TM eigenmode for a 1μm waveguide for the wavelength .775μm. Top right is the fundamental TE eigenmode for the wavelength 1.55μm.

5.5.2 Fabrication Parameters

The fabrication parameters are presented in the following format: Epitaxy, Process Flow, Reticle details, Wafer Layout and Cleaving plan.

Epitaxy

The unprocessed wafer was semi-insulating GaAs on top of which were four epitaxially grown layers of GaAs with varying Aluminum concentrations. The relevant parameters are presented in table 5.1.

Layer	Material	Thickness	Doping level (cm^{-3})	Species	Dopant
4	GaAs	5nm	$< 10^{15}$	N/A	N/A
3	$Al_{.6}Ga_{.4}As$	4μm	$< 10^{15}$	N/A	N/A
2	$Al_{.4}Ga_{.6}As$	1μm	$< 10^{15}$	N/A	N/A
1	$Al_{.6}Ga_{.4}As$	.5μm	$< 10^{15}$	N/A	N/A
0	n-type GaAs	625mn	2×10^{18}	Si	n

Table 5.1: Wafer Epitaxy

Reticle

DW2000 was used to produce a 1" round reticle of the various different designs. The reticle consisted of three segments. The first segment featured waveguides that were straight except for their DQPM sections. The second segment featured waveguides that were adiabatically turned so that their DQPM sections were oriented at 45° with respect to the DQPM sections in the first part. This was mainly to make sure that regardless of the wafer layout, one of the two sections would be directed properly with respect to the underlying crystal. The third segment consisted of plain straight 1um test guides. This would allow a comparison of the performance of DQPM designs to unperturbed waveguides. In each segment, there were 8 sets of 12 waveguides. The waveguides were nominally 1μm wide but tapered out to 3μm to facilitate coupling. Waveguides were approximately 8 mm long from taper to taper and spaced at intervals of 100μm. Each waveguide was designed with a 'sister' waveguide of equal length that did not incorporate DQPM. Those that did incorporate DQPM consisted of smooth circular s-bends similar to those shown for perturbative DQPM. The angles subtended by $l_c/2$ were 9°, 12°, 15°, 22.5°, 30°, and 45°. Each set differed in the number of unit cells ranging from 1, 2, 3, 5, 9, 15, 20, and 30 unit cells. Lastly, 13μm trenches were incorporated on either side of a waveguide.

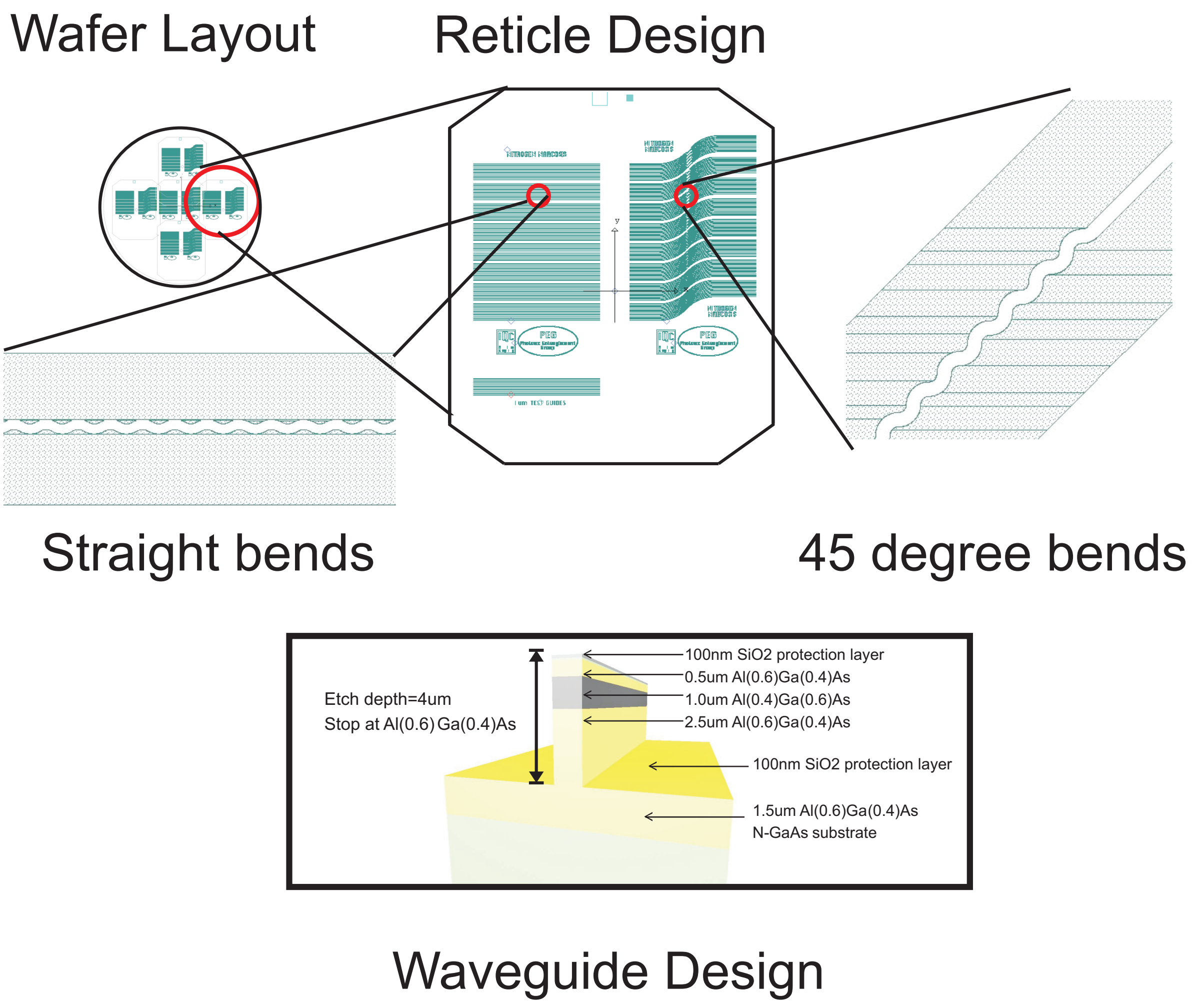

Figure 5.11: The main fabrication structures, from the basic epitaxy and reticle mask design to the wafer layout. Three sections on the reticle are shown – straight bends placed along a crystallographic axis, 45° bends placed at an angle to the crystallographic axis, and straight test waveguide sections.

Process Flow

The wafer was grown by the Canadian Photonics Fabrication Center via MOCVD on two 3” n-GaAs wafers. The structures were patterned using an electron beam and lithography was accomplished with a multilayer mask. The fine features of the bend structures were transferred with a ‘best effort’ fidelity at an e-beam grid of 12.5nm. The ridges were created via deep dry etching using a chlorine based chemistry to a depth of 4μm, stopping 1.5μm above the substrate in the lower cladding. The wafer was cleaned and pacified with a thin 100nm protective layer of SiO_2.

Wafer layout and cleaving

Because the reticle was approximately 1” in diameter and the wafer was 3” in diameter, there was an opportunity to build redundancy into the fabrication process. Thus, 5 reticles were placed in a cross pattern on the wafer. After the fabrication process, the wafer was cleaved into 10 sections, each containing one of the design segments.

Fabrication and Waveguiding results

The first fabrication results for DQPM structures are shown below in figure 5.12.

The figure contains three pictures, two of which are fabrication related. Of those, one is a closeup of a ridge waveguide (labeled (1)) and the other is a lower magnification view of a particular design reminiscent of a cross between optimal and perturbative first-order DQPM (labeled (2)). The ridge shown has an approximate 4:1 height to width aspect ratio and is approximately 1μm wide. The design should show an appreciable field, but as seen from figure 5.12, the ridges suffered from significant surface roughness in the gallium rich core layer. It is believed that this fabrication issue is quite detrimental towards the successful generation of the second harmonic in this structure.

Originally, it was difficult to achieve guiding in the structures and it is still unclear as to why that was the case. However, further testing that occurred 1 year later on shorter cleaved samples revealed that the structures *were* able to guide light. The modes at the output contained some features that lay deep in the substrate, but it is not clear what exactly caused them. The facet image shown in figure 5.12 (labeled (3)) shows one of the many ridge waveguides flanked by 12-13um trenches. No significant second harmonic was measured, but only a handful of waveguides were tested. Much more work is still required to fully explore this first attempt at fabricating DQPM waveguides.

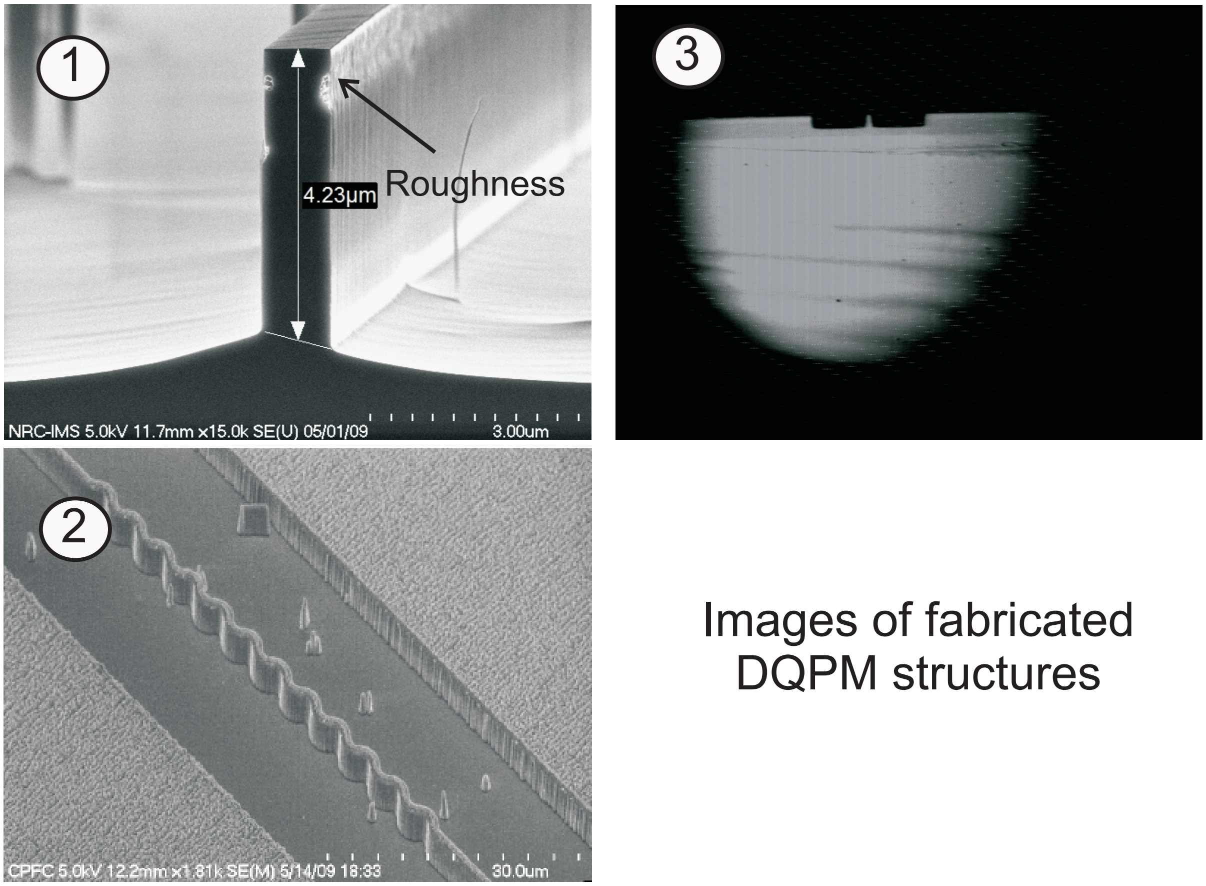

Figure 5.12: Pictures of our initial DQPM structures. The epitaxial structure consists of a 4μm bottom cladding of $Al_{.6}Ga_{1-.6}As$, a 1μm $Al_{.4}Ga_{1-.4}As$ core, a 0.5μm top cladding of $Al_{.6}Ga_{1-.6}As$, and a 0.1μm GaAs top layer. CounterClockwise from top left. 1) Closeup of ridge structure. 2) A DQPM design featuring the first-order perturbative scheme. 3) Facet image obtained with experimental setup.

5.6 Discussion

Success of these designs will depend on how the conversion efficiency compares to the various loss mechanisms. As there are in principle an infinite number of variations that might work, the actual design must incorporate fabrication methods as an input variable. Modeling should be performed to best predict design behaviour based on the available fabrication capabilities. Future work should take into account related issues like etching and regrowth processes and their effects on insertion and bend loss. Lastly, the basic theory may need some modification to allow for modal conversion along the waveguide structure.

6 BRAGG REFLECTION WAVEGUIDES

The layout of the chapter is as follows: Bragg Reflection Waveguides (BRW) are introduced and presented from a historical perspective. The waveguide structure is developed along with some basic theory showing how it can solve the phase matching problem. This is followed by a calculation of the spatial eigenmodes that provide phase matching for telecommunications wavelengths and their second harmonic. The meat of the chapter is concerned with presenting experimental evidence for spontaneous parametric down conversion (SPDC) of a picosecond pulsed ti:sapph laser that is mediated by a ridge BRW. A brief discussion outlining the obstacles and challenges that remain ends the chapter. The chapter represents a culmination of most of the experimental effort put forth during the course of completing this thesis.

6.1 Introduction

Recall again that at the heart of SPDC there are three main ingredients: strong laser fields, highly nonlinear material, and the right conditions for phase matching between the pump and daughter photons. It is also a major theme of this thesis to investigate technology that compactifies these requirements, be it to enter the marketplace or to facilitate scalability.

Enter Gallium Arsenide (GaAs). GaAs is a material system that can provide the first two ingredients. It is already ubiquitously used for integrated optoelectronics and, via alloys formed from Aluminum for example, it was one of the first materials to demonstrate a diode quantum well laser [73]. It is a strong non-linear material – up to three times as large as that of the strongest non-linear tensor component[1] of Lithium Niobate [74]. It is transparent from about .8 to 12μm and it can be robustly packaged and integrated. It is an attractive candidate for an integrated source of photon pairs.

However, there are two major drawbacks: The first stems from the fact that GaAs is not inherently birefringent. This prohibits phase matching between the fundamental and harmonic wavelengths. The second arises because GaAs is a direct bandgap semiconductor. Thus, one and two photon absorption / emission processes can complicate the measurement of SPDC. Ideas have been proposed to combat the first problem of phase matching. Methods vary from inducing birefringence, [75], exploiting out of plane excitation in linear waveguides [76], to employing various methods of quasi-phase matching by wafer bonding or domain inversion upon regrowth [77][78]. However, in most of these cases, final packaged solutions of an on-chip laser coupled to such phase or quasi-phase matched regions still pose significant challenges in fabrication and device efficiency.

---

[1] $d_{33} \approx 30$ pm/V for LiNbO3

Formed by the addition of Aluminum, the relative simplicity of AlGaAs Bragg Reflection Waveguide (BRW) structures represent the next step for full scale integration of all three ingredients. Recently, it has been shown that their design can be tailored to provide for the necessary phase matching [79]. AlGaAs BRW's consist of alternating layers of different aluminum concentrations whose thicknesses are on the order of half or a quarter of the desired optical wavelength (see figure 6.5). The layers can be grown epitaxially and the final structure is photolithographically patterned, and as such relatively straightforward to make. The optical confinement layers in the Bragg structure are an order of magnitude greater than typical quantum well layer thicknesses that provide electronic confinement, so the structure is potentially easy to adapt to integrated quantum well lasers. They are an ideal candidate for building a complete integrated source for quantum information. In this chapter strong experimental evidence for SPDC from AlGaAs BRW waveguides is presented. This builds the case that these structures are a good contender in the race towards integrating quantum technology.

6.2 Historical Perspective of Bragg Reflection Waveguides in AlGaAs

First examined by Pochi Yeh and Amnon Yariv in the mid 1970's [80], the story of the BRW began in the context of a waveguide laser whose guiding region was gaseous – an example where it was necessary to guide power in a *low* index region. They concluded that by bounding the core region with periodic or stratified media, the condition for Bragg reflection could be obtained, and that it was possible to do so (guide power) with theoretically no loss. They borrowed concepts from solid state physics such as Bloch-Floquet theory and band strucure and showed that bound modes of the composite waveguide existed in the stop band of the Bragg material. The Bragg structure effectively prohibited the propagation of those modes such that within only a small number of unit cells, the field evanescently decayed to zero, and no light was lost outside the structure. The composite structure became known as the Bragg Reflection Waveguide. Two papers followed which described the general theory of electromagnetic propagation in periodic media [81] and some of the potential applications. Within the context of phase matching, a particular feature of the BRW was that the effective indices of the bound modes of the structure were lower than those of its constituent materials.[2]

Spurred by advances in lithography and crystal growth techniques, this idea was pursued by A. Helmy and co-workers [79][82] some 25 years later with the goal of phase matching for Second Harmonic Generation (SHG) and other non-linear interactions that underpin devices like the Optical Parametric Oscillator (OPO). Using the notion that

---

[2] the index could even be lower than 1

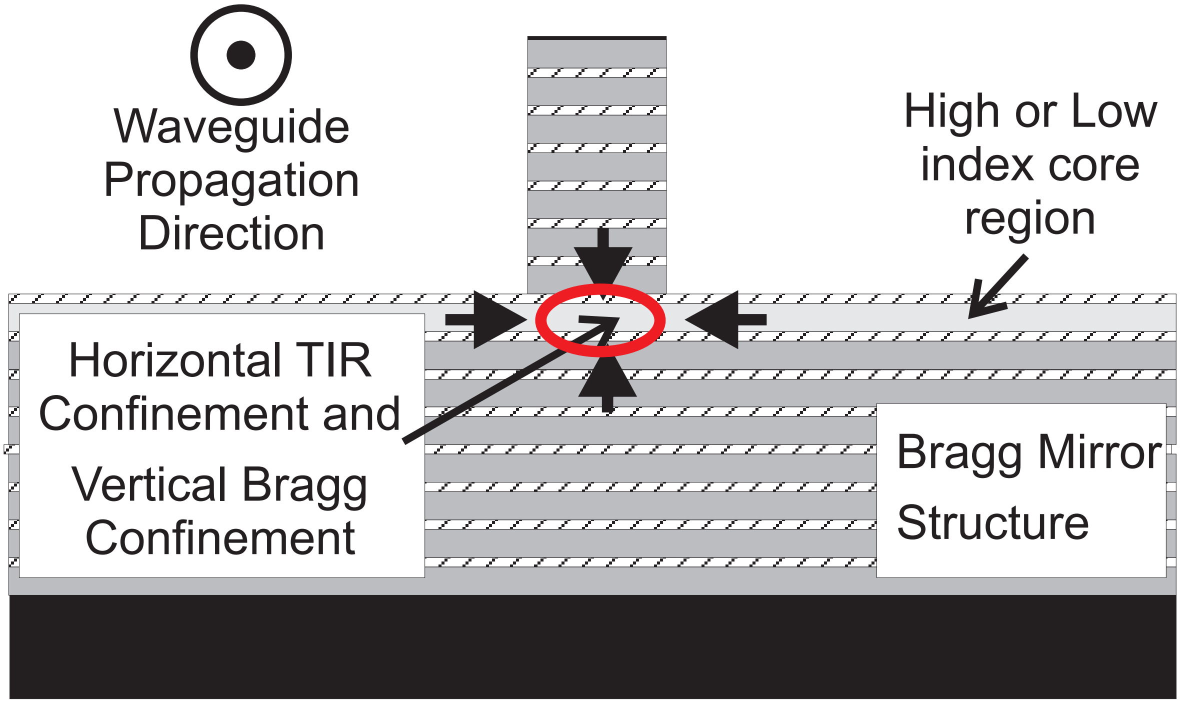

Figure 6.1: A schematic of a ridge Bragg Reflection Waveguide. The ridge breaks horizontal translational symmetry and provides confinement via total internal reflection for modes in the core layer, below the wafer surface. The Bragg mirrors confine the light vertically.

Bragg reflection is a phenomenon that depends only on index contrast (and not the absolute index value), the integrated BRW was proposed with a core index that was *higher* than at least one of the constituent materials in the Bragg reflector. Thus, in one dimension, a mode could be guided in the high index core region via the process of total internal reflection (TIR), while in an orthogonal dimension, a mode could be guided via Bragg reflection. Each would have their own semi-independently tunable effective index of refraction. A diagram of the proposed idea can be seen in figure 6.5

Non-linear optical interactions such as SHG involve wavelengths that are vastly different from each other. In the case of SHG, phase matching is required between the fundamental mode and the second harmonic. As most materials exhibit normal chromatic dispersion, then in order to phase match a fundamental wave with its second harmonic, the second harmonic wave would need to speed up. Because the effective index of a Bragg mode could be lowered, it was proposed that the second harmonic wave would be confined by Bragg reflection, whilst the fundamental mode be guided via TIR. Because the two guiding conditions were semi-independent it was theoretically possible to phase match the fundamental and second harmonic waves.

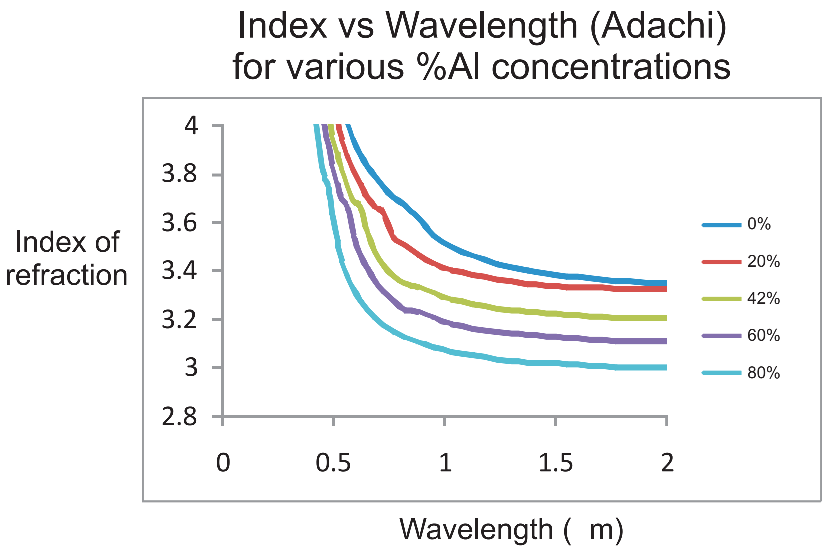

Figure 6.2: The index of refraction for AlGaAs between .7 and 2μm for varying concentrations of Aluminum.

In parallel, studies of the non-linear susceptibility ($\chi^{(2)}$) of various semiconductors were initiated in the 1960's [83]. Since then Gallium Arsenide (GaAs) and other zinc-blende type semiconductors have been at the forefront of investigation. The symmetry of zinc-blende restricts the non-linear susceptibility tensor to six equivalent non-zero elements. $\chi^{(2)}_{xyz} = \chi^{(2)}_{yzx} = \chi^{(2)}_{zxy} = \chi^{(2)}_{xzy} = \chi^{(2)}_{yxz} = \chi^{(2)}_{zyx}$. Over the past four decades, there have been discrepancies in the estimation of $\chi^{(2)}$, its chromatic dispersion, and how to theoretically model this dispersion. One of the more recent works provides experimental data over a wide range of second harmonic photon energies [84]. What is clear is that there is a significant non-linearity for wavelengths in the visible to near infra-red where $\chi^{(2)}$ is estimated to be around 100pm/V. This value is three to four times bigger than Lithium Niobate, which is the standard non-linear element in many OPO's and which is also a standard element used to facilitate SPDC in the telecommunications band.

Because GaAs is deemed to have such great potential in optoelectronic device applications, most of its properties are rather well known. Adding Aluminum to Gallium Arsenide produces the well known ternary compound Aluminum Gallium Arsenide (AlGaAs). Aluminum Arsenide is very well lattice matched to GaAs, and so aluminum can be mixed with gallium without inducing very many defects in the final crystal structure. Optically, its index of refraction decreases with increasing aluminum content [85] [86]. Sample relationships derived from data published by Adachi [85] are shown in figure 6.2.

Multi-layer structures with varying concentrations of Aluminum can be grown either via molecular beam epitaxy (MBE) or metalorganic vapour phase epitaxy (MOVPE) on a Gallium Arsenide substrate. Further to these state of the art growth techniques, a wealth of knowledge and technology has been developed in the areas of lithography, patterning and etching.

In 2007, the group led by A. Helmy were the first to demonstrate phase matching between a TIR guided mode at 1550nm and a guided Bragg mode at 775nm in an AlGaAs BRW [31]. They produced and measured second harmonic generation (SHG) by pumping a slab BRW with picosecond pulsed light from an OPO at 1587nm. This marked the beginning of a set of experiments with ridge BRW's that have since shown continuous wave (CW) SHG [87], difference frequency generation (DFG) [88], as well as novel interactions between the guided TIR and Bragg modes of the BRW [89].

There results represent the state of the art for enabling non-linear optical interactions using the integrated ridge BRW.[3]

6.3 Phase Matching Theory of BRW

To analyze the Bragg Reflection Waveguide the principle waveguide coordinates are setup as in figure (6.3): The x-coordinate is directed normal to the wafer surface – perpendicular to the Bragg layers. The z-coordinate points along the guiding direction or propagation direction. The y-coordinate lies in the plane of the Bragg layers perpendicular to both x and z.

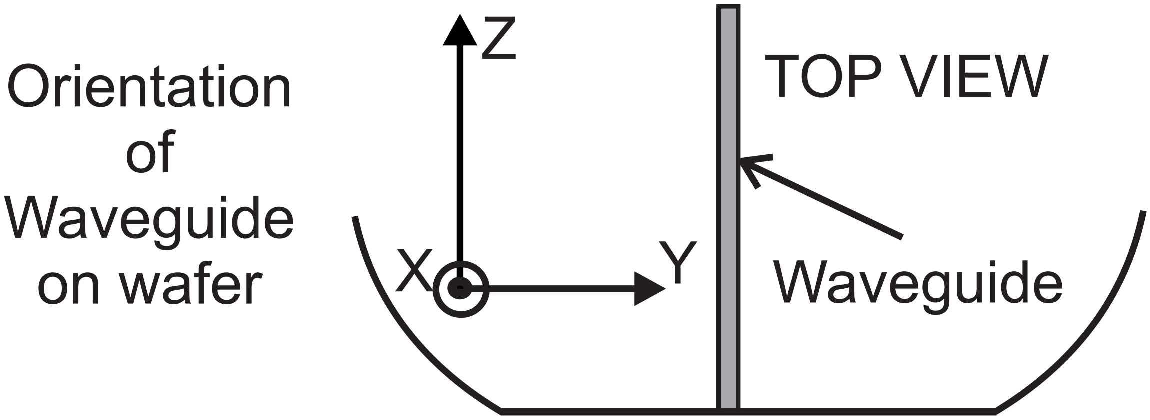

Figure 6.3: Diagram of the waveguide co-ordinate system that is relevant for the phase matching theory section of this chapter.

---

[3] It should be mentioned that in addition, the same group is investigating BRW diode lasers [90] in what is most surely an effort to combine both the laser and non-linear source into one monolithic device.

To develop the concept and setup the equations, invariance is assumed in the y direction[4]. Thus, $\partial/\partial y = 0$. We will consider the theoretical concept of pure TE modes[5] restricting $\vec{E}$ to point solely in the y direction. Thus $\vec{E}$=$(0, E_y(x,z,t), 0)$. Assuming a z dependence of the form $e^{i\beta z}$, then $\vec{E}(x,z,t)$=$E_y(x)e^{i(\omega t-\beta z)}$. The wave equation becomes

$$\frac{\partial^2 E_y(x)}{\partial x^2} + \left(\frac{\omega^2}{c^2}n^2(x) - \beta^2\right)E_y(x) = 0 \tag{6.1}$$

Where β=$2\pi n_{\text{eff}}/\lambda$=$k_0 n_{\text{eff}}$. λ and k_0 pertain to the free space wavelength and wavenumber, and n_{eff} is the effective index of refraction for the mode. Thus β is the mode wavenumber or propagation constant. The wave equation can be re-written as

$$\frac{\partial^2 E_y(x)}{\partial x^2} + k^2(x)E_y(x) = 0 \tag{6.2}$$

where

$$k^2(x) = \left(\frac{\omega^2}{c^2}n^2(x) - \beta^2\right) \tag{6.3}$$

is the wavenumber in the Bragg direction. β is written in terms of k_0 (the free space wavenumber). Using the free space relationship ω/c=k_0, then the wavenumber in the ith Bragg layer is given by the relation

$$k_i = k_0\sqrt{n_i^2 - n_{\text{eff}}^2} \tag{6.4}$$

The subscript i will denote the particular layer - c (core), a (first Bragg layer), b (second Bragg layer). With these relationships and assumptions, the setup is finished.

The solutions for $E_y(x)$ are now written down for a waveguide with core thickness t_c, first and second Bragg layer thicknesses of t_a and t_b, and thus a corresponding Bragg period of $\Lambda = a + b$. The analysis follows West et al. [82], which in turn references the original analysis by Yariv and Yeh [80]. For simplicity, only the lowest-order mode is considered. The solution in the core layer is

$$E_y(x) = C_1 \cos(k_c x) \text{ for } |x| \leq \frac{t_c}{2} \tag{6.5}$$

while the solution in the Bragg region is

$$E_y(x) = C_2 E_K(|x| - \frac{t_c}{2})e^{\pm i(K|x| - \frac{t_c}{2})} \text{ for } |x| > \frac{t_c}{2} \tag{6.6}$$

---

[4] Invariance in y is not true for a ridge waveguide, but simplifies the analysis while still demonstrating the novel phase matching technique that the BRW provides

[5] modal analysis shows there is no such thing

K is known as the Bloch wave vector and k_c is the standard core wave vector in the x direction. C_1 and C_2 are constants to be determined. Note that because of the periodic nature of the Bragg structure, the bloch function $E_K(x+\Lambda)$=$E_K(x)$,

Because the index structure in the x direction is symmetric → $n(x)$=$n(-x)$, and the field is also assumed to be symmetric (lowest-order) the analysis of [82] proceeds for $x > 0$ noting that $E_y(x)$=$E_y(-x)$.

It is perhaps not instructive to go through the entire analysis here, as the procedure is lengthy. In words, the steps are to

- Diagonalize a unit cell translation matrix that relates the complex amplitudes of left (-x) and right (+x) traveling waves in one unit cell to those of an adjacent cell.
- Observe that the Bloch condition or periodicity can also relate those amplitudes.
- Set up an eigenvalue equation to relate the Bloch function to the translation matrix
- Solve for the eigenvalues and eigenvectors
- Relate the eigenvalues to the Bloch wave vector
- Relate fields in adjacent slabs within a unit cell via a transfer matrix
- Use boundary conditions (continuity in Ey and Hz ($\partial E_y(x)/\partial x$)) and write down the full solution for $E_y(x)$
- obtain a propagation constant that is related to the thicknesses of the core and Bragg layers

Knowing the relationship obtained for the propagation constant ahead of time (equation 6.4), a hand-waving justification for its form can provide an intuitive route to n_{eff}. It is well known that a Quarter Wave (QW) $\lambda/4$ Bragg stack maximally reflects light for the wavelength λ (maximally in the sense that the least number of Bragg layers is required to achieve a certain reflectivity). In essence λ lies precisely in the middle of the stop band for the Bragg structure. By introducing (and tuning) a defect region, light with a wavelength λ could live in the host Bragg material if it was confined to that defect region. The optimal defect parameters can be conjectured by realizing that if a QW stack *destructively* interferes, then a Half Wave (HW) stack *constructively* interferes[6]. Thus, by visually examining a Bragg stack, the optimal defect would be a layer that is *optically* twice the thickness of the Bragg layers.

That is in the QW condition

$$k_a t_a = k_b t_b = \frac{\pi}{2} \tag{6.7}$$

---

[6] Higher integer multiples of these wavelengths would also work since phase is always modulo 2π

then from equation 6.4

$$k_c t_c = k_0 \sqrt{n_c^2 - n_{\text{eff}}^2} t_c = \pi \tag{6.8}$$

Solving for n_{eff} gives

$$n_eff = \left[n_c^2 - \left(\frac{\lambda}{2t_c} \right)^2 \right]^{1/2} \tag{6.9}$$

This means that the thickness of the core layer can tune the effective index of the waveguide for the Bragg mode. The Bragg layer thicknesses are then chosen accordingly to fulfill the QW condition.

6.3.1 SHG in BRW's

As a first approximation, SHG can be modeled using equation 6.10 from chapter 2 reproduced here.

$$\frac{d}{dz} E_3(z) = -i\omega_3 \sqrt{\frac{\mu_0}{\epsilon_3}} \frac{d_{\text{eff}}}{2} (E_1)^2 e^{i\Delta k z} \tag{6.10}$$

where the replacements $2\omega \longrightarrow \omega_3$, $\omega \longrightarrow \omega_1$, $\epsilon_{2\omega} \longrightarrow \epsilon_3$, ,$\mathrm{E}_{2\omega} \longrightarrow \mathrm{E}_3$ and $\mathrm{E}_\omega \longrightarrow \mathrm{E}_1$ have been made.

For GaAs, which belongs to the $\bar{4}3m$ crystal class, the effective coupling between the harmonic and fundamental waves is given by

$$\begin{aligned} d_{\text{eff}} &= \sum_{ijk} d_{ijk} a_{3i} a_{1j} a_{1k} \\ &= d_{36} a_{3z'} a_{1x'} a_{1y'} \end{aligned} \tag{6.11}$$

where a_3, and a_1 are unit vectors in the polarization directions of the fields E_3 and E_1. The orthogonal co-ordinate system (x', y', z') that aligns itself with the principal crystallographic directions is introduced because it is not necessarily related to the (x, y, z) co-ordinate system of the waveguide.

As all three directions are present in d_{eff}, then d_{eff} is *non-zero* if and only if electric fields are produced in all three principal crystallographic directions. Although the electric component of a propagating EM wave is predominantly planar, a plane making an arbitrary angle with respect to a co-ordinate system will in general cut across all three principal directions. Thus, a non-zero d_{eff} is generally not that difficult to satisfy. However, since growth of GaAs is usually perpendicular to a crystal plane, any waveguide fabricated on the surface of a GaAs wafer will have at least one dimension in common

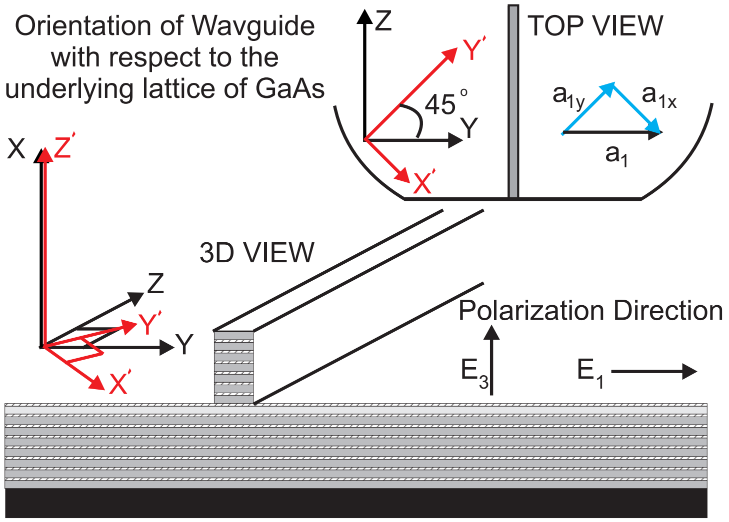

Figure 6.4: A schematic of the Bragg Reflection Waveguide as it would need to be placed on a GaAs substrate. The growth direction is Z'. d_{36} is non-zero if the angle between Y and Y' is non-zero. Here we show the optimal waveguide direction of 45° with respect to the Y' axis.

with the crystallographic axes. This then implies that the waveguide direction of propagation should not be pointed along a principle crystallographic direction, as there will also be no coupling and no appreciable growth of SHG. Under these assumptions, SHG in a linear waveguide can only occur if the waveguide propagation direction makes some angle with respect to the other two crystallographic directions. This is shown in figure 6.4. As there is no preferred crystallographic direction, optimal SHG will occur when this angle is 45°.

6.3.2 Type-0, Type-I, and Type-II Processes

Both type-I and type-II upconversion processes are expected in a ridge BRW that is situated with its propagating axis along the 110 crystal direction. In the type-I case, the pump is horizontally polarized (TE)[7] and the components of the field project along the y and z directions. This means that the produced SHG field must be polarized vertically (TM) along the crystal growth direction. In the type-II case, the pump is directed at 45 degrees with respect to the growth direction and in the facet plane. In this condition, there are nominally two possible processes that could occur. The first

---

[7] Horizontally polarized light is also commonly referred to as Transverse Electric (TE), whereas vertically polarized light can be referred to as Transverse Magnetic (TM)

is the original type-I process where two pump photons couple into the aforementioned horizontal mode and produce vertically polarized SHG. The second process combines a vertically polarized (z directed) photon with a horizontally polarized (x-y) photon. Due to dispersion, typically only one will be phase matched. In the experiment both the type-I and type-II processes were observed and were distinguishable (in terms of their phase matching).

A third unexpected process was also observed. The process has been called a type-0 upconversion process. In this process, both the fundamental and second harmonic modes are vertically polarized. Recalling the form of the $\chi^{(2)}$ tensor for AlGaAs, such a process is strictly forbidden because there is only one crystallographic direction with a field component, namely z. Examining the bilinear tensor reveals that $\chi^{(2)}_{zzz} = \frac{1}{2}d_{33}$ =0. This discrepancy was rectified by noting that the Bragg mode field could contain a strong forward component along the waveguide propagation direction [89]. The forward component projects onto the plane and excites the remaining two crystal directions. As the vertical fundamental mode differs from the horizontal fundamental mode, the phase matching conditions are different, justifying its distinction from the normal type-I condition.

6.4 Sample Structure and Fabrication

The experiments were conducted with ridge BRW's made using standard nanofabrication techniques. Grown by vapour phase epitaxy, they were photolithographically patterned and etched. The final structure is shown in figure 6.5. The design is detailed in [31], and reproduced here for the reader's benefit.

Beginning with a GaAs crystal substrate cut for growth in the (001) direction, a 0.5μm layer of GaAs was first grown on top of the substrate to act as a buffer layer. This was followed by the lower cladding which consisted of 14 layers or 7 periods of a quarter wave Bragg stack. Each period consisted of a 123.7nm thick layer of 25% aluminum ($Al_{0.6}Ga_{0.4}As$) and a 391.4nm thick layer of 75% aluminum ($Al_{0.2}Ga_{0.8}As$). On top of the lower cladding, the waveguide core layer was grown with a thickness of 300nm and an aluminum concentration of 40% ($Al_{0.4}Ga_{0.6}As$). Lastly, a top cladding consisting of 7 periods of the same Bragg configuration was grown, and the whole structure was capped with a 50nm layer of GaAs.

Photoresist was applied to the wafer which was masked and exposed in 5mm square sections. This transferred the waveguide patterns to the photoresist. After developing away the exposed regions, a low power BCL_3/Ar reactive ion etch (RIE) removed the top cladding in the exposed regions. What remained were sets of six waveguides with varying widths between approximately 2.8μm, 2.8μm, 3.1μm, 3.7μm, 4.4μm, and 4.8μm. As alluded to, the mask was oriented on the wafer such that the waveguides were directed

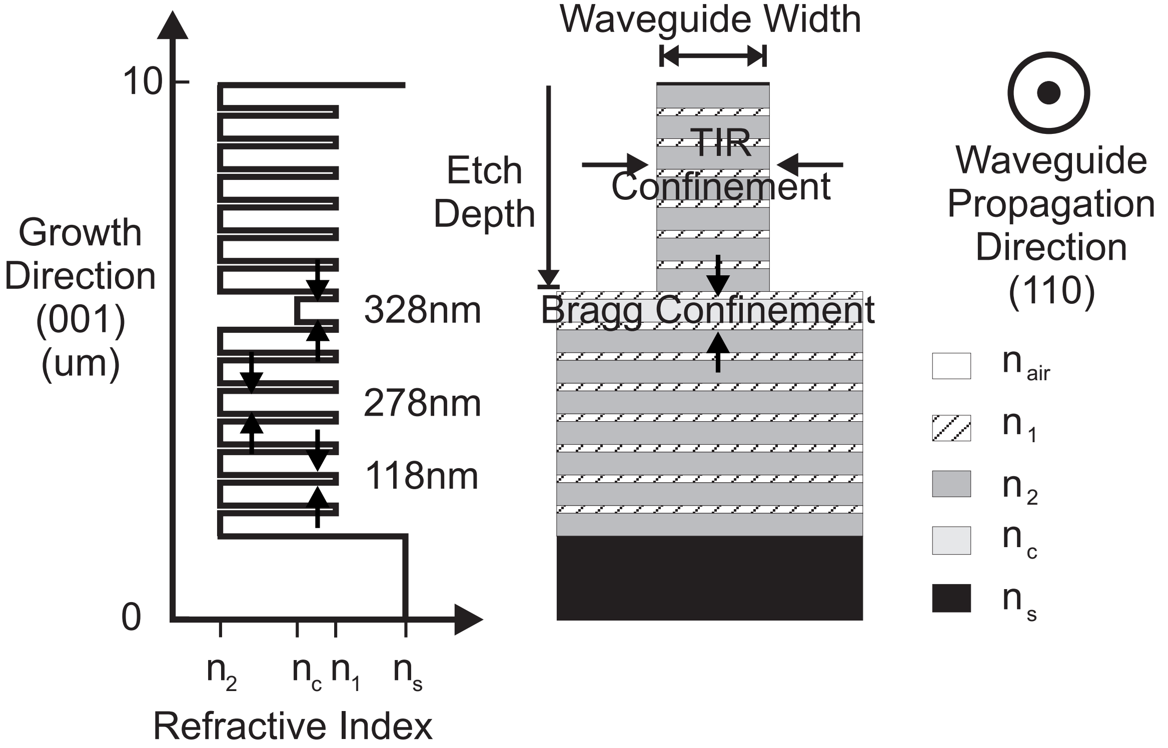

Figure 6.5: A schematic of ridge Bragg Reflection Waveguide. The ridge provides confinement horizontally via total internal reflection, while the bragg mirrors confine the light vertically.

along the (110) direction (45° with respect to the principle crystallographic directions. The final chip was a cleaved section about 15mm wide and 1.7mm long.

6.4.1 Numerical Modeling in FDTD

Using a commercial mode solver called Mode Solutions by Lumerical Solutions Inc., the structures were modeled according to the design just discussed. Mode Solutions is capable of solving the full vector wave equation, calculating the spatial overlap of two modes and tracking a mode over a range of wavelengths. The material parameters were obtained from the designer (A. Helmy) according to reference [91] and a spatial index profile was created. The modes corresponding to both the TIR and Bragg modes were found for a particular frequency and then tracked using a wavelength scan. The effective index was plotted over a reasonable region and the results are shown in figure 6.6.

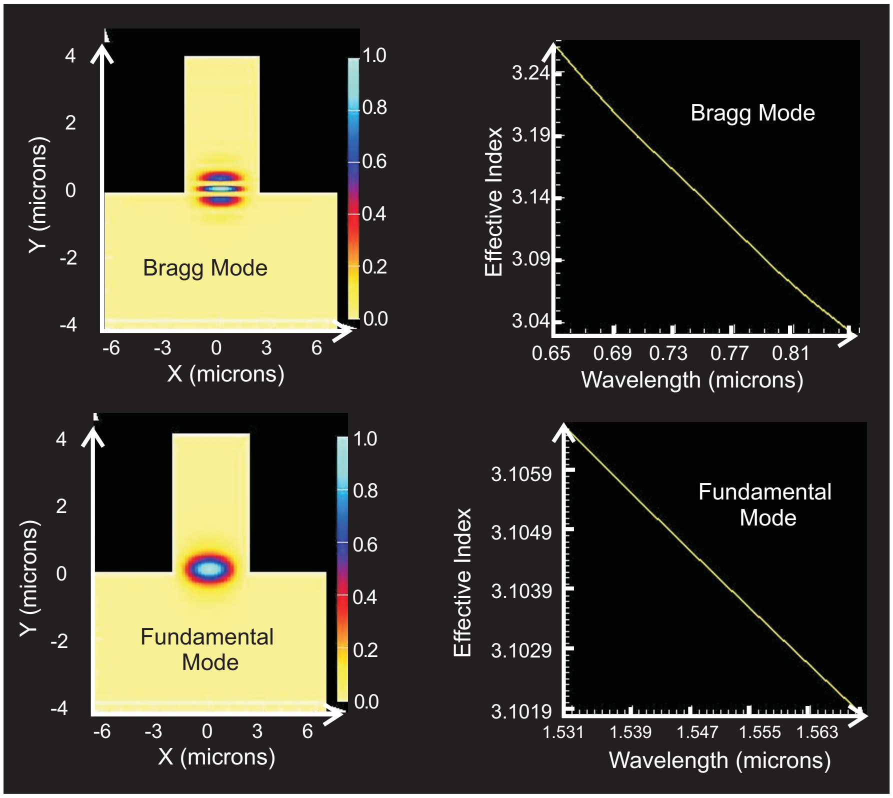

Figure 6.6: Intensity plots for the TIR fundamental mode (bottom left) phase matched with a Bragg second harmonic mode (top left). The Bragg mode shows the expected vertical 'side' lobes. The effective index vs wavelength for the two modes are plotted to the right. Phase matching occurs for somewhere in the vicinity of 777nm.

6.5 Experiment

Using the experimental setup and methods outlined in chapter 3, the phase matching condition was first verified by examining the spectrum of the second harmonic (SH) from each of the waveguides. Power in the second harmonic was inferred by integrating the area under the spectrum and applying an appropriate conversion factor. Using this, the dependence of the SH power on the input power was verified. While the Fabry Perot method predicts a free spectral range of around .2nm for fundamental light, resonances were not observed, and the linear loss in the waveguide was estimated from the insertion loss. From this, the SH efficiency was inferred. The tunability of the waveguides was examined by plotting the wavelength of the resonant peaks in the spectra with respect to the waveguide widths. The guides were then pumped with light at the SH wavelength and appropriate filters were applied to the collection optics. Subsequent measurements of the time difference between two multimode single photon detector signals provided evidence of time-correlated light at the fundamental wavelength and confirmed the SPDC process.

6.5.1 Up Conversion

Spectroscopy : Type-0, Type-I, and Type-II

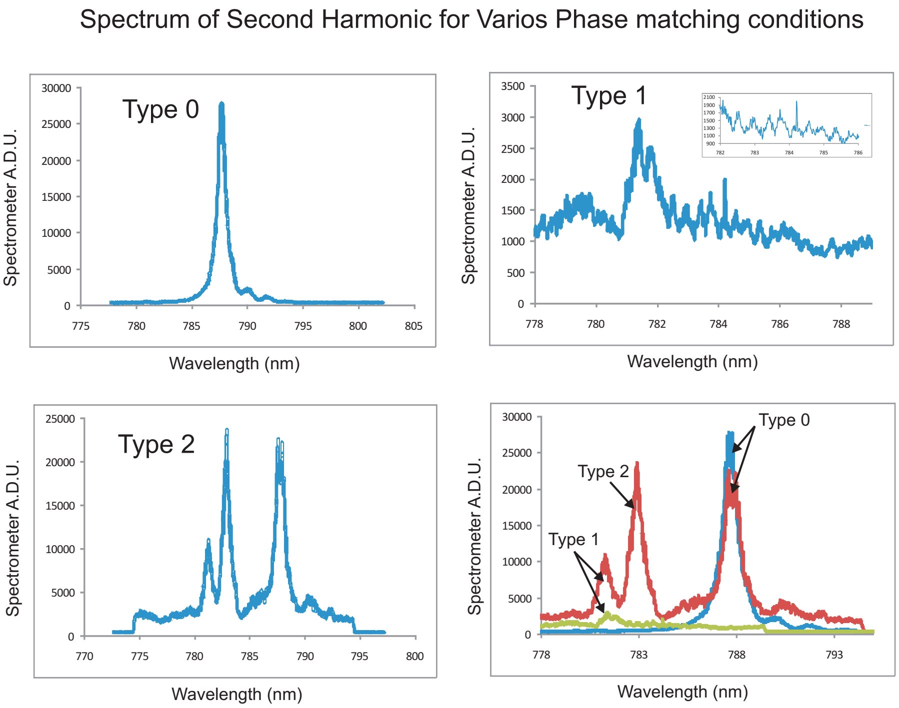

Figure 6.7: Pictures of a the various spectra acquired for a ridge BRW pumped with TM (type-0), TE (type-I), and 45° (type-II) polarized fundamental light scanned from 1560nm to 1590nm. In the type-0 process, the pump wavelength that produces the resonant up conversion signal at 788nm is roughly at 1576nm. Relatively weak but still significant upconversion takes place at around 781.5nm for the type-I process, corresponding to a pump wavelength of approximately 1563nm. The inset shows oscillations but cannot be attributed to any reasonable etalon or fabry perot effects. When the same guide is pumped with 45° light, both the TE and TM phase matching resonances at 781.5nm and 788nm are evident, in addition to a third resonance at 783.5nm. This third peak is attributed to a type-II process.

Pumping the fundamental TM mode into the waveguide facilitated type-0 up conversion. A scan over a reasonable range of fundamental light determined which wavelength satisfied the phase matching condition for that particular guide.

Type-I up conversion was investigated by pumping the waveguide with the fundamental TE mode. The resonant SH mode is phase matched at a wavelength approximately 6.5nm lower than in the type-0 configuration.

The spectrum obtained when pumping both TE and TM polarized light (i.e. light polarized at 45°) excited both the type-0 and type-I resonances plus an additional resonance occurring in between the type-0 and type-I phase matching conditions. This process was not readily observed in all of the different waveguides.

The results are shown in figure 6.7.

Discussion

It is interesting to compare the spectra of the different phase matching conditions as well as the spectra obtained across different waveguide widths. Many waveguides were tested at various different times and coupling scenarios. The results for all three pumping conditions for the above waveguide are plotted together and shown in the bottom right picture of figure 6.7. This clearly shows that there are three distinct processes that the waveguide mediates. Due to possible coupling differences, the absolute maxima should only be used as a rough comparison of the process efficiency. Consistently however, the type-0 process and type-II process appeared more efficient than the type-I process. This is even more convincing when regarding the overall insertion loss[8]. Still as the linear loss in the guide cannot be separated from the pump to Bragg mode coupling, it remains impossible to conclude if and what type of interaction is mediated more than another.

Another interesting trend is found by looking at the type-II configuration and observing the effect of waveguide width on all of the resonant wavelengths. Plots for all six widths are shown as separate graphs in order to avoid clutter. The plots are normalized to their highest value and at first glance it is difficult to tell what resonant wavelength is attributed to what type of process. Cross referencing the type-II scans with their proper type-0 and type-I scan data (not shown), an approximate dependence of the resonant wavelength (for a particular process) on waveguide width can be inferred. The results are shown in figure 6.8.

---

[8] see discussion on insertion loss below

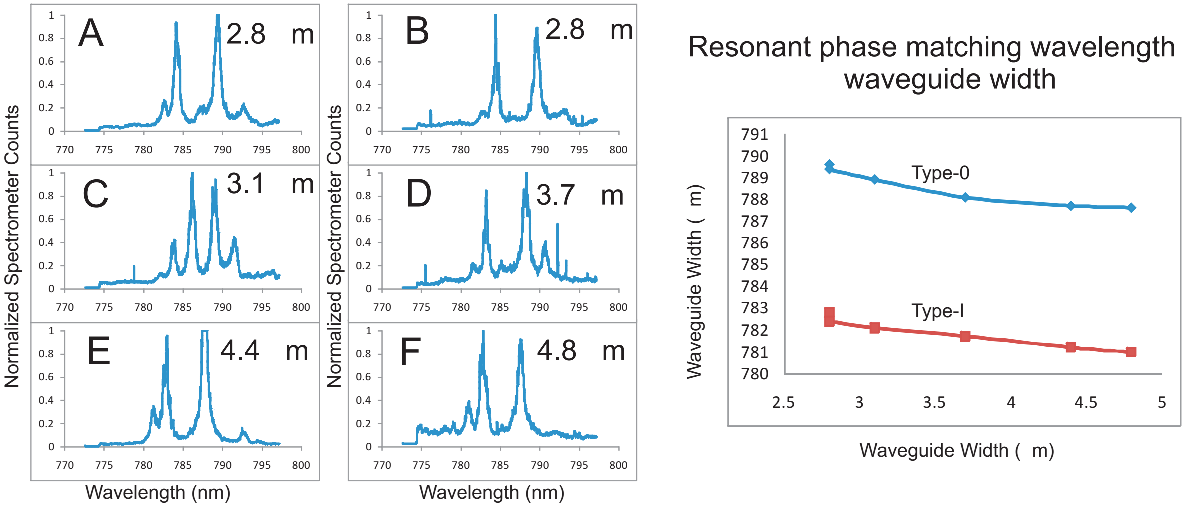

Figure 6.8: Six spectra, one for each waveguide width, acquired in the type-II pumping configuration showing, if applicable, all three interactions in the same plot. In order from A to F the widths are increasing and are 2.8μm, 2.8μm, 3.1μm, 3.7μm, 4.4μm, and 4.8μm. The graph shows a rough approximation of the dependence of the resonant wavelength on the waveguide width.

Insertion and Linear Loss - TM

A 4.8μm waveguide from the sample was chosen and pumped in the upconversion configuration (right to left) with TM polarized fundamental light in the vicinity of 1577nm. In this configuration, the transmission of the setup is approximately 9.48% without the waveguide inserted (from the power measured at P2 to the multimode coupler – see appendix table A.2 and figure A.4). Upon waveguide insertion, the transmission of the setup dropped to roughly 0.036%. This is a factor of about 263 and can be attributed to the waveguide facet reflectivity and coupling to the input and output of the guide as well as the linear loss in the waveguide. For a facet transmission of approximately 73% and coupling at the input and output facet estimated at 30% and 90% respectively, then the transmission in the waveguide is approximately 2.64%, or a loss factor of about 38. Each waveguide was 1.7mm long, putting the linear loss coefficient at 2.14/mm for fundamental TM polarized light.

Insertion and Linear Loss - TE

The same waveguide (used in the type-0 configuration) was pumped in the up-conversion configuration with TE polarized fundamental light in the vicinity of 1566nm. In this configuration, the transmission of the setup is approximately 15.68% (from P2 to the multimode coupler – see appendix table A.2 and figure A.4). With the waveguide inserted, the transmission drops to 0.064%. This is a loss factor of about 245. This is very close to the loss observed with type-0 pumping, and, for similar coupling and facet transmission, a loss coefficient of around 2.1/mm is estimated.

The transmission for light polarized at 45° was not explicitly evaluated. However, for an optimized polarizer setting, the coupling was insignificantly different, indicating that the linear loss of the guide is on par with that found for both TE and TM pumped fundamental light.

The loss estimates can be loosely compared with loss estimates found in the literature for similar structures. As an example, the group led by A. Helmy at the University of Toronto inferred linear loss using the Fabry-Perot method. Their estimates are a factor of 10 lower [92], claiming approximately 2.0/cm and 2.2/cm for TE and 45° polarized light in 2.17mm long waveguides. They estimate 71% facet transmission and 49% input coupling.

Power Analysis

A rough sample calculation that determines the expected SHG produced from a ridge BRW is developed using equation (6.10). For this analysis, it is assumed that the pump field, E_1, is polarized in the x'-y' plane and propagates in the x'-y' plane, then the z coordinate can be written as a function of x' and y'. In this case, $a_{1x'}=\sin(\frac{\Pi}{4})=\frac{1}{\sqrt{2}}$, $a_{1y'}=-\cos(\frac{\Pi}{4})=\frac{1}{\sqrt{2}}$, and $a_{1z'}=1$. For the BRW's discussed here, there is no phase mismatch, so $\Delta k = 0$. Further, for a first approximation, it is assumed that the index of refraction for both E_1 and E_3 are the same and equal to 3.4, and that the spatial area of the modes at both the fundamental and second harmonic are also equivalent. The calculation proceeds with caution here because this is definitely not the case - the spatial profile for the Bragg mode is very different than the fundamental mode. Nonetheless, to find E_3 after a distance L, equation 6.10 can easily be integrated as

$$\begin{aligned} E_3(L) &= \int_0^L -i\omega_3\sqrt{\frac{\mu_0}{\epsilon_3}}\frac{d_{36}a_{3z'}a_{1x'}a_{1y'}}{2}(E_1)^2 e^{i\Delta kz}dz \\ &= \int_0^L i\omega_3\sqrt{\frac{\mu_0}{\epsilon_3}}\frac{d_{36}}{4}(E_1)^2 dz \\ &= \Gamma\int_0^L dz \\ &= \Gamma L \end{aligned} \tag{6.12}$$

Where $\Gamma=i\omega_3\sqrt{\frac{\mu_0}{\epsilon_3}}\frac{d_{36}}{4}E_1^2$, and $\epsilon_3=\epsilon_r\epsilon_0$. For the SI values of $\epsilon_0=8.854\times10^{-12}$F/m and

μ_0=4π×10^{-7}H/m, d_{36}=72×1.255×10^{-12}×8.854×10^{-12}m/V, and ϵ_r=n^2=3.4^2 we can evaluate what the pump field is in a 2μm diameter circle under the assumption that a total of P=100μW of power is coupled into the structure. Note that to gain knowledge of the electric field, we use the irradiance or time averaged value of the poynting vector, in units of watts/m^2. The formula for irradiance is

$$<s>=\frac{\epsilon_3 v E_1^2}{2} \tag{6.13}$$

where v is the speed at which light arrives at the detector (in this case v is the phase velocity, c/n).

$$\begin{aligned} E_1^2 &= \frac{2nP}{n^2\epsilon_0 Ac} \\ &= \frac{6.6\times 100\times 10^{-6}}{3.4^2 8.854\times 10^{-12}\pi\times 10^{-12} 3\times 10^8} \\ &= 7.26\times 10^9\frac{V^2}{m^2} \end{aligned} \tag{6.14}$$

For 790nm light, and a 1.7mm long waveguide, this puts the second harmonic field strength at E_3^2 = 4.5×$10^5\frac{V^2}{m^2}$. Since the ratio of the square of the fields gives a rough estimate of the ratio of the respective powers, the SH intensity is approximately 0.006% of the fundamental.

Using similar calculations to those just developed, a plot of the *expected* back facet second harmonic power (for front facet powers similar to those used in the experiment) is shown in the right graph of figure 6.9. The left graph of that same figure shows the actual *inferred* dependence of the back facet second harmonic power. The inferred result pertains to the type-0 configuration where the pump is vertically polarized.

Efficiency calculations

To arrive at an estimate of the measured efficiency of the guide in the type-0 configuration the pump power just after the front facet needs to be compared to the second harmonic power just before the back facet. The front facet power is obtained by measuring the power at P2 multiplied by the transmission of the first pellicle (78%), the transmission of the first objective (95%), and the coupling and facet transmission (30% and 73%). Ignoring for the moment the linear loss in the guide, the power in the second harmonic inside the back facet can be obtained in a similar fashion. That is, using the spectrometer calibration, the power in the coupling fiber is estimated and then degraded by the transmission from the back facet to the fiber coupler. The following

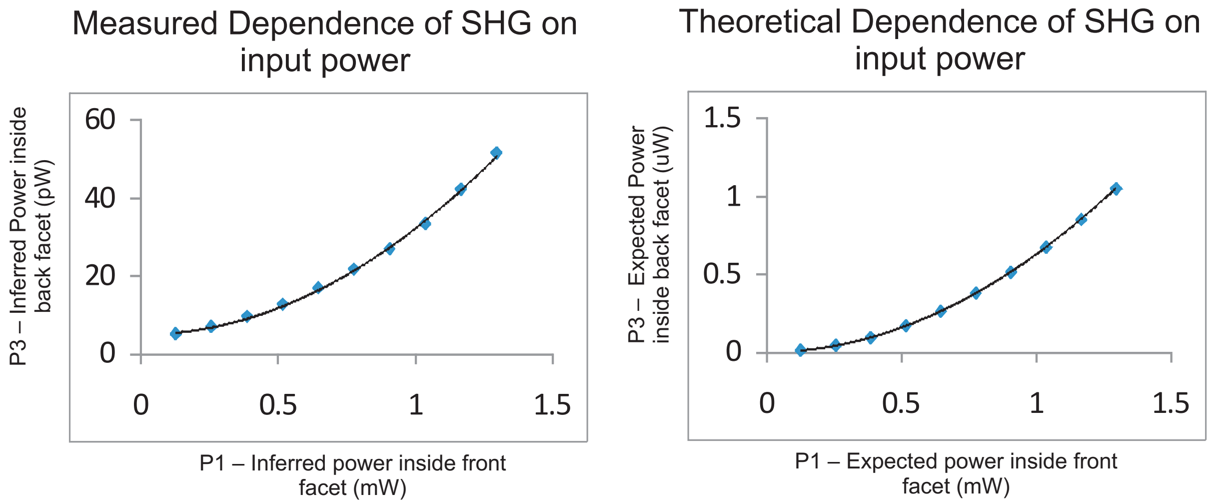

Figure 6.9: Left: Experimentally measured dependence of the power (inferred at the back facet) in the second harmonic as a function of the input power (inferred at the front facet). Right: Theoretical dependence of the power at the end of the waveguide (back facet) in the second harmonic as a function of the input power at the front facet. Both show a quadratic dependence on the input power.

transmission parameters are assumed: multimode coupling (90%), objective transmission (80%), objective coupling (90%) and back facet transmission (73%).

A reasonable parameter that quantifies the efficiency in waveguides is the length normalized efficiency. It is defined as $\eta = P_{2\omega}/P_{\omega}^2 \mathrm{L}^2$. The length normalized efficiency can be obtained from the slope of the graph of $P_{2\omega}/P_{\omega}^2$. Graphs of $P_{2\omega}/P_{\omega}^2$ were produced from the same data given in figure 6.9. They are shown in figure 6.10.

From the slopes of the two curves in figure 6.10, and for L=1.7mm, the measured length normalized internal conversion efficiency can be estimated as $3.13{\cdot}10^{-4}$%/W/mm^2 or $3.13{\cdot}10^{-2}$%/W/cm^2, while the theoretical prediction yields 22%/W/mm^2 or 2200%/W/cm^2.

Discussion

The two plots in figure 6.9 may at first glance seem quite similar, but their relative magnitudes are very different. The measured result shows a y-intercept. This implies a second harmonic field at zero input power. This is most reasonably explained by the order in which the power measurements were made. Due to the limitations of the experiment, coupling could significantly alter over time. Thus, measurements were often made in as short a time as possible. Tuning the pump laser from low to high power produced reliable and immediate power increases. When making the power measurements, optimal coupling was achieved for the lowest power and from then onwards, the pump power was manually increased, and a spectrum manually recorded. This implies

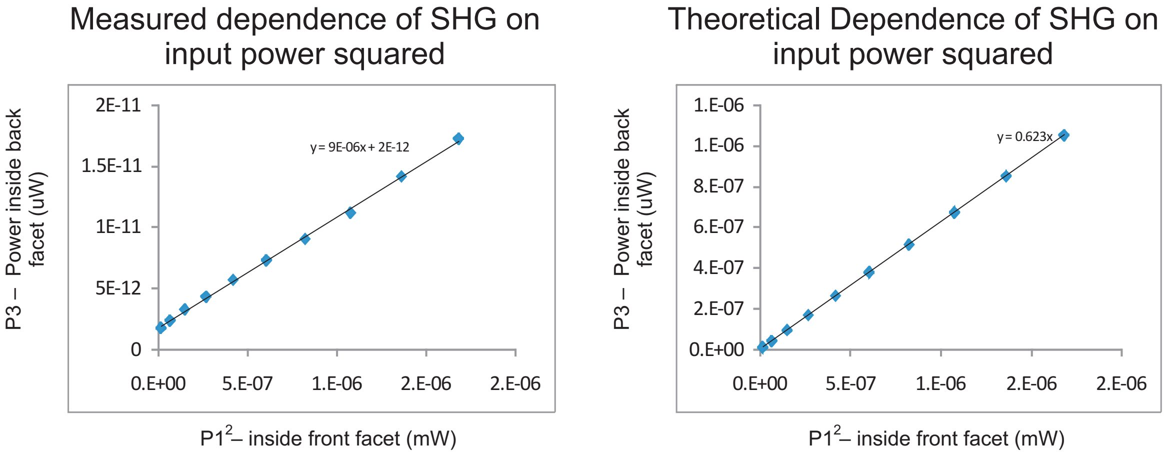

Figure 6.10: Left: Experimentally measured dependence of the power (inferred at the back facet) in the second harmonic as a function of the square of the input power (inferred at the front facet). Right: Theoretical dependence of the power (inferred at the back facet) in the second harmonic as a function of the square of the input power at the front facet. In both cases, the dependence should be linear.

that the recording time between the first and last spectrum was equal to the experiment duration. As it was rare that the coupling and alignment would become more favorable with time, the most likely result is that the dependence of the output SH power on the input power is less than quadratic. This could explain the apparent offset.

The second point to note is the magnitude of the expected power in the second harmonic. The value of $3.13{\cdot}10^{-2}\%/\mathrm{W/cm}^2$ can be compared to what is currently the state of the art in form birefringent AlGaAs waveguides where a measured efficiency of $1500\%/\mathrm{W/cm}^2$ has been reported[93]. Given the coupling and assumptions, the inferred efficiency is approximately 70000 times less than expected. Even accounting for the loss in the guide (factor of about 38), there is still a large discrepancy. There are a few possible theories to explain this discrepancy. Ignoring for the moment a grave miscalculation of the area of the confined mode, then possible reasons are that a) the estimate of d_{36} is incorrect (presence of aluminum decreases the coupling), b) the Bragg mode is not well coupled to the multimode fiber, c) the fundamental mode overlap with the Bragg mode has not been accounted for (both in the theoretical and inferred calculations). Most likely it is c) as the energy in the Bragg mode is distributed over the core and cladding. In essence, either the coupling in the guide is overestimated – (be it power, mode-overlap, or the effective non-linearity) or if the power is there, then the ability of the collection optics to couple the Bragg mode has been severely overestimated.

6.5.2 Down Conversion

Once a waveguide was spectrally characterized, the wavelength setting for the main laser was aligned to one of the favorable resonant up conversion wavelengths and then pumped into the sample. The measurement setup was then configured according to figure 3.2 where a detection event by a single photon detector (Alice) conditoned a second single photon detector (Bob) to open for detection. The results (shown in figures 6.11 through 6.15) were acquired from a particular waveguide that was different than the one analyzed above for up conversion. In particular, a 4.4μm waveguide from the sample was chosen and pumped in the downconversion configuration with TM (vertically) polarized harmonic light in the vicinity of 789nm. The output was filtered with Schott glass designed to cut out the pump wavelength (RG1000 and RG850) as well as a custom built edge filter with a cut on frequency of 1560nm.

The reason for the additional edge filter is the following: Initially, after applying appropriate filters to eliminate the pump light (RG1000 and RG850), barely noticeable amounts of power still remained – approximately a few digital positions above the ambient power levels – picowatts at best.

This level of light saturated the first single photon detector - confirmed by observing that the trigger and detection rates were very nearly equal. Two attempts were made at determining the spectra of this mystery light using a sensitive InGaAs absorber / Si CCD camera combination along with a spectrograph fashioned with appropriate gratings. On both occasions the conclusions were that the emitted light was very broad. This was inferred by noticing a distinct signal that remained unchanged across a variety of grating positions. Bypassing the sample the signal disappeared and it was determined that this light was indeed emitted from the sample.

Initially thought to be SPDC, this idea was immediately ruled out when its presence was detected long after the arrival of the optical pulse. That is, when making the conditional coincidence measurements between Alice and Bob (in order to infer the presence of SPDC), there appeared distinct time correlations between Alice and Bob throughout the entire duration of Bobs gate. These correlations were strongest with the arrival of the pulse, and exhibited a decay in strength until the next pulse arrived. Because there were detector correlations between pulses (even accounting for the timing jitter of the experiment), the correlations could not have arisen from a such a unique simultaneous event such as SPDC.

This new 'background' had the following behaviour. Because of the finite (but constant) constantly repeating (with the pulse train) probability of detecting this light at Bob, Bob was more likely to stop the clock earlier in the gate then later. Thus, the appearance of the background was a sloped 'saw tooth' type of appearance where the saw tooth had the shape of a decaying exponential. The exponential nature of the decay was more/less evident with increasing/decreasing pump or the if signal was filtered less/more.

The background light will from here on in be referred to as simply *fluorescence* but the cause of this physical phenomenon still remains unclear. One explanation is the presence of broadband but deep impurities existing roughly at an energy of half the bandgap of the semiconductor. A second explanation has roots in the growth technique. In general conversation with other colleagues who look at AlGaAs structures for other purposes, fluorescence has been observed in MOCVD grown samples that is absent in samples grown via Molecular Beam Epitaxy. The suspected cause is the presence of carbon that gets embedded in the crystal during the growth, although what physical mechanism is responsible for the emission remains unclear. Nonetheless, the edge filter helped to eliminate most of the fluorescence.

Timing Data

As a brief overview, the main result that is evident from all the collected conditional coincidence measurements is the existence of a weak SPDC signature from one BRW waveguide on the chip. In an attempt to optimize the initial results (trying to eliminate the so called fluorescence), various experimental configurations along with other waveguides were tried and tested , but all produced similar, often worse looking data sets than those initially acquired. Thus, the data sets shown here pertain to one guide and were acquired within the span of about 2 weeks.

The important raw TAC data sets are summarized and displayed in figure 6.11. The figure shows data acquired in three different experimental configurations. In the first configuration, by adjusting an internal delay, Alice was synchronized as best as possible (see appendix figure A.6) to the arriving pulse while Bob's internal delay was bypassed. The correct arrival time was identified as somewhere in the vicinity of 84 ns (see appendix figure A.7). The data pertaining to just this configuration are shown in 6.12 and 6.13. The second configuration was achieved by adjusting Bob's internal delay from bypass to a nominal setting of 6ns (the true delay was closer to 10-11ns). Two data sets were acquired and they are shown in 6.14. The effect of adding delay in Bob's detection circuit was to move the weak SPDC signal closer to the start of Bob's gate. The third experimental configuration involved changing Alices delay from 14.2ns to 15.0ns. The result is shown in 6.15. Changing Alices delay had the effect of somewhat desynchronizing her detection window with the arriving optical pulse.

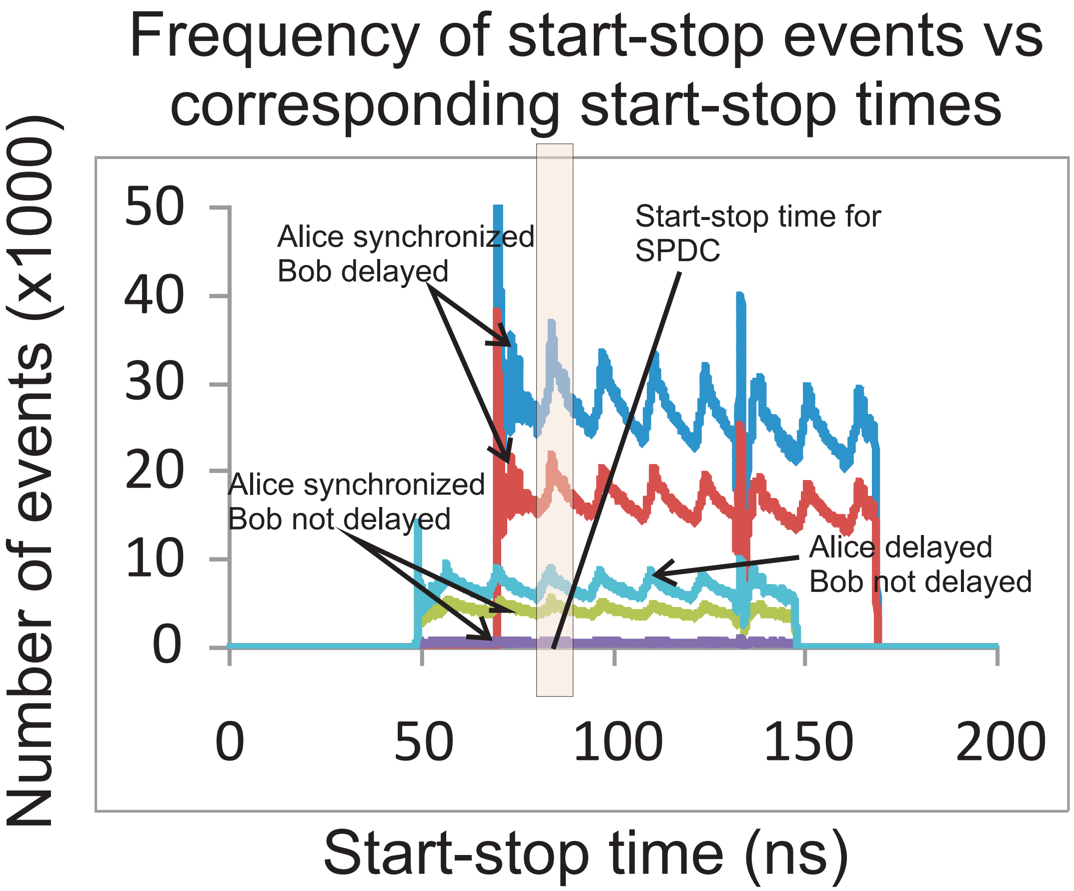

Figure 6.11: A collection of the relevant data sets that show SPDC. The periodic signal is attributed to relatively strong fluorescence following a pump pulse. The strength of this signal was dependent on how well the sample was coupled as well as on the pump power. Because the SPDC signal is weak, the vertical band in the picture shows where the reader should look and corresponds with the expected arrival time of photons produced via SPDC.

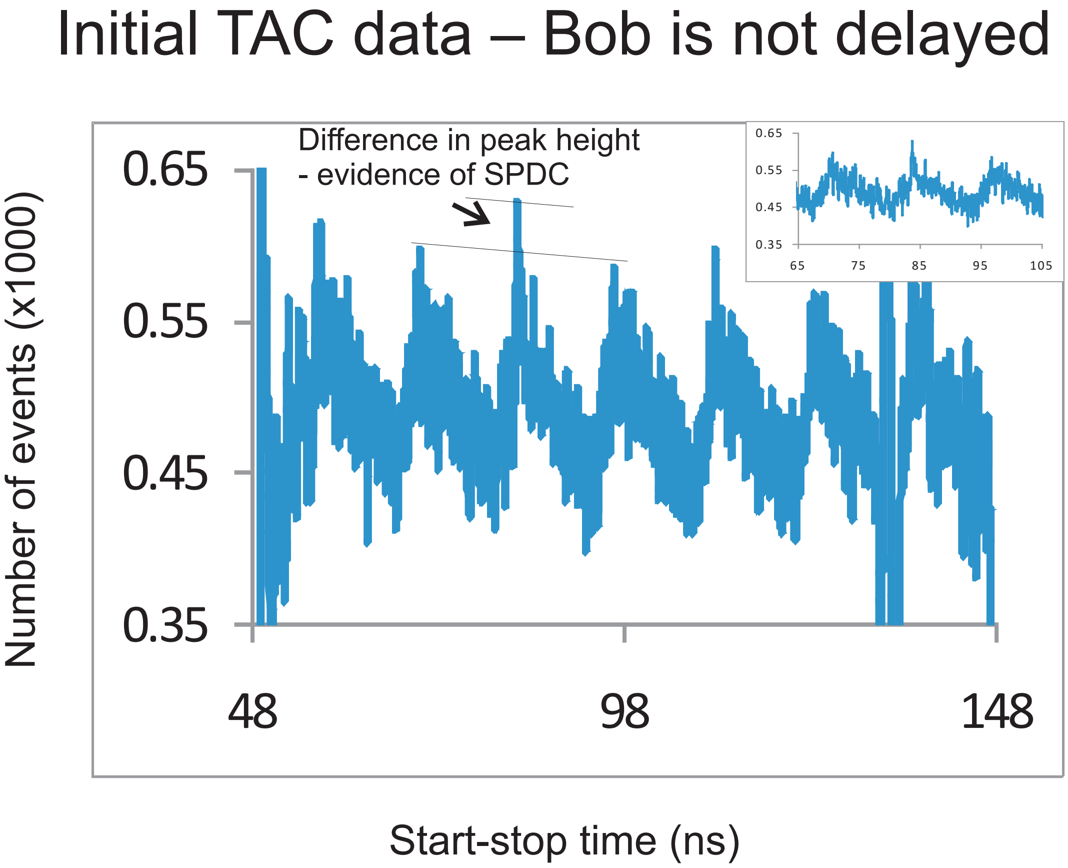

Figure 6.12: A sample data set taken from the output of the TAC. The expected arrival time of a coincident photon is around 84ns, and there is a small but noticeable peak at this time (see inset). The periodic noise background is attributed to fluorescence from the sample, and is correlated with the pump frequency of 76MHz.

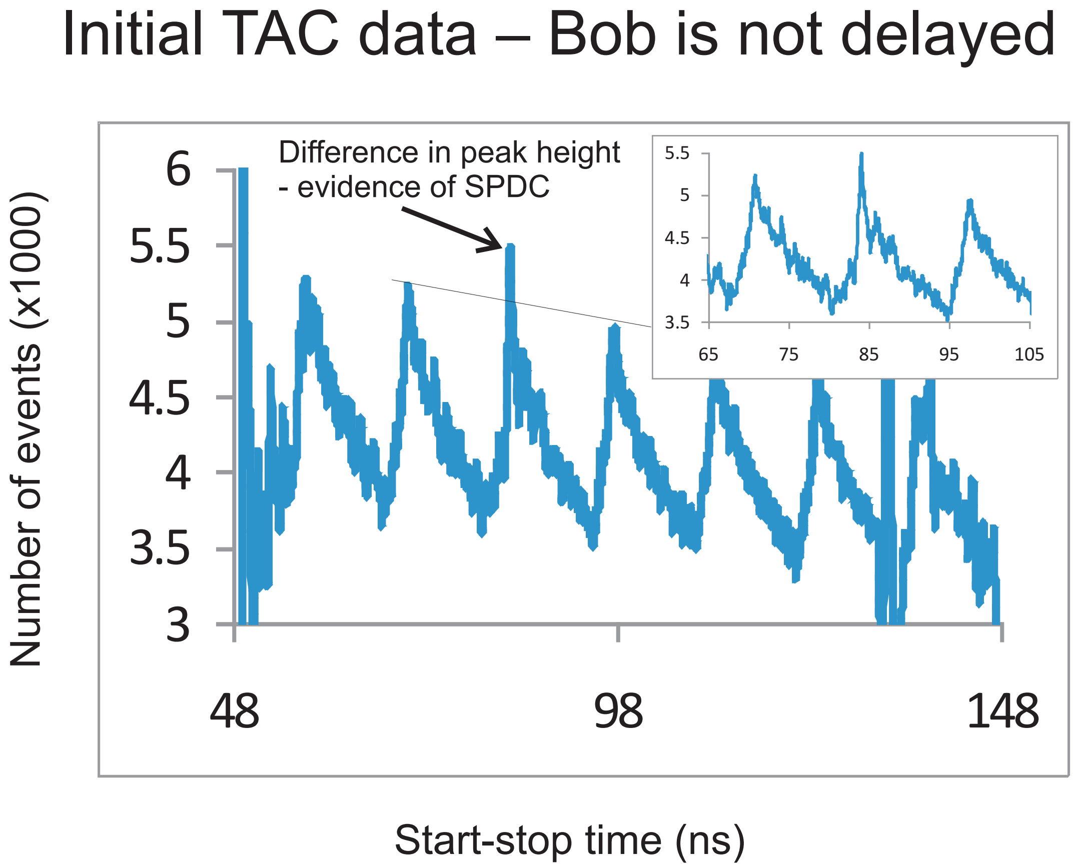

Figure 6.13: Another sample data set taken from the output of the TAC. This time, the total run time is longer. At 84ns, the peak is slightly more noticeable (see inset). Note the trend in the periodic noise background which decreases with increasing gate time. It is attributed to fluorescence from the sample, and is correlated with the pump frequency of 76MHz.

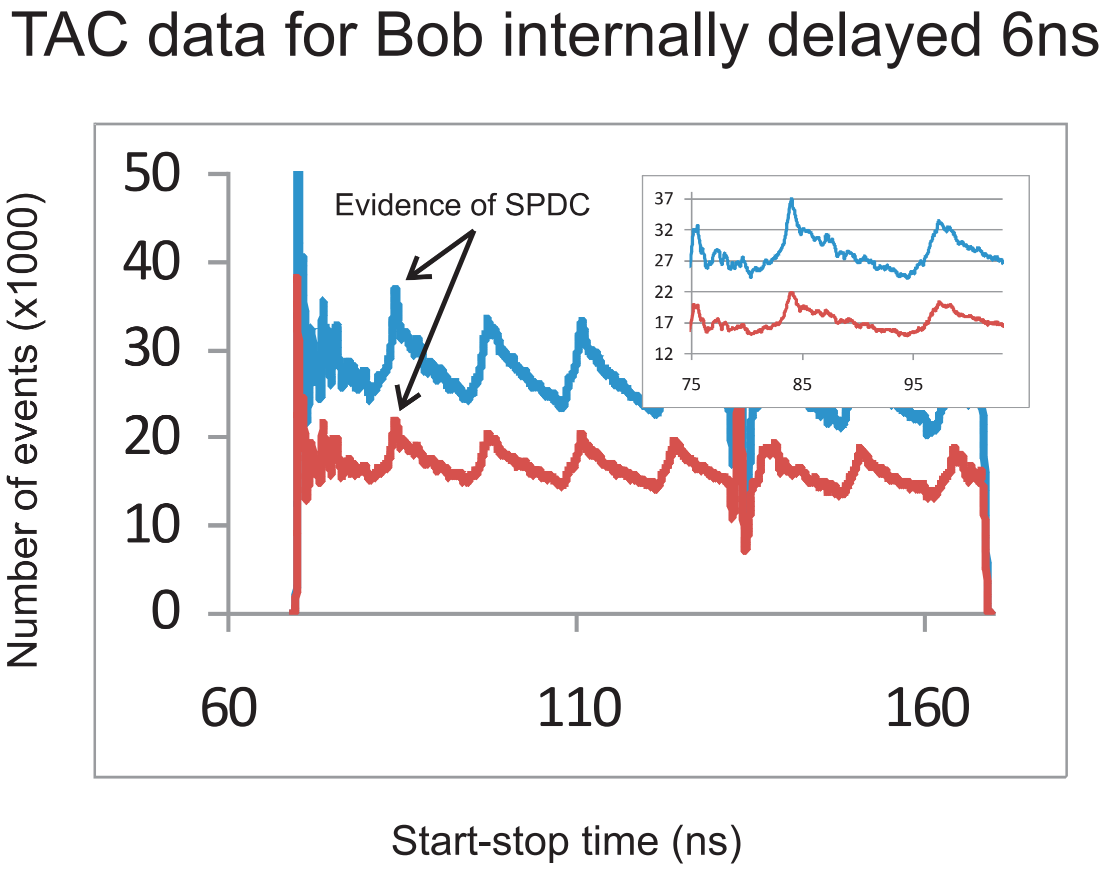

Figure 6.14: A sample data set taken from the output of the TAC. The expected arrival time of a coincident photon is still at 84ns, but Bob has been delayed and so his gate starts closer to the expected signal. The two curves represent different data taken on different dates.

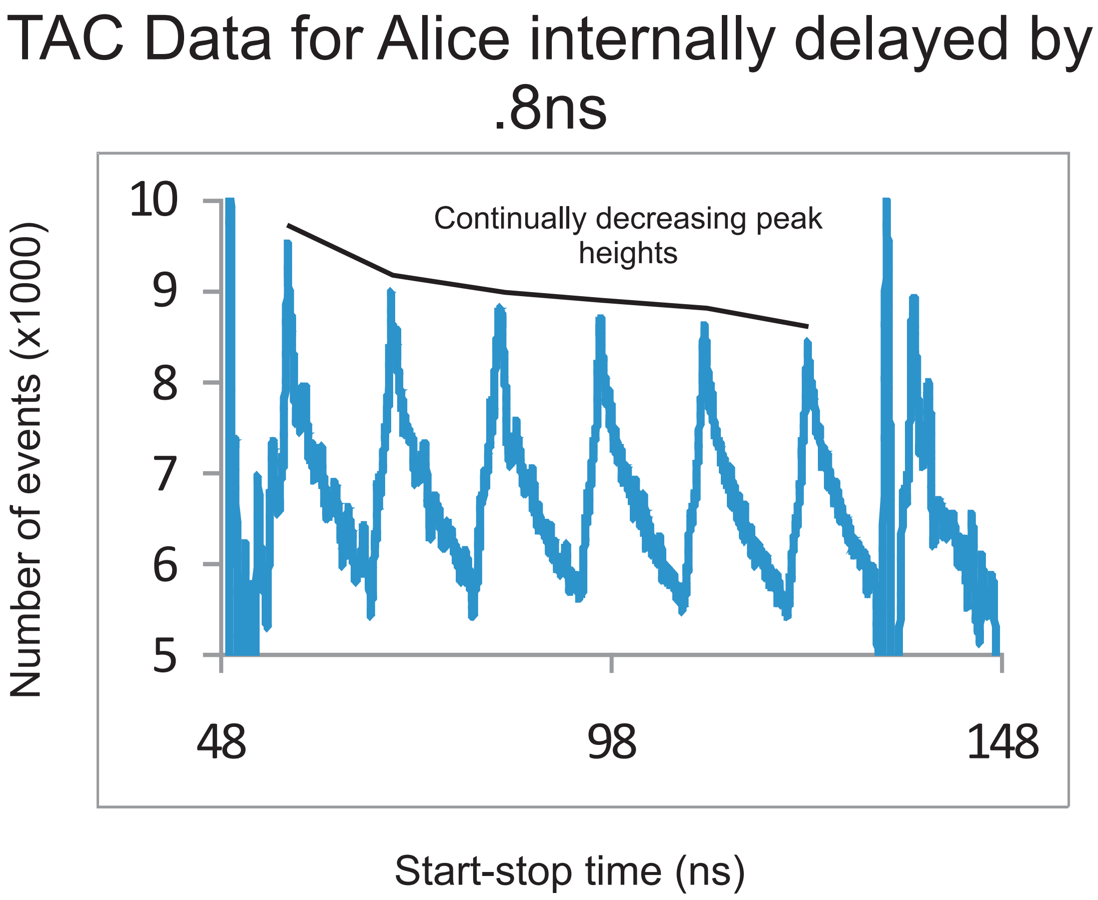

Figure 6.15: A sample data set where Alice has been de-synchronized with the incoming pulse and is therefore more likely to simply detect spurious emission or dark counts. As there is no time correlated pair arriving at Bob, what little signal there was has been washed out.

Experimental Analysis

The raw data just shown presents three major problems when attempting to infer the SPDC efficiency of the waveguide. Those problems are:

1) The data was acquired over as much as 28800 seconds or 8 hours. As the sample position could move significantly (more than the waveguide width) over this duration, the coupling of the pump beam to the Bragg mode could be drastically different at the beginning and end of the experiment[9]

2) The data was clearly mired by the presence of light within the signal bandwidth that did not exhibit the expected time correlation of SPDC. This effect has been labeled as 'fluorescence'. It is unknown what effect the coupling issues (problem 1) have on the fluorescence but throughout all the data sets, the fluorescence seemed to decay exponentially between pulses.

3) The pump light was sent through approximately 12 meters of single mode fiber. In the pulsed configuration the peak power was approximately 3250 times greater than a comparable cw experiment. Such peak intensities can excite non-linear behaviour in glass (see figure A.8) . Thus, it cannot be easily determined how much pump power overlapped with the optimal wavelength for phase matching.

The analysis proceeds in two different directions. The first direction involves an analysis of the raw data obtained in figure 6.13. To work around problems 1) and 3) it will be assumed that the coupling was constant over the 28800 seconds and that all the power in the pump overlapped with the correct phase matching wavelength.

The data was analyzed under the following pretense: For times away from the expected coincidence time, correlations between Alice and Bob would be periodic with a period determined by the repetition rate of the input pump laser. In order to achieve this periodic look, the data was detrended to account for the degrading likelihood of an event to occur at later times in either of Alice or Bobs gate. Next, the data set was coarse grained into 1ns bins to account for the approximate timing jitter in the experiment. Lastly, the data was shifted in time so that a zero delay time corresponded to the expected coincidence time for the produced pair.

Following the outline just stated and omitting data points at or near the expected coincidence time (zero delay), successive bins that were separated by the pulse period were compared. In particular those bins with the greatest number of counts were taken to represent an indication of the maximum background signal. For those bins, it was assumed that each bin value would be normally distributed about a mean allowing the standard deviation (σ) of this set of bin values to be calculated. Two standard devia-

---

[9] This is thought to arise from ambient temperature drifts causing thermal expansion of the flexure mechanisms in the sample stage. As the data was acquired in May 2010 during the spring, a time known for fluctuating temperatures, it was normal to have the temperature drift by a few degrees during the time of the experiment.

tions above the mean was used as an upper signal level below which one could be 95% confident that similarly obtained data would lie. The previously omitted data point was then re-inserted and compared to this 95% confidence level. This allowed an inference of whether or not the re-inserted data point could reasonably be attributed to the background or some other physical process (pair production).

The result of this analysis is plotted in figure 6.16.


Raw Data Set - Detrended and time shifted for SPDC coincidence occurring at zero delay

Binned Data set (1ns bin size)

Maximum measured coincidence counts plotted at their corresponding measured delay times.
(Vertical error bars represent square root of total count in bin).

Maximum measured coincidence counts plotted at their corresponding measured delay times.
(dashed line is 2 standard deviations above the mean background red horizontal line)

Figure 6.16: A sample data set analyzed. Top left is the raw data set. Top right is the raw data set binned into 1ns bins. The bottom left sifts the maximum values (from the binned data set) occurring at intervals equal to the optical pump repetition period. The error bars are estimated by assuming the count distribution is poissonian. The bottom right picture depicts an average (≈ 82262 cts) of the maximum values (with the zero delay bin omitted) and establishes a 95% confidence interval around that mean. The SPDC signature (≈ 85845 cts) is clearly outside this interval and in fact is almost 5 standard deviations away from this mean.

The peak background average count rate was estimated to be approximately 82263 ± 287 cts. The standard deviation was estimated to be ≈ 770 cts. The upper 95% confidence interval (2σ) was established to be 83803 cts. The peak at zero delay was measured to be 85844 ± 292 cts., lying almost 5σ away from the peak background average level so that with good confidence, the net count attributed to pair production is 3580 ± 580 cts. Due to a setting on the TAC, the analog to digital conversion underestimated the counts by a factor of 2. Thus the net coincidence count was determined to be approximately 7162 ± 1160 cts. Ignoring problem 1), a conservative estimate for the observed coincidence count rate is then approximately .25 ± .04 counts per second.

Based on this measurement, an estimate of the actual pair production rate can be arrived at by using the formulas provided in chapter 3 to determine the coincidence count rate. It is re-written here as equation 6.15.

Recall that equation 6.15 holds when the pair per pulse probability arriving at the detectors is low. It estimates the number of pairs detected in one second (N_{SPDC}) as

$$N_{SPDC} = \frac{N_p}{pulse}\epsilon\eta^2\epsilon_d^2 R_A r_{BS}, \tag{6.15}$$

where N_p is the number of pump photons, ϵ is the SPDC efficiency, η is the transmission of one of the photons in the pair from the time it was created in the waveguide until it reaches either Alice or Bob, ϵ_d is Alice and Bobs detector efficiency (assumed to be the same in this case), R_A is Alices trigger rate (no. of observed pulses per second) from SPDC[10], and r_{BS} is the beam splitter asymmetry. As Alices trigger rate (R_A) was approximately 2.1MHz, and the experiment length was 28800 seconds, there were approximately $2.1\cdot10^6\times2.88\cdot10^4 = 6.05\cdot10^{10}$ pulses observed and only 7162 total counts, and so the probability of multiple pairs per pulse arriving at the detectors is clearly irrelevant.

Then one can interpret equation 6.15 as

$$N_{SPDC}^{meas.} = N_{SPDC}^{act.}\eta^2\epsilon_d^2 r_{BS} \tag{6.16}$$

where

$$N_{SPDC}^{act.} = \frac{N_p}{pulse}\epsilon R_A \tag{6.17}$$

is the number of SPDC events actually needed to be produced in the waveguide in order to observe the measured coincidence counts.

Table 6.1 displays the relevant transmission parameters to determine η. For the analysis, errors are reported based on an inference of what the actual maximum and minimum values for the relevant parameters would be, rather than on an approximation to first order. From this table, η is approximately $0.02^{+0.008}_{-0.006}$. The detector efficiency

---

[10] Note that due to the fluorescence Alices trigger rate is not solely from SPDC, nonetheless, the analysis proceeds as if this was the case.

Position	Transmission	Est. Error
Waveguide Loss (1/2L)	6%	.35%
Back Facet	73%	2%
56x	90%	5%
CVI filter	99%	1%
Polarcor	95%	1%
Gold Mirrors	95%	1%
12mm Schott Glass	75%	3%
Multimode coupling	90%	5%
Total single photon transmission (η)	0.02	$^{+0.008}_{-0.006}$

Table 6.1: Estimation of η, the transmission of a single photon created at 1/2L in the waveguide to a detector.

ϵ_d was approximately 0.1±0.01. Accounting for the multi-mode fiber beam splitter (r_{BS} = 0.43±0.036), $N^{act.}_{SPDC}$ jumps to approximately $133{,}000^{+8\cdot 10^5}_{-8\cdot 10^4}$ pairs per second. Because Alices trigger rate was only 1/32 that of the actual optical pulse rate – approximately 2.1Mhz – there were approximately $0.06^{+0.38}_{-0.04}$ pairs/pulse.

We can estimate how efficient the waveguide is at producing photon pairs by finding the number of photons in the Bragg mode per pulse. This is done by converting the estimated power in the Bragg mode per pulse to a photon number per pulse.

For the data in figure 6.13 the input average power at P2 was approximately 12 mW vertically polarized. Table 6.2 below describes the estimated transmission for all the elements in the setup until the pump light has propagated approximately half way along the waveguide in the Bragg mode. The result is an estimated $125^{+64}_{-46}\mu$W of pump power in the Bragg Mode.

Position	Transmission	Est. Error	Est. Power
Approx. Start Power	—	10%	12mW
Pellcle	67%	1%	8.1mW
100x obj.	80%	5%	6.5mW
Front Facet	73%	2%	4.7mW
Est. Bragg Mode Coupling	50%	5%	2.4mW
Waveguide Loss (1/2L)	6%	.35%	125μW
Estimated Power in Bragg Mode	—	—	$125\,^{+64}_{-46}\mu$W

Table 6.2: Estimated coupling to the Bragg Mode for Type-0 SPDC

Recall that the repetition rate of the pump laser was approximately 76MHz. Thus for an estimated average power of 125μW in the Bragg mode (at 790nm), the number of photons per pulse is approximately $6{,}500{,}000^{+3.37\cdot 10^6}_{-2.40\cdot 10^6}$. This puts the internal conversion efficiency at approximately

$$\begin{aligned} \epsilon &= \frac{0.06}{6.5\cdot 10^6}\frac{\text{pairs}}{\text{pump photon}} \qquad (6.18) \\ &= .0000000098^{+1\cdot 10^{-7}}_{-7\cdot 10^{-9}}. \qquad (6.19) \end{aligned}$$

If we ignore the Bragg mode coupling factor of 0.5, this efficiency is reduced accordingly to approximately $5\cdot 10^{-9}$.

Typically photon pair sources are characterized both by the number of pairs they produce per second per unit of power and by that number further divided into bandwidth. Due to the weakness of the observed signal, the bandwidth of the down converted photons was unable to be determined. However, to compare the estimated pair rate here with those in the literature, one can imagine the pump power being scaled up by 8 to give 1mW of power in the Bragg Mode. An additional factor of 32 would account for all the light produced in the other pulses. Re-inserting the linear loss of the waveguide and the back facet reflection (a detrimental factor of about 40) and assuming all parameters scale linearly we can estimate a pair production rate exiting the waveguide of approximately $1.3\cdot 10^6$ pairs/s/mW.

Compared to current waveguided sources (see tables 6.4 and 6.3 and earlier results [94]) such a rate can be useful, however, one would have to inject 0.1W into the setup to get 1 mW into the Bragg mode.

It can be concluded that the dominant device issues that prevent this rate from being achieved are the waveguide loss and the Bragg mode coupling. Combined with low detector efficiencies and the difficulties in removing the fluorescence background the device is extremely difficult to utilize. Additionally, the bandwidth of the biphotons still need determination

Even though the experimental results were disappointing, the BRW represents a new archetype pair photon source and so further efforts were also directed at investigating the behaviour of the fluorescence. A second direction for analyzing the data was undertaken to improve the clarity of the results. It involved the construction of two programs to remove the fluorescence background from the raw data.

The first program was constructed in LabVIEW 8.6 and involved directly simulating the detector behaviour for the experimental conditions. The inputs were the probability for observing an SPDC event, a fluorescence event, and a dark event, along with the relevant detection parameters. The program was granulated into 1ns time segments and divided into two detector modules representing Alice and Bob. In each 1ns time

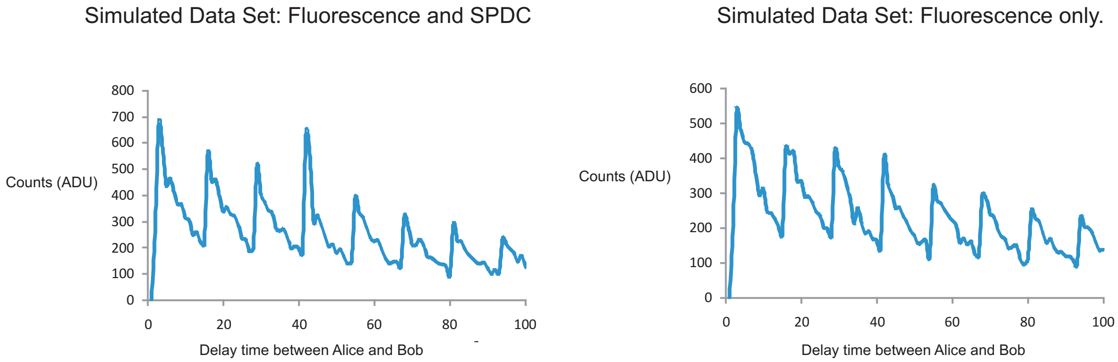

Figure 6.17: Results from a 1 second simulation in LabVIEW with increased probabilities (when compared to actual experimental conditions) for fluorescence and for SPDC. Here the probability to observe an SPDC pair was 0.01 per pulse, and the fluorescence probability is 0.1 per pulse with a time constant of 13ns. The behaviour of the simulation shows alot of the same features as the real data sets presented earlier. Here the correct arrival time from an SPDC event was set to occur at 40ns into Bobs gate.

segment, a random number was created for Alice. If the random number was less than the combined probability for seeing either of the three possible events, Alice did not register an event and did not trigger Bob. Conversely, if she did register an event, then the Bob module was run and a similar procedure was followed. The only difference with the Bob module was that if the triggering event was a result of an SPDC photon, then there was a significantly greater probability that Bob would see the pair photon and register an event. Unfortunately, due to the chosen programming language and the thesis time constraints, a full 28800 seconds could not be simulated and the parameters iterated to recreate the observed data. As such to get a feel for the program, elevated probabilities were chosen to verify the behaviour and confirm the overall behaviour. The results are shown in figure 6.17.

A second program was given to the author[11] to remove the exponential signal directly from the observed data sets. The program could be modified according to the detector configurations pertaining to the observed data set. The main goal of the program was to recreate the observed optical signal from the fluorescence only. The program first modeled the fluorescence signal as repeated decaying exponentials each truncated after a time equivalent to the period of the pulsed main laser. Both of Alice and Bobs gates were constructed as top hats. Alices response to the fluorescence was modeled as a convolution of her gate with the arriving fluorescence, and the coincidence response was modeled as a convolution of Bobs response with Alices response. The resulting signal was iteratively modified (by eye) to fit the observed data as best as possible. It was

---

[11] Thanks to G. Weihs.

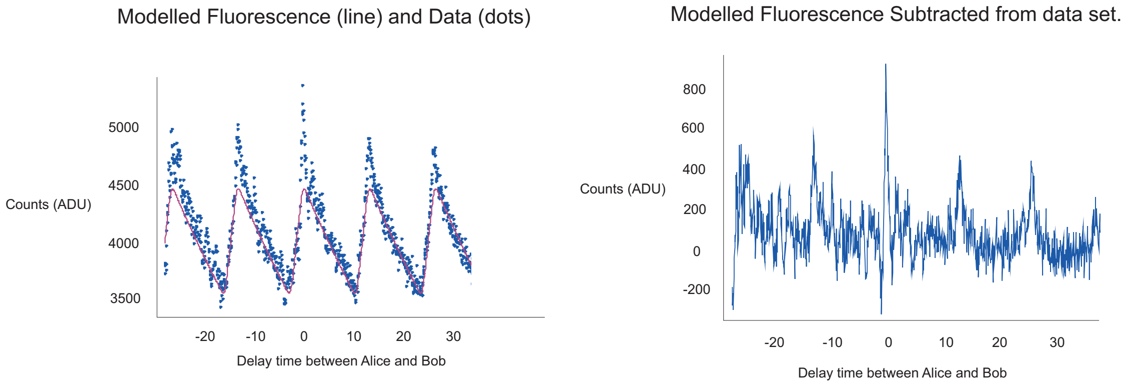
Modelled Fluorescence (line) and Data (dots)

Modelled Fluorescence Subtracted from data set.

Figure 6.18: Results from the fluorescence simulation. The left figure shows the simulated signal alongside the raw data. The right figure shows the difference between the two. The SPDC signature in the right figure is now easily distinguishable as a result of the modeled 'background' subtraction.

then subtracted from the raw data. The results are shown in figure 6.18.

The results just presented should be compared to figure 4.7 in chapter 4, which displays a clear SPDC timing signature. That result was obtained by performing a similar experiment using a similar setup with a commercially obtained sample of PPLN.

The lack of this clear signature in the present data has one main explanation. It is surmised that the basic issue is the inability of the author to predominantly excite the Bragg mode. What is apparent is that there are other physical processes that are excited, such as the fluorescence and coupling to the other available modes of the structure. Thus, when attempting to look for downconversion, it may not even be possible to excite *only* the Bragg mode in these structures. This is only a conjecture, but the fluorescence was always observed and may be unavoidable in further experiments with these structures[12].

---

[12] As it turns out, the latest sample tested after the oral defense of this thesis has shown significant improvements – very little if any fluorescence and a clear SPDC signature!

Source Comparison			
Source Description	Pair Rate (10^6/s/mW/THz)	λ_c(nm)	comment
PPKTP[95]	83	900/1300	inferred (type-0)
PPKTP [95]	250	900/1300	inferred (type-II)
Rb-PPKTP [96]	100	1316	inferred (type-II)
Microstructure fiber [97]	$0.1^{\ddagger}$	690/800	measured 4WM
PPKTP [28]	$6.3^{\ddagger 13}$	810	measured (type-II)
PPLN [98]	$3\cdot 10^{8\ddagger 14}$	1310	inferred (type-II)
PPLN [99]	$6\cdot 10^{8\ddagger 15}$	1550	inferred (type-II)

Table 6.3: Spectral Brightness of some SPDC sources in literature. ‡ means the value is inferred from the publication. ‘Inferred’ means ‘exiting waveguide’ and accounting for collection inefficiencies.

Source Comparison			
Source Description	Total Pair Rate (10^6/s/mW)	λ_c(nm)	comment
PPKTP [96]	20	1316	inferred type-II degenerate
PPKTP [100]	.12	1552	inferred type-II degenerate
PPKTP [28]	73	810	inferred type-II degenerate
PPLN [98]	15	1310	inferred type-II degenerate
PPLN [99]	100	1550	inferred type-II degenerate
BRW-AlGaAs**	1.3	1550	inferred type-0 degenerate

Table 6.4: Total Flux of some recent SPDC sources found in the literature. Inferred means ‘exiting waveguide’, and accounting for collection inefficiencies. ** is our result and comes with the caveat of requiring .1W of input power.

Theoretical Analysis

Having seen how the waveguide actually performs, it is useful to verify how the waveguide should perform. In this final section, the tools necessary for a direct calculation of the biphoton wavefunction as it applies to waveguides is presented. The discussion relies heavily on an article published by Yang et al. [101], and references their equations. The articles main use is in its full treatment of the fields that exist in an optically confining structure like that of a waveguide. This includes the effect of dispersion on the mode normalization along with a quantized pump field. The main outputs of the paper are the direct calculation of the state of the downconverted light $|\Psi\rangle$. As will be seen, this will directly facilitate an inference of the theoretical down conversion efficiency and rate of pair production from the Bragg reflection waveguide.

The state of the downconverted light is written as

$$|\Psi\rangle = e^{\beta C_{II}^{\dagger} + H.C.}|\text{vac}\rangle \tag{6.20}$$

where $|\text{vac}\rangle$ is the vacuum state, and the amplitude parameter $|\beta|^2$ will, in the limit that $|\beta| \ll 1$, be the probability of producing a pair of photons, i.e.

$$\begin{aligned} |\Psi\rangle &= |\text{vac}\rangle + \beta C_{II}^{\dagger}|\text{vac}\rangle \ldots && (6.21) \\ &= |\text{vac}\rangle + \beta|\text{II}\rangle \ldots, && (6.22) \end{aligned}$$

where

$$|\text{II}\rangle = C_{II}^{\dagger}|\text{vac}\rangle = \frac{1}{\sqrt{2}}\int dk_1 \int dk_2 \phi(k_1,k_2) c_{k_1}^{\dagger} c_{k_2}^{\dagger}|\text{vac}\rangle. \tag{6.23}$$

$C_{II}^{\dagger}$ is an operator that creates two photons and characterizes their distribution over wavevectors according to $\phi(k_1,k_2)$ via the photon creation operators $c_{k_1}^{\dagger}$ and $c_{k_2}^{\dagger}$.

In this notation, $c_{k_1}^{\dagger}$ creates a photon with a wavevector k_1 and satisfies the commutation relationships

$$[c_{k_1}^{\dagger}, c_{k_2}^{\dagger}] = 0, \tag{6.24}$$

and

$$[c_{k_1}, c_{k_2}^{\dagger}] = \delta(k_1 - k_2). \tag{6.25}$$

On its own, $|\text{II}\rangle$ is a normalized two photon state

$$\langle \text{II}|\text{II}\rangle = 1, \tag{6.26}$$

so that

$$\int dk_1 \int dk_2 |\phi(k_1, k_2)|^2 = 1. \tag{6.27}$$

The distribution $\phi(k_1, k_2)$ characterizes the biphoton wavefunction. The square of the amplitude β characterizes the probability of getting the biphoton. Thus, $\beta C_{II}^{\dagger}|\text{vac}\rangle$ gives complete information about the two photon component of the output state[16]. The biphoton wavefunction is itself decomposed into a function $\phi_p(k)$ characterizing the pump laser field and a phase matching function $S(k_1, k_2, k)$ as

$$\phi(k_1, k_2) = \frac{2\sqrt{2}\pi\alpha}{\beta} \frac{i}{\hbar} \int dk \phi_p(k) S(k_1, k_2, k) \delta(\omega - \omega_1 - \omega_2) \tag{6.28}$$

where ω, ω_1, and ω_2 are the corresponding frequencies of the pump, signal and idler modes with wavevector k, k_1, and k_2 respectively.

Restricting the forthcoming analysis to pump and down converted light that are co-directional (avoiding phase matching situations where the output photons may be counter-propagating [76]), then

$$|\text{II}\rangle = C_{II}^{\dagger}|\text{vac}\rangle = \frac{1}{\sqrt{2}} \int_0^{\infty} dk_1 \int_0^{\infty} dk_2 \phi(k_1, k_2) c_{k_1}^{\dagger} c_{k_2}^{\dagger} |\text{vac}\rangle, \tag{6.29}$$

where the limits on the integration in equation 6.29 are now from 0 to ∞.

For this thesis, the pump pulse will be modeled as a Gaussian coherent state specified by an average photon number $|\alpha|^2$ centered about a frequency ω_0 with a characteristic spectral width $\Delta\omega$. That is,

$$\tilde{\phi}_p(\omega) = \left(\sqrt{\frac{\pi}{2}}\Delta\omega\right)^{-1/2} e^{-[(\omega-\omega_0)/\Delta\omega]^2}, \tag{6.30}$$

where $\tilde{\phi}_p(\omega)$ is related to $\phi_p(k(\omega))$ as

$$\tilde{\phi}_p(\omega) = \sqrt{\frac{dk_s\omega}{d\omega}} \phi_p(k(\omega)). \tag{6.31}$$

The phase matching function $S(k_1, k_2, k)$ is re-written as follows:

$$S(k_1, k_2, k) = \sqrt{\frac{\hbar\omega\hbar\omega_1\hbar\omega_2}{(4\pi)^3\epsilon_0}} \frac{\sigma(k - k_1 - k_2)\bar{\chi}^{(2)}}{\bar{n}^3} \frac{e^{i\nu(k,k_1,k_2)}}{\sqrt{A(k, k_1, k_2)}}, \tag{6.32}$$

---

[16] keeping in mind the adherence to the conditions where the series expansion of the polarization response is valid

where $\bar{\chi}^{(2)}$ and $\bar{n}$ represent the average second order non-linear susceptibility and average index of refraction that the problem at hand admits respectively. It is worth commenting on the nature of these average parameters. It turns out that their value is a matter of choice, and so long as that choice is adhered to throughout the calculation, the form of the biphoton will remain correct and valid. Their use enables this formalism to be directly applicable to most available software packages that solve the full vector wave equation mentioned briefly in section 2.1.4.

The phase mismatch Δk is accounted for by $\sigma(k - k_1 - k_2)$ as

$$\sigma(\Delta k) = \int dz s(z) e^{i\Delta k z}, \tag{6.33}$$

where $s(z)$ conveys the z dependence of $\chi^{(2)}$. For example, in periodically poled materials $s(z)$ would alternate in sign with the poling half period. Otherwise, $s(z) = 0$ outside the interaction region, and for materials where $\chi^{(2)}(z) \to \chi^{(2)}$, $s(z) = 1$ between $-L/2$ and $L/2$, where L is the length of the non-linear crystal along the direction of propagation.

The strength of the non-linear response depends not only on the coherent response of the medium to the input pump field, but on the spatial and phase overlap of the interacting modes. The symbol $e^{i\nu(k,k_1,k_2)}$ in essence quantifies the phase overlap for the three modes specified by (k, k_1, k_2) and the symbol $A(k, k_1, k_2)$ estimates the spatial overlap of the three modes. Together they are recast as

$$\frac{e^{i\nu(k,k_1,k_2)}}{\sqrt{A(k,k_1,k_2)}} = \frac{N(k_1,k_2,k)}{\sqrt{D(k_1)D(k_2)D(k)}}, \tag{6.34}$$

where

$$N(k_1,k_2,k) = \iint dxdy \frac{\chi^{(2)}_{hij}(x,y)}{\bar{\chi}^{(2)}} e_h^{k_1}(x,y) e_i^{k_2}(x,y) e_j^{*k}(x,y) \tag{6.35}$$

and

$$D_{k'} = \iint dxdy \mathbf{e}^*_{k'}(x,y) \cdot \mathbf{e}_{k'}(x,y) \frac{n^2(x,y;\omega_{k'})}{\bar{n}^2} \frac{v_{ph}(x,y;\omega_{k'})}{v_{gr}(x,y;\omega_{k'})} \tag{6.36}$$

where $e_h^{k'}$ is the field component along the h crystal direction for the mode k', $k' \in \{k, k_1, k_2\}$, and where $\mathbf{e}_{k'}(x,y)$ is the electric field vector for the mode k' at position (x,y). The phase and group velocities for the mode are symbolized by $v_{ph}(x,y;\omega_{k'})$ and $v_{gr}(x,y;\omega_{k'})$ and are given by

$$v_{ph}(x,y;\omega_{k'}) = \frac{c}{n(x,y;\omega_{k'})} \tag{6.37}$$

$$v_{gr}(x,y;\omega_{k'}) = \frac{v_{ph}(x,y;\omega_{k'})}{1 + \frac{\omega_{k'}}{n(x,y;\omega_{k'})} \frac{\partial}{\partial \omega_{k'}} n(x,y;\omega_{k'})} \tag{6.38}$$

For situations where ω is a monotone increasing function of k for all frequencies involved (normal dispersion), the above formalism can be converted from momentum space (k) to frequency space ω as follows:

$$\tilde{\phi}(\omega_1,\omega_2) = \sqrt{\frac{dk_1}{d\omega_{k_1}}}\sqrt{\frac{dk_2}{d\omega_{k_2}}}\phi(k_1,k_2) \tag{6.39}$$

The pre-factors under the square root sign ensure that $\tilde{\phi}(\omega_1,\omega_2)$ stays normalized. $\tilde{\phi}(\omega_1,\omega_2)$ becomes

$$\tilde{\phi}(\omega_1,\omega_2) = \frac{2\sqrt{2}\pi\alpha}{\beta}\frac{i}{\hbar}\sqrt{\frac{dk_1(\omega_1)}{d\omega_1}}\sqrt{\frac{dk_2(\omega_2)}{d\omega_2}}\int d\omega\sqrt{\frac{dk(\omega)}{d\omega}}\tilde{\phi}_p(\omega)S(k_1(\omega_1),k_2(\omega_2),k(\omega))\delta(\omega-\omega_1-\omega_2). \tag{6.40}$$

The benefits of this special but realistic situation are now that the integral over frequency is trivial due to the Dirac delta function, and furthermore, the normalization condition on $\tilde{\phi}(\omega_1,\omega_2)$ (guaranteed by the normalization condition on $\phi(k_1,k_2)$) can still be used to find β.

The Delta function implies that $\omega \rightarrow \omega_1+\omega_2$, and because of this, equation (6.40) will be written in a simpler and more compact fashion as follows:

1) The prefactor terms that keep the frequency representation of the biphoton normalized will be compactly expressed as:

$$\sqrt{\frac{dk_1(\omega_1)}{d\omega_1}}\sqrt{\frac{dk_2(\omega_2)}{d\omega_2}}\sqrt{\frac{dk(\omega_1+\omega_2)}{d(\omega_1+\omega_2)}} \rightarrow G(\omega_1+\omega_2,\omega_1,\omega_2) = \mathbb{G} \tag{6.41}$$

2) The factors of $\hbar\omega$ etc. coming from the quantization will be compactly written as:

$$\sqrt{\hbar(\omega_1+\omega_2)\hbar\omega_1\hbar\omega_2} \rightarrow H(\omega_1+\omega_2,\omega_1,\omega_2) = \mathbb{H} \tag{6.42}$$

3) The function representing the pump laser field ($\tilde{\phi}_p(\omega)$) will be shortened to

$$\left(\sqrt{\frac{\pi}{2}}\Delta\omega\right)^{-1/2} e^{-[(\omega-\omega_0)/\Delta\omega]^2} \rightarrow \left(\sqrt{\frac{\pi}{2}}\Delta\omega\right)^{-1/2} \Phi_p \tag{6.43}$$

4) The phase matching function $\sigma(k-k_1-k_2)$ will be shortened to

$$\sigma(k-k_1-k_2) \rightarrow \sigma(k(\omega_1+\omega_2)-k_1(\omega_1)-k_2(\omega_2)) = \mathbb{S} \tag{6.44}$$

All remaining terms are essentially given constants or chosen constants based on the physical situation. Denoting the product of most of these constants as C'', the biphoton wavefunction of equation (6.40) can be succinctly written as

$$\tilde{\phi}(\omega_1, \omega_2) = \frac{\alpha}{\beta} C'' \mathbb{G}\mathbb{H}\Phi_p \mathbb{S} \tag{6.45}$$

where

$$C'' = \frac{i2\sqrt{2}\pi}{\hbar} \frac{L\bar{\chi}^{(2)}}{\sqrt{(4\pi)^3 \epsilon_0} \bar{n}^3} \frac{e^{i\nu(k,k_1,k_2)}}{\sqrt{A(k,k_1,k_2)}} \cdot \left(\sqrt{\frac{\pi}{2}} \Delta\omega \right)^{-1/2}. \tag{6.46}$$

This formalism will be used to calculate the expected pair production rate from Bragg reflection waveguides and will serve as a comparison to the rates obtained from experimental measurement.

6.5.3 Application to BRW waveguides

To predict the photon pair generation rate for the BRW waveguides, the theoretical formalism just described will be needed. As alluded to, this formalism is particularly useful when numerical solutions for the eigenmodes of the structure are generated. In this case, commercial software called MODE Solutions was used to generate those numerical solutions. The following analysis follows closely that of the worked example in Yang et al. [101].

To begin, the first two quantities to calculate are the phase and group velocities found in equation 6.37. All that is needed is the index profile. Because the field modes will be used later in equations 6.35 and 6.36, and since those equations involve the group and phase velocities, the group and phase velocities will only be calculated at points corresponding to the meshed structure where the field modes are calculated. The accuracy of this approach will thus depend on how well the structure is meshed.

Since the BR waveguide consists of many layers but only three materials, the dispersion of the three materials is calculated using tabulated index of refraction data from the literature [91]. The local phase and group velocities are then assigned to the point (x,y) in the profile of the BR waveguide.

Once a group velocity and phase velocity profile are created, it is necessary to see what processes are mediated by the ridge in order to choose the appropriate field components in the triple product found in equation (6.35).

Recall the non-linear susceptibility tensor $\chi^{(2)}$ for GaAs and recall that the waveguide is directed diagonally between two orthogonal crystallographic directions. The principle crystallographic directions are denoted as before by primed co-ordinates, {X′,Y′,Z′} with Z′ being the growth direction. The numerical mode solver MODE Solutions knows nothing about the underlying material and orients the waveguide to propagate in the Z direction with the X direction in the plane of the crystal and the Y direction along the growth direction.

Let the second harmonic field be $\vec{E_S}$ = (E$_{X'}$,E$_{Y'}$,E$_{Z'}$)$_S$ and the fundamental field $\vec{E_F}$ = (E$_{X'}$,E$_{Y'}$,E$_{Z'}$)$_F$ where F and S denote the fundamental and second harmonic channels that are phase matched.

In the GaAs crystal frame of reference, the following 2^{nd} order processes between the two channels are allowed:

$$E_{X'_S} \propto \chi^{(2)}_{X'Y'Z'} E_{Y'_F} E_{Z'_F} \tag{6.47}$$
$$E_{Y'_S} \propto \chi^{(2)}_{Y'Z'X'} E_{Z'_F} E_{X'_F} \tag{6.48}$$
$$E_{Z'_S} \propto \chi^{(2)}_{Z'X'Y'} E_{X'_F} E_{Y'_F} \tag{6.49}$$

A vector in the crystal reference frame can be described in the mode solver reference frame via the following transformations

$$\begin{aligned} \hat{q}_{X'} &= \frac{1}{\sqrt{2}}(\hat{q}_X - \hat{q}_Z) \\ \hat{q}_{Y'} &= \frac{-1}{\sqrt{2}}(\hat{q}_X + \hat{q}_Z) \\ \hat{q}_{Z'} &= \hat{q}_Y \end{aligned} \tag{6.50}$$

where $\hat{q}$ represents a unit vector. The outputs of the mode solver are of the form $\vec{E_S}$ = (E_X, E_Y, E_Z) and $\vec{E_F} = (E_X, E_Y, E_Z)$

Since $\chi^{(2)}_{X'Y'Z'}$=d_{14}=$\chi^{(2)}_{Y'Z'X'}$=d_{25}=$\chi^{(2)}_{Z'X'Y'}$=d_{36}=d_{eff} then equations (6.47,6.48,6.49) transform to

$$\frac{1}{\sqrt{2}}(E_X - E_Z)_S \leftarrow d_{\text{eff}} \frac{-1}{\sqrt{2}}(E_X + E_Z)_F (E_Y)_F \tag{6.51}$$
$$\frac{-1}{\sqrt{2}}(E_X + E_Z)_S \leftarrow d_{\text{eff}} (E_Y)_F \frac{1}{\sqrt{2}}(E_X - E_Z)_F \tag{6.52}$$
$$(E_Y)_S \leftarrow d_{\text{eff}} \frac{-1}{\sqrt{2}}(E_X + E_Z)_F \frac{1}{\sqrt{2}}(E_X - E_Z)_F \tag{6.53}$$

Evidently, equations (6.51)&(6.52) represent type-II SPDC where a horizontally polarized pump photon fissions into a horizontally polarized fundamental photon and a vertically polarized fundamental photon. On the other hand, equation (6.53) represents type-I SPDC where a vertically polarized pump photon fissions into two horizontally polarized pump photons.

Note that the subscripts label a single mode so that the two type-II processes require a fundamental mode that has field contributions to all three crystallographic directions.

Although in high index waveguides there can be a significant forward component to the polarization, much of the field is still directed transverse to the propagation axis. This implies that for the orientation just described, the strongest SPDC process might naturally be the third type-I process where the phase matched modes would be $\vec{E}_S \rightarrow (0, E_Y, 0)_S$ and $\vec{E}_F \rightarrow (E_X, 0, 0)_F$.

In this case the E_X component of a horizontally polarized (TE) fundamental field would decompose onto the crystal X′ and Y′ axes while the pump field would be mainly vertically polarized (TM) along the Z′ axis.

However, there are cases where the waveguide permits degeneracy. Degeneracy is useful for the fundamental fields because there are two modes there. For example, if both a TM and TE fundamental mode are degenerately phase matched to the pump field, it could be that the type-II process produces the most efficient SPDC. Here the phase matched modes would be

$$\begin{aligned} \vec{E}_S &\rightarrow (E_X, 0, 0)_S \\ \vec{E}_F^{TE} &\rightarrow (E_X, 0, 0)_F^{TE} \\ \vec{E}_F^{TM} &\rightarrow (0, E_Y, 0)_F^{TM} \end{aligned} \tag{6.54}$$

where the superscript labels the degeneracy. In contrast to the type-I process, the pump field would decompose onto either the X′ or the Y′ axis, all of the TM fundamental mode could be used in the coupling, while the other degenerate TE fundamental mode would decompose onto the Y′ / X′ axis.

Interestingly, neither of the processes just discussed were experimentally observed to produce SPDC data. This is not to say that they don't exist, just that there were significant experimental issues that needed to be overcome to observe SPDC, and when it was observed, oddly enough it pertained to a type 0 SPDC process where a vertically polarized pump photon at frequency ω down converted into pairs of vertically polarized fundamental photons at a frequency $\omega_1 = \omega_2 \approx 2\omega$. Clearly this is not allowed by the above model. Its presence was resolved in Helmly et al. [89] and has been discussed earlier in this chapter. Despite this fact, the following calculation proceeds for the type-I process, as it is more intuitive.

Code was written in MATLAB 7.5.0 R2007b to facilitate calculations. For the chosen modes, the result for the BRW structure is $D_k = 2.0573 \cdot 10^{-11}\mathrm{m}^2$ and $D_{k_1} = 1.7122 \cdot 10^{-11}\mathrm{m}^2 = D_{k_2}$

A value of $N(k_1, k_2, k) = -1.4892 \cdot 10^{-14} + i3.7220 \cdot 10^{-16}\mathrm{m}^2$ is calculated using $\bar{n} = 1$, and $\bar{\chi}^{(2)}$=100 pm/V. Recall that the choice of these average parameters is a matter of 'bookkeeping' and will not effect the validity of the results in any way.

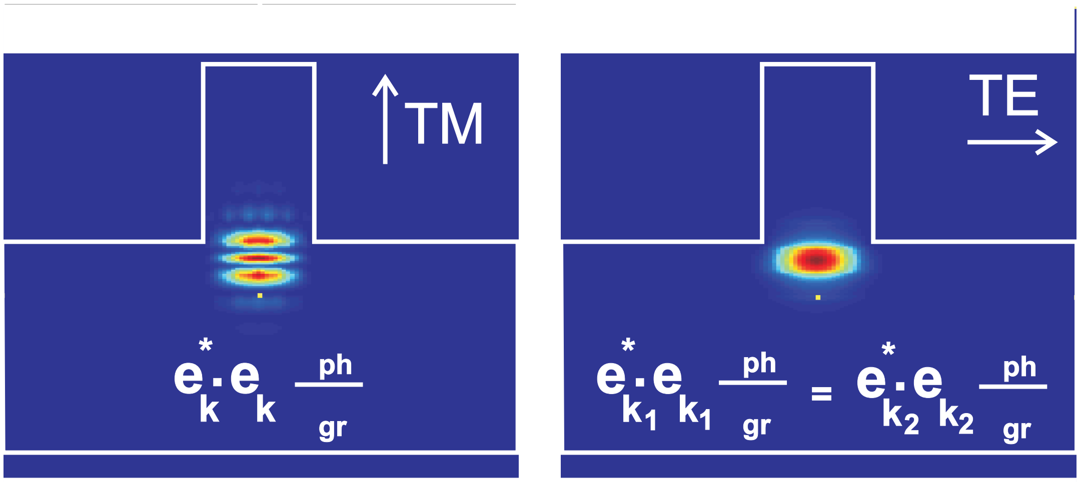

Figure 6.19: Plot of the results for equation (6.36) which calculates the quantity $D_{k'}$, a sort of generalized field normalization for such ridge waveguide structures. It involves terms such as $\mathbf{e}^*_{k'}(x,y) \cdot \mathbf{e}_{k'}(x,y)$ for $k' \in (k, k_1, k_2)$. The vertically polarized Bragg mode is on the left, while the horizontally polarized fundamental mode is shown on the right.

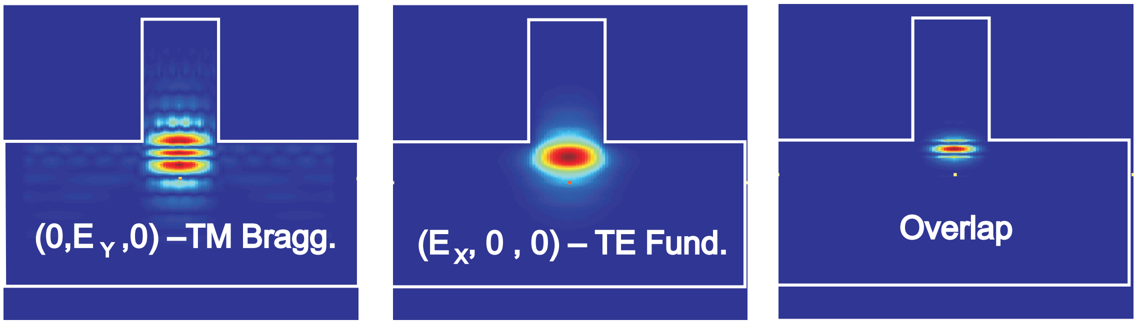

Figure 6.20: Plot of the results for equation (6.35) which essentially calculates the overlap of the field components required by the material in order to facilitate SPDC.

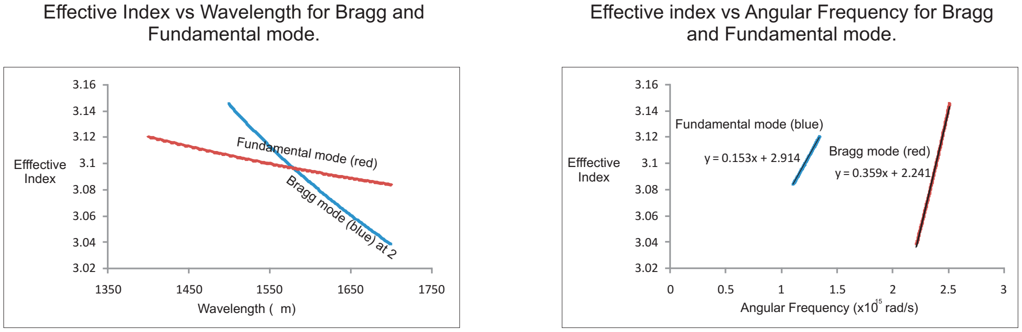

Figure 6.21: Dispersion characteristics of the Bragg mode and fundamental modes. The Bragg mode wavelength has been multiplied by two in the first graph. From the first graph, it is evident that the Bragg/Fundamental modes are phase matched somewhere in the vicinity of 783nm/1566nm.

Then the value of

$$\frac{e^{i\nu(k,k_1,k_2)}}{\sqrt{A(k,k_1,k_2)}} \approx -1.9175 \cdot 10^2 + i4.7926\frac{1}{m} \tag{6.55}$$

Since there is no periodic poling or any modulation of the second order susceptibility tensor along the direction of propagation then $s(z) = 1$ and equation (6.33) gives

$$\sigma(\Delta k) = \int_{L/2}^{L/2} dz e^{i\Delta kz} = L\mathrm{sinc}(\Delta kL/2). \tag{6.56}$$

In the experiment, the Bragg mode is inherently phase matched to the fundamental mode, so to investigate the behaviour of Δk, both the Bragg mode and the fundamental mode were followed numerically over a range of wavelengths to determine their dispersion. In contrast to the ridge guide analyzed by Yang et al. [101], the dispersion of the modes of interest around the phase matched frequency is much more severe.

From figure 6.21, a linear approximation for the dispersion relation n(ω) is used. Let n(ω)=M$_S\omega$+B$_S$, n(ω_1)=M$_{F_1}\omega_1$+B$_{F_1}$ and, n(ω_2)=M$_{F_2}\omega_2$+B$_{F_2}$, where M$_S$ is the slope of the line for n(ω), and where M$_{F_1}$ and M$_{F_2}$ are the slopes for the lines relating to n(ω_1) and n(ω_2). If the fundamental modes are degenerate (as is the case here), then M$_{F_1}$ =M$_{F_2}$ and the intercept B$_{F_1}$ =B$_{F_2}$.

The phase mismatch can be re-written explicitly as a function of the Bragg and fundamental frequencies as

$$\begin{align}
\Delta k &= k(\omega)-(k_1(\omega_1)+k_2(\omega_2)) \tag{6.57}\\
&= \frac{1}{c}\left[\omega n(\omega)-\omega_1 n(\omega_1)-\omega_2 n(\omega_2)\right] \tag{6.58}\\
&= \frac{1}{c}\Big[M_S\omega^2-M_F(\omega_1^2+\omega_2^2)+B_S\omega-B_F(\omega_1+\omega_2)\Big] \tag{6.59}\\
&= \frac{1}{c}\Big[(\Delta M+M_F)\omega^2-M_F(\omega_1+\omega_2)^2+2M_F(\omega_1\omega_2)+(\Delta B+B_F)\omega-B_F(\omega_1+\omega_2)\Big] \tag{6.60}\\
&= \frac{1}{c}\Big[(\Delta M)(\omega_1+\omega_2)^2+2M_F(\omega_1\omega_2)+(\Delta B)(\omega_1+\omega_2)\Big] \tag{6.61}\\
& \tag{6.62}
\end{align}$$

where B$_{F_1}$=B$_{F_2}$=B$_F$ so that ΔB = B$_S$-B$_F$, and where M$_{F_1}$=M$_{F_2}$=M$_F$ so that ΔM = M$_S$-M$_F$, and where we have used the fact that ω=$\omega_1+\omega_2$ from the impending delta function.

For the numerical simulation, M$_S$=3.59·10$^{(-16)}$s/rad, B$_S$=2.241, M$_F$=1.53·10$^{(-16)}$s/rad, and B$_F$=2.914. This implies that ΔB=2.241-2.914=-0.673 and ΔM=2.06·10$^{(-16)}$s/rad.

Keeping the delta function in mind, the phase matching term $S(k_1(\omega_1), k_2(\omega_2), k(\omega))$ can be rewritten as

$$S(\omega_1,\omega_2)=C\mathbb{H}\mathbb{S}, \tag{6.63}$$

where the constant C is

$$C=\frac{L\bar{\chi}^{(2)}}{\sqrt{4\pi)^3\epsilon_0\bar{n}^3}}\frac{e^{i\nu(k,k_1,k_2)}}{\sqrt{A(k,k_1,k_2)}}, \tag{6.64}$$

and $\mathbb{H}$ has already been defined as before,

$$\mathbb{H}=\sqrt{\hbar(\omega_1+\omega_2)\hbar\omega_1\hbar\omega_2} \tag{6.65}$$

and where the phase matching information contained in the sinc function is symbolized by $\mathbb{S}$:

$$\mathbb{S}=\mathrm{sinc}((\frac{1}{c}\Big[(\Delta M)(\omega_1+\omega_2)^2+2M_F(\omega_1\omega_2)+(\Delta B)(\omega_1+\omega_2)\Big])L/2). \tag{6.66}$$

The product of the pump spectral function and the phase matching function then becomes :

$$\tilde{\phi}_p(\omega_1+\omega_2)S(\omega_1,\omega_2)=C'\Phi_p\mathbb{H}\mathbb{S}. \tag{6.67}$$

where

$$C'=\frac{L\bar{\chi}^{(2)}}{\sqrt{(4\pi)^3\epsilon_0\bar{n}^3}}\frac{e^{i\nu(k,k_1,k_2)}}{\sqrt{A(k,k_1,k_2)}}\cdot\left(\sqrt{\frac{\pi}{2}}\Delta\omega\right)^{-1/2} \tag{6.68}$$

The prefactors in the frequency representation of the biphoton wavefunction can be evaluated using the linear approximations for the behaviour of the mode index vs mode frequency. Then $\frac{d}{d\omega_1}k_1(\omega_1)=\frac{d}{d\omega_2}k_2(\omega_2)=\frac{1}{c}(2\mathrm{M}_F\omega_F+\mathrm{B}_F)$ and $\frac{d}{d\omega}k(\omega)=\frac{1}{c}(2\mathrm{M}_S\omega+\mathrm{B}_S)$ so that $\mathbb{G}$ is found to be

$$\mathbb{G} = \sqrt{\frac{(2M_F\omega_1 + B_F)(2M_F\omega_2 + B_F)(2M_S(\omega_1 + \omega_2) + B_S)}{c^3}} \tag{6.69}$$

and then the biphoton wavefunction of equation (6.40) is

$$\tilde{\phi}(\omega_1, \omega_2) \quad = \quad C''\frac{\alpha}{\beta}\mathbb{G}\Phi_p\mathbb{H}\mathbb{S}, \tag{6.70}$$

where the constant C″ is

$$C'' = \frac{i2\sqrt{2}\pi}{\hbar}\frac{L\bar{\chi}^{(2)}}{\sqrt{(4\pi)^3\epsilon_0}\bar{n}^3}\frac{e^{i\nu(k,k_1,k_2)}}{\sqrt{A(k,k_1,k_2)}}\cdot\left(\sqrt{\frac{\pi}{2}}\Delta\omega\right)^{-1/2}. \tag{6.71}$$

The normalization condition

$$\int_0^\infty d\omega_1 \int_0^\infty d\omega_2 |\tilde{\phi}(\omega_1, \omega_2)|^2 = 1 \tag{6.72}$$

will allow a determination of β and thereby the probability of producing a photon pair.

There are three important physical processes that now need consideration. The first is absorption, the second is the ability of the waveguide to support biphotons at frequencies below the cut-off frequency, and the third is energy conservation. Although equation (6.73) formally allows both the signal and idler photons to *both* go out to infinity together (clearly not conserving energy with the pump photon) there will be a natural suppression from the overlap of the phase matching function with the pump. The second point concerns the waveguide cut-off frequency where below a certain frequency there do not exist real solutions to the wave equation for the waveguide in question. Simulations predict a cutoff wavelength of around 3.8μm or a cut-on frequency of around 80 THz. The first process is neglected but should be kept in mind as an ultimate termination on the bandwidth of the biphotons.

Including the effects of the cutoff frequency, the normalization can be re-written as

$$\int_{\omega_c}^\infty d\omega_1 \int_{\omega_c}^\infty d\omega_2 |\tilde{\phi}(\omega_1, \omega_2)|^2 = 1. \tag{6.73}$$

To optimally choose the pump wavelength the condition

$$\mathrm{sinc}(\Delta k(\omega_1, \omega_2)) = 0 \tag{6.74}$$

needs to be satisfied. This implies that

$$(\Delta M)(\omega_1 + \omega_2)^2 + 2M_F(\omega_1\omega_2) + (\Delta B)(\omega_1 + \omega_2) = 0 \tag{6.75}$$

Optimizing for the condition when the biphoton is frequency degenerate ($\omega_1 = \omega_2 = \omega_0/2$), then

$$\omega_0 = -\frac{\Delta B}{\Delta M + M_F/2} \tag{6.76}$$

and, it will be assumed that the line width $\Delta\omega$ is approximately a factor of 10^4 smaller than ω_0.

In the experiment, the waveguide length was L≈1700μm, so the constant C″ is found to be approximately -2.9995·10^{20} -i1.1992·10^{22} $m^{3/2}J^{-3/2}s^{1/2}$.

A plot of the main contributing functions to the biphoton wavefunction, $\phi(\omega_1, \omega_2)$ and sinc($\Delta k(\omega_1, \omega_2)$), are shown in figure (6.22) along with a plot of the square of the wavefunction neglecting β and α.

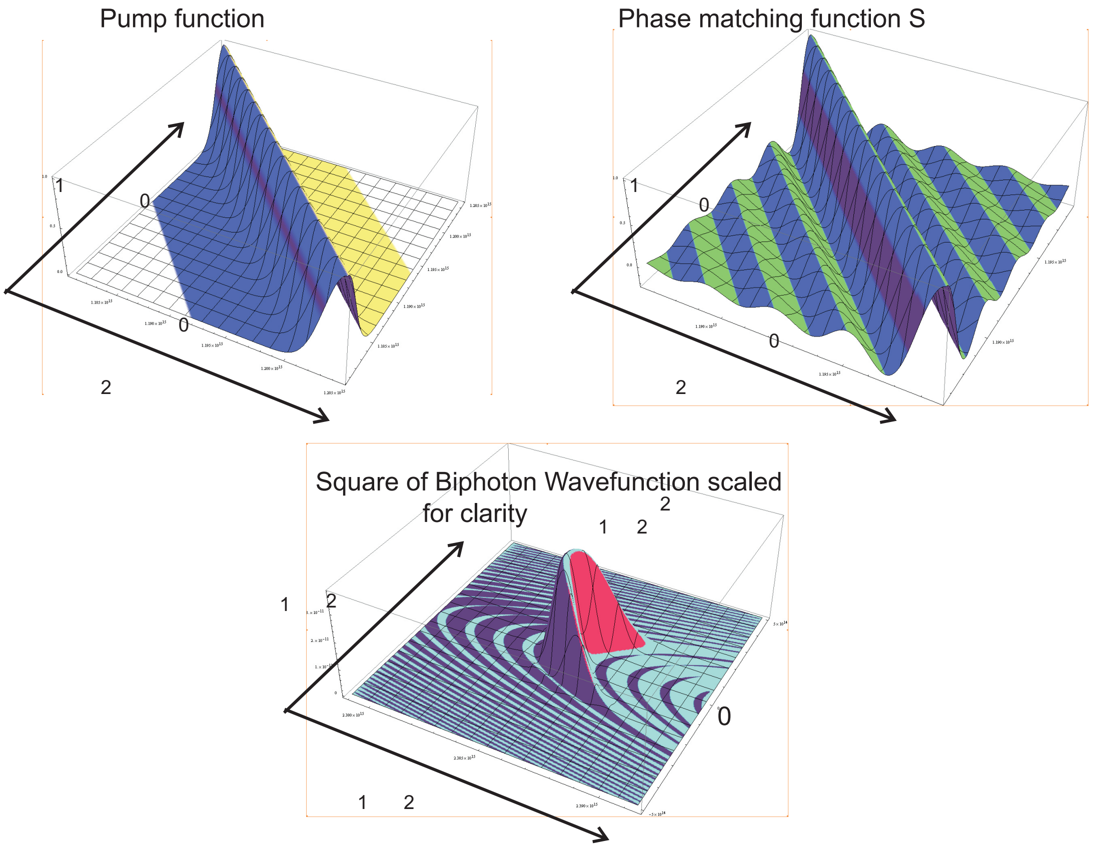

Figure 6.22: Plot of the results for $\phi_p(\omega_1, \omega_2)$, sinc($\Delta k(\omega_1, \omega_2)$), and —G($\omega_1, \omega_2$)$\phi_p(\omega_1, \omega_2)$H($\omega_1, \omega_2$)S($\omega_1, \omega_2$)|^2 which is proportional to the square of the biphoton wavefunction.

Numerical integration techniques are used to evaluate equation (6.73) giving the probability (β^2) of getting the biphoton as

$$\beta^2 = 2.91 \cdot 10^{-10} \alpha^2 \tag{6.77}$$

Since α^2 represents the number of pump photons, and as there are two photons per down conversion event, the number of down converted photons is predicted to be $2\beta^2$=$5.8 \cdot 10^{-10} \alpha^2$. The efficiency of SPDC is then ϵ=$2.91 \cdot 10^{-10}$.

Summary

Having provided a detailed calculation of the type-I down conversion process in Bragg reflection waveguides, the relative parameters for the type-0 process is presented as a comparison in table 6.5. The type-0 process is not so intuitive, because it involves a projection of the forward field component of the fundamental mode, which although weak, does have a reasonable overlap with the vertical Bragg mode.

	Process Comparison	
Variable	Type I TM-TE	Type 0 TM-TM
Phase Matching Wavelength	1580nm	1571nm
D_k	$2.06 \cdot 10^{-11}\mathrm{m}^2$	$2.06 \cdot 10^{-11}\mathrm{m}^2$
D_{k_1}	$1.71 \cdot 10^{-11}\mathrm{m}^2$	$1.78 \cdot 10^{-11}\mathrm{m}^2$
D_{k_2}	$1.71 \cdot 10^{-11}\mathrm{m}^2$	$1.78 \cdot 10^{-11}\mathrm{m}^2$
$N(k_1, k_2, k)$	$-1.49 \cdot 10^{-14} + i3.7 \cdot 10^{-16}\mathrm{m}^2$	$-4.6 \cdot 10^{-15} + i1.21 \cdot 10^{-16}\mathrm{m}^2$
$\frac{e^{i\nu(k,k_1,k_2)}}{\sqrt{A(k,k_1,k_2)}}$	$-1.92 \cdot 10^2 + i4.8\ \frac{1}{m}$	$-0.57 \cdot 10^2 + i1.5\ \frac{1}{m}$
M_S	$3.6 \cdot 10^{-16}$s/rad	$3.6 \cdot 10^{-16}$s/rad
B_S	2.241	2.241
M_F	$1.53 \cdot 10^{(-16)}$s/rad	$1.55 \cdot 10^{(-16)}$s/rad
B_F	2.914	2.92
ΔB	-0.673	-0.674
ΔM	$2.06 \cdot 10^{-16}$s/rad	$2.04 \cdot 10^{-16}$s/rad
SPDC Efficiency	$2.91 \cdot 10^{-10}$	$2.65 \cdot 10^{-11}$

Table 6.5: A table that allows a comparison of the relative values of similar variables calculated for Type-I and Type-0 processes for AlGaAs BRW's.

6.6 Future work, Open questions and Conclusions

Comparison - Theory and Experiment

It is useful to compare the theoretically predicted SPDC efficiency for both the type-I and type-0 processes with the experimentally observed efficiency. The first point to notice is the prediction that the type-I process is more efficient. This was not observed as the type-0 process seemed to dominate the upconversion process and was the only process that produced observable photon pairs. This remains largely an open question and requires further investigation. The second point to notice is the discrepancy between the predicted type-0 efficiency ($2.65 \cdot 10^{-11}$) and the efficiency inferred from observations in the lab ($9.8 \cdot 10^{-9}$). The most obvious reasons for this discrepancy are 1) the simulation parameters are not truly indicative of the actual sample parameters, and 2) the waveguide loss remains uncertain - recall that the Fabry Perot method for determining this parameter failed and a much weaker measurement of the overall insertion loss was used to infer the waveguide loss. For example, if the waveguide loss was a factor of 7 better (more akin to what is observed by the group at the University of Toronto), then the prediction would be almost in agreement with what was observed.

Future work

The following steps are what the author would take to continue an investigation of SPDC from BRW waveguides.

The steps would be to:

- Investigate the origins of the fluorescence.
- Improve the stability of the experimental setup.
- Repeat the data set on waveguide 12 (type-0 SPDC) with a bandpass filter.
- Find a waveguide with a strong type-I process and employ polarization filtering at the output.
- Investigate the efficacy of creating a proper Bragg mode to mediate the expected SPDC process. Similar work has been attempted by a spanish group led by J.P Torres. [102].
- Modify the growth method to observe its effect on the fluorescence. Additionally, perhaps design a taper into the waveguide to facilitate better coupling to the Bragg mode.

Open Questions

The BRW waveguide requires a Bragg mode to excite SPDC. To integrate this structure with a laser diode on a single substrate will require a BRW laser that emits the same Bragg mode. This may or may not be a difficult task, but is a possible line of future investigation if laboratory methods fail to produce better results.

There are also a few experimental puzzles left to be sorted: The first is the failure to observe significant Fabry Perot fringes (see appendix figures A.1, A.2) during attempts to ascertain the waveguide loss. The second is the lack of similar data produced by the other waveguides on the chip. I hope to try to have answers for these questions in the near future.

Conclusions

The author is confident that type-0 spontaneous parametric down conversion (SPDC) has been observed for the first time in ridge Bragg Reflection Waveguides (BRW). In fact, a stronger and clearer SPDC signal has subsequently been observed by the author in a 3^{rd} generation BRW sample recently obtained after the oral defense of this thesis. Furthermore, many of the other questions have been resolved, and it is unfortunate that the data cannot be included herein. Briefly: 1) the fluorescence is all but non-existent, 2)the stability of 8 hours is no longer necessary because 3) the signal is much stronger due to a design change the increases the overlap of the Bragg and fundamental modes. The data for this experiment is expected to be published in the near future.

7 WAVEGUIDE SOURCES OF ENTANGLED PHOTONS

This chapter is strictly an outlook chapter. It is meant to show a future direction for waveguide sources. Two different proposals are discussed and both envision the production of an entangled biphoton state using waveguides. The first design fuses together two differently oriented waveguides with similar type-I phase matching conditions. Entanglement is created by simultaneously facilitating the down conversion process in both waveguides. The second design involves a single waveguide that trespasses two QPM regions with distinctly different type-II phase matching conditions. Entanglement is created by controlling the temperature of the host crystal. At the present time, there are no quantitative results that validate the ability of the proposed concepts to generate entanglement, but upconversion experiments have successfully been performed in both cases.

7.1 Proposal 1

Brief Introduction

As mentioned in the introduction, a common technique to produce non degenerate pairs (pairs with different frequencies) of polarization entangled photons involves the use of a Sagnac interferometer. This technique involves pumping a non-linear crystal with two counter propagating beams of intense light that is type-I phase matched to light centered at roughly half the pump frequency. In one arm of the interferometer, the optical input and output beams are rotated 90 degrees. Output light from both arms are combined at a polarizing beam splitter (PBS) where information about the polarization of the light exiting the PBS is unknown and quantum entanglement is generated. Light at the pump wavelength is filtered out of both PBS outputs and the signal is split by wavelength. The Sagnac source has its drawbacks. Because it is bi-directional, the optical elements need to be tailored for both wavelengths, and versions that involve fiber coupled crystals suffer from phase instabilities.

It would be desirable to have a fiber coupled source that can produce such a state in a stable manner. Ideally, one would pump unidirectionally, thereby eliminating dual wavelength optics. The following design has the potential to satisfy these requirements. The design is referred to as a sandwich source. The design is pending a formal patent, the provisional of which has been filed at the United States Patent and Trademark Office under United States Provisional Patent Application No. 61/412,010. I am the sole author of the provisional filing.

What is Claimed

The invention claims that a polarization entangled biphoton state similar to equation 1.8 can be produced with two down conversion crystals that are sandwiched on top of one another by focussing pump light at the interface between the two crystals. The wavelength of the pump is chosen to be at approximately the second harmonic wavelength with respect to the wavelength of the desired output biphoton state. The crystals support type-I phase / quasi-phase matching of the input wavelength to the wavelength of the biphoton state. In order to produce entanglement, the two crystals must have their respective down conversion photons emitted with polarizations that are *not parallel* to each other. Optimally, one of the down conversion crystals needs to produce down conversion photons with polarization *perpendicular* to those produced by the other crystal. An embodiment of this invention involves the use of waveguides to increase the efficiency of production of the entangled state, although it is not necessary. This particular embodiment is described herein.

Conceptual Design

The name of the invention is called a ‘waveguide sandwich source’. To demonstrate the invention claimed - namely that of a type-I polarization entangled photon source – it is imagined that the invention comprises of the following: two down conversion crystals each fashioned with what will be called ‘component’ waveguides.

The waveguide in the first crystal will be called ‘component waveguide 1’. The surface of component waveguide 1 is oriented such that the down converted photons produced in component waveguide 1 have polarizations that are co-linear with the surface normal. Denoting the normal direction to the surface of component waveguide 1 as *Vertical*, then this waveguide can produce photons in the state $|V_i, V_s\rangle$, where the subscript s, i denote the designation of ‘signal’ and ‘idler’ photons.

The waveguide in the second crystal will be called ‘component waveguide 2’. The surface of component waveguide 2 is oriented such that the down converted photons produced in component waveguide 2 have polarizations that are in the plane of the surface. Denoting the plane of the surface of component waveguide 2 as *Horizontal*, then this waveguide can produce photons in the state $|H_i, H_s\rangle$.

The invention sandwiches the two crystals together, one on top of the other, such that component waveguide 1 and component waveguide 2 are physically on top of one another. They are aligned optically to form a single ‘composite waveguide’. As these component waveguides combine to form the composite waveguide, then the composite waveguide can produce pairs of photons in either of the states $|V_i, V_s\rangle$ or $|H_i, H_s\rangle$.

Figure 7.1 shows a conceptual view of the waveguide sandwich source and how entanglement is generated.

Obstacles

To create the aforementioned *entangled* state using the *composite* waveguide it is important to remove distinguishing information concerning which *component* waveguide was responsible for creating any particular photon pair.

One way to do this is to make the component waveguides as identical as possible. To this end, the present embodiment of the invention involves both crystals of the same material with the same phase matching condition.

It may not be the case, but it is expected that even if the two component waveguides were fabricated from the same material, there may still exist some differences, particularly in the phase matching condition. One way to compensate for this difference is to temperature tune the phase matching condition for one of the two component waveguides. This can be accomplished with a thermo-electric cooler or a suitably built oven that will need to be attached to one of the down conversion crystals.

In that embodiment (where the same material is used and the same phase matching condition is employed), then, as a consequence of the type-I condition, the required input or 'pump' light necessary to excite the down conversion process needs to be linearly polarized in some direction. Because there is an approximate 90 degree rotation of the physical orientation of one of the component waveguides with respect to the other, then to excite *both* component waveguides simultaneously, the pump light for the composite waveguide needs to be polarized approximately half way between that required to optimally excite either of the individual component waveguides. This direction will be referred to as the 45 degree direction.

It is envisioned that a second piece of distinguishing information concerning where the photon pair was produced might arise from the different spatial location of the optical mode. This arises from the physically distinct location of the component waveguides.

One way to remove such spatial information is to couple both of the modes in the emerging light into a single mode fiber, thereby eliminating this 'location' information. A second more elegant way would be to fabricate the component waveguides in such a way that the composite waveguide behaves as a single mode waveguide. This is an additional claim that pertains to the embodiment of the invention – that the component waveguides be made such that the core size (the region where the light is confined) of each component waveguide be made approximately half of its normal size (normal size for single mode operation). This would make the composite waveguide ”sandwich mode” more closely approximate that of a single mode waveguide and would thereby optimize the coupling efficiency to single mode fiber on the output.

Thirdly, there may arise a dispersion condition whereby the photons produced in one of the component waveguides will travel at a different speed than those produced in the other component waveguide. This effect is expected to be minimal. Such modal

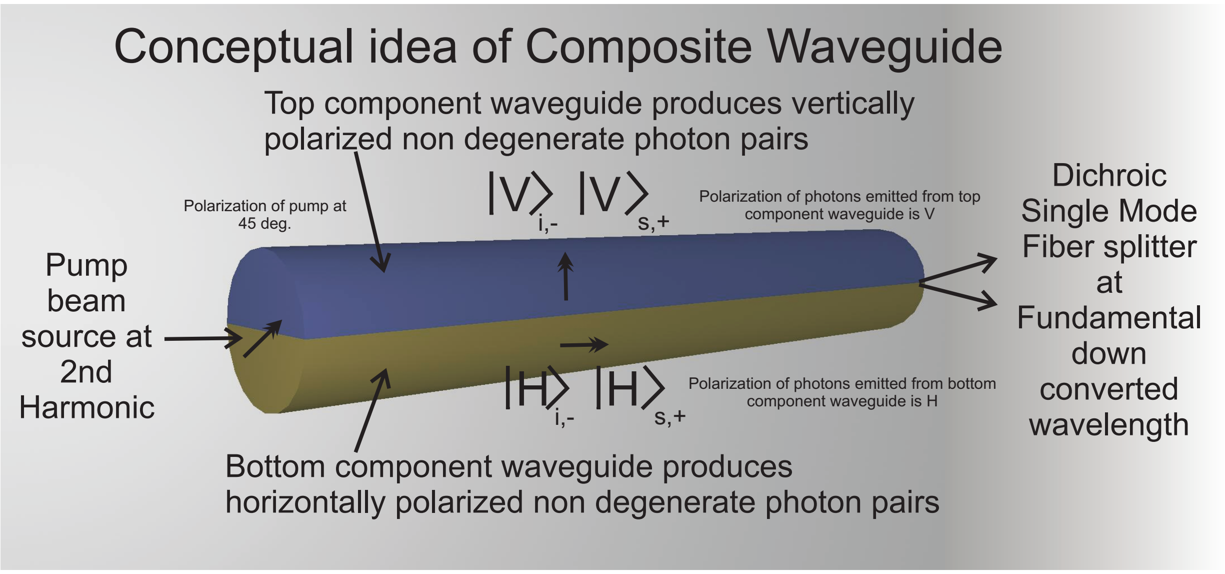

Figure 7.1: A cross section or side view of the composite waveguide. This diagram shows how the sandwich source works. At the input, the pump injects 45 degree polarized light, stimulating the down conversion reaction in both component waveguides. The output is collected into a single mode fiber, the pump wavelength is filtered out, and the down conversion light is split based on wavelength. In each arm of the splitter it is impossible know if the photon there has vertically polarized or horizontally polarized light. Only after it has been properly measured can this knowledge be obtained. This is the crucial component for generating entanglement between the photons in the pair. See the conceptual design for a more detailed explanation.

dispersion can be compensated for by using additional optical elements.

7.1.1 Comments

What makes the invention compact and stable is that the composite waveguide can be directly fiber coupled at both of the crystal facets. By using a standard dichroic fiber splitter on the output, the desired non-degenerate entangled state can be achieved, almost completely (save the non-linear crystal) in fiber and in a phase stable manner. The result is an extremely simple, robust and compact source of non-degenerate polarization entangled photons. Below are some further comments on the design:

- The design is not limited to waveguides, but can be used with bulk material, where instead of a waveguide, light could be focussed approximately over the center of the two mating surfaces between the two crystals.

- The design is not limited to periodically poled lithium niobate, but to any mate-

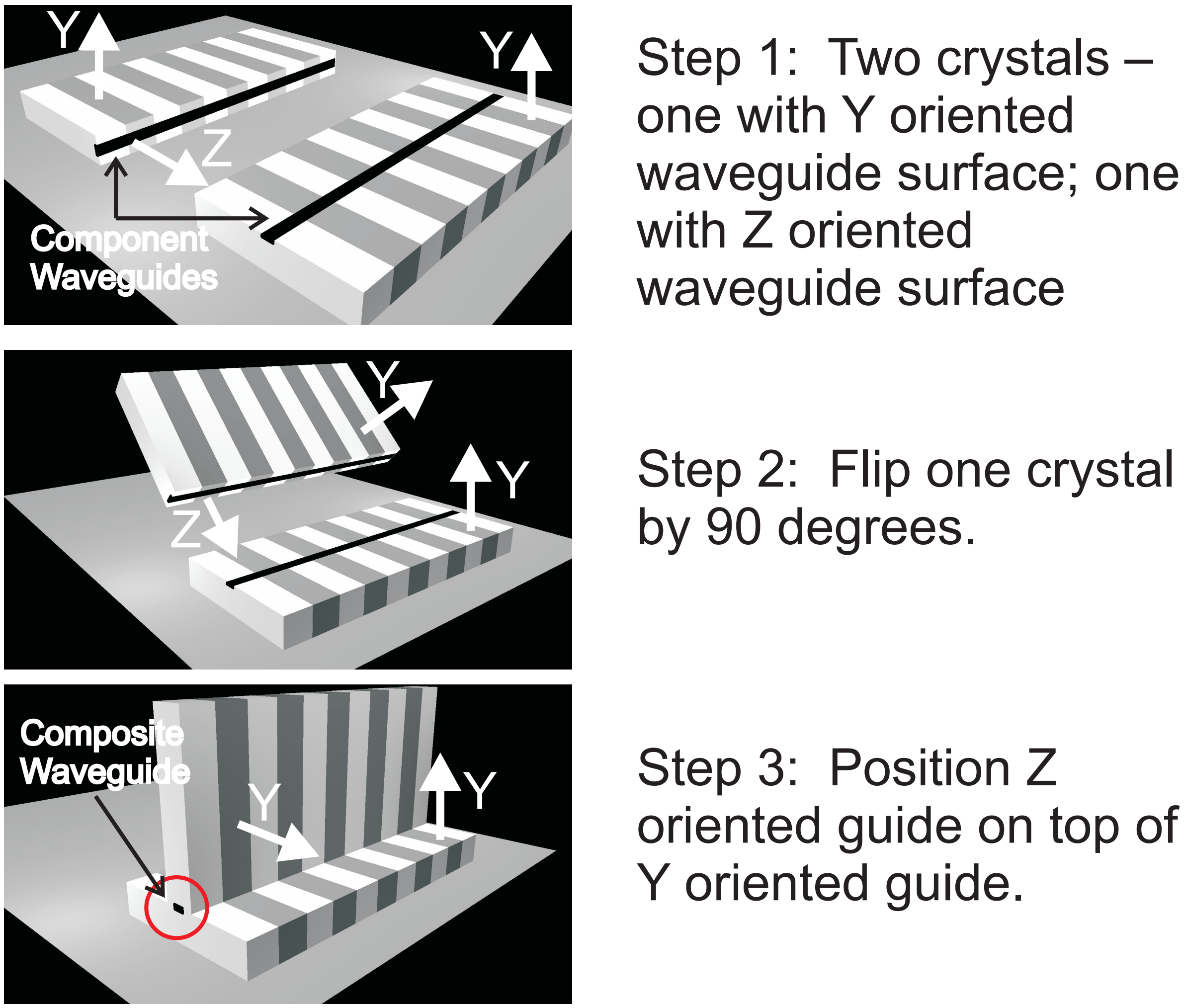

Figure 7.2: A diagram of how to build the source. In this particular diagram, the idea is conveyed with the 'T' shape, but is not necessary. Conceptually, the steps are to fabricate two component waveguides on two perpendicular sides of a non-linear crystal cut for type 1 phase matching of the second harmonic to the fundamental light. Here the crystal is shown with a periodic pattern of light and dark to mimic the notion of a periodically poled quasi-phase matched crystal. Flip one crystal by 90 degrees and place it on top of the other crystal such that the component waveguides align directly on top of each other for the length of the crystal. This forms a composite waveguide. If the composite waveguide supports both the fundamental and second harmonic light, then the composite waveguide can in principle be directly fiber coupled (or free space coupled) and pumped unidirectionally with second harmonic light polarized at 45 degrees between the expected output polarizations of the down converted light from each component waveguide.

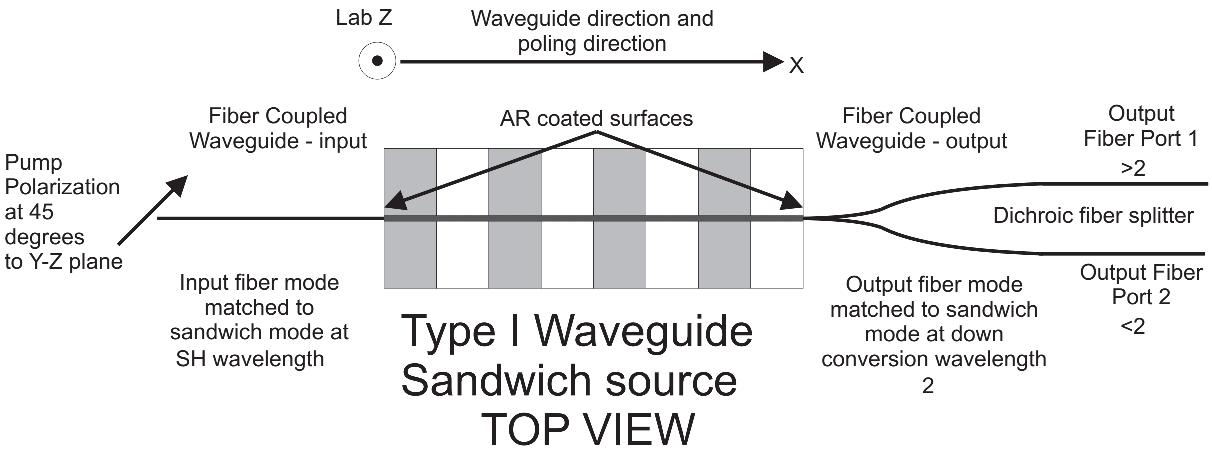

Figure 7.3: For the worked example, this is a diagram of what the source might actually look like with fiber coupling. The top view is given, but the waveguides are drawn in, although they would not be visible as they are shown here. By polarizing the input light half way (45 degrees) between the optimal directions for each component crystal, the phase matching conditions for SPDC in both the upper and lower component crystals will be satisfied. There will be negligible dispersive effects or phase instability. The output light is split deterministically by wavelength and the differing colors will be polarization entangled.

rial, such as periodically poled pottasium titanyl phosphate (PPKTP), or Beta-Barium Borate (BBO). So long as the medium can achieve the required phase matching.

- The technique deals with type-I phase matching and can be degenerate or non-degenerate, the only issue in the degenerate case is that the pairs can only be split probabilistically (most likely using a 50/50 beam splitter or cascaded splitters).
- The device can be tuned by appropriately choosing the dimensions of the component waveguides and their inherent orientation. For example, there will likely be an optimal waveguide profile for each component (most likely smaller than a standard waveguide) so that the composite waveguide behaves more like a single waveguide and couples better to a single mode fiber.
- If one of the component waveguides phase matches differently than the other, the difference can rectified by changing the temperature of the component waveguide. As the component guide will be in intimate contact with the other component guide, there will likely be an optimal phase matching temperature for both component guides.
- Possible design parameters could conceivably require mating one component waveguide from one material to another from a different material.
- As a final comment, the pump wavelength also needs to be tuned to optimally excite the component waveguides. Optimal in the sense of producing the most useful ‘visible’ rate of entangled photon pairs. For example if coupling is better for one of the component guides, the input polarization can be tuned away from 45 degrees to favor the lesser coupled waveguide in order to balance the process.

7.2 Proposal 2

The concept behind this proposal was only recently brought to the authors attention by Thomas Jennewein. A first attempt at the design has already been implemented with a waveguide fabricated in a periodically poled Potassium Titanyl Phosphate (PPKTP) crystal. This material has a significant bilinear susceptibility and is a standard material in many down conversion sources. As opposed to Lithium Niobate, it is used mainly for shorter wavelength conversion from 800nm → 400nm. In the present implementation, it contains two regions that are each furnished with their own different poling period. The crystal mediates Quasi-Phase Matched (QPM) non-degenerate type-II down conversion and incorporates the concepts illustrated in figure 2.1 and figure 2.2 found in the discussion concerning temperature tuning at the end of chapter 2.

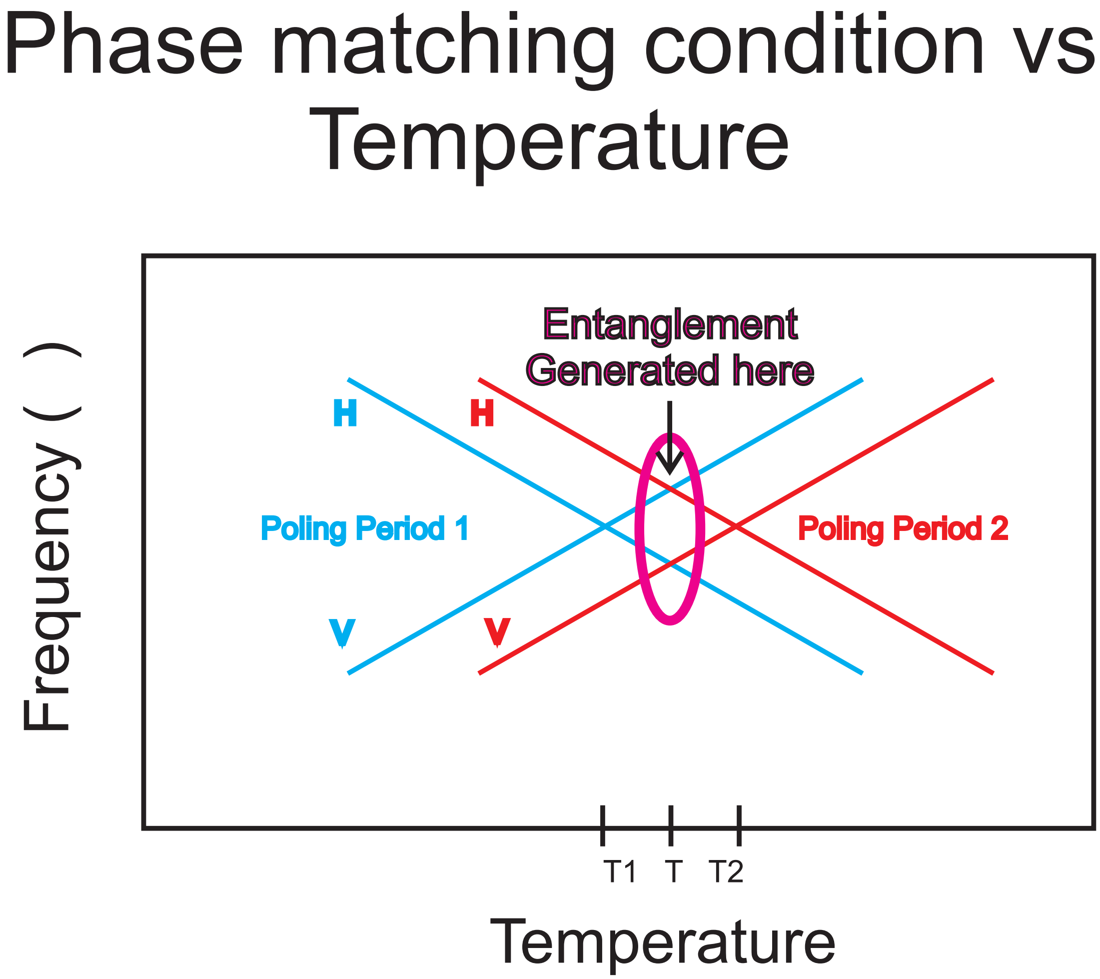

Figure 7.4: Diagram of the conceptual type-II phase matching conditions for a crystal with two regions of different poling periods. For some temperature T1, the type-II phase matching condition is degenerate for poling period 1 while for another temperature T2, the type-II phase matching condition is degenerate for poling period 2. Away from these temperatures, the degeneracy is lifted. Thus, between T1 and T2, there exists a temperature T at which the now non-degenerate signal and idler photons generated by either region will be indistinguishable in frequency. This can lead to entanglement.

Temperature tuning can be used to generate entangled photons in the following manner: Consider a periodically poled down conversion crystal with *two* regions distinguished only by their different *different* poling periods. Such a crystal will have two corresponding sets of frequency vs temperature relationships for both signal and idler SPDC photons pertaining to both of the poling periods. The situation is depicted in figure 7.4.

Without loss of generality, imagine a temperature where the section of the crystal containing the *first* poling period creates frequency *degenerate* type-II SPDC photons. Call this temperature T1. Similarly, imagine a different temperature where the section of the crystal containing the *second* poling period also creates frequency *degenerate* type-II SPDC photons. Denote this temperature as T2.

Recall that there is a strict energy correlation between the signal and idler photon. Further, that the slope of the frequency vs temperature curve for the signal and idler photons relating to either poling period must be equal and opposite. Then for some temperature T between T1 and T2, if an SPDC process occurred, information regarding the state of polarization of the signal and idler photons (which are now frequency *non-degenerate*) will be unavailable. At this temperature, the biphoton state can attain the maximally entangled state given in equation 1.8.

Preliminary Results - Up Conversion

As alluded to, a doubly poled PPKTP sample was obtained and placed in a third waveguiding setup. The main difference between the third setup and those previously discussed are that the third setup contains optics that are designed for the wavelength range 400nm-800nm. The sample was designed by T. Jennewein using permittivity data from ADVR. The poling periods were chosen to facilitate non-degenerate SPDC at 778nm and 843nm at a temperature of 300K. Energy conservation implies that to generate SPDC at these wavelengths, the pump wavelength needs to be approximately 404nm. It is schematically shown in figure 7.5 along with a sample spectrum of the second harmonic output measured at room temperature. The latter picture was obtained by scanning the pump laser over the range 804nm - 820nm. There are clearly two resonant peaks at approximately 403nm and 407nm and they are roughly consistent with the measurements characterizing the room temperature behaviour of the sample made by the manufacturer. The presence of two peaks confirmed the double poling period.

Obstacles

Some immediate foreseeable obstacles that can potentially degrade the entanglement are

- The spectral power output of the SPDC process from both regions at the interme-

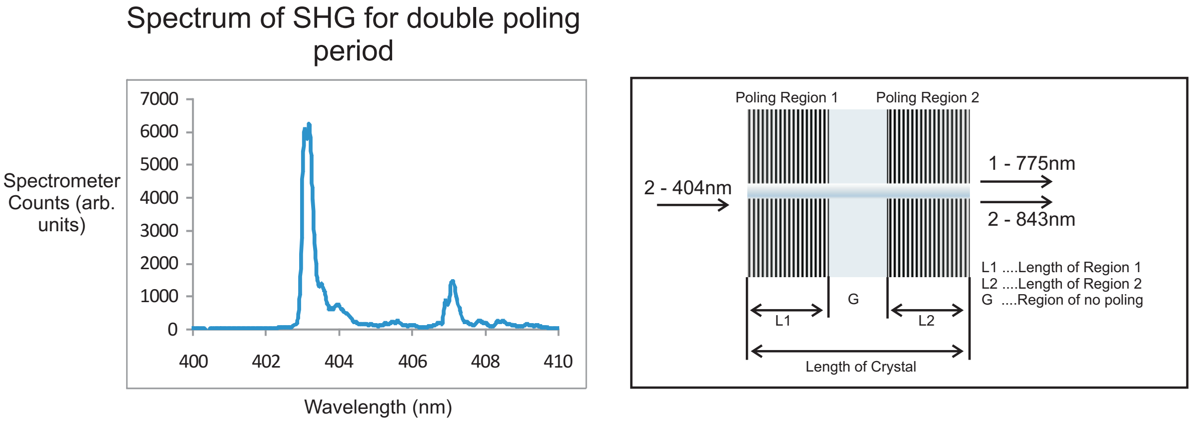

Figure 7.5: Spectrum of the second harmonic output from the double poled PPKTP sample from ADVR. Phase matching resonances are around 403nm and 407nm.

diate temperature T should maximally overlap. If the temperature T facilitates the second process more than the first, the entanglement will degrade. This is related to how locally similar the two sets of dispersion curves are. For similar poling periods, this is expected to be not too detrimental.

- Polarization information may exist if the dispersion between signal and idler is significant enough to produce a definite time ordering (based on the polarization) of the emitted photons.

Outlook

Much more work still needs to be done to verify the intended properties. Already, a custom oven has been fashioned to control the crystal temperature, and it is hoped that in the near future, the main laser can be doubled to enable SPDC experiments. Nonetheless, the design seems to be a very promising step in the development of future compact entangled photon sources.

8 CONCLUDING REMARKS

To summarize, the two main results of the thesis were :

1) The proposal to solve the phase matching problem - Directional Quasi Phase Matching, and 2) The experimental evidence for Spontaneous Parametric Down Conversion from ridge Bragg Reflection Waveguides. In addition, two novel proposals for entangled photon sources were also very briefly discussed.

Overall, the thesis influences those that wish to develop stronger sources of photonic quantum information resources. It should really be viewed as a platform from which to base future investigation. Exploiting the directional dependence of the bilinear susceptibility is definitely worth a second look, if not in AlGaAs, but in other less restrictive material systems where the coherence length is more forgiving. For instance, the creation of spectrally pure photons in Lithium Niobate using DQPM techniques poses relatively milder challenges than a similar endeavor in AlGaAs. On the other hand, if one can control the fabrication parameters and demonstrate the effectiveness of AlGaAs in wavelength conversion, its relatively simple structure makes it an extremely attractive and cheap phase matching solution.

The main experimental result - the small but weak SPDC signature measured from ridge BRWs - while not groundbreaking, should really be reviewed by all groups interested in pursuing BRWs as viable sources of photon pairs. The modal phase matching offered by the BRW structure is perhaps the best approach to developing an integrated single or entangled photon source. Indeed, the latest results that have occurred in our lab after the oral defense of this thesis have shown significant improvements in the design and fabrication. So much so that the same measurements made with the same setup have produced dramatically better results. BRWs therefore *need* to be investigated further to properly evaluate their potential in integrated wavelength conversion processes. If SPDC can be better controlled in BRWs, it opens up a wealth of possibilities. As an example, it is not hard to imagine creating on chip photonic structures out of BRWs that mimic the interferometric schemes mentioned. Coupled with a properly tuned diode laser would yield a fully integrated entangled photon source.

Envisioning the long term future success of BRWs, the waveguide sandwich and double poling period proposals for entangled photons will ultimately only be an intermediate step. However, their maturity and the wealth of experience already gathered in those material systems will make them exceedingly useful in the short term.

BIBLIOGRAPHY

[1] K.K. Wong. *Properties of Lithium Niobate*. Institution of Engineering and Technology, 2002. xii, 50

[2] Paul G. Kwiat, Klaus Mattle, Harald Weinfurter, Anton Zeilinger, Alexander V. Sergienko, and Yanhua Shih. New high-intensity source of polarization-entangled photon pairs. *Phys. Rev. Lett.*, 75(24):4337–4341, Dec 1995. 1, 2

[3] E. Bocquillon, C. Couteau, M. Razavi, R. Laflamme, and G. Weihs. Coherence measures for heralded single-photon sources. *Phys. Rev. A*, 79(3):035801, Mar 2009. 1

[4] C. Erven, C. Couteau, R. Laflamme, and G. Weihs. Entangled quantum key distributionover two free-space optical links. *Opt. Express*, 16(21):16840–16853, 2008. 1

[5] Charles H. Bennett, Gilles Brassard, Claude Crépeau, Richard Jozsa, Asher Peres, and William K. Wootters. Teleporting an unknown quantum state via dual classical and einstein-podolsky-rosen channels. *Phys. Rev. Lett.*, 70(13):1895–1899, Mar 1993. 1

[6] Harry Buhrman, Richard Cleve, John Watrous, and Ronald de Wolf. Quantum fingerprinting. *Phys. Rev. Lett.*, 87(16):167902, Sep 2001. 1

[7] Charles H. Bennett and Stephen J. Wiesner. Communication via one- and two-particle operators on einstein-podolsky-rosen states. *Phys. Rev. Lett.*, 69(20):2881–2884, Nov 1992. 1

[8] E. Knill, R. Laflamme, and G. J. Milburn. A scheme for efficient quantum computation with linear optics. *Nature*, 409(7):46–52, 2001. 1

[9] W. H. Louisell, A. Yariv, and A. E. Siegman. Quantum fluctuations and noise in parametric processes. i. *Phys. Rev.*, 124(6):1646–1654, Dec 1961. 2

[10] J. P. Gordon, W. H. Louisell, and L. R. Walker. Quantum fluctuations and noise in parametric processes. ii. *Phys. Rev.*, 129(1):481–485, Jan 1963. 2

[11] Morton H. Rubin, David N. Klyshko, Y. H. Shih, and A. V. Sergienko. Theory of two-photon entanglement in type-ii optical parametric down-conversion. *Phys. Rev. A*, 50(6):5122–5133, Dec 1994. 2, 23

[12] D. N. Klyshko. Coherent Photon Decay in a Nonlinear Medium. *Soviet Journal of Experimental and Theoretical Physics Letters*, 6:23–+, July 1967. 2

[13] B. R. Mollow and R. J. Glauber. Quantum theory of parametric amplification. i. *Phys. Rev.*, 160(5):1076–1096, Aug 1967. 2

[14] B. R. Mollow and R. J. Glauber. Quantum theory of parametric amplification. ii. *Phys. Rev.*, 160(5):1097–1108, Aug 1967. 2

[15] S. E. Harris, M. K. Oshman, and R. L. Byer. Observation of tunable optical parametric fluorescence. *Phys. Rev. Lett.*, 18(18):732–734, May 1967. 2

[16] Douglas Magde and Herbert Mahr. Study in ammonium dihydrogen phosphate of spontaneous parametric interaction tunable from 4400 to 16 000 å. *Phys. Rev. Lett.*, 18(21):905–907, May 1967. 2

[17] David C. Burnham and Donald L. Weinberg. Observation of simultaneity in parametric production of optical photon pairs. *Phys. Rev. Lett.*, 25(2):84–87, Jul 1970. 2

[18] C. K. Hong and L. Mandel. Higher-order squeezing of a quantum field. *Phys. Rev. Lett.*, 54(4):323–325, Jan 1985. 2

[19] C. K. Hong and L. Mandel. Theory of parametric frequency down conversion of light. *Phys. Rev. A*, 31(4):2409–2418, Apr 1985. 2

[20] C. K. Hong, Z. Y. Ou, and L. Mandel. Measurement of subpicosecond time intervals between two photons by interference. *Phys. Rev. Lett.*, 59(18):2044–2046, Nov 1987. 2

[21] R. Ghosh, C. K. Hong, Z. Y. Ou, and L. Mandel. Interference of two photons in parametric down conversion. *Phys. Rev. A*, 34(5):3962–3968, Nov 1986. 2

[22] T. H. MAIMAN. Stimulated optical radiation in ruby. *Nature*, 187:493–494, Aug 1960. 4

[23] P. A. Franken, A. E. Hill, C. W. Peters, and G. Weinreich. Generation of optical harmonics. *Phys. Rev. Lett.*, 7(4):118–119, Aug 1961. 4

[24] D. A. Kleinman. Theory of second harmonic generation of light. *Phys. Rev.*, 128(4):1761–1775, Nov 1962. 4

[25] J. A. Armstrong, N. Bloembergen, J. Ducuing, and P. S. Pershan. Interactions between light waves in a nonlinear dielectric. *Phys. Rev.*, 127(6):1918–1939, Sep 1962. 4, 52

[26] Agata M. Branczyk, T. C. Ralph, Wolfram Helwig, and Christine Silberhorn. Optimised generation of heralded fock states using parametric down conversion. 2009. 4

[27] M.M. Fejer, G.A. Magel, D.H. Jundt, and R.L. Byer. Quasi-phase-matched second harmonic generation: tuning and tolerances. *Quantum Electronics, IEEE Journal of*, 28(11):2631 –2654, nov. 1992. 5, 52

[28] Marco Fiorentino, Sean M. Spillane, Raymond G. Beausoleil, Tony D. Roberts, Philip Battle, and Mark W. Munro. Spontaneous parametric down-conversion in periodically poled ktp waveguides and bulk crystals. *Opt. Express*, 15(12):7479–7488, 2007. 5, 118

[29] G. Leo, V. Berger, C. OwYang, and J. Nagle. Parametric fluorescence in oxidized algaas waveguides. *J. Opt. Soc. Am. B*, 16(9):1597–1602, 1999. 5

[30] Luigi Scaccabarozzi, M. M. Fejer, Yijie Huo, Shanhui Fan, Xiaojun Yu, and James S. Harris. Enhanced second-harmonic generation in algaas/alxoy tightly confining waveguides and resonant cavities. *Opt. Lett.*, 31(24):3626–3628, Dec 2006. 5

[31] A. S. Helmy, B. Bijlani, and P. Abolghasem. Phase matching in monolithic bragg reflection waveguides. *Opt. Lett.*, 32(16):2399–2401, 2007. 5, 89, 94

[32] A. Helmy, P. Abolghasem, J. Stewart Aitchison, B. Bijlani, J. Han, B. Holmes, D. Hutchings, U. Younis, and S. Wagner. Recent advances in phase matching of second-order nonlinearities in monolithic semiconductor waveguides. *Laser and Photonics Reviews*, pages 1–15, Sep 2010. 5

[33] R. Hanbury Brown and R. Q. Twiss. Correlation between photons in two coherent beams of light. *Nature*, 177:27–29, Jan 1956. 6

[34] P. Grangier, G. Roger, and A. Aspect. Experimental Evidence for a Photon Anticorrelation Effect on a Beam Splitter: A New Light on Single-Photon Interferences. *EPL (Europhysics Letters)*, 1(4):173–179, February 1986. 6

[35] A. Burlakov, D. Klyshko, S. Kulik, and M. Chekhova. Fourth-order interference between independent biphotons. *JETP Letters*, 69:831–838, 1999. 10.1134/1.568098. 10

[36] Barry C. Sanders. Entangled coherent states. *Phys. Rev. A*, 45(9):6811–6815, May 1992. 10

[37] Yoon-Ho Kim, Maria V. Chekhova, Sergei P. Kulik, Morton H. Rubin, and Yanhua Shih. Interferometric bell-state preparation using femtosecond-pulse-pumped spontaneous parametric down-conversion. *Phys. Rev. A*, 63(6):062301, May 2001. 10

[38] Marco Fiorentino, Gaétan Messin, Christopher E. Kuklewicz, Franco N. C. Wong, and Jeffrey H. Shapiro. Generation of ultrabright tunable polarization entanglement without spatial, spectral, or temporal constraints. *Phys. Rev. A*, 69(4):041801, Apr 2004. 10

[39] Taehyun Kim, Marco Fiorentino, and Franco N. C. Wong. Phase-stable source of polarization-entangled photons using a polarization sagnac interferometer. *Phys. Rev. A*, 73(1):012316, Jan 2006. 10

[40] Robert W. Boyd. *Nonlinear Optics, Third Edition*. Academic Press, 3 edition, April 2008. 19, 62

[41] Zhaoming Zhu and Thomas Brown. Full-vectorial finite-difference analysis of microstructured optical fibers. *Opt. Express*, 10(17):853–864, 2002. 23

[42] Timothy E. Keller and Morton H. Rubin. Theory of two-photon entanglement for spontaneous parametric down-conversion driven by a narrow pump pulse. *Phys. Rev. A*, 56(2):1534–1541, Aug 1997. 23

[43] Hannes Hubel, Deny R. Hamel, Alessandro Fedrizzi, Sven Ramelow, Kevin J. Resch, and Thomas Jennewein. Direct generation of photon triplets using cascaded photon-pair sources. *Nature*, 466:601–603, Jul 2010. 26

[44] R. S. Weis and T. K. Gaylord. Lithium niobate: Summary of physical properties and crystal structure. *Applied Physics A: Materials Science Processing*, 37:191–203, 1985. 10.1007/BF00614817. 48

[45] Koichiro Nakamura, Jonathan Kurz, Krishnan Parameswaran, and M. M. Fejer. Periodic poling of magnesium-oxide-doped lithium niobate. *Journal of Applied Physics*, 91(7):4528 –4534, April 2002. 50

[46] Dongfeng Xue and Kenji Kitamura. An estimation of nonlinear optical properties of lithium niobate family ferroelectrics by the chemical bond model. *Japanese Journal of Applied Physics*, 42(Part 1, No. 9B):6230–6233, 2003. 50

[47] J. L. Jackel, C. E. Rice, and J. J. Veselka. Proton exchange for high-index waveguides in linbo3. *Applied Physics Letters*, 41(7):607 –608, October 1982. 51

[48] Torben Veng and Torben Skettrup. Dilute-melt, proton-exchange slab waveguides in linbo3: a new fabrication and characterization method. *Appl. Opt.*, 36(24):5941–5948, 1997. 51

[49] Yu. N. Korkishko, V. A. Fedorov, T. M. Morozova, F. Caccavale, F. Gonella, and F. Segato. Reverse proton exchange for buried waveguides in linbo3. *J. Opt. Soc. Am. A*, 15(7):1838–1842, 1998. 51

[50] M. Goodwin and C. Stewart. Proton-exchanged optical waveguides in y-cut lithium niobate. *Electronics Letters*, 19(6):223 –224, 17 1983. 51

[51] J.L. Jackel, C.E. Rice, and J.J. Veselka. Composition control in proton-exchanged linbo3. *Electronics Letters*, 19(10):387 –388, 12 1983. 51

[52] K.K. Loi, E.Y.B. Pun, and P.S. Chung. Proton-exchange optical waveguides in z-cut linbo3 using toluic acid. *Electronics Letters*, 28(6):546 –548, 1992. 51

[53] Jayaraman Senthil Selvan, Masatoshi Fujimura, and Toshiaki Suhara. Fabrication of zn-indiffused linbo_3 optical waveguides by diffusing sol–gel spin-coated zno film at low-pressure atmosphere. *Japanese Journal of Applied Physics*, 43(8A):5313–5315, 2004. 51

[54] M. Yamada, N. Nada, M. Saitoh, and K. Watanabe. First-order quasi-phase matched linbo3 waveguide periodically poled by applying an external field for efficient blue second-harmonic generation. *Applied Physics Letters*, 62(5):435 – 436, February 1993. 51

[55] G. D. Miller. *Periodically poled lithium niobate: Modeling, fabrication, and nonlinear optical performance*. PhD thesis, STANFORD UNIVERSITY, 1998. 52

[56] Robert G. Batchko, Dennis R. Weise, Tomas Plettner, Gregory D. Miller, Martin M. Fejer, and Robert L. Byer. Continuous-wave 532-nm-pumped singly resonant optical parametric oscillator based on periodically poled lithium niobate. *Opt. Lett.*, 23(3):168–170, 1998. 52

[57] Zhensong Cao, Ling Han, Wanguo Liang, Lunhua Deng, Huan Wang, Changqing Xu, Weijun Zhang, Zhiben Gong, and Xiaoming Gao. Ultrabroadband tunable continuous-wave difference-frequency generation in periodically poled lithium niobate waveguides. *Opt. Lett.*, 32(13):1953–1955, 2007. 53

[58] R. T. Horn and G. Weihs. Directional Quasi-Phase Matching in Curved Waveguides. *ArXiv e-prints*, August 2010. 60

[59] Zhenshan Yang, Philip Chak, Alan D. Bristow, Henry M. van Driel, Rajiv Iyer, J. Stewart Aitchison, Arthur L. Smirl, and J. E. Sipe. Enhanced second-harmonic generation in algaas microring resonators. *Opt. Lett.*, 32(7):826–828, 2007. 60, 61

[60] A. M. Brańczyk, A. Fedrizzi, T. C. Ralph, and A. G. White. Engineered optical nonlinearity for a quantum light source. *ArXiv e-prints*, May 2010. 61, 68, 69, 77

[61] P. P. Absil, J. V. Hryniewicz, B. E. Little, P. S. Cho, R. A. Wilson, L. G. Joneckis, and P.-T. Ho. Wavelength conversion in gaas micro-ring resonators. *Opt. Lett.*, 25(8):554–556, 2000. 61

[62] Yannick Dumeige and Patrice Féron. Whispering-gallery-mode analysis of phase-matched doubly resonant second-harmonic generation. *Phys. Rev. A*, 74(6):063804, Dec 2006. 61

[63] C. van Dam, L.H. Spiekman, F.P.G.M. van Ham, F.H. Groen, J.J.G.M. van der Tol, I. Moerman, W.W. Pascher, M. Hamacher, H. Heidrich, C.M. Weinert, and M.K. Smit. Novel compact polarization converters based on ultra short bends. *Photonics Technology Letters, IEEE*, 8(10):1346 –1348, oct. 1996. 69

[64] S.S.A. Obayya, B.M.A. Rahman, K.T.V. Grattan, and H.A. El-Mikati. Analysis of polarisation rotation in cascaded optical waveguide bends. *Optoelectronics, IEE Proceedings -*, 149(2):75 –80, apr. 2002. 69

[65] Henghua Deng, D.O. Yevick, and S.K. Chaudhuri. Bending characteristics of asymmetric soi polarization rotators. *Photonics Technology Letters, IEEE*, 17(10):2113 – 2115, oct. 2005. 69

[66] L.H. Spiekman, Y.S. Oei, E.G. Metaal, F.H. Groen, P. Demeester, and M.K. Smit. Ultrasmall waveguide bends: the corner mirrors of the future? *Optoelectronics, IEE Proceedings -*, 142(1):61 –65, feb. 1995. 69

[67] A. Jiang, S. Shi, G. Jin, and D. W. Prather. Performance analysis of three dimensional high index contrast dielectric waveguides. *Optics Express*, 12:633–+, February 2004. 69

[68] Richard Espinola, R. Ahmad, F. Pizzuto, Michael Steel, and Richard Osgood. A study of high-index-contrast 90 degree waveguide bend structures. *Opt. Express*, 8(9):517–528, 2001. 69

[69] M. Austin and P. Flavin. Small-radii curved rib waveguides in gaas/gaalas using electron-beam lithography. *Lightwave Technology, Journal of*, 1(1):236 – 240, mar. 1983. 69

[70] R.J. Deri, E. Kapon, and L.M. Schiavone. Bend losses in gaas/algaas optical waveguides. *Electronics Letters*, 23(16):845–847, 1987. 69

[71] Maite Volatier, David Duchesne, Roberto Morandotti, Richard Ars, and Vincent Aimez. Extremely high aspect ratio gaas and gaas/algaas nanowaveguides fabricated using chlorine icp etching with n2-promoted passivation. *Nanotechnology*, 21(13), 2010. 70

[72] S. Adachi, Institution of Electrical Engineers, and INSPEC (Information service). *Properties of aluminium gallium arsenide*. EMIS datareviews series. IEE, INSPEC, 1993. 78

[73] R. Dingle, W. Wiegmann, and C. H. Henry. Quantum states of confined carriers in very thin $al_xga_{1-x}as$-gaas-$al_xga_{1-x}as$ heterostructures. *Phys. Rev. Lett.*, 33(14):827–830, Sep 1974. 85

[74] Ichiro Shoji, Takashi Kondo, Ayako Kitamoto, Masayuki Shirane, and Ryoichi Ito. Absolute scale of second-order nonlinear-optical coefficients. *J. Opt. Soc. Am. B*, 14(9):2268–2294, 1997. 85

[75] A. Fiore, E. Rosencher, V. Berger, N. Laurent, N. Vodjdani, and J. Nagle. Huge birefringence in oxidized gaas/alas optical waveguides for phase-matched nonlinear frequency conversion. pages 231 – 232, jun. 1996. 85

[76] S. Ducci, L. Lanco, J.-P. Likforman, X. Marcadet, J.A.W. van Houwelingen, H. Zbinden, G. Leo, and V. Berger. Counterpropagating twin photons in the telecom range: a narrow-bandwidth semiconductor source. pages 1 –1, jun. 2007. 85, 120

[77] C. F. Dewey and L. O. Hocker. Enhanced nonlinear optical effects in rotationally twinned crystals. *Applied Physics Letters*, 26(8):442 –444, apr. 1975. 85

[78] D. E. Thompson, J. D. McMullen, and D. B. Anderson. Second-harmonic generation in GaAs 'stack of plates' using high-power CO2 laser radiation. *Applied Physics Letters*, 29:113–115, July 1976. 85

[79] A. S. Helmy. Phase matching using bragg reflection waveguides for monolithic nonlinear optics applications. *Opt. Express*, 14(3):1243–1252, 2006. 86

[80] Pochi Yeh and Amnon Yariv. Bragg reflection waveguides. *Optics Communications*, 19(3):427 – 430, 1976. 86, 90

[81] Pochi Yeh, Amnon Yariv, and Chi-Shain Hong. Electromagnetic propagation in periodic stratified media. i. general theory. *J. Opt. Soc. Am.*, 67(4):423–438, 1977. 86

[82] Brian R. West and Amr S. Helmy. Properties of the quarter-wave bragg reflection waveguide: theory. *J. Opt. Soc. Am. B*, 23(6):1207–1220, 2006. 86, 90, 91

[83] R. K. Chang, J. Ducuing, and N. Bloembergen. Dispersion of the optical nonlinearity in semiconductors. *Phys. Rev. Lett.*, 15(9):415–418, Aug 1965. 88

[84] S. Bergfeld and W. Daum. Second-harmonic generation in gaas: Experiment versus theoretical predictions of $\chi^{(2)}_{xyz}$. *Phys. Rev. Lett.*, 90(3):036801, Jan 2003. 88

[85] S. Adachi. Gaas, alas and alxga1-x as: material parameters for use in research and device applications. *J. Appl. Phys.*, 58(3):R1, 1985. 88

[86] R. G. Kaufman, G. R. Hulse, D. J. Vezzetti, A. L. Moretti, K. A. Stair, G. P. Devane, and T. E. Bird. Measurement of the refractive index of alxga1-xas and the mode indices of guided modes by a grating coupling technique. *Journal of Applied Physics*, 75(12):8053 –8059, jun. 1994. 88

[87] Payam Abolghasem, Junbo Han, Bhavin J. Bijlani, Arghavan Arjmand, and Amr S. Helmy. Continuous-wave second harmonic generation in bragg reflectionwaveguides. *Opt. Express*, 17(11):9460–9467, 2009. 89

[88] Jun-Bo Han, Payam Abolghasem, Dongpeng Kang, Bhavin J. Bijlani, and Amr S. Helmy. Difference-frequency generation in algaas bragg reflection waveguides. *Opt. Lett.*, 35(14):2334–2336, 2010. 89

[89] Payam Abolghasem, Junbo Han, Bhavin J. Bijlani, and Amr S. Helmy. Type-0 second order nonlinear interaction in monolithic waveguides of isotropic semiconductors. *Opt. Express*, 18(12):12681–12689, Jun 2010. 89, 94, 125

[90] Bhavin J. Bijlani and Amr S. Helmy. Bragg reflection waveguide diode lasers. *Opt. Lett.*, 34(23):3734–3736, 2009. 89

[91] S. Gehrsitz, F. K. Reinhart, C. Gourgon, N. Herres, A. Vonlanthen, and H. Sigg. The refractive index of al[sub x]ga[sub 1 - x]as below the band gap: Accurate determination and empirical modeling. *Journal of Applied Physics*, 87(11):7825–7837, 2000. 95, 123

[92] P. Abolghasem, Junbo Han, B.J. Bijlani, A. Arjmand, and A.S. Helmy. Highly efficient second-harmonic generation in monolithic matching layer enhanced

al_xga_{1-x} as bragg reflection waveguides. *Photonics Technology Letters, IEEE*, 2009. 100

[93] Marco Ravaro, Jean-Pierre Likforman, Sara Ducci, Vincent Berger, and Giuseppe Leo. Parametric generation in algaas/alox waveguides: Performances and perspectives. In *Conference on Lasers and Electro-Optics/Quantum Electronics and Laser Science Conference and Photonic Applications Systems Technologies*, page CThC1. Optical Society of America, 2007. 103

[94] S. Tanzilli, H. De Riedmatten, H. Tittel, H. Zbinden, P. Baldi, M. De Micheli, D.B. Ostrowsky, and N. Gisin. Highly efficient photon-pair source using periodically poled lithium niobate waveguide. *Electronics Letters*, 37(1):26 –28, January 2001. 115

[95] A versatile waveguide source of photon pairs for chip-scale quantum information processing. *Opt Express*, 17(8):6727–40, 2009. 118

[96] Tian Zhong, Franco N. Wong, Tony D. Roberts, and Philip Battle. High performance photon-pair source based on a fiber-coupled periodically poled ktiopo4 waveguide. *Opt. Express*, 17(14):12019–12030, Jul 2009. 118

[97] J. Fan, M. D. Eisaman, and A. Migdall. Quantum state tomography of a fiber-based source of polarization-entangled photon pairs. *Opt. Express*, 15(26):18339–18344, Dec 2007. 118

[98] A. Martin, V. Cristofori, P. Aboussouan, H. Herrmann, W. Sohler, D. B. Ostrowsky, O. Alibart, and S. Tanzilli. Integrated optical source of polarization entangled photons at 1310 nm. *Opt. Express*, 17(2):1033–1041, Jan 2009. 118

[99] Go Fujii, Naoto Namekata, Masayuki Motoya, Sunao Kurimura, and Shuichiro Inoue. Bright narrowband source of photon pairs at optical telecommunication wavelengths using a type-ii periodically poled lithium niobate waveguide. *Opt. Express*, 15(20):12769–12776, Oct 2007. 118

[100] P. G. Evans, R. S. Bennink, W. P. Grice, T. S. Humble, and J. Schaake. Bright source of spectrally uncorrelated polarization-entangled photons with nearly single-mode emission. *Phys. Rev. Lett.*, 105(25):253601, Dec 2010. 118

[101] Zhenshan Yang, Marco Liscidini, and J. E. Sipe. Spontaneous parametric down-conversion in waveguides: A backward heisenberg picture approach. *Phys. Rev. A*, 77(3):033808, Mar 2008. 119, 123, 127

[102] Gabriel Molina-Terriza, Stefano Minardi, Yana Deyanova, Clara I. Osorio, Martin Hendrych, and Juan P. Torres. Control of the shape of the spatial mode function of photons generated in noncollinear spontaneous parametric down-conversion. *Phys. Rev. A*, 72(6):065802, Dec 2005. 132

[103] Sareh Taebi, Mohammadreza Khorasaninejad, and Simarjeet Singh Saini. Modified fabry-perot interferometric method for waveguide loss measurement. *Appl. Opt.*, 47(35):6625–6630, 2008. 155

Fabry Perot Loss Estimates

Linear Loss

Linear loss in a waveguide describes the amount of light lost as a function of distance along the waveguide propagation direction. There are essentially two reasons for why a waveguide exhibits linear loss. The main reason is due to non-uniformity of the index of refraction over the spatial mode profile of the propagating wave. This arises from variations in the physical dimensions of the structure (e.g. sidewall roughness) *along the direction of propagation*, or weak confinement (allowing the mode to extend into the cladding). Scattering from non-uniformities or point defects within the material represents the other main source of loss.

The Fabry-Perot (FP) technique is a relatively simple method that allows the experimentalist to quantify the linear loss of a waveguide. If the end facets of the waveguide reflect enough of the waveguide mode, then a measurable Fabry-Perot cavity is formed. For certain wavelengths the cavity will act as a resonator and constructively interfere, while for others, destructive interference will occur. If the loss is assumed wavelength independent, which is reasonable over a few nm , then the amount of interference will depend on the roundtrip linear loss in the guide. Thus a measurement of the transmission intensity vs wavelength should be related to the intrinsic loss per unit distance of the waveguide.

The main difficulty facing the experimenter is how to separate the linear loss in the waveguide from the reflectivity estimates of the facet. Estimates can be significant if the linear loss is small. Ideas on how to modify the technique to avoid this have been put forward [103], but for the purposes of this thesis, the reflectivities are theoretically calculated. The benefits of the FP technique are that calculated loss is independent of the coupling efficiency.

For a waveguide of length L, the total linear loss in the waveguide is given by

$$G = e^{-\alpha L} \tag{A.1}$$

where the linear loss coefficient (α) is given by

$$\alpha = -\frac{1}{L} ln\left(\frac{1}{R}\frac{\sqrt{r}-1}{\sqrt{r}+1}\right) \tag{A.2}$$

Here,r is the ratio of the maximum to minimum transmission intensity, and R is the facet reflectivity.

For incident light that is perpendicular to the facet, the reflectivity of the facet is given by

$$R = \left(\frac{n_{\text{eff}} - 1}{n_{\text{eff}} + 1}\right)^2 \tag{A.3}$$

where n_{eff} is the effective index of the waveguide mode.

The wavelength separation between successive transmission maxima is known as the Free Spectral Range (FSR) and is calculated as

$$\Delta\lambda = \frac{\lambda^2}{2n_{\text{eff}}L} \tag{A.4}$$

The FSR is a useful check to verify cavity length.

Experimental results

The following wavelength scans were an attempt to find the linear loss in the waveguide for the facets that showed evidence of SPDC in chapter 5. The free spectral range is approximately .2nm at 1550nm for the 1.7mm cavity formed by the end facets of the waveguide. There are no obvious resonances seen.

However, the first facets obtained from the designer did show appreciable etalon effects. This is shown in figure A.3.

For this figure, the FSR is about .24nm, which gives a cavity length of 1.57mm – fairly close to 1.7mm. The ratio of the maxima to minima averages to about 1.88. Thus, the linear loss co-efficient for this waveguide can be inferred and is found to be approximately .325/mm.

Useful Figures and Tables

Experiment Characterization - Optical efficiencies

Spectrometer Characterization

As the SPEC-10 camera for the SP2750 was so sensitive, it was necessary to calibrate the camera using a stack of attenuators. However, the detector heads for the available

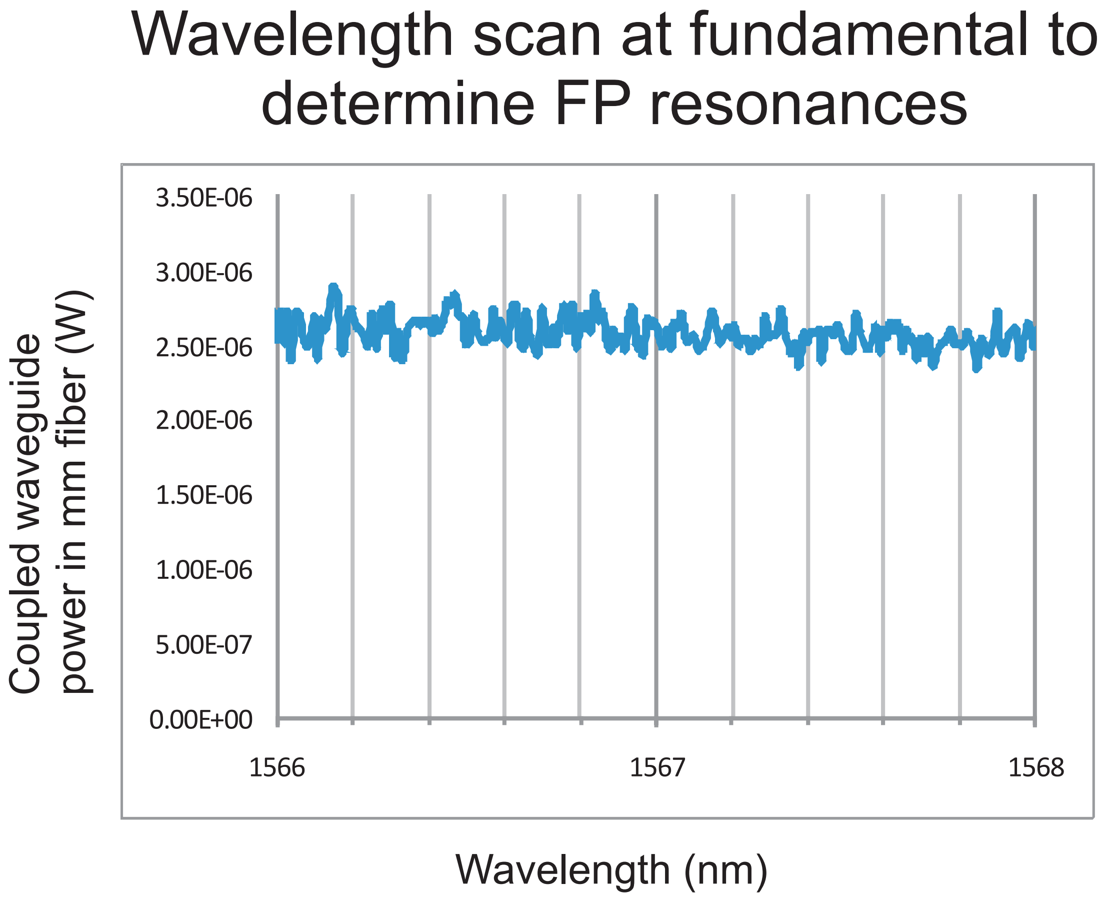

Figure A.1: Power vs wavelength scan for pump in TE mode for BRW guide - 2nd sample

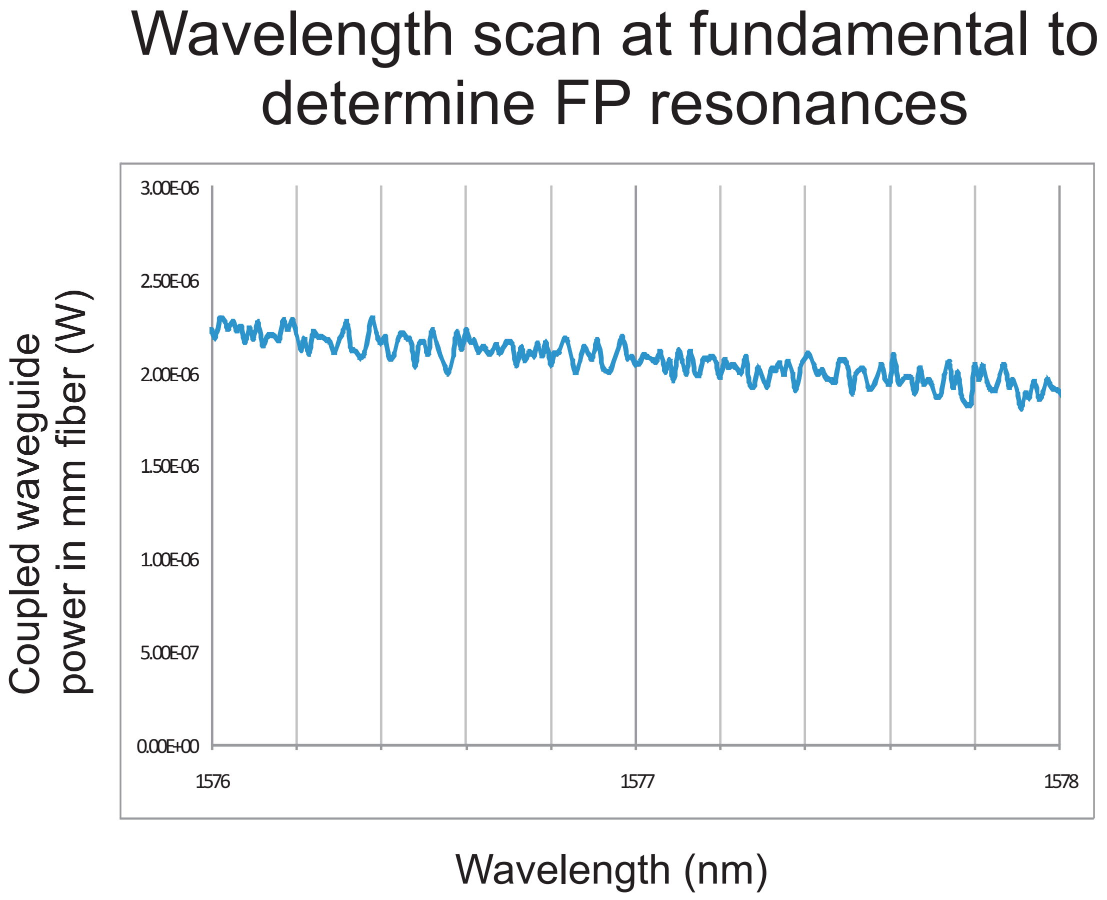

Figure A.2: Power vs wavelength scan for pump in TM mode for BRW guide - 2nd sample.

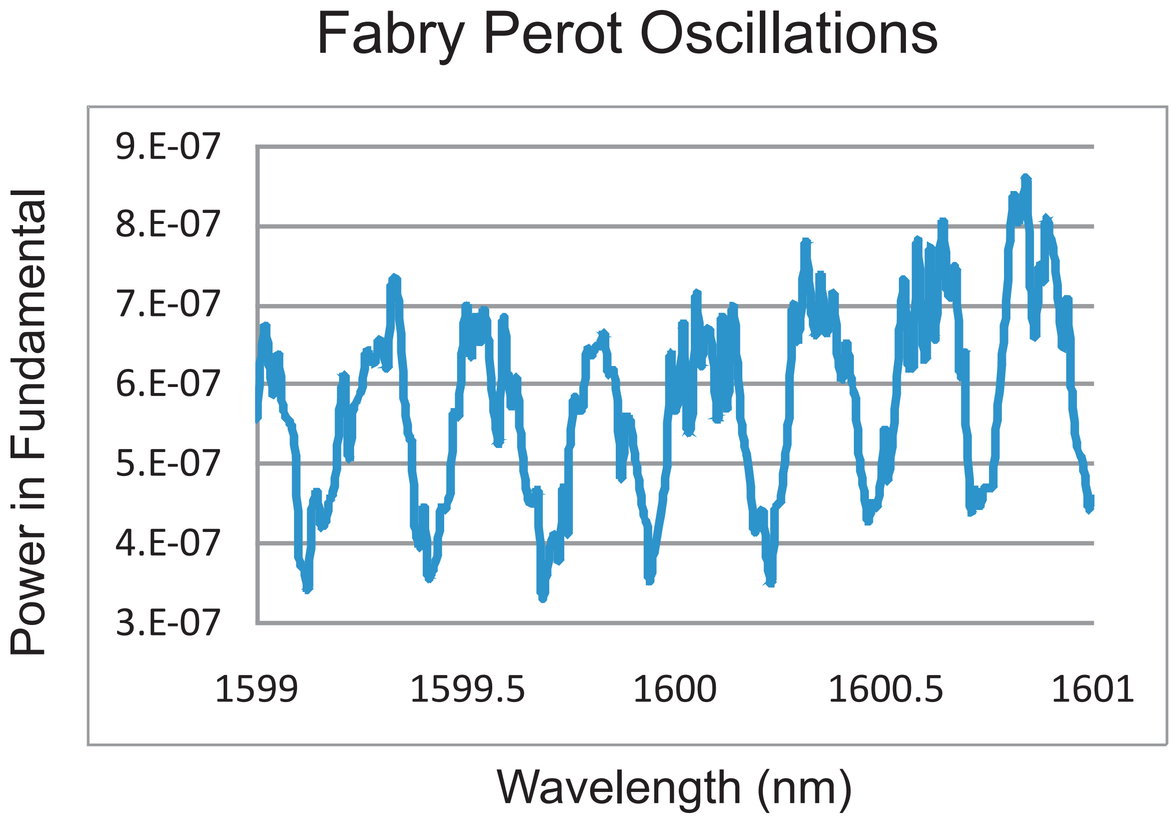

Figure A.3: Power vs wavelength scan for pump in TE mode for BRW guide - first sample

Transmission at 790nm	CW	Pulsed	CW	Pulsed
Position	TE	TE	TM	TM
1	100%	100%	100%	100%
2	92%	91%	94%	92%
3 no obj.	89%	88%	62%	62%
4 no obj.	79%	78%	57%	56%
4 no obj. polarcor in	74%	61%	43%	42%
3	51%	46%	36%	36%
4	46%	41%	32%	32%
4 polarcor in	42%	34%	24%	26%
coupled mm 50:50 AR splitter	21%	18%	15%	14%

Table A.1: Transmission through the setup for CW at 790nm. To be used with figure A.5

power meters were unable to measure power through the entire stack for even the highest available powers (Watts) at the stack input. Thus, the stack was split into two units. The linearity of each stack of attenuators over a range of powers was verified and their loss was estimated. The two stacks were combined and the power arriving at the spectrometer slits could be inferred. The calibration factor is approximately 5×10^{-13}Watts per count. The area under the signal on the spectrometer was taken as a representation of the power in the signal. This calibration was performed at 790nm using the 1200 lpm grating where the acquisition time was 1 second.

Transmission at 1580nm CW		
Position	TE	TM
1	100%	100%
2	95%	96%
3 no obj.	91%	59%
4 no obj.	88%	56%
4 no obj. polarcor in	61%	39%
3	28%	18%
4	23%	15%
4 polarcor in	16%	10%
coupled mm	16%	9%

Table A.2: Transmission through the setup for CW at 1580nm. To be used with figure A.4

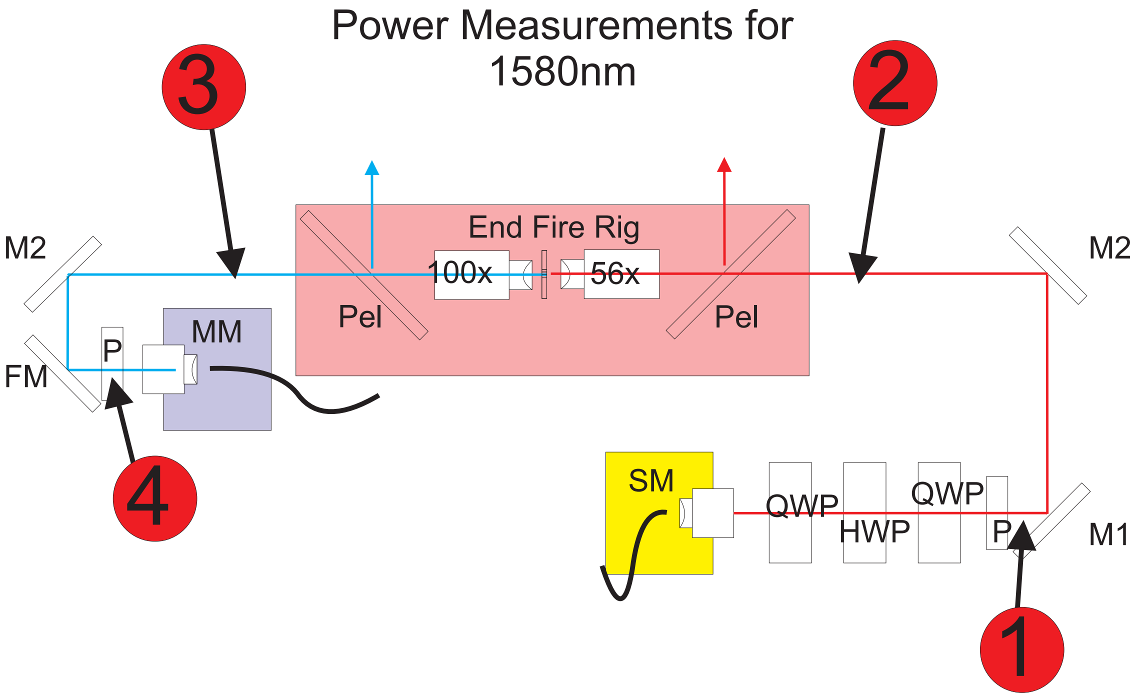

Figure A.4: A diagram of the setup for obtaining transmission measurements of the setup in the down conversion configuration – from left to right.

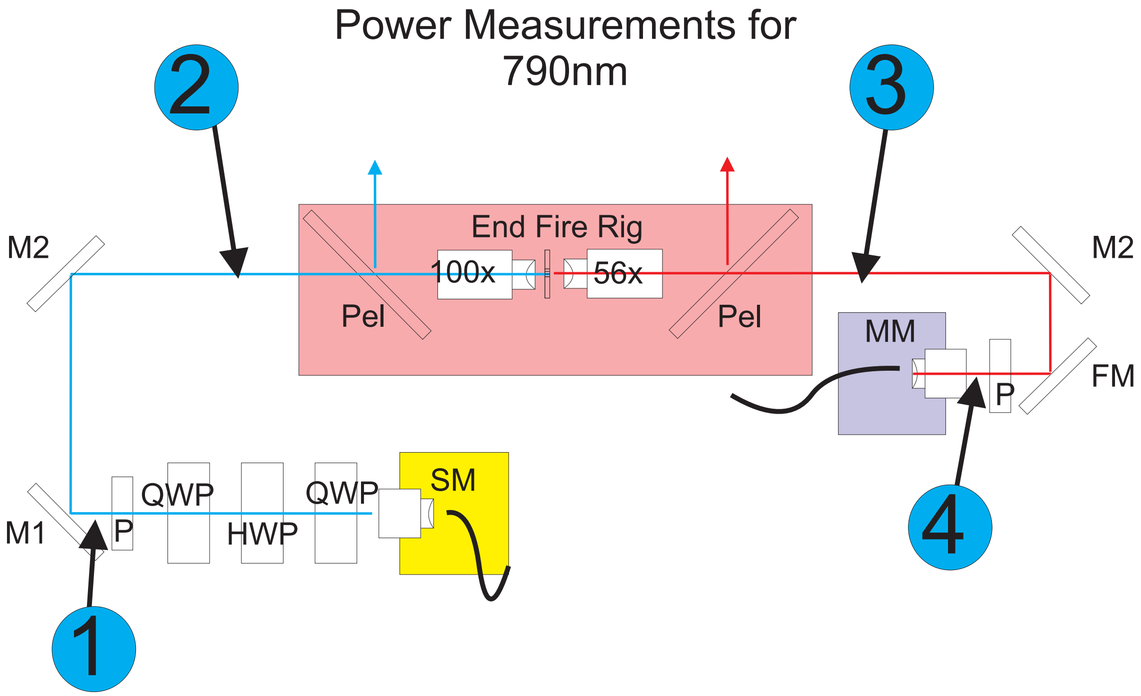

Figure A.5: A diagram of the setup for obtaining transmission measurements in the down conversion configuration – from left to right.

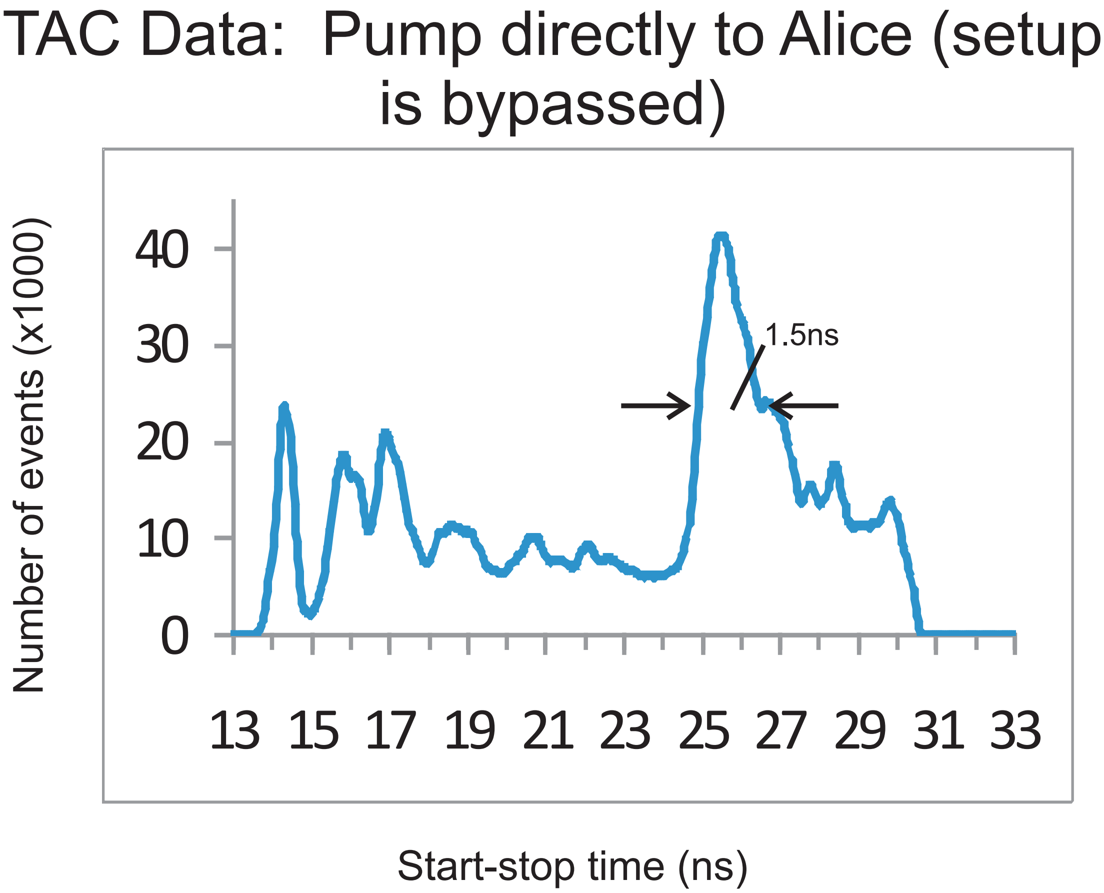

Figure A.6: The minimum time resolution of the experimental setup. The pulse from the laser was sent directly to Alice. The TAC was started on a trigger from the fast photodiode and stopped by a detection event. Roughly speaking, even though the optical pulse is only a few picoseconds, the width seen here is approximately 1.5 to 2ns.

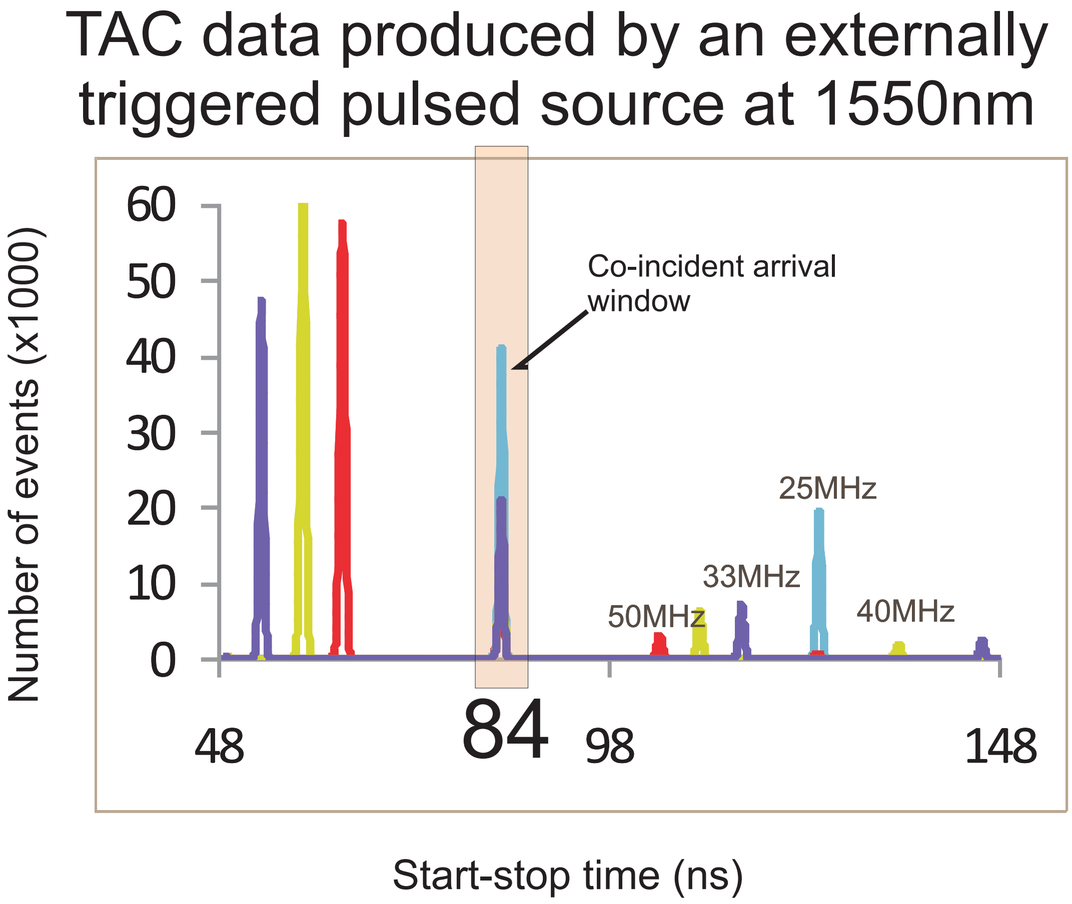

Figure A.7: An externally triggered pulsed source at 1550nm was injected into the setup at low intensity. Alice was armed synchronously with the arrival of this pulse. Bob's detection circuit was such that he would be able to detect the arrival of the same pulse within his detection window. This produced a peak at time t* in the data recorded by the BH card. Bobs window was large enough that for high enough optical frequencies, previous and successive pulses were also detected. However, the true coincidence time is independent of the pulse frequency, so by changing the frequency and noting which detection peak consistently remains, the true coincidence time can be found. This clearly occurred around the vicinity of 84 nanoseconds after the TAC started.

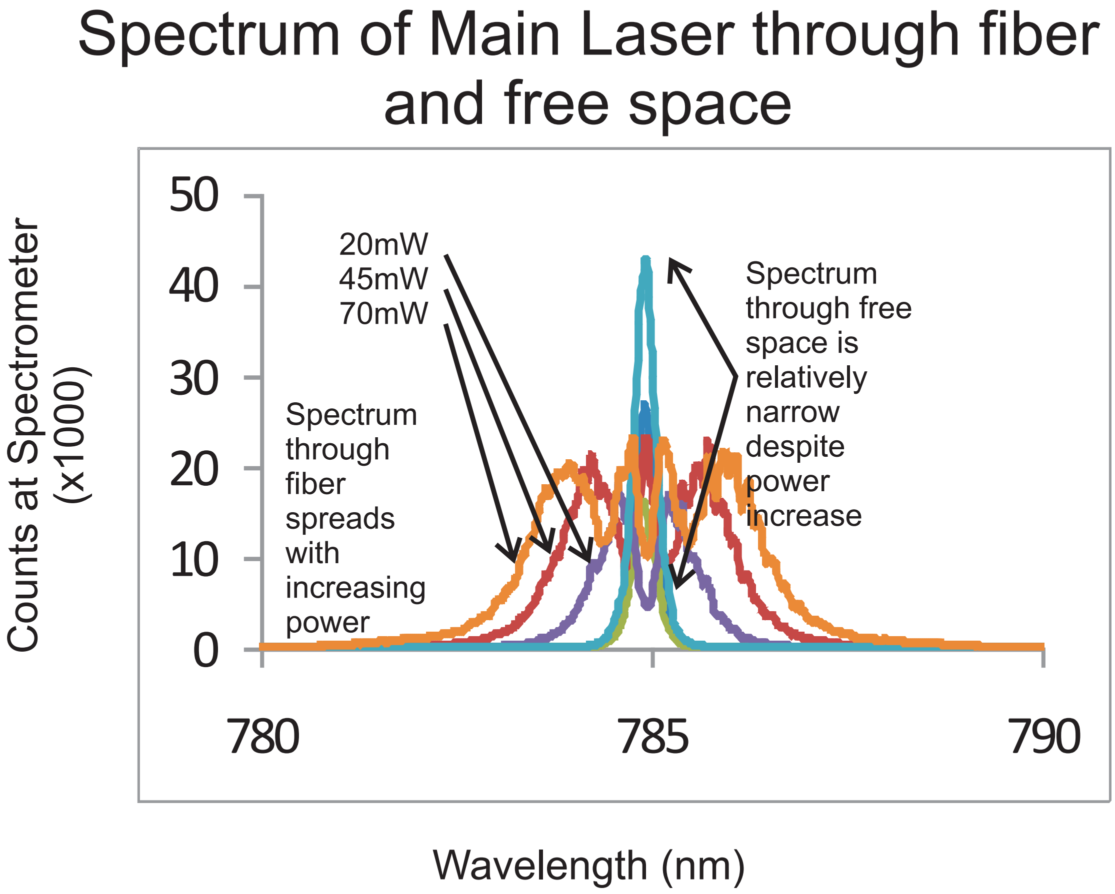

Figure A.8: The effect of fiber coupling the pump laser (pulsed) into the end fire rig. For increasing power, the spectrum gets only wider and in some cases, the spectral power decreases as a result of an increase in pump power. On the other hand, for free space, the spectrum stays nice and narrow. The benefit of the fiber scenario are that the output mode is nice and Gaussian. The fiber acts as a spatial filter.